



Marcello Congro Dias da Silva

**Experimental and numerical investigation of damage and
stress transfer mechanisms in cement materials**

Tese de Doutorado

Thesis presented to the Programa de Pós-graduação em Engenharia Civil of PUC-Rio in partial fulfillment of the requirements for the degree of Doutor em Ciências – Engenharia Civil.

Advisor: Prof. Deane de Mesquita Roehl

Co-Advisors: Prof. Flávio de Andrade Silva
Prof. Janine Domingos Vieira

Rio de Janeiro
May 2024



Marcello Congro Dias da Silva

**Experimental and numerical investigation of damage and
stress transfer mechanisms in cement materials**

Thesis presented to the Programa de Pós-Graduação em Engenharia Civil of PUC-Rio in partial fulfillment of the requirements for the degree of Doutor em Ciências – Engenharia Civil. Approved by the Examination Committee:

Prof. Deane de Mesquita Roehl

Advisor

Departamento de Engenharia Civil e Ambiental – PUC-Rio

Prof. Flávio de Andrade Silva

Co-Advisor

Departamento de Engenharia Civil e Ambiental – PUC-Rio

Prof. Janine Domingos Vieira

Co-Advisor

Departamento de Engenharia Civil – UFF

Prof. Lourdes Maria Silva de Souza

Departamento de Engenharia Civil e Ambiental – PUC-Rio

Prof. Oscar Aurelio Mendoza Reales

Departamento de Engenharia Civil – UFRJ

Prof. Murillo Vinícius Bento Santana

Institut Universitaire de Technologie – INSA Rennes

Prof. Luís Antônio Guimarães Bitencourt Júnior

Departamento de Estruturas e Geotecnia – USP

Rio de Janeiro, May 9th 2024.

All rights reserved.

Marcello Congro Dias da Silva

Marcello Congro holds a Bachelor's Degree in Civil Engineering from Pontifical Catholic University of Rio de Janeiro (2018) and an MSc Degree in Structural Engineering at Pontifical Catholic University of Rio de Janeiro (2020). Since 2016, he works at Tecgraf Institute/PUC-Rio, in the Multiphysics and Multiscale Modeling Group. In 2020, started the doctoral program at PUC-Rio. In 2024, started working as an aggregate professor at PUC-Rio.

Bibliographic data

Silva, Marcello Congro Dias da

Experimental and numerical investigation of damage and stress transfer mechanisms in cement materials / Marcello Congro Dias da Silva ; advisor: Deane de Mesquita Roehl ; co-advisors: Flávio de Andrade Silva, Janine Domingos Vieira. – 2024.

190 f. : il. color. ; 30 cm

Tese (doutorado)–Pontifícia Universidade Católica do Rio de Janeiro, Departamento de Engenharia Civil e Ambiental, 2024.

Inclui bibliografia

1. Engenharia Civil e Ambiental - Teses. 2. Cimento. 3. Dano. 4. Interface. 5. Método dos Elementos Finitos. 6. Arrancamento. I. Roehl, Deane de Mesquita. II. Silva, Flávio de Andrade. III. Vieira, Janine Domingos. IV. Pontifícia Universidade Católica do Rio de Janeiro. Departamento de Engenharia Civil e Ambiental. V. Título.

CDD: 624

Acknowledgments

In these years of PhD, I went through several years of dedication and effort, with personal and academic challenges. Several people have passed by me, and I would like to express my gratitude to some of them.

To my parents, Márcia and Nelson, and all my family, for everything they've always done for me, in addition to the love, caring, and unconditional daily support;

To my advisor, Prof. Deane Roehl, for all your patience, generosity, trust, and guidance throughout this work, in addition to all the teachings, advice and opportunities that have been granted in my academic and professional career. I would also like to thank you for the opportunity to be part of the Multiphysics Modeling and Simulation Group at Tecgraf Institute. Thank you for always trusting in my work and, above all, for being a great example and reference in my professional and academic life;

To my co-advisor, Prof. Flávio de Andrade Silva, for all the support, help, and advice given throughout the PhD journey. I also thank you for all the opportunities granted and for the research cooperation we have started during these years (and I hope that many more come ahead!);

To my co-advisor, Prof. Janine Domingos Vieira, for all the support, kindness, friendship and funny moments. Your support and our exchanges were essential during the development of this thesis. Thank you so much for everything and I hope our research cooperation can continue in the next years!

To Prof. Lourdes Maria Silva de Souza, for all the guidance, support, friendship, advice and ear tugs in the most crucial moments of this PhD. I am very grateful for you having closely accompanied me during this time. Without your support, this work would not have been the same. Thank you very much!

To Prof. Luís Bitencourt Júnior, Prof. Oscar Reales and Prof. Murillo Santana for agreeing to participate in this thesis committee and for all the availability and suggestions;

To Prof. Fernanda Lins Gonçalves Pereira, for all your friendship, advice and support throughout my academic career. You have always cheered for me, thank you for everything!

To Dr. Felipe Pinheiro, for always helping me with the experimental procedures developed in this thesis and for all the friendship. To all my friends of PUC-Rio, in special to Fernanda Salgado, Kíssila Goliath, Osmar Alexandre, Vítor Monteiro, and Fr. José Abel de Sousa, SJ for all your friendship and support;

To all LEM/DEC laboratory staff, in special to Euclides Moura, for the unwavering support throughout the execution of the experimental tests for this thesis;

To all my friends of Tecgraf Institute, in special to Dr. Marcelo Teixeira, for all your friendship and daily support. Extensive thanks also to Dr. Pedro Lobo, for always helping me with fruitful discussions and advice. Finally, I would like also to acknowledge all members of Multiphysics Modeling and Simulation Group, for all the partnership since I was an intern (in 2016!);

To Hélio Velez and Cláudio Guilherme, my best friends of this life, for always being by my side;

To Renato Gabriel, Caio Roncisvalle, Luis Paulo Andrioli and Lucas Repsold, for the old friendship and for all the support outside PUC-Rio;

To Prof. Hans Joakim Skadsem and Dr. Katherine Béltran-Jiménez, for all the hospitality and support during my research stay at Norway during the PhD;

For all those who, even if they are not explicitly mentioned here, have always supported me and helped me along this path;

To PUC-Rio, a place that, without a doubt, is my second home. I am grateful for all the moments and opportunities that have been given to me since I graduated. I experienced unforgettable moments at this university that were of great importance for my personal and professional growth, which will forever be linked to my story. It's always great to be here. Thank you very much!

This study was financed in part by the Coordenação de Aperfeiçoamento de Pessoal de Nível Superior - Brasil (CAPES) - Finance Code 001.

Abstract

Silva, Marcello Congro Dias da; Roehl, Deane de Mesquita (Advisor); Silva, Flávio de Andrade (Co-Advisor); Vieira, Janine Domingos (Co-Advisor). **Experimental and numerical investigation of damage and stress transfer mechanisms in cement materials.** Rio de Janeiro, 2024. 190p. Tese de Doutorado – Departamento de Engenharia Civil e Ambiental, Pontifícia Universidade Católica do Rio de Janeiro.

The interaction between cement and other constituents plays an important role in several engineering applications, such as in the construction and oil and gas (O&G) industries. In the construction industry, fiber-reinforced cementitious composites (FRC) have gained wide prominence for their excellent mechanical properties. Fibers can increase the post-cracking strength of the composite, improving concrete durability and controlling crack propagation in the cement matrix. Moreover, they perform a bridging mechanism at the interface, changing the material post-peak behavior. On the other hand, in the O&G industry, cement and steel are essential structural elements that should ensure well integrity and provide zonal isolation. This interaction is considered critical since a strong bond may prevent the generation of microannulus leakage paths along the cement and steel interface, which also can lead to crack propagation.

In this sense, a comprehensive study of the damage mechanisms developed at the cement interface is essential in both applications to understand the material mechanical behavior. Therefore, it is possible to develop finite element models that consider the pullout mechanisms (debonding, adhesion, and friction) and the interface parameters that govern the local mechanical behavior of cement. While numerous experimental studies and numerical models exist, the current state-of-the-art lacks formulations investigating damage mapping and stress transfer interactions at the cement interface, particularly considering different cement matrix types and steel fiber geometries.

This thesis addresses a critical gap in the literature by proposing the numerical modeling of interfacial debonding and damage evolution mechanisms for cement advanced materials and well integrity applications. Elastoplastic finite element models, incorporating surface-based cohesive formulations with contact, are employed to simulate cement interface behavior. Additionally, mechanical characterization tests and microCT analyses are conducted to validate and support

the numerical model results, assessing shear strength and damage propagation at the cement interface. Therefore, this research can offer insights for engineers across disciplines to enhance mechanical performance and prototype new advanced materials by damage evolution investigation. The developed finite element models emerge as valuable tools for cost-effective evaluations of cement performance through reliably simulating pullout/pushout behavior.

Keywords

Cement; Damage; Interface; Finite Element Method; Pullout; Fiber/matrix interaction.

Resumo

Silva, Marcello Congro Dias da; Roehl, Deane de Mesquita (Orientadora); Silva, Flávio de Andrade (Coorientador); Vieira, Janine Domingos (Coorientadora). **Investigação experimental e numérica do dano e mecanismos de transferência de tensão em materiais cimentícios**. Rio de Janeiro, 2024. 190p. Tese de Doutorado – Departamento de Engenharia Civil e Ambiental, Pontifícia Universidade Católica do Rio de Janeiro.

A interação entre o cimento e outros constituintes desempenha um papel importante em várias aplicações de Engenharia, como nas indústrias de construção civil e de óleo e gás (O&G). Na indústria da construção, os compósitos cimentícios reforçados com fibras (CRF) ganharam grande destaque por suas excelentes propriedades mecânicas. As fibras podem aumentar a resistência crítica à fissuração do compósito, melhorando a durabilidade do concreto convencional e controlando a propagação de fissuras na matriz cimentícia. Além disso, as fibras desenvolvem um mecanismo de ponte de transferência de tensões na interface, alterando o comportamento pós-pico do compósito. Por outro lado, na indústria de O&G, cimento e aço são elementos estruturais essenciais que devem garantir a integridade de poços e fornecer isolamento para a passagem de fluidos, especialmente em cenários de abandono. Esse mecanismo na interface é considerado crítico, uma vez que uma interação não eficaz pode permitir a formação de caminhos de vazamento no microanular ao longo da interface cimento-aço, gerando a formação de fissuras.

Neste sentido, um estudo abrangente dos mecanismos de dano desenvolvidos na interface do cimento é essencial em ambas as aplicações para entender o comportamento mecânico do material. Portanto, faz-se necessário o desenvolvimento de modelos de elementos finitos que considerem os mecanismos de *pullout* (descolamento, adesão e atrito) e os parâmetros de interface que governam o comportamento mecânico local do cimento. Embora existam numerosos estudos experimentais e modelos numéricos na literatura, o estado-da-arte atual carece de formulações que investiguem os mecanismos de mapeamento de dano e as interações de transferência de tensão na interface do cimento, especialmente considerando diferentes tipos de matriz de cimento e geometrias de fibra de aço.

Esta tese aborda uma lacuna crítica na literatura ao propor a modelagem numérica do descolamento interfacial e mecanismos de evolução de dano para

materiais cimentícios avançados e em aplicações de integridade de poços. Modelos de elementos finitos elastoplásticos, incorporando formulações coesivas baseadas em superfícies de contato, são empregados para simular o comportamento da interface do cimento. Além disso, ensaios experimentais de caracterização mecânica e análises de microtomografia são realizados para validar e apoiar os resultados do modelo numérico, avaliando a resistência ao cisalhamento e a propagação de dano na interface do cimento. Assim sendo, esta pesquisa pode oferecer contribuições para engenheiros de diferentes áreas aprimorarem o desempenho mecânico e prototipar novos materiais avançados por meio da investigação da evolução do dano. Os modelos de elementos finitos desenvolvidos emergem como ferramentas valiosas para avaliações de desempenho do cimento de maneira eficaz, simulando confiavelmente o comportamento de *pullout/pushout*.

Palavras-chave

Cimento; Dano; Interface; Método dos Elementos Finitos; Arrancamento; Interação fibra/matriz.

Content

1 Introduction	23
1.1. Thesis background	23
1.2. The Damage and Fracture of Materials and Advanced Cementitious Materials research lines	25
1.3. Objectives of the thesis	27
1.4. Thesis outline	27
2 Interfacial debonding and stress transfer mechanisms in cement materials	30
2.1. Overview	30
2.1.1. Cement-based materials and stress transfer mechanisms	31
2.2. Pullout behavior of cement composite materials	34
2.2.1. Bonding	35
2.2.2. Critical embedment length and fiber rupture	36
2.2.3. Pullout mechanisms for straight fibers	37
2.2.4. Pullout mechanisms for hooked-end fibers	39
2.2.5. Influence of fiber type in pullout tests	41
2.2.6. Influence of fiber orientation and matrix strength in pullout tests	43
2.3. Interfacial damage mechanisms	46
2.4. Damage due to anchorage failure in deformed fibers	51
2.5. Experimental methods for damage mapping	53
3 Experimental tests	59
3.1. Matrix A	60
3.1.1. Materials and methods	60
3.1.2. Results	67
3.2. Matrix B	74
3.2.1. Materials and methods	74
3.2.2. Results	75

	11
4 Numerical modeling	84
4.1. Analytical and finite element models for pullout	84
4.2. Numerical methodology	89
4.2.1. Cement matrix	89
4.2.2. Steel fiber	94
4.2.3. Fiber/matrix interface	95
4.3. Results and discussions	100
4.3.1. Proof of concept models	101
4.3.2. Developed pullout models	117
5 Numerical case study on the pushout shear strength of conventional and expanding cement-casing sections for well integrity	137
5.1. The cement/casing interface problem in O&G applications	137
5.2. Finite element models for pushout tests	142
5.3. Sensitivity analyses	144
5.4. Mesh convergence tests	147
5.5. Results	148
5.5.1. Conventional class G sections	148
5.5.2. Expanding cement sections	153
6 Conclusions and suggestions for future works	160
6.1. Conclusions	160
6.2. Suggestions for future works	162
6.2.1. Improvements in the experimental workflow	162
6.2.2. Improvements in the mathematical model	163
6.2.3. Applications to other material types	163
References	164
A. Appendix A	183
B. Appendix B	186

List of Figures

Figure 1.1 – (a) Fiber deformation during pullout captured by scanning electron microscope (courtesy from TU Dresden); (b) Schematic representation before pullout (Adapted from [12]).	24
Figure 1.2 – Thesis outline with the main steps.	29
Figure 2.1 – Phases of conventional concrete or fiber-reinforced cement-based materials.	30
Figure 2.2 – Structure of a cement composite material (Adapted from [35]).	31
Figure 2.3 – Representation of the stress distribution stages during fiber pullout (Adapted from [12]).	33
Figure 2.4 – Distribution of shear stresses along the fiber: (a) for intact composite and (b) for cracked composite (Adapted from [36]).	34
Figure 2.5 – Mechanisms for fiber/matrix interface interactions (Adapted from [47]).	35
Figure 2.6 – Schematic representation of fiber bridging/debonding in pullout tests (Adapted from [47]).	36
Figure 2.7 – Pullout load-end slip curve for a smooth straight fiber (Adapted from [48]).	38
Figure 2.8 – Mechanisms for the straight smooth fiber pullout test (Adapted from [48]).	39
Figure 2.9 – Pullout load-end slip curve for a hooked-end fiber.	40
Figure 2.10 – Mechanisms for the hooked-end fiber pullout test (Adapted from [48]).	41
Figure 2.11 – Distinct steel fiber geometries (undeformed or deformed shapes) (Adapted from [58]).	42
Figure 2.12 – Typical pullout responses for distinct steel fibers considering different matrix compressive strengths (f_c) and embedded lengths (L_e) (Adapted from [48]).	43
Figure 2.13 – Pullout relationships for hooked-end fibers from a high strength cement matrix (85 MPa) at several inclination angles; UTS = ultimate tensile strength.	44

Figure 2.14 – (a) Bending of a fiber across a crack; (b) components of crack bridging force (Adapted from [36]).....	45
Figure 2.15 – Orientation effects for distinct fiber types (Adapted from [22]).	46
Figure 2.16 – Damage development after fiber break formation: (a) crack propagation, (b) matrix yielding, (c) debonding at the interface (Adapted from [75]).	47
Figure 2.17 – Damage events leading to the final failure of a composite considering unidirectional loading (Adapted from [75]).....	48
Figure 2.18 – Scan images of a fiber in distinct pull-out stages, where the lower images are magnifications of the upper images (Adapted from [92]).	51
Figure 2.19 – CMOD-time responses for (a) polymeric fiber-reinforced concrete and (b) steel fiber-reinforced concrete (Adapted from [94]).....	52
Figure 2.20 – Typical experimental setup for AE methods (Adapted from [102]).	54
Figure 2.21 – Microcracks evaluated through the optic microscope and by fluorescent methods: (a) open nicol; (b) crossed nicol; (c) open nicol with UV; bit.: betume; m.c.: microcrack (Adapted from [103]).	55
Figure 2.22 – X-ray acquisition and reconstruction process (Adapted from [106]).	56
Figure 2.23 – Distribution map of Young’s modulus in the cement sample (Adapted from [114])......	57
Figure 2.24 – Distribution map of hardness in the cement sample (Adapted from [114]).	57
Figure 3.1 – Schematic workflow for the experimental tests carried out in this thesis.	59
Figure 3.2 – Flow test carried out with Matrix A.....	61
Figure 3.3 – Setup for the uniaxial compression tests in Matrix A.	62
Figure 3.4 – Schematic representation and specimen dimensions for the pullout tests.	63
Figure 3.5 – Specimens for the pullout test (“R” for straight and “G” for hooked-end steel fiber).	63
Figure 3.6 – (a) Pullout test configuration and (b) detail for the specimen fixation.	64
Figure 3.7 – (a) Zeiss-Xradia 510 Versa equipment for the microCT analyses; (b) schematic representation of the CT scanning and specimen region of interest.....	66
Figure 3.8 – X-ray scanned volume for the straight steel fiber in Matrix A.	66

Figure 3.9 – Stress-strain representative curve for the uniaxial compressive test of Matrix A.....	67
Figure 3.10 – Pullout load-displacement of the straight steel fiber in Matrix A.	68
Figure 3.11 – Pullout load-displacement of the hooked-end steel fiber in Matrix A.	68
Figure 3.12 – Pullout load-displacement of the straight steel fiber in the poorly consolidated Matrix A.....	70
Figure 3.13 – Pullout load-displacement of the hooked-end steel fiber in the poorly consolidated Matrix A.	70
Figure 3.14 – Micrograph (0.4x) of straight steel fiber in Matrix A:.....	71
Figure 3.15 – Micrograph (0.4x) of hooked-end steel fiber in Matrix A: (a) before pullout; (b) partial debonding (fiber pullout of 7 mm). Damaged areas are indicated in red color.....	72
Figure 3.16 – Micrograph (1x) of straight steel fiber in poorly consolidated Matrix A: (a) before pullout; (b) after pullout. Damaged areas are indicated in red color.....	73
Figure 3.17 – Micrograph (1x) of hooked-end steel fiber in poorly consolidated Matrix A: (a) before pullout; (b) after pullout. Damaged areas are indicated in red color.....	73
Figure 3.18 - Stress-strain curve for the uniaxial compressive test for Matrix B.....	75
Figure 3.19 – Setup for the indirect tensile test.	76
Figure 3.20 - Stress-strain curve for the indirect tensile test for Matrix B.....	77
Figure 3.21 – Pullout load-displacement of the straight steel fiber for Matrix B.....	78
Figure 3.22 – Pullout load-displacement of the hooked-end steel fiber for Matrix B.	78
Figure 3.23 – Comparison of the pullout response for the straight steel fiber considering distinct types of cement matrix.	79
Figure 3.24 – Comparison of the pullout response for the hooked-end steel fiber considering distinct types of cement matrix.	80
Figure 3.25 – Micrograph (0.4x) of straight steel fiber in Matrix B: (a) before pullout; (b) partial debonding (fiber pullout of 7 mm). Damaged areas are indicated in red color.....	81

Figure 3.26 – Micrograph (0.4x) of hooked-end steel fiber Matrix B: (a) before pullout; (b) partial debonding (fiber pullout of 7 mm). Damaged areas are indicated in red color.....	81
Figure 3.27 – New configuration for the microCT analyses for the <i>S03</i> samples: (a) schematic representation; (b) X-ray scanned volume.	82
Figure 3.28 – Micrograph (0.4x) of the hook region in Matrix B: (a) before pullout; (b) partial debonding (fiber pullout of 7 mm). Damaged areas are indicated in red color.....	82
Figure 3.29 – Micrograph (0.4x) of the hook region in Matrix B after entire pullout. Damaged areas are indicated in red color.	83
Figure 4.1 - Analytical stress-slip (τ - Δ) pullout model proposed by Lawrence [122].	85
Figure 4.2 – Pullout analytical model proposed by Naaman [43].	86
Figure 4.3 – Representative pullout model proposed by Sujivorakul et al. [55]	87
Figure 4.4 – Finite element formulations carried out for modeling adhesive bonding (Adapted from [56]).	88
Figure 4.5 – Schematic representation of the surface-based contact formulation.....	88
Figure 4.6 – Dependence of stress-strain curve in compression for CDP model (Adapted from [140]).	93
Figure 4.7 – Dependence of stress-strain curve in tension for CDP model (Adapted from [140])......	93
Figure 4.8 – Required input parameters for the CDP model.....	94
Figure 4.9 – Exponential traction-separation response for the cohesive zone interaction.....	97
Figure 4.10 – Friction behavior in the tangential direction for the pullout FE models.....	98
Figure 4.11 – Pressure-overclosure model (Adapted from [153]).	99
Figure 4.12 – Contact detection using the maximum detection distance (Adapted from [154])......	100
Figure 4.13 – Schematic setup representation of the pullout test performed by Cox (Adapted from [155]).	101
Figure 4.14 – Matrix compressive behavior for Cox’s experimental test.	102
Figure 4.15 – Matrix tension behavior for Cox’s experimental test.	102
Figure 4.16 – Fiber post-peak behavior for Cox’s experimental test.....	103

Figure 4.17 – Geometry and boundary conditions for the straight fiber proof of concept model.	104
Figure 4.18 – Mesh dependence tests considering (a) coarse mesh with ~265 elements; (b) intermediate mesh with ~620 elements; (c) fine mesh with ~3930 elements.	105
Figure 4.19 – Pullout load-displacement curves considering three distinct meshes and the experimental reference for the straight pullout proof of concept model.	106
Figure 4.20 – Straight fiber pullout mechanisms detected in the numerical model (stress units in MPa).....	107
Figure 4.21 – Interface behavior for the hooked-end fiber pullout model.	108
Figure 4.22 – Mesh dependence tests considering (a) coarse mesh with ~777 elements; (b) intermediate mesh with ~1450 elements; (c) fine mesh with ~3500 elements.	109
Figure 4.23 – Pullout load-displacement curves considering three distinct meshes and the experimental reference for the hooked-end pullout proof of concept model.	110
Figure 4.24 – Hooked-end fiber pullout mechanisms detected in the second conceptual model.....	111
Figure 4.25 – Shear stress transfer mechanisms detected by second conceptual model: (a) first step of the analysis; (b) during the fiber hook deformation; (c) and (d) at fiber debonding; (e) final steps of the analysis.....	113
Figure 4.26 – Normal stress-normal opening behavior at one interface fiber node of the model.	114
Figure 4.27 – Shear stress-slip opening behavior at one interface fiber node of the model.....	114
Figure 4.28 – Plastic strain evolution at the pullout model: (a) first steps; (b) during fiber debonding; (c) after fiber debonding.....	115
Figure 4.29 – Pareto chart of the standardized effects for the maximum pullout load in straight fiber proof of concept model.	116
Figure 4.30 – Pareto chart of the standardized effects for the maximum pullout load in hooked-end fiber proof of concept model.	116
Figure 4.31 – Boundary conditions adopted for the model and contact region between the surfaces (in green color).	119
Figure 4.32 – Pullout load-displacement experimental and numerical results for the straight fiber in Matrix A.	121

Figure 4.33 – Shear stress transfer mechanisms detected for the straight fiber in Matrix A model: (a) at the first step; (b) at peak load); (c) during debonding; (d) during friction.	122
Figure 4.34 – Plastic strain concentration in the upper part of the specimen captured by the numerical model at $\delta = 1$ mm.	123
Figure 4.35 – Concentration of damage for the straight steel fiber in Matrix A (region of interest) at $\delta = 7$ mm: (a) numerical model; (b) microCT analysis.....	123
Figure 4.36 – Pullout load-displacement experimental and numerical results for the straight fiber in Matrix B.	125
Figure 4.37 – Shear stress transfer mechanisms detected for the straight fiber in Matrix B model: (a) at the first step; (b) at the peak load; (c) during debonding; (d) during friction.	126
Figure 4.38 – Plastic strain concentration in the upper part of the specimen in Matrix B captured by the numerical model at $\delta = 1$ mm.....	127
Figure 4.39 – Concentration of damage for the straight steel fiber in Matrix B at $\delta = 7$ mm: (a) numerical model; (b) microCT analysis.	127
Figure 4.40 – Boundary conditions adopted for the 3D model for the hooked-end steel fiber.	128
Figure 4.41 – Contact region between the fiber/matrix surface (in yellow color).	129
Figure 4.42 – Pullout load-displacement experimental and numerical results for the straight fiber in Matrix A.	130
Figure 4.43 – Shear stress transfer mechanisms detected for the hooked-end fiber in Matrix A model: (a) at the first step; (b) at the peak load; (c) during debonding; (d) during friction.	131
Figure 4.44 – Plastic strain concentration on the specimen captured by the numerical model at $\delta = 1$ mm.....	132
Figure 4.45 – Concentration of damage for the hooked-end steel fiber in Matrix A at $\delta = 7$ mm: (a) numerical model; (b) microCT analysis.	132
Figure 4.46 – Pullout load-displacement experimental and numerical results for the straight fiber in Matrix B.	133
Figure 4.47 – Shear stress transfer mechanisms detected for the hooked-end fiber Matrix B model: (a) at the first step; (b) at the peak load; (c) during debonding; (d) during friction.	134
Figure 4.48 – Plastic strain concentration captured by the numerical model at $\delta = 5$ mm.....	135

Figure 4.49 – Concentration of damage for the hooked-end steel fiber in Matrix B at $\delta = 7$ mm: (a) numerical model; (b) microCT analysis.	135
Figure 5.1 – (a) Sections cut for pushout testing; (b) Cement sections inside the 2-meter casing before the cut for pushout experiments (Adapted from [34]).	141
Figure 5.2 – Boundary conditions for the model and contact region between the surfaces (in green color).	144
Figure 5.3 – Pareto chart of the standardized effects for the pushout maximum load in conventional class G samples.	146
Figure 5.4 – Response surface plots: (a) Peak load variation in terms of friction coefficient and damage initiation parameter; (b) Peak load variation in terms of exponential damage parameter and cohesive interface stiffness....	147
Figure 5.5 – Pushout load-displacement experimental and numerical results for section ‘C’ conventional cement.....	148
Figure 5.6 – Pushout load-displacement experimental and numerical results for section ‘D’ conventional cement.....	149
Figure 5.7 – Pushout load-displacement experimental and numerical results for section ‘E’ conventional cement.....	149
Figure 5.8 – Plastic flag for section ‘C’: (a) $\delta = 0.1$ mm; (b) $\delta = 1$ mm; (c) $\delta = 4$ mm.	151
Figure 5.9 – Plastic strain evolution for section ‘C’: (a) $\delta = 0.1$ mm; (b) $\delta = 1$ mm; (c) $\delta = 4$ mm.....	152
Figure 5.10 – Pushout load-displacement experimental and numerical results for section ‘E’ expanding cement.	153
Figure 5.11 – Pushout load-displacement experimental and numerical results for section ‘G’ expanding cement.....	154
Figure 5.12 – Plastic flag for section ‘E’: (a) $\delta = 0.1$ mm; (b) $\delta = 1$ mm; (c) $\delta = 4$ mm.	155
Figure 5.13 – Plastic strain evolution for section ‘E’: (a) $\delta = 0.1$ mm; (b) $\delta = 1$ mm; (c) $\delta = 4$ mm.....	156
Figure 5.14 – Plastic strains associated with the pushout load-displacement curve for conventional cement section ‘C’.	158
Figure 5.15 – Plastic strains associated with the pushout load-displacement curve for expansive cement section ‘E’.	159
Figure A.1 – Uniaxial compressive tests for Matrix A.	183
Figure A.2 – Uniaxial tensile tests for Matrix A [13].	184
Figure A.3 – Uniaxial compressive tests for Matrix B.	184

Figure A.4 – Indirect tensile tests for Matrix B.....	185
Figure B.1 – Micrograph (0.4x) of straight steel fiber in Matrix A: (a) before pullout; (b) partial debonding (fiber pullout of 7 mm). Microcracks/damage in (b) are not marked in red.	186
Figure B.2 – Micrograph (0.4x) of hooked-end steel fiber in Matrix A: (a) before pullout; (b) partial debonding (fiber pullout of 7 mm). Microcracks/damage in (b) are not marked in red.	187
Figure B.3 – Micrograph (0.4x) of straight steel fiber in poorly consolidated Matrix A: (a) before pullout; (b) partial debonding (fiber pullout of 7 mm). Microcracks/damage in (b) are not marked in red.	187
Figure B.4 – Micrograph (0.4x) of hooked-end steel fiber in poorly consolidated Matrix A: (a) before pullout; (b) partial debonding (fiber pullout of 7 mm). Microcracks/damage in (b) are not marked in red.	188
Figure B.5 – Micrograph (0.4x) of straight steel fiber in Matrix B: (a) before pullout; (b) partial debonding (fiber pullout of 7 mm). Microcracks/damage in (b) are not marked in red.	188
Figure B.6 – Micrograph (0.4x) of hooked-end steel fiber in Matrix B: (a) before pullout; (b) partial debonding (fiber pullout of 7 mm). Microcracks/damage in (b) are not marked in red.	189
Figure B.7 – Micrograph (0.4x) of the hook region in Matrix B: (a) before pullout; (b) partial debonding (fiber pullout of 7 mm). Microcracks/damage in (b) are not marked in red.	189
Figure B.8 – Micrograph (0.4x) of the hook region in Matrix B after entire pullout. Microcracks/damage are not marked in red.	190

List of Tables

Table 2.1 – Effect of several methods for interfacial performance of steel fiber-reinforced concrete [79].	49
Table 2.2 – Effect of several methods for mechanical global behavior of fiber-reinforced concrete [79].	50
Table 3.1 – Matrix A mix proportions.	60
Table 3.2 – Image acquisition data for the microCT analyses.	65
Table 3.3 – MicroCT scans carried out in this research.	65
Table 3.4 – Matrix B mix proportions.	74
Table 4.1 – Interface parameters for the straight pullout proof of concept model.	105
Table 4.2 – Interface parameters for the hooked-end pullout proof of concept model.	109
Table 4.3 – Elastic and mechanical parameters for the matrix A.	118
Table 4.4 – Elastic and mechanical parameters for the steel fiber.	118
Table 4.5 – Interface parameters for Matrix A and straight steel fiber after the calibration with the experimental results.	120
Table 4.6 – Elastic and mechanical parameters for Matrix B.	124
Table 4.7 – Interface parameters for Matrix B and straight steel fiber after the calibration with the experimental results.	124
Table 4.8 – Interface parameters for Matrix A and hooked-end steel fiber after the calibration with the experimental results.	129
Table 4.9 – Interface parameters for Matrix B and straight steel fiber after the calibration with the experimental results.	133
Table 5.1 – Constitutive parameters for the conventional class G cement.	143
Table 5.2 – Elastic parameters for the steel casing.	143
Table 5.3 – Constitutive parameters for the expanding cement.	143
Table 5.4 – Interface parameters for the conventional class G cement and the steel casing after the calibration with the experimental results.	145
Table 5.5 – Interface parameters for the expanding cement and the steel casing after the calibration with the experimental results.	145

List of Abbreviations

2D	Two-dimensional
3D	Three-dimensional
AE	Accoustic emission
CCC	Central circumscribed composite design
CDP	Concrete damage plasticity
CM	Compression meridian
CMOD	Crack mouth opening displacement
C-S-H	Calcium silicate hydrate
DEC	Department of Civil and Environmental Engineering
DIC	Digital Image Correlation
DOE	Design of Experiments
FE	Finite element
FEM	Finite Element Method
FRC	Fiber-reinforced cementitious composites
GFRP	Glass fiber-reinforced polymer
ITZ	Interfacial Transition Zone
LVDT	Linear variable differential transformer
NORCE	Norwegian Research Center
O&G	Oil and gas
P&A	Plug and abandonment
PVA	Polyvinyl
RSM	Response Surface Methodology
SCA	Silane coupling agent
TM	Tensile meridian
UTS	Ultimate tensile strength
XFEM	Extended Finite Element Method
ZnPh	Zinc phosphate

“It is not how much we do, but how much love we put into doing. It is not how much we give, but how much love is put into giving.”

Mother Teresa

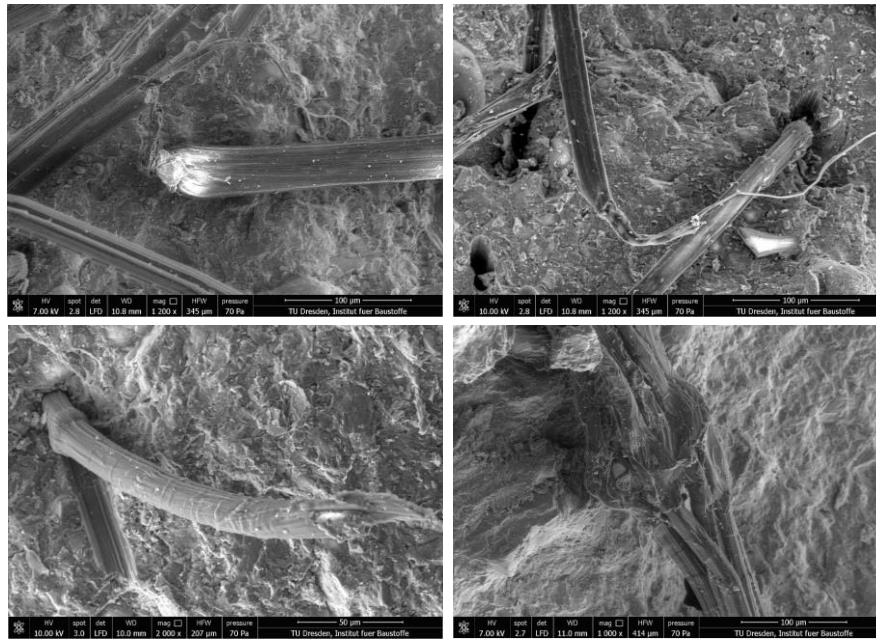
1 Introduction

1.1. Thesis background

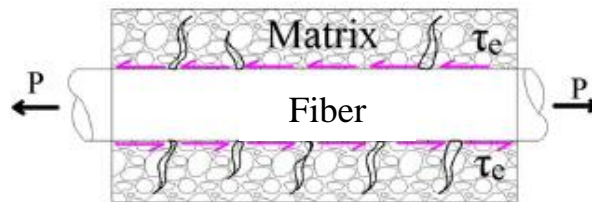
In the last decades, fiber-reinforced cementitious composites (FRC) have gained wide prominence in the construction industry for their excellent mechanical properties. They can increase the critical cracking strength of the composite [1], [2], improving concrete durability and controlling crack propagation [1]–[4].

The inclusion of fibers in the cement matrix also influences the stress transfer mechanisms. In this process, the effects of debonding, adhesion, and friction at the fiber/matrix interface play an essential role in the crack propagation behavior of the composite. After matrix cracking initiation, fibers start to develop a bridging mechanism, changing the post-cracking behavior of the composite [5], [6]. The stress transfer mechanisms are associated with the interfacial bond properties of the fiber/matrix region. According to Abdallah et al. [7], the interface is where tensile forces are transmitted to the fibers and the surrounding cement matrix. In regions where the bond is weak, fiber pullout occurs at low loading levels, and the fiber does not contribute to controlling crack propagation. On the other hand, if the bond is strong, damage mechanisms start at the cement interface and influence the global mechanical behavior of concrete. Consequently, additional studies regarding the bond failure mechanisms are necessary to investigate the mechanical behavior of FRC at a local level of observation.

Several studies are reported in the literature [8]–[10] regarding the interaction between fiber and matrix and their interfacial properties, especially for the manufacturing process of the composite, where the bonding/debonding mechanisms are essential to understand the stress transfer around the fiber. In this sense, interfacial properties affect the stress transfer mechanisms at the fiber/matrix interface. Therefore, weak interface bonding may lead to ineffective stress transfer and the development of microcracks at the interface [11]. Figure 1.1 (a) presents the effects of debonding and deformation developed at PVA fiber during a pullout test, while Figure 1.1 (b) presents a schematic representation of this mechanism.



(a)



(b)

Figure 1.1 – (a) Fiber deformation during pullout captured by scanning electron microscope (courtesy from TU Dresden); (b) Schematic representation before pullout (Adapted from [12]).

The proper control of the fiber bridging effect and damage evolution mapping in the fiber adjacencies is key to material design and prototyping since these materials are desired to present greater durability performance. Damage mapping can further aid in identifying critical regions within the composite, particularly concerning crack propagation.

The significance of studying mechanisms occurring at the cement interface extends beyond the construction industry, finding substantial relevance in the oil and gas sector, specifically in Plug and Abandonment (P&A) operations and well integrity management. For instance, this subject has gained prominence, mainly driven by environmental concerns and regulatory activities requiring the long-term safe and ecologic storage of CO₂. Compromising well integrity can result in costly remedial operations and substantial environmental contamination. Hence, the integrity of the cement sheath and its interaction with the casing pipe is crucial for

ensuring well integrity, aiming to establish zonal isolation without creating any leakage pathway within the microannulus between these two materials. To prevent the formation of a microannulus, a strong bond between the cement and the casing is necessary, which leads to the investigation of the damage mechanisms at this interface.

While several experimental studies and numerical models have been presented in the literature, the current state-of-the-art lacks formulations specifically addressing the exploration of mechanisms involved in damage mapping and stress transfer interactions at the cement interface. Furthermore, the damage evolution mapping and the comprehensive study of stress transfer mechanisms can help engineers develop and prototype new advanced materials that can be applied in construction and oil and gas (O&G) industries, improving their mechanical performance and, consequently, the operation of a given system during its entire life.

1.2.

The Damage and Fracture of Materials and Advanced Cementitious Materials research lines

In the Graduate Program of the Department of Civil and Environmental Engineering (DEC) at PUC-Rio, extensive research has been undertaken within the Advanced Cementitious Materials research line. The primary objective of these studies is to deepen the understanding of the mechanical behavior of fiber-reinforced concrete and other construction materials. Laboratory investigations focus on analyzing the post-cracking behavior of FRC, encompassing distinct fiber types [12]–[17] and subjecting them to direct tensile tests, bending, or pullout tests, for example. Additionally, dedicated experimental studies have explored the interface of cement composite materials, with a specific emphasis on natural fibers [15], [18].

Another research line at DEC/PUC-Rio, namely the Damage and Fracture of Materials, also addresses FRC materials, emphasizing developing numerical techniques for the computational simulation of damage mechanisms, crack propagation, and mechanical behavior applicable to multiple Civil Engineering scenarios [12], [19]–[21]. Several applications within these topics involve the

cohesive interface element and the Extended Finite Element Method (XFEM) formulations for modeling cracks in brittle or quasi-brittle materials.

The contributions of the Multiphysics Modeling and Simulation Group at the Tecgraf Institute stand out in this context. Their work emphasizes studies across multiple observation scales, incorporating the coupling of various physical effects (thermal, chemical, mechanical, and hydraulic). This promising research line contributes to academic knowledge and offers practical solutions for the construction industry (e.g., construction materials) and the oil and gas sector (e.g., geomechanical applications in multiple scales, well abandonment investigations, and reservoir/well modeling). A comprehensive understanding of interactions at the mesoscale is achieved by integrating the knowledge derived from laboratory experiments with numerical formulations. This integrated approach aids in elucidating material behavior on a global level.

This doctoral thesis builds upon the scientific works undertaken within the two research lines since 2017. Over the years, several studies have been carried out, encompassing the numerical modeling of cementitious materials with applications ranging from macroscale simulations using homogenization methods [12], [21]–[26], the development of numerical formulations based on the Finite Element Method at the mesoscale [27]–[29], establishment of workflows combining artificial intelligence methods with finite element simulations [22], [30], [31], sensitivity analysis of parameters in cementitious composite materials [32], pullout modeling [33], and, more recently, cement modeling for applications in the oil and gas industry [34].

During this period, a collaboration between PUC-Rio and the University of Stavanger/Norway under the BRANOR (*Knowledge-sharing between the Norwegian Continental Shelf and the Brazilian Offshore on Well Abandonment*) project took place. Part of this thesis was developed in an exchange program at the Norwegian Research Center (NORCE) for four months, under the supervision of Prof. Hans Joakim Skadsem and Dr. Katherine Béltran-Jiménez, both with expertise in well-integrity applications.

1.3. Objectives of the thesis

This thesis proposes the numerical modeling of interfacial debonding and damage evolution mechanisms for advanced cement materials and well integrity applications. Elastoplastic constitutive models, such as the concrete damage plasticity model and surface-based cohesive formulations considering contact, are carried out to model the local behavior of cement. In order to support and validate the numerical model's results, pullout/pushout tests and microCT analyses are carried out at the laboratory to evaluate the shear strength and the damage propagation between cement and other constituents at the interface region. The applications consider straight and hooked-end steel fibers and two distinct types of cement: Matrix A (compressive strength of 40 MPa) and Matrix B (compressive strength of 80 MPa).

Considering the O&G industry, the application's primary goal is to study the pushout shear strength of conventional and expanding cement-casing sections. Elastoplastic finite element models are developed to predict the pushout behavior of the tested cement sections for P&A applications. Additionally, the computational model is calibrated using recent full-scale pushout experimental measurements. Sensitivity analyses are also conducted to study which model parameters influence the pushout response since many contact variables do not have a physical interpretation.

Furthermore, this investigation can help engineers from different areas to prototype new advanced materials that can be applied to improve their mechanical performance. The developed FE models can be valuable tools for simulating the pullout/pushout behavior, enabling cost-effective evaluations of cement performance. Therefore, the workflow formed by the execution of experimental tests and the developed numerical models emerges as an interesting novelty introduced by this thesis.

1.4. Thesis outline

The thesis is organized into six chapters. Chapter 1 presents the thesis introduction with a brief contextualization and motivation for the research development. Moreover, the main characteristics concerning the mechanical

behavior of cement advanced materials and the fiber/matrix interface properties are summarized.

Chapter 2 comprehensively overviews cementitious composite materials and the mechanics underlying their stress transfer mechanisms. Subsequently, it details the various mechanisms involved in the pullout of straight and hooked fibers while examining the fiber types' impact on these experiments. The chapter concludes with an extensive literature review focused on damage mechanisms at the fiber/matrix interface, along with an exploration of the techniques and experimental procedures for damage mapping.

Chapter 3 summarizes the experimental program developed throughout this thesis. The chapter is organized based on the experiments carried out and categorized by the type of cementitious matrix used during the experimental program. Within each section, the materials and methods employed, mechanical characterization of the matrix through uniaxial tensile and compression tests, pullout tests considering straight and hooked steel fibers, and, lastly, the microCT analyses conducted before and after the pullout test are presented.

Chapter 4 provides a comprehensive overview of the numerical modeling developed in this doctoral thesis. The chapter presents key analytical and finite element models used in the literature to simulate pullout behavior. Next, the entire mathematical formulation of the finite element numerical methodologies employed in this work are presented, encompassing elastoplastic constitutive models and contact formulations. Finally, the chapter presents the models' results, along with validations against experimental curves and microCT images showcased in Chapter 3.

Chapter 5 focuses on debonding modeling and the study of the cement interface in applications within the oil and gas industry, particularly in scenarios involving pushout tests for well integrity. The chapter frames the issue of microannulus formation between the cement and steel casing, illustrating the problem and presenting the latest numerical and experimental developments in the literature on this subject. At the end of the chapter, the results of the developed numerical models are presented, along with sensitivity analyses regarding numerical contact parameters and a comparison of the evolution of damage regions in the two types of studied cement.

Finally, Chapter 6 will present the thesis conclusions, including recommendations for future research.

The thesis scheme is presented in Figure 1.2.

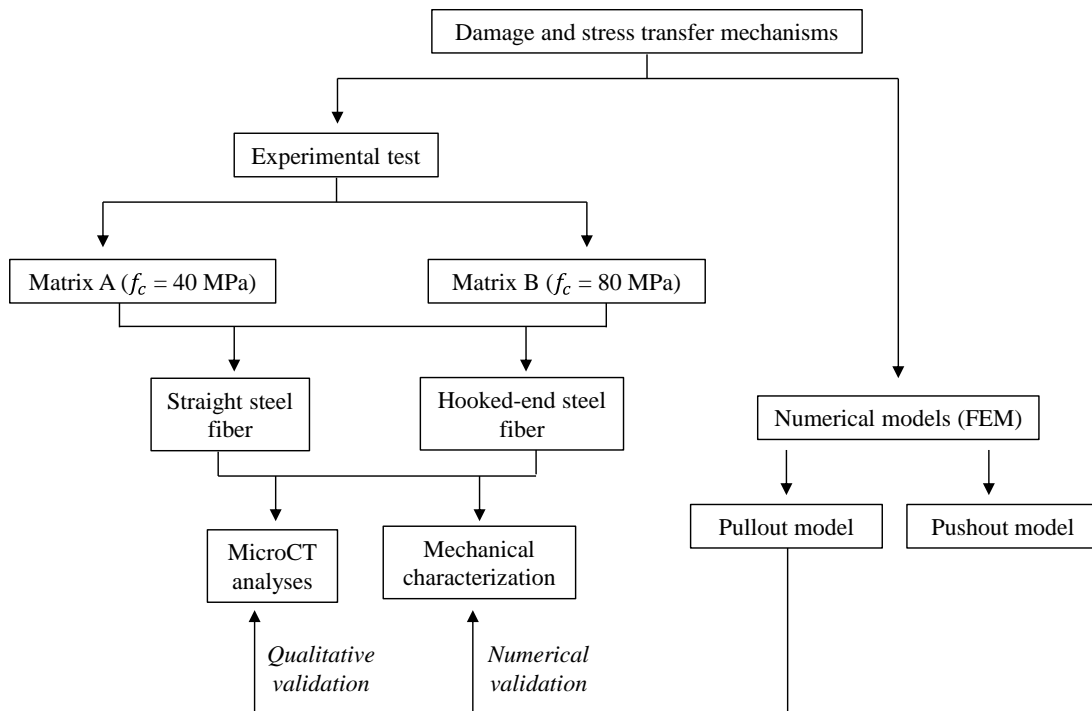


Figure 1.2 – Thesis outline with the main steps.

2 Interfacial debonding and stress transfer mechanisms in cement materials

2.1. Overview

In recent years, several researchers and structural engineers have developed numerical techniques to represent and predict material and structure mechanical behavior. From the observation scale of the structure, fiber-reinforced concrete is often considered homogeneous and isotropic. However, when observing the material at a closer level, the composite is highly heterogeneous and formed by multiple phases: cement paste, fibers, fine aggregates, voids, and capillary pores, as indicated in Figure 2.1. Given the fibrous reinforcement and cementitious matrix interaction, it is necessary to consider the heterogeneity effects on the composite's nonlinear mechanical behavior [12], [35].

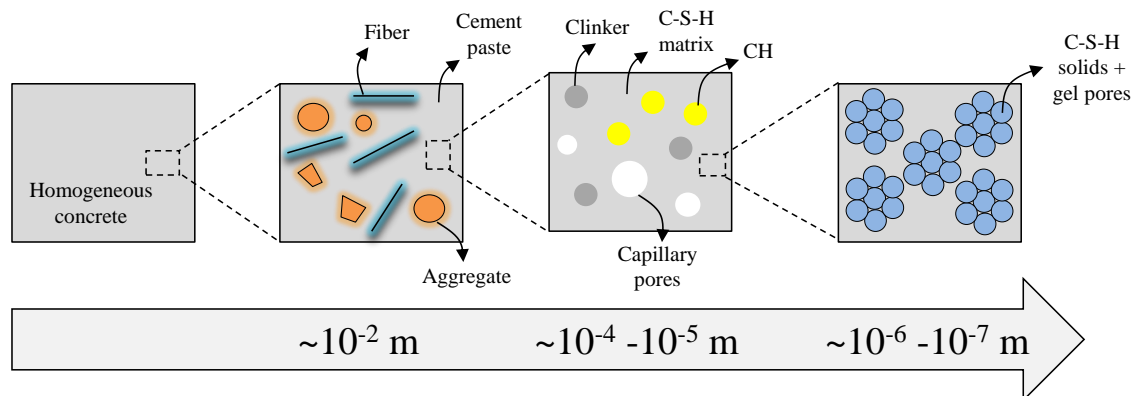


Figure 2.1 – Phases of conventional concrete or fiber-reinforced cement-based materials.

The properties of fiber-reinforced cementitious materials are dependent on the properties of each phase of the composite, as presented in Figure 2.2. Therefore, in order to predict their behavior, three components must be taken into consideration: (i) the cementitious matrix, (ii) the fiber reinforcement, and (iii) the interaction between the fiber and the matrix. From the behavior of each phase, it is

possible to infer and understand the global behavior of the composite material in a more comprehensive way.

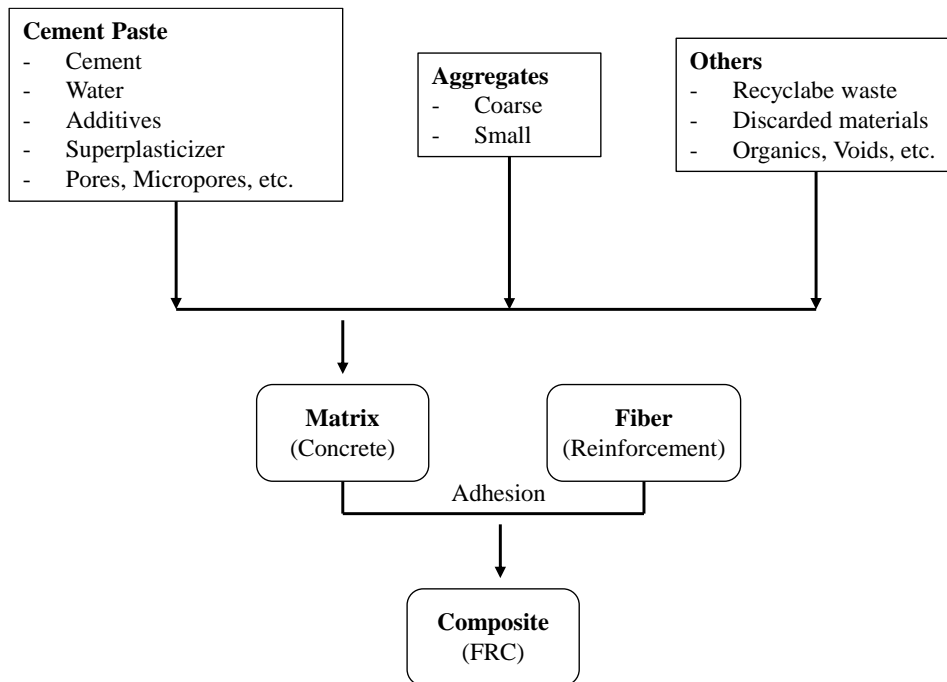


Figure 2.2 – Structure of a cement composite material (Adapted from [35]).

2.1.1.

Cement-based materials and stress transfer mechanisms

In cement composite materials, the matrix is the phase that supports, separates, and protects the fibers. The primary function of the matrix phase is to transfer and redistribute forces within the composite. It can be composed by several elements, such as cement, mineral or chemical additives, coarse aggregates, pores, among others [36], [37]. The second constituent of the structure of a cementitious composite material is the reinforcement, characterized by the presence of fibers. These can take on different types of geometries, and it is necessary to consider two levels of description for their complete characterization: the shape of the individual fibers and their respective dispersion in the cement matrix [4], [5], [36].

Concerning the geometry of the fibers incorporated into the cementitious matrix, they do not have a perfectly cylindrical shape but are deformed in different ways to improve their mechanical anchorage with the matrix. In this way, they can also assume more complex geometries, with polygonal cross-sections or even longitudinally twisted, to allow an adequate anchorage without harming the workability during the process of mixing the concrete with the referred

reinforcement [39], [40]. It is important to emphasize that fibers improve ductility, increase the material's deformation capacity, prevent or stop the propagation of cracks, especially in the case of a brittle matrix such as concrete, improve volumetric stability, and increase tensile strength post-cracking of the composite.

Finally, the region between the fiber and the matrix is called the interfacial transition zone (ITZ) and has different properties from the cement paste. The microstructure of the ITZ in cement composite materials is directly related to the nature of the matrix particles. During the hydration process, the cement particles react to form hydrated calcium silicate (C-S-H) gel and calcium hydroxide crystals. During the stage of new particles generation, pores can be identified in the fiber region. Two main reasons explain this phenomenon: (i) the retention and release of water by the fibers and (ii) the inefficient packing of the grains that are next to the fibers [13], [36], [39], [41].

Regarding the fiber-matrix interaction, a typical mechanism of the interface region between the fiber-matrix is the stress transfer bridge. The fibers act by transferring the stresses across the cracks to the concrete matrix, preventing them from propagating. This mechanism generates the material cracking control [21], [36], [38], defined as the stress transfer bridge.

The processes involved in the fiber-matrix interaction are located in a relatively small volume of the matrix around the fibers. In addition, the matrix microstructure around this region can be quite distinct from other areas, generating effects that are not always predicted by the analytical models that often assume a uniform matrix in this region. Understanding the stress transfer mechanisms provides a reasonable basis for predicting the stress-strain curve of the composite material and its fracture mode (whether ductile or brittle) [12], [14], [36], [39].

According to Sujivorakul & Naaman [42], the stress transfer process is divided into three phases. The first phase occurs before the crack opening process, governed essentially by an elastic behavior: the fiber is fully embedded into the cementitious matrix. Therefore, fiber and matrix have the same strain until the shear stress is greater than the adhesion between the two constituents. The second phase corresponds to partial fiber debonding, reducing the stress transfer between the cementitious matrix and the fiber. Finally, the fiber completely debonds from the matrix, moving as a rigid body. In this stage, the interfacial shear stress is governed by fiber-matrix friction [12]. Figure 2.3 illustrates the stress distribution process

along with the fiber that intersects a crack and the stress transfer process described in the previous paragraphs.

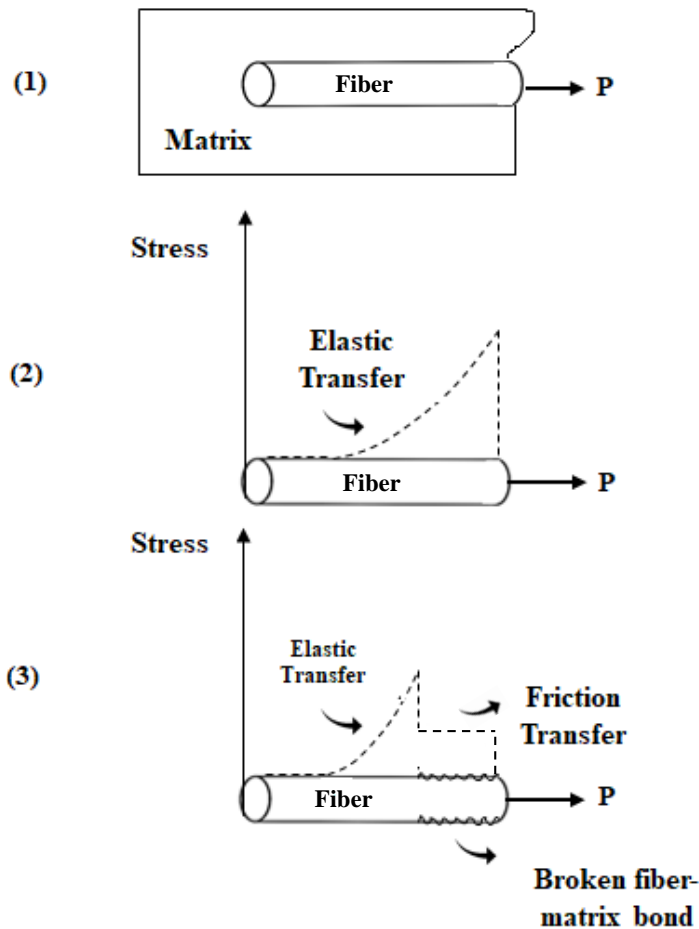


Figure 2.3 – Representation of the stress distribution stages during fiber pullout (Adapted from [12]).

The change from the elastic stress transfer to the friction stress transfer occurs when the interfacial shear stresses are more significant than the shear strength at the fiber-matrix interface (τ_{au}). Fiber debonding initiates when this occurs and the friction shear stress will act at the interface (Figure 2.4). Such debonding can occur before the first crack appears which is not expected. This fact can vary according to the adhesion shear stress at the interface or the shear stress at the cementitious matrix [12], [14], [36], [43].

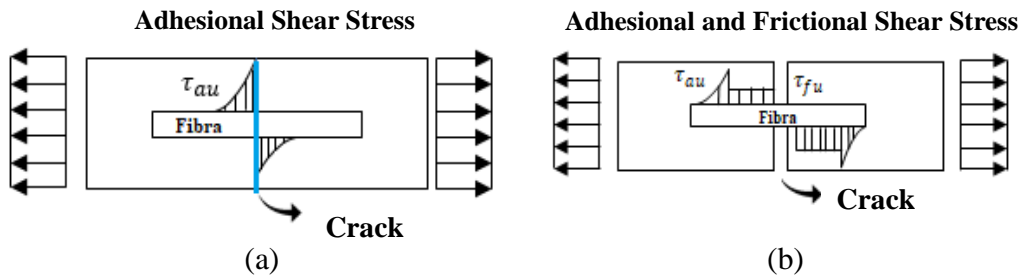


Figure 2.4 – Distribution of shear stresses along the fiber: (a) for intact composite and (b) for cracked composite (Adapted from [36]).

The higher the porosity, the smaller the adhesion between fiber and matrix [13], [14]. During the crack initiation process, there is a concentration of tensile stresses at the crack ends due to the reduction of their effective area. When the stress is equivalent to the matrix strength, concrete suddenly fails, cancelling any residual strength value [44].

The steps involving crack propagation are described by Rossi et al. [45] in three stages: (i) the first one involves the microcracking process (continuous material damage); (ii) the second stage is characterized by the coalescence of microcracks, following the directions of the principal strains. From a mechanical point of view, there is a process of strain concentration that generates the emergence of one or several major fractures; and (iii) the third stage, where the macro crack propagates in the direction of the principal tensile strain [12], [14].

Concerning interface modeling, the main models are the pullout and tension vs. fiber slip curves. Analytical models were created to predict the values that can be obtained from experimental tests. These models calculate the force and slip for each stage (elastic, non-linear and frictional). In fiber-reinforced concrete applications, pullout tests are often carried out to measure the force required to pull the fiber out [43], [46].

2.2. Pullout behavior of cement composite materials

The interface behavior of fiber-reinforced cement-based materials is challenging and complex, mainly due to the several mechanisms in this region. In this sense, it is crucial to understand these mechanisms to choose the proper mathematical formulation for the numerical modeling of the mechanical behavior of these composites.

In order to investigate the mechanisms in the interface region, pullout tests are carried out. Therefore, the following sections present some essential theoretical aspects that need to be understood to develop numerical formulations/models. Figure 2.5 summarizes the mechanisms for fiber/matrix interactions at the interface region.

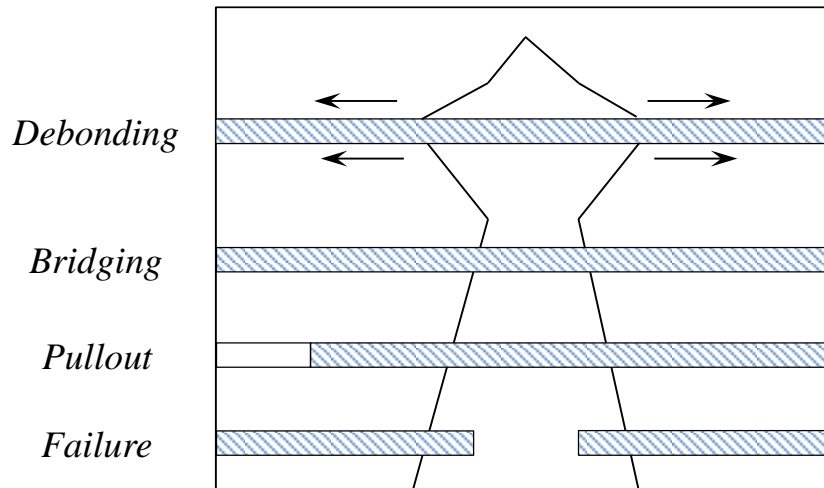


Figure 2.5 – Mechanisms for fiber/matrix interface interactions (Adapted from [47]).

2.2.1. Bonding

The adhesion or chemical bond is defined as the bond between the fiber and cement matrix adjacencies. According to Naaman & Najm [43] and Cunha [48], the bond is the first activated mechanism during the pullout. In this stage, the fiber and matrix strains are fully compatible, and the fiber/matrix interface does not present any level of damage. Naaman & Shah [46] point out that the bond improvement observed in a single pullout test does not promote equal improvement globally. In this sense, fiber deformation processes can give the mechanical bond, which results in local interactions between the cementitious matrix and the fiber on a smaller scale. On the other hand, it can be seen as a roughening effect [49].

In recent decades, several fibers have been crimped, indented, or hooked, improving the fiber mechanical anchorage to the matrix. Smooth fibers present a distinct bond mechanism since the slip mainly depends on chemical adhesion, rupture and friction. Some authors (e.g. [43], [50], [51]) also list the fiber-to-fiber interlock as an important mechanism for bonding. However, this phenomenon is only observed in composites with high levels of volumetric fraction (up to 10%) [50], which is not reasonable for fiber-reinforced concrete applications.

Bartos [52] and Gray [53] defined two types of bond according to the nature of stress transfer and type of interface: the first one is classified as the shear bond, which is related to the transfer of the parallel stresses to the longitudinal fiber axis. This type of bond assures deformation compatibility between fiber and matrix. If the shear bond stress is higher than a limit value, a relative fiber displacement for the cement matrix is observed. Therefore, it corresponds to a friction mechanism. The second type of bond is called tension bond: this stress component enables to resist forces perpendicular to the interface. It can be activated due to mechanical stresses or physical mechanisms, such as concrete shrinkage. For single fiber models, this bond type is usually neglected [43].

The mechanics of the fiber-matrix interfacial bond are highly sophisticated as a result of different interactions between linear and nonlinear modes: physical/chemical bond, interfacial debonding, plastic material strains, mechanical bond deformations, and frictional sliding. According to Chin & Xiao [54], from a general point of view, the fiber bridging/debonding pullout mechanism is a possible failure for fiber-reinforced concrete, as shown in Figure 2.6.

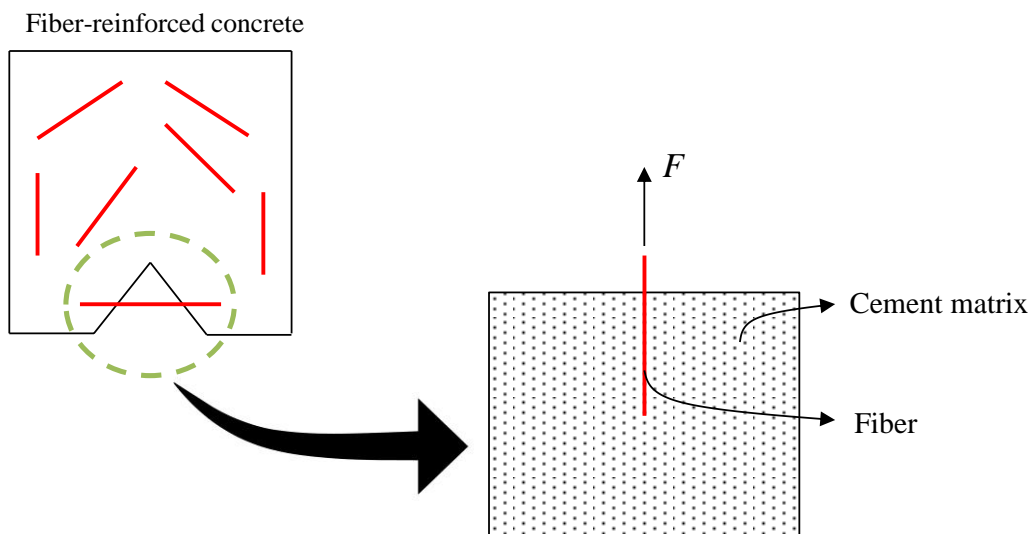


Figure 2.6 – Schematic representation of fiber bridging/debonding in pullout tests (Adapted from [47]).

2.2.2. Critical embedment length and fiber rupture

The stress transfer mechanisms at the fiber/matrix interface play an important role in the failure mode of fiber-reinforced concrete. Two failure modes can be

verified after matrix cracking for a straight fiber without anchorage: (i) fiber rupture and (ii) fiber sliding [48].

The most basic model assumes balancing the forces on a straight fiber subjected to tension load. Suppose uniform adherence distribution $\bar{\tau}$ is verified along the fiber. In that case, the critical embedment length can be expressed according to Equation 2.1, where σ_{fu} refers to the fiber rupture stress and d_f is the fiber diameter.

$$L_{f,crit} = \frac{\sigma_{fu} d_f}{4\bar{\tau}} \quad (2.1)$$

Fiber will fail if the fiber embedment length is higher than $L_{f,crit}$. On the other hand, fiber sliding will be detected if the fiber embedment length is smaller than the critical embedment length. However, other parameters can also influence the pullout mechanisms, such as fiber orientation, geometry configuration and fiber/matrix interfacial bond stress not being constant over the fiber embedded length [47].

2.2.3. Pullout mechanisms for straight fibers

Figure 2.7 presents a typical pullout load-slip (F- δ) curve for a straight and smooth fiber. The curve can be divided into three distinct steps, represented in Figure 2.7 as specific points: A, B and C.

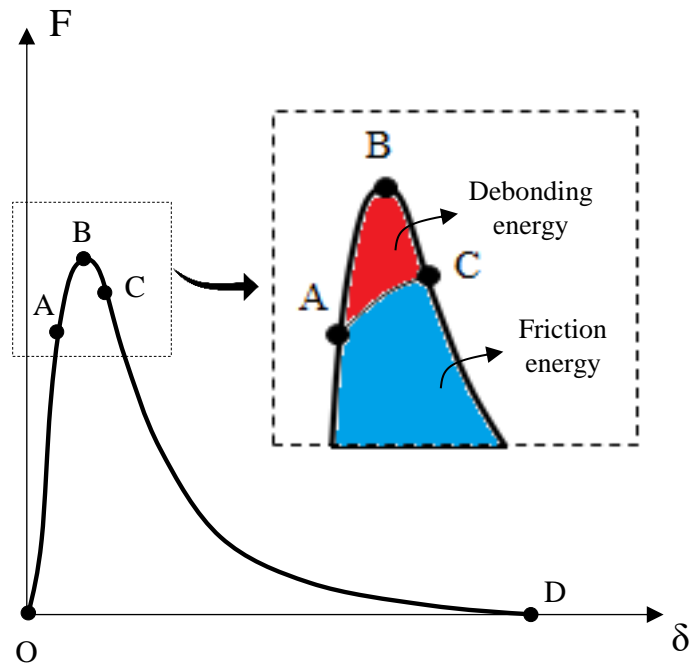


Figure 2.7 – Pullout load-end slip curve for a smooth straight fiber (Adapted from [48]).

The first stage (O-A) refers to the elastic phase, where the fiber and the concrete matrix stresses are generated due to the adhesive bond. Next, the second step (A-B) describes fiber debonding. At point A, the maximum shear stress is reached and the fiber starts to debond. As the slip increases, the fiber continues to debond (point B). During this process, the stresses due to friction start to increase until the fiber has fully lost adhesion. The final step (B-D) considers the pullout of the fully debonded fiber, where region C-D refers to fiber pullout due to frictional slip [55]–[57].

Figure 2.7 also represents the areas under the pullout load-slip curve for debonding and pure friction mechanisms. The pullout energy for debonding and friction is directly related to the fiber embedded length up to fiber rupture. During debonding, the frictional stress increases, which leads to local shear stress characterized by debonding and friction. The contribution of each phenomenon is undetermined because only the combined response can be measured in a pullout test. Figure 2.8 presents the schematic representation of each stage presented in Figure 2.7 [43], [46], [48].

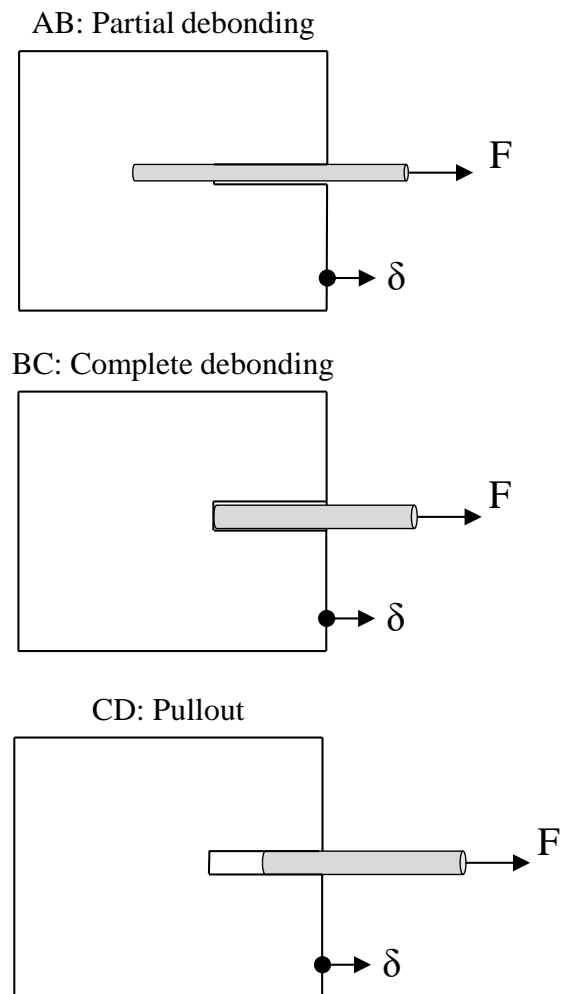


Figure 2.8 – Mechanisms for the straight smooth fiber pullout test (Adapted from [48]).

2.2.4. Pullout mechanisms for hooked-end fibers

Alternatively, Figure 2.9 presents the pullout load-slip curve for hooked-end fibers and the comparison with the straight fiber pullout curve.

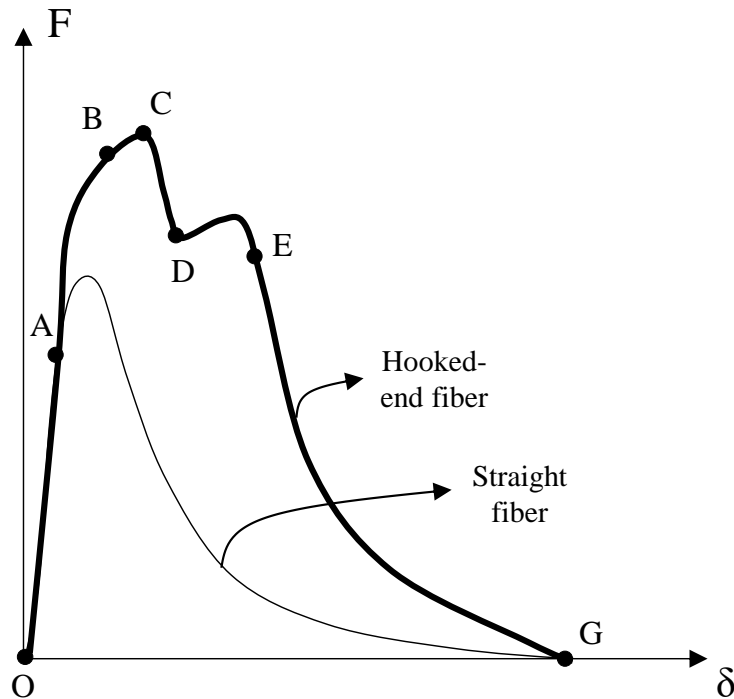


Figure 2.9 – Pullout load-end slip curve for a hooked-end fiber.

As in the smooth straight fiber pullout curve, the first step (O-A) is fully elastic and describes the full adhesive bonding between the fiber and the cementitious matrix. The second step (A-B) describes the fiber debonding. In contrast to the straight fiber, the pullout load increases until point C due to the mechanical anchorage of the fiber hook. At point C, the fiber end passes the first corner in the surrounding concrete matrix, in which fiber plastic deformation has already started. During the C-E stage, the fiber is subjected to deformation until the end hook of the fiber straightens out. Next, at stage D-E, the fiber end passes the second corner in the surrounding concrete matrix, and an increase in the pullout load can be observed. Finally, stage E-G refers to the phase where the fiber is pulled out under frictional resistance. The hooked-end fiber is not entirely straight, leading to a higher frictional resistance than in the straight fiber configuration [55]–[57].

The pullout behavior for a hooked-end fiber is also described by adhesive bonding, debonding, and friction at the fiber-matrix interface. However, specific differences in the pullout load-displacement curve can be observed due to the nonlinear deformation of the fiber end hook and the concrete matrix. Figure 2.10 summarizes the main mechanisms that are observed during hooked-end fiber pullout tests.

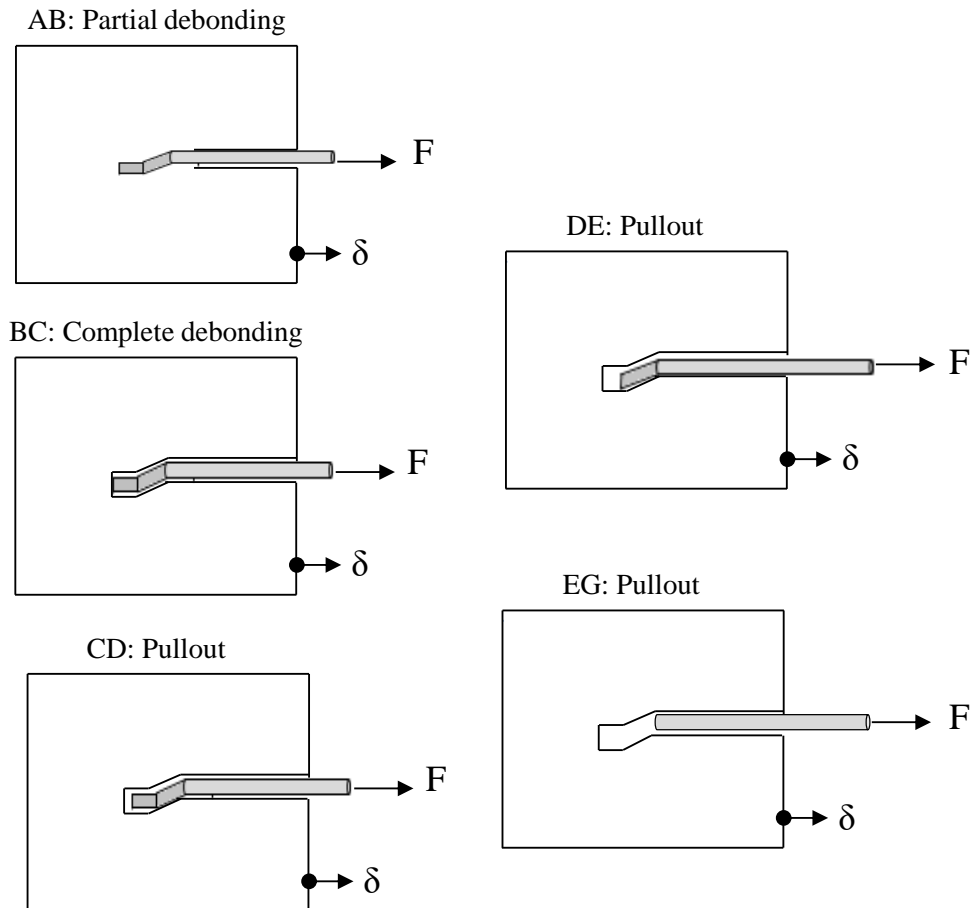


Figure 2.10 – Mechanisms for the hooked-end fiber pullout test (Adapted from [48]).

2.2.5. Influence of fiber type in pullout tests

As previously discussed in Section 2.1.1, several types of fibers can be applied to fiber-reinforced concrete applications. They can be classified according to their chemical/physical properties (density, surface roughness, fire resistance, among others), fiber material (natural, organic, mineral, among others), or mechanical properties (tensile strength, Young's modulus, adhesion properties, among others). Due to the distinct manufacturing processes available in the construction industry, the mechanical properties differ for each fiber. Therefore, these distinct properties impact the pullout behavior and, consequently, the global behavior of fiber-reinforced concrete [58].

Due to the weak bond between the fiber/matrix interface, the pullout energy from a straight fiber is small. In order to solve this challenge, several fiber treatments can be carried out by optimizing the fiber anchorage properties, such as

roughening or inducing other mechanical deformations [59]. Concerning this point, steel fibers have a primary advantage over other fibers since they can be easily deformed and indented to improve their anchorage to cement matrix. Figure 2.11 shows distinct types of steel fibers according to their geometric shapes.

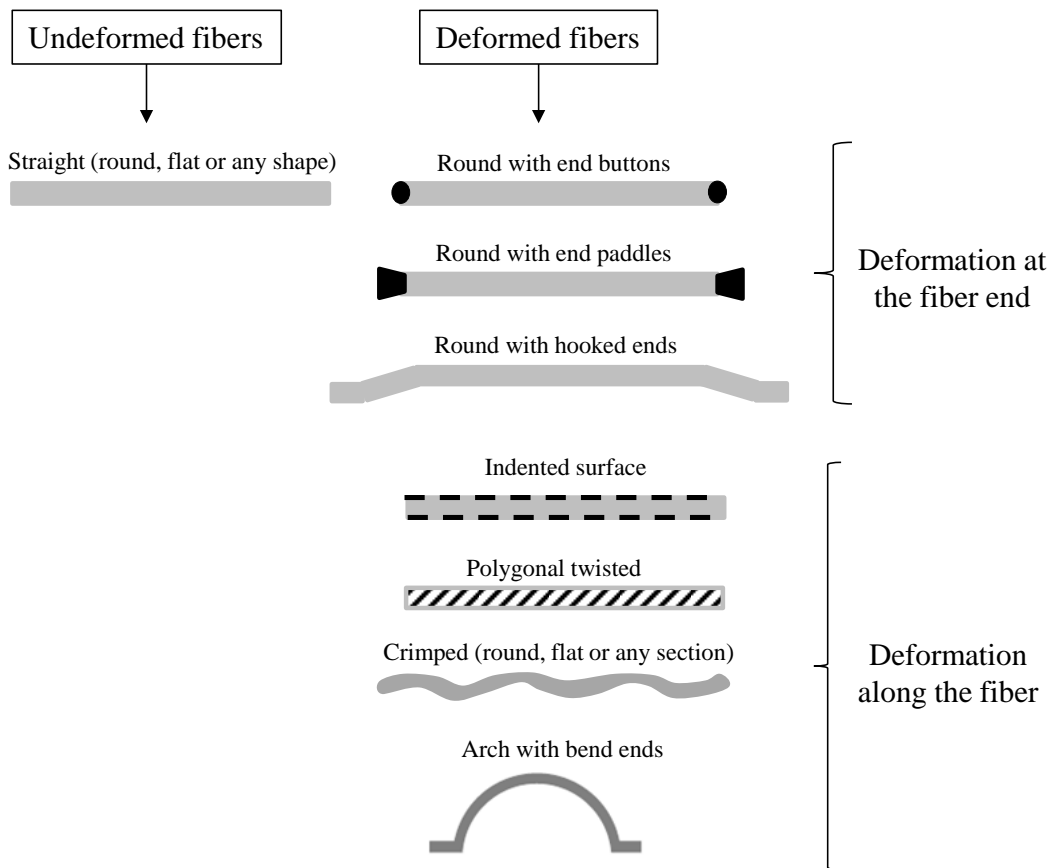


Figure 2.11 – Distinct steel fiber geometries (undeformed or deformed shapes) (Adapted from [58]).

Figure 2.12 compares the pullout responses for distinct types of deformed fibers adopting different embedded lengths (L_e) and matrix compressive strengths (f_c). It is observed that the peak pullout load and the pullout energy are considerably higher for deformed fibers than for straight/smooth ones. When increasing the lateral fiber surface area, there is an increase in frictional and adhesive bond forces for the same cross-section and the fiber, leading to a higher pullout resistance [48]. On the other hand, the additional fiber stiffness provided by the untwisting process will provide a slip hardening behavior.

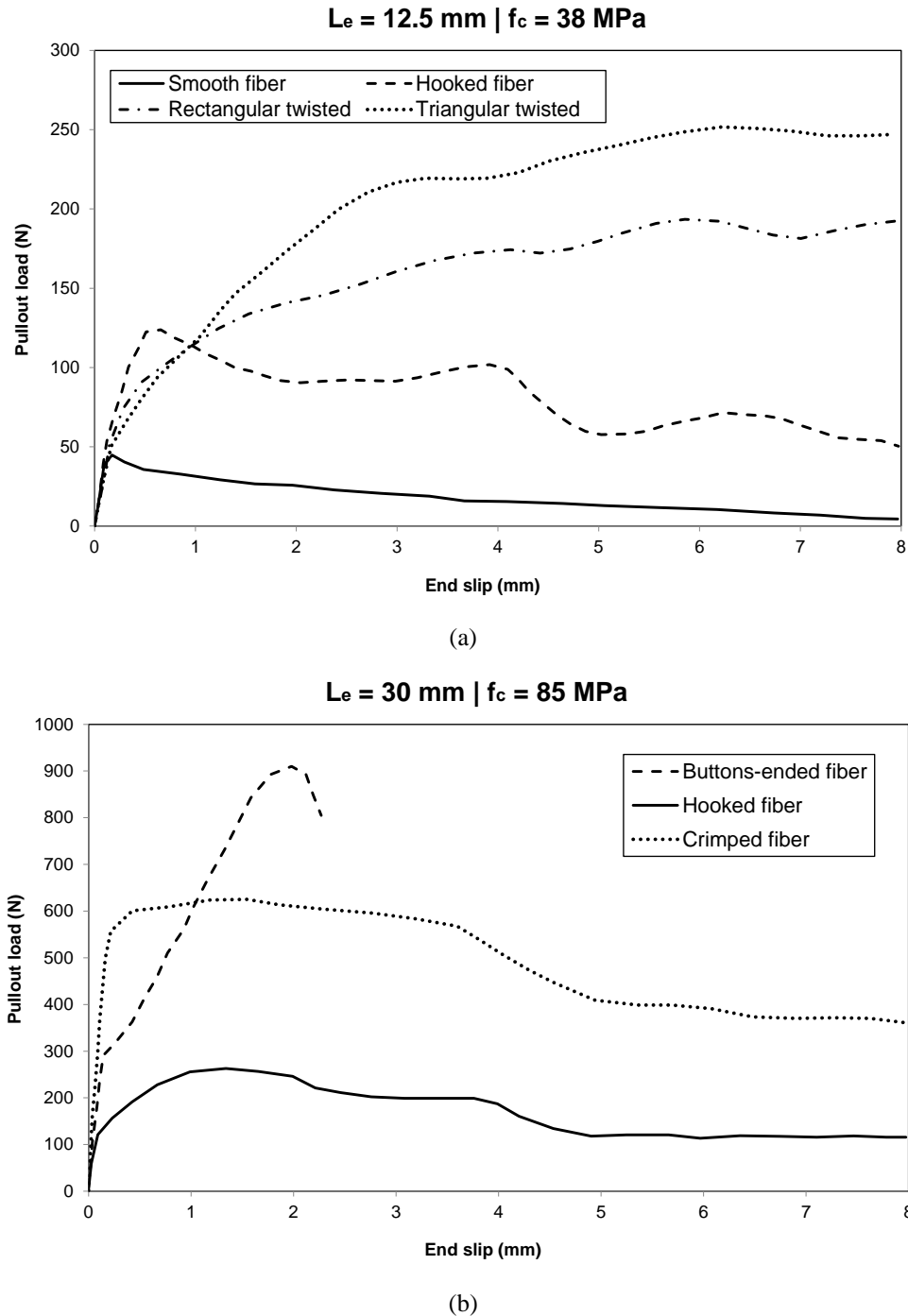


Figure 2.12 – Typical pullout responses for distinct steel fibers considering different matrix compressive strengths (f_c) and embedded lengths (L_e) (Adapted from [48]).

2.2.6. Influence of fiber orientation and matrix strength in pullout tests

Figure 2.13 presents the pullout relationships for hooked-end fibers with different inclination angles. The ultimate fiber tensile strength (UTS) is also represented in this figure. It is observed that the fiber with an inclination of 45° and 60° fractured below the ultimate tensile strength [60]. The high-stress

concentrations can explain this fact at the fiber bending point. According to Banthia et al. [60], the additional shear stresses in inclined fibers will promote the fiber intercrystal slippage on a smaller scale, reducing the material yield and ultimate strength.

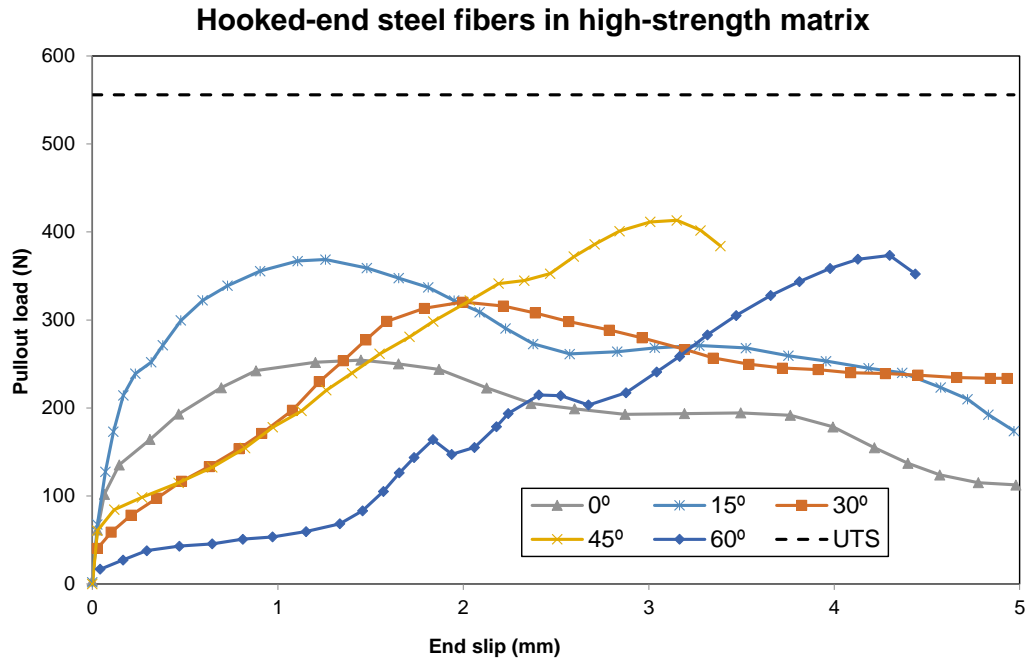


Figure 2.13 – Pullout relationships for hooked-end fibers from a high strength cement matrix (85 MPa) at several inclination angles; UTS = ultimate tensile strength. (Adapted from [48]).

The peak load and toughness are, in general, higher for inclination angles between 0° and 20°. Higher angles often lead to a lower pullout load in the first stage of the pullout behavior. Depending on fiber type, matrix strength and other parameters, the maximum pullout load may increase with the fiber inclination until an angle of 45° [46], [60].

For uncracked composites, the orientation efficiency can be determined in two ways. The first one assumes that the composite is subjected to deformation only in the applied stress direction. Alternatively, the second hypothesis assumes that the strains occur in the other directions of the composite. For the first case, the pullout load of fibers oriented at an angle θ is given by Equation 2.2.

$$P_{pullout} = \cos^4 \theta \quad (2.2)$$

For fibers aligned in multiple directions, the orientation efficiency η_θ is given by Equation 2.3, where a_θ is the proportion of fibers oriented at an angle θ .

$$\eta_{\theta} = \sum a_{\theta} \cos^4 \theta \quad (2.3)$$

When analyzing the orientation effect at the post-cracking zone, the local fibers bending around the crack should be considered, which geometric considerations can induce. The orientation effects determined by a conventional composite material approach include an implicit assumption of orientation with a constant fiber angle along the crack. However, local bending of the fiber around the crack will induce bending stresses in the fibers and, at the same time, will lead to local compressive stresses in the matrix [36]. A complex stress state will be developed, and the global behavior will depend on the balance between the stiffness and ductility of the matrix and the fiber. Within this context, two different situations must be considered [36], [39]:

i. Ductile fibers bonding the crack in a brittle matrix: if the fiber is ductile and with a low modulus, it will be pulled off easily, and a pin effect can be induced, causing an increase in pullout strength;

ii. Brittle fibers connecting the crack in a ductile matrix: if the fiber is brittle and has a higher Young's modulus, there is an accumulation of local bending stresses in the fiber, which are superimposed to the axial tensile stress, which can lead to premature fiber rupture. In turn, this rupture can result in lower efficiency than expected compared to a linear fiber with an angle of inclination, assuming only axial forces. Figure 2.14 presents a schematic representation of this approach.

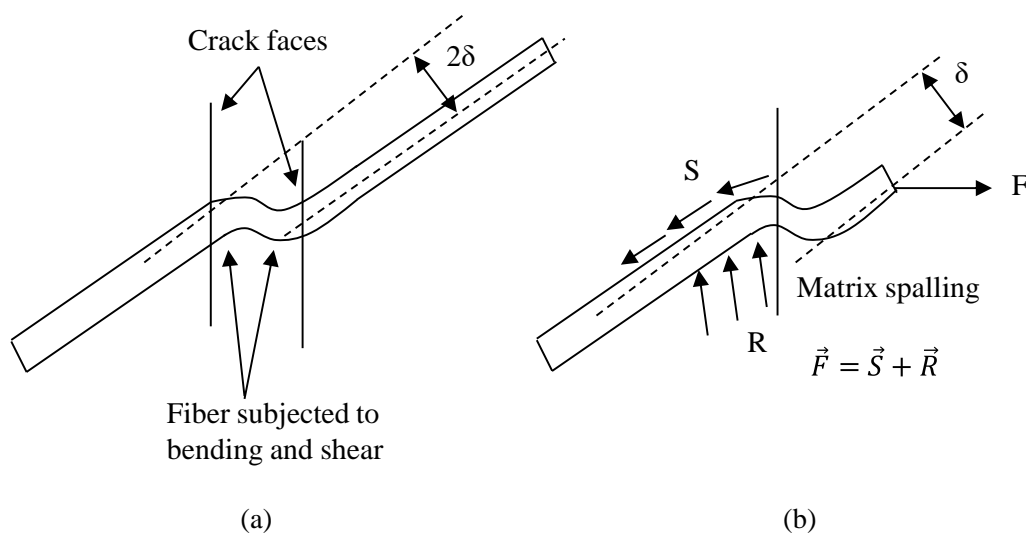


Figure 2.14 – (a) Bending of a fiber across a crack; (b) components of crack bridging force (Adapted from [36]).

These concepts may account for a range of orientation effects observed in a variety of FRC systems, as presented in Figure 2.15. An increase in the orientation angle in a composite with brittle and ductile fibers (carbon, for example) reduces pullout strength. The opposite occurs for ductile and low-modulus fibers (polypropylene, for example): a pullout strength increases with orientation [36], [46].

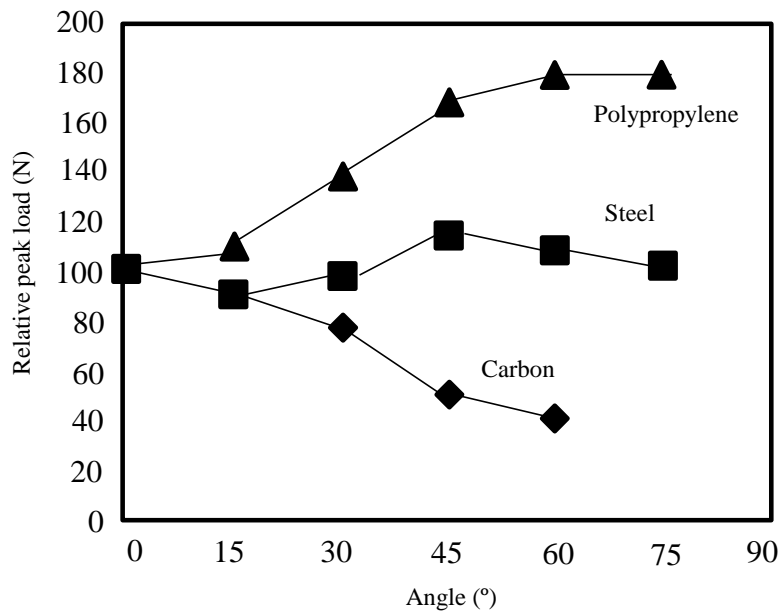


Figure 2.15 – Orientation effects for distinct fiber types (Adapted from [22]).

Moreover, Jamee et al. [61] emphasized that the composition and compressive strength of the cement matrix directly influence the pullout characteristics of hooked steel fibers. Similarly, Isla et al. [62] observed that fibers extracted from mortars with higher compressive strength demonstrate increased pullout strength. Therefore, as the matrix strength increases, there is a corresponding increase in matrix stiffness, compelling the fibers to undergo more deformation for sliding.

2.3. Interfacial damage mechanisms

Damage mechanisms in cement composite materials gather several processes that take place at the material level of the composite according to different physical degradation mechanisms, such as fiber pullout [63]–[65], crack propagation in the cement matrix [66], [67], interfacial debonding [68]–

[70], and fiber breakage [71], [72]. All the previous studies reported in the literature pointed out that fiber/matrix interfacial debonding plays an essential role in the predominant damage mechanism and the progressive degradation of the effective behavior [73]. Therefore, it is essential to study the stress state in and around the fiber in order to understand the macroscopic mechanical behavior of FRC.

According to Xia et al. [74], the tensile load in a discrete fiber-reinforced concrete loaded in the fiber direction is mainly carried by the stiff fibers. Once the fiber strain to failure is much smaller than the matrix strain to failure, and when loaded in quasi-static tension in the fiber direction, the first fiber breaks occur in random positions. This process is due to the defect distribution in fibers, which leads to the fiber break during the loading stage. In this sense, a stress transfer mechanism between the fibers near the broken fiber is observed. Pupurs [75] points out that, depending on the fiber, matrix, and interface properties, several events may influence the fiber break, as presented in Figure 2.16: (a) the crack can propagate from fiber to the cement matrix until the neighboring fiber arrests it, where it may cause a fiber break or may be deflected as a debond crack growing along with the fiber interface; (b) shear yielding of the cement may occur at the fiber break tip, blunting the crack or (c) a debond crack may grow from the fiber break along with the interface. The debond crack can grow in composite materials until it meets another debond crack growing with the same or neighboring fiber. In this sense, cracks coalesce into one larger crack, leading to the composite failure (Figure 2.17).

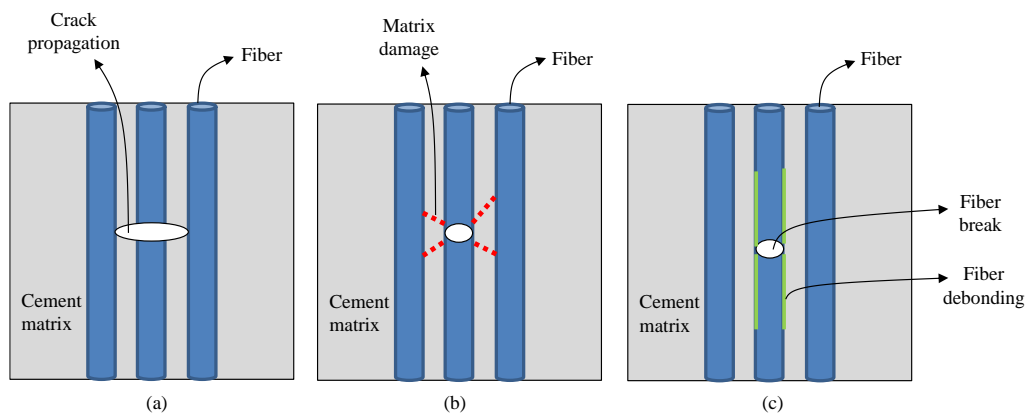


Figure 2.16 – Damage development after fiber break formation: (a) crack propagation, (b) matrix yielding, (c) debonding at the interface (Adapted from [75]).

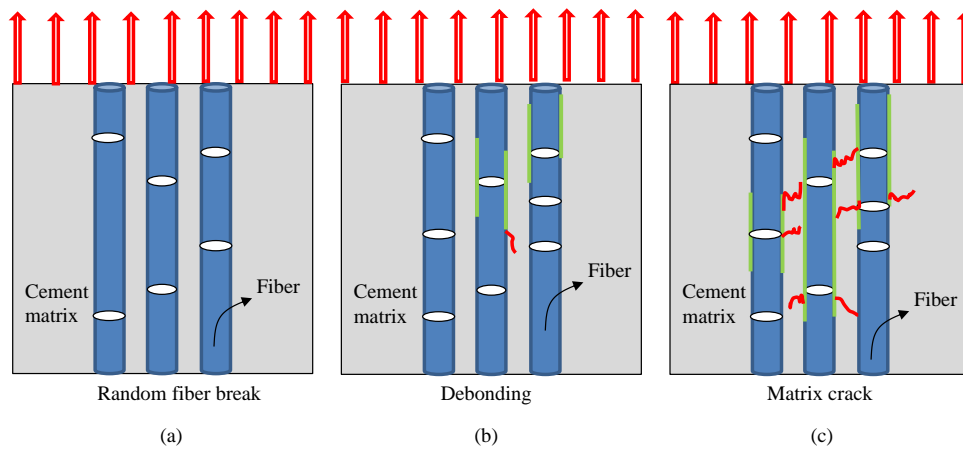


Figure 2.17 – Damage events leading to the final failure of a composite considering unidirectional loading (Adapted from [75]).

During the stress transfer mechanism, the stress concentration in the neighboring fibers around the broken fiber and the ineffective longitudinal length over which the broken fiber recovers load-carrying capacity are the most relevant parameters. Therefore, the transverse stress concentration governs the fiber damage process, establishing a critical damage cluster size and determining the composite tensile strength related to the *in-situ* fiber strength and the size-scaling of the composite strength [74], [75]. Consequently, predictions regarding the composite failure require detailed studies about the micromechanical stress state around the broken fibers as a function of the material properties. Several methods have been applied to the investigation of stress distribution at the micromechanical scale, such as the shear-lag model [76], [77], Green's function method [74], and the Finite Element Method [78].

The mechanical strength of the cement matrix provides the circumferential compressive normal stress around the fiber, which is a crucial issue in terms of interface friction. The dense matrix microstructure benefits friction strength at the interface and the geometric deformation of the fiber contributes to a strong anchorage force at the interface. At the same time, for steel fibers, the hydrophobic nature leads to the formation of a weak bond at the interface, reducing the pullout resistance of steel fibers from the cement matrix [79].

Moreover, the microstructure and the matrix mechanical strength are key points by the performance of the ITZ [80]. The shape of the steel fibers

influences the anchorage force at the fiber/matrix interface. Several shapes of steel fibers have been developed to improve interfacial performance [81], [82]. Additionally, distinct methods have been proposed to modify steel fibers' surface [83], [84] since a dense microstructure is desirable for good interfacial performance. Table 2.1 summarizes the effect of several methods carried out to improve the fiber/matrix interfacial performance [79], such as fiber shape, fiber diameter, fiber embedded length and angle, and matrix strength, among others. Therefore, in order to better investigate the surrounding region between fiber and matrix, pullout tests are carried out.

Table 2.1 – Effect of several methods for interfacial performance of steel fiber-reinforced concrete [79].

Method	Variable	Improvement
Mechanical properties of cementitious matrix	Water to binder ratio	10-25% in pullout load
Mechanical properties of cementitious matrix	Autoclave curing and steam curing	85-110% in interfacial bonding
Mechanical properties of cementitious matrix	Content of silica fume	9-40% in interfacial bonding
Mechanical properties of cementitious matrix	Content of nanomaterials (nano-SiO ₂ , nano CaCO ₃ , etc)	40-55% in interfacial bonding and 70-230% in pullout energy
Physical arrangement of steel fiber	Corrugated steel fiber	140-300% in interfacial bonding and 250-350% in pullout energy
Physical arrangement of steel fiber	Hooked steel fiber	240-700% in interfacial bonding and 190-400% in pullout energy
Physical arrangement of steel fiber	Embedded length	30-50% in pullout load
Physical arrangement of steel fiber	Embedded angle	20-80% in interfacial bonding
Physical arrangement of steel fiber	Fibers distance	5-20% in interfacial bonding and 15-20% in pullout load
Chemical modification of fiber surface	ZnPh coating	20-70% in pullout load
Chemical modification of fiber surface	SCA modification	35-75% in interfacial bonding and 20-85% in pullout energy
Chemical modification of fiber surface	Plasma treatment	20-30% in pullout load and energy
Chemical modification of fiber surface	Nanomaterials coating	70-80% in interfacial bonding and 60-70% in pullout energy

According to Zhou et al. [79], Chan et al. [85] and Wu et al. [86], the addition of silica fume to the cement matrix can change the interfacial performance of steel fiber-reinforced concrete, where the optimal content of silica fume for interfacial bonding strength ranges between 25 to 35% [85], [86]. In addition, the adoption of nanomaterials as additives can also improve the interfacial bonding since the filling and chemical reactivity of nanomaterials lead to a dense microstructure and high mechanical strength [81], [82]. As previously reported in Table 2.1, the interfacial bonding strength and pullout energy of hooked fibers were three and four times greater compared to straight fibers [64]. The increase in bonding area can benefit the stress transfer mechanism at the interface, improving the performance of steel fiber-reinforced concrete. Moreover, the interfacial bonding strength of straight fibers increased 20% when the fiber embedded angle varied from 0° to 30° [87], [88]. Table 2.2 presents the effect of enhancement approaches on the global mechanical behavior of fiber-reinforced concrete.

Table 2.2 – Effect of several methods for mechanical global behavior of fiber-reinforced concrete [79].

Method	Variable	Improvement
Mechanical properties of cementitious matrix	Water to binder ratio	30% in compressive strength and 60% in flexural strength
Mechanical properties of cementitious matrix	Content of silica fume	10-30% in compressive and flexural strength
Physical arrangement of steel fiber	Corrugated steel fiber	60% in compressive strength
Physical arrangement of steel fiber	Hooked steel fiber	50% in compressive strength
Chemical modification of fiber surface	ZnPh coating	20% in flexural and tensile strength
Chemical modification of fiber surface	SCA modification	15% in compressive and flexural strength; 50% in peak toughness under dynamic load
Chemical modification of fiber surface	Plasma treatment	10% in compressive strength

Experimental tests are crucial for explaining and investigating the surrounding region between fiber/matrix interface. In this sense, microtomography techniques are used to investigate the damage mechanisms at the microscopic scale involved in the load distribution between mortar and

fibers [89]–[91]. The aim is to detect and characterize in 3D the microscopic nature and the evolution of interfacial debonding and associated damage mechanisms in the matrix close to the fiber region.

2.4.

Damage due to anchorage failure in deformed fibers

Concerning the fiber/matrix interaction, the evolution of damage in this region plays an essential role in analyzing the mechanical behavior of fiber-reinforced cement-based materials. Nieuwoudt [92] carried out a study and concluded that fracture could occur in the surrounding region of fiber in the cement matrix as the fiber is pulled out, especially in the case of hooked-end or undulated steel fibers. When such damage progresses with time and load level due to microcracking and local crushing produced by the sustained loading, the pullout is facilitated. Figure 2.18 presents CT scan images of a single fiber at different stages of pullout presented in the work of Nieuwoudt [92].

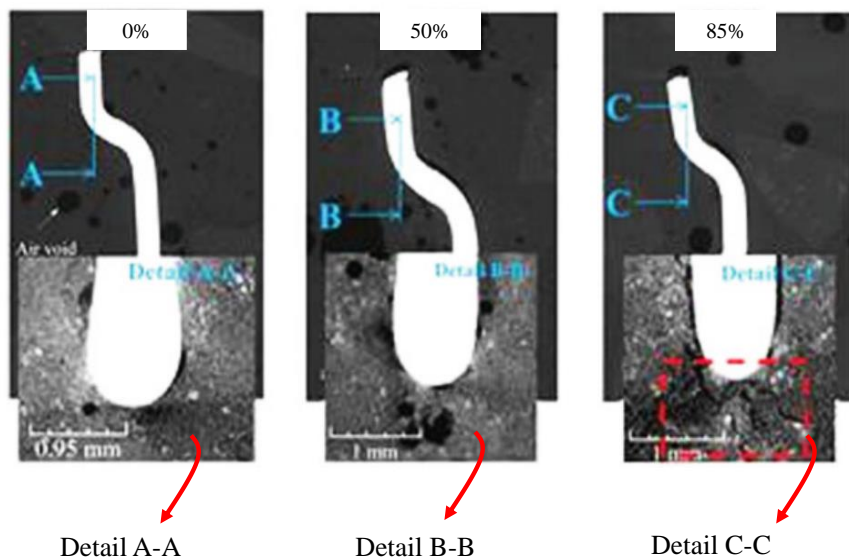
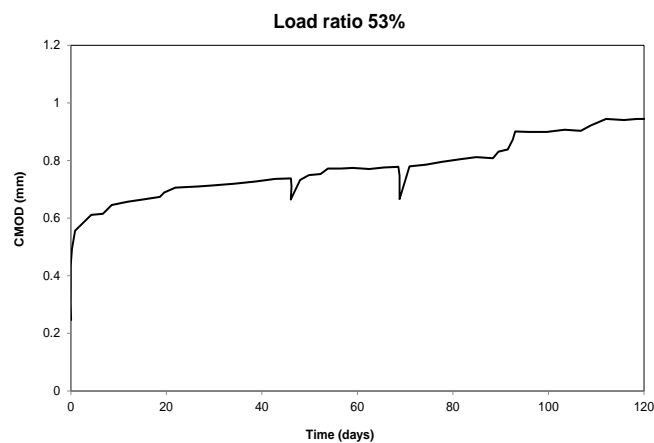


Figure 2.18 – Scan images of a fiber in distinct pull-out stages, where the lower images are magnifications of the upper images (Adapted from [92]).

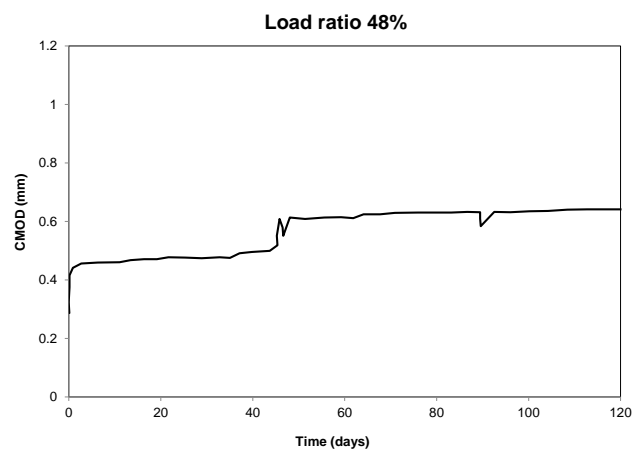
In the case of straight fibers with lower Young's modulus, like the polymeric ones, such damage is not expected to be significant. These fibers can experience creep, especially at higher temperatures, due to their viscoelastic nature. The relaxation of the stress in the fiber will decrease the bridging effect, leading to crack widening and further propagation. It is important to highlight that significant differences can be observed among polymeric fibers, such as the polymer family,

shape, texture, and production processes. On the other hand, steel fibers hardly experience any creep at ambient temperature [93], [94].

When a strain-softening fiber-reinforced concrete is subjected to constant loading, crack propagation and widening with time can be expected. Eventually, sudden failure can occur after tertiary creep response when the load ratio is high enough. However, when strain-hardening fiber-reinforced concrete behavior is expected, multiple cracking will widen with time without any failure behavior. Gettu et al. [94] studied the CMOD-time response considering distinct load ratios for steel and polymeric fiber reinforced concrete (Figure 2.19 (a) and (b), respectively). They concluded that the creep crack widths increase with the loading level, and the increase of crack widths due to sustained loading can be expected to be more in polymeric fiber-reinforced concrete. Moreover, the pullout mechanisms due to mechanical anchorage and adherence influence creep behavior [94].



(a)



(b)

Figure 2.19 – CMOD-time responses for (a) polymeric fiber-reinforced concrete and (b) steel fiber-reinforced concrete (Adapted from [94]).

2.5. Experimental methods for damage mapping

From the stress generation developed in the composite, the microscopic damage gradually evolves within the material's internal structure until the subsequent development of macroscopic cracks. Therefore, it is possible to point out the relationship between the material microstructure and its mechanical properties since the experimental evaluation of damage is essential to understand the composite global mechanical behavior.

Many techniques have been developed to detect and map damage at various stages in cement composite materials. However, it is not possible to list a single technique capable of analyzing this variable considering all types of loads, test conditions, material type, and failure modes since all experimental techniques have advantages and limitations. The application of each technique can be based on the type of equipment available, sample size, type of analysis, among others. In order to assess the presence of damage in quasi-brittle materials due to a given loading, several studies have been carried out in the literature using different methods, such as acoustic emission methods (AE), fluorescent methods, X-ray CT method, digital image correlation (DIC) methods, or nanoindentation/microindentation techniques.

The acoustic emission method is commonly used to analyze the location of cracks and the type of crack present in cementitious materials/rocks during the loading stage. In order to assess the arrival time and the energy of an elastic wave caused by microcracking, sensors are fixed to the surface of the sample [95], [96] to capture this information. The elastic waves propagate within the range of ultrasonic frequencies, generated due to the quick release of energy within a given material. It is a non-destructive method that detects and analyzes the waves generated from localized sources when a material is conveniently subjected to a specific stress level [97]. On the other hand, this method makes estimating crack length and width difficult [98]. It is a technique often used in the literature for detecting and mapping damage to materials and structures, especially regarding health structure monitoring applications in concrete structures and cementitious materials [99]–[101]. The technique helps extract the microcrack details, such as location, type, and extent, to validate the numerical models. Figure 2.20

schematically shows the typical setup of an acoustic emission test for damage detection.

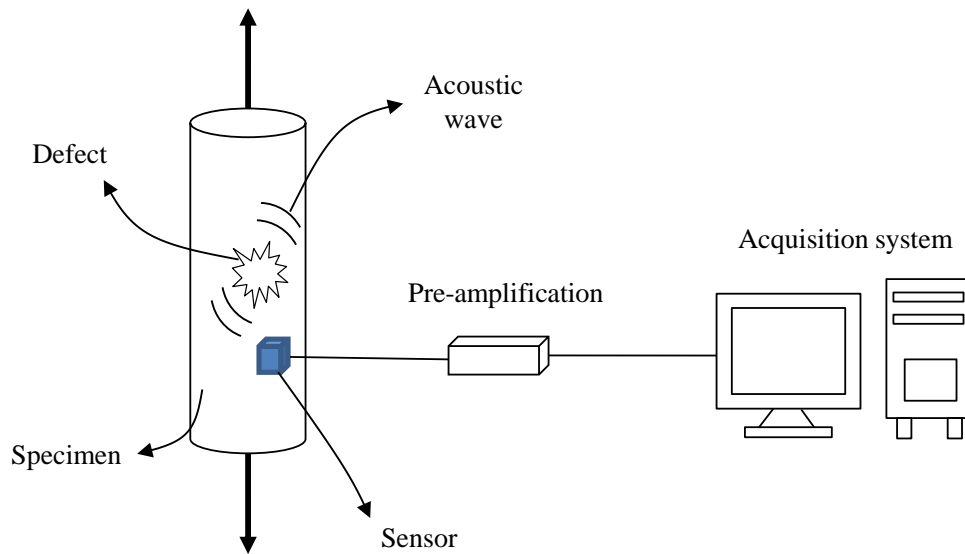


Figure 2.20 – Typical experimental setup for AE methods (Adapted from [102]).

Fluorescent methods are also possible techniques to observe and quantify microcracks and the damage evolution in a specimen by image analysis after injection of a low-viscosity resin with dye into the microcracks. Wajima et al. [103] and Chen et al. [104] studied the effects of microscopic pore spaces and microcracks filled with a synthetic resin mixed with fluorescent ink under ultraviolet light for applications in an oil and gas reservoir, as illustrated in Figure 2.21. Therefore, it is possible to map the formation of microcracks satisfactorily; however, once the specimen is cut, the results of the analyses are only described in two dimensions [98].

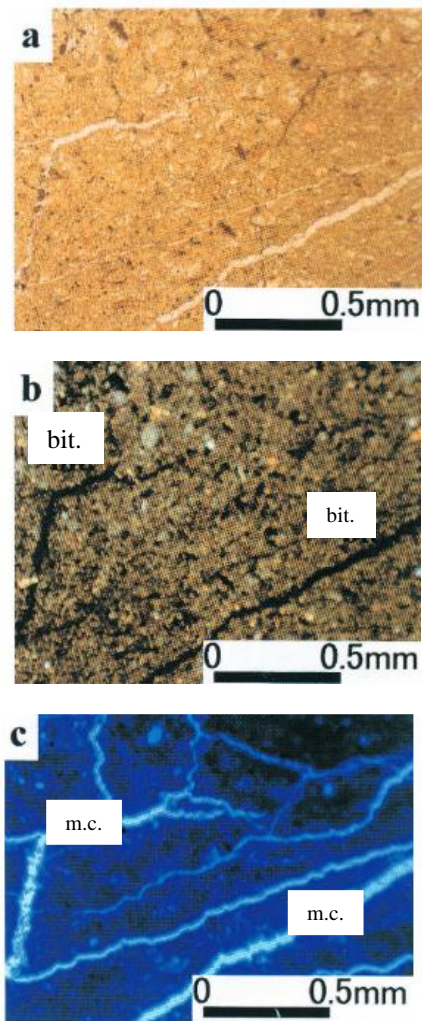


Figure 2.21 – Microcracks evaluated through the optic microscope and by fluorescent methods: (a) open nicol; (b) crossed nicol; (c) open nicol with UV; bit.: betume; m.c.: microcrack (Adapted from [103]).

Alternatively, the microCT technique is another non-destructive method that can be carried out to study the internal material structure with three-dimensional images. The basic principle of the microCT is a source emitting X-ray that is attenuated as it passes through the sample until reaching the detector. This procedure is done as the specimen holder rotates 360° about a single axis at a certain step, generating a sequence of projection images [105]. The projection images are reconstructed using mathematical principles of tomography, finally providing a sequence of 2D slices that compose the 3D image [105], [106]. Figure 2.22 presents the schematic workflow for the microCT image acquisition and generation of the 2D slices.

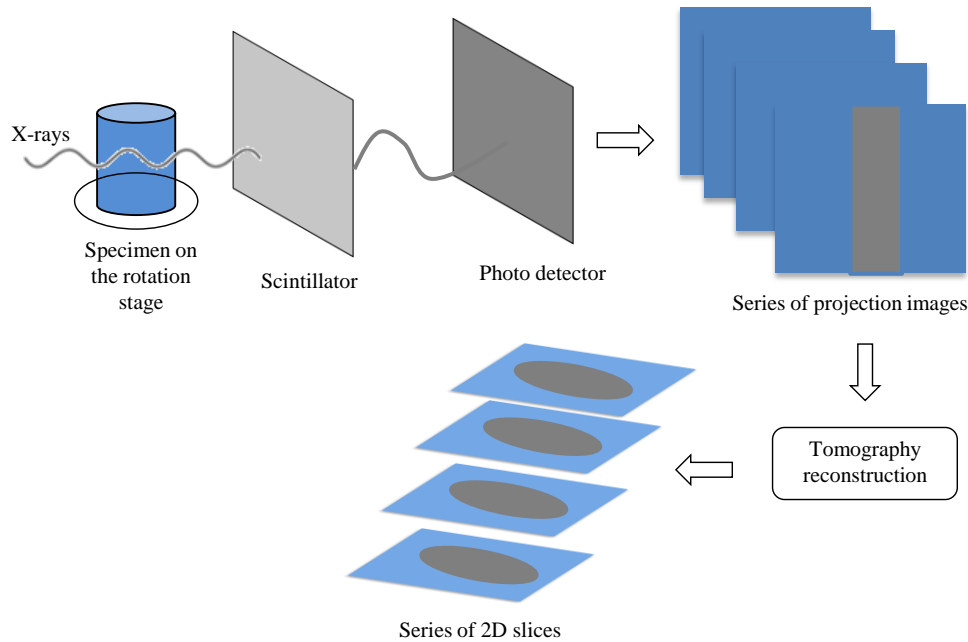


Figure 2.22 – X-ray acquisition and reconstruction process (Adapted from [106]).

Landis et al. [107] used the methodology in mortars, studying the relationship between the fracture energy and the area of the induced crack during the performance of uniaxial compression tests. Wang et al. [108] observed voids and cracked surfaces using the X-ray CT methodology, suggesting the development of a damage tensor to represent the damage. Later, Elaqla et al. [89] used the same methodology to identify the damage mechanisms and the crack propagation during compression tests on mortar specimens. Sugiyama et al. [90] applied X-ray tomography with a resolution of $0.5 \mu\text{m}$ to analyze the deteriorated mortar, visualizing the effects of the diffusion tortuosity present in the material's internal structure. Another work in the area involved the studies by Promentilla et al. [91], who applied a microfocus to characterize the internal structure of the mortar by freeze-thaw action. More recently, Ren et al. [109] and Huang et al. [110] suggested 2D and 3D mesoscale finite element models based on X-ray computed tomography images to investigate the microscale damage and crack propagation behavior in concrete. Tian et al. [111] also tried to quantify the internal meso-cracking of concrete to estimate the damage in a uniaxial compression test using a helical tomography. However, much of the research regarding the investigation of damage in concrete using X-ray microCT is focused mainly on apparent fractures produced inside the sample, with little research dealing with the formation of microcracks before the stress peak in tests of compression or direct tension. Jung et al. [112]

demonstrated the quantitative analysis of the microcracking process of a concrete specimen during a uniaxial compression cyclical test before the appearance of an apparent fracture using three-dimensional X-ray computed tomography images, similar as reported in the previous works of Lorenzoni [105], [106].

DIC is also a technique that has been applied to detect concrete deformation and mesoscopic damage. The main goal of this methodology is to analyze the speckle image before and after the specimen deformation via image correlation matching [113]. However, previous research has focused on macroscopic cracks inducing structural damage identification, and few studies are carried out considering microcracks or microdamage evolution.

Finally, nanoindentation is an additional method that has been carried out in the literature to investigate the evolution of damage in cement composite materials. Lukovic et al. [114] have studied the mechanical parameters in cement materials using nanoindentation and microscopy analysis. The microscopy images make it possible to perform the needle penetration test in a small cement block and map the distribution of mechanical properties (*e.g.*, Young modulus) along the block. Since the damage variable is related to the material stiffness, it is possible to determine the evolution of the damage in the sample according to the progress of the nanoindentation test. Figure 2.23 and Figure 2.24 present images taken from the indentation analysis where the Young modulus and hardness distribution in a region of the cement block are indicated.

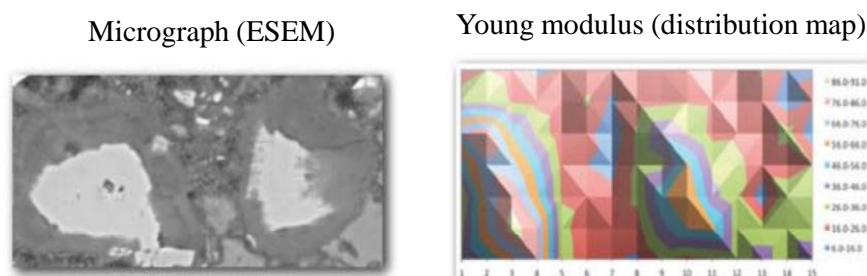


Figure 2.23 – Distribution map of Young's modulus in the cement sample (Adapted from [114]).

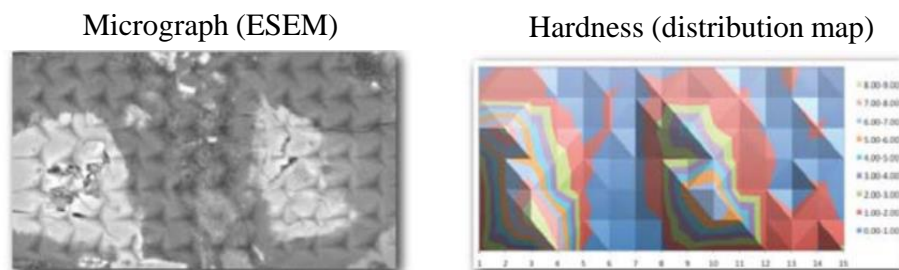


Figure 2.24 – Distribution map of hardness in the cement sample (Adapted from [114]).

In some specific cases, microindentation is also carried out, considering a very similar setup. It requires the polishing of composite samples with fibers perpendicular to the surface and consists of pressing the extremity of fiber through an indenter until fiber debonding [114].

In this sense, for quantifying microscopic damage at the interface of the composite material, the techniques mentioned above are the most typically used in the literature. The best methodology will depend on each research goal, setup availability, expected level of detail, and image quality generated by the equipment.

3 Experimental tests

This chapter presents the experimental program developed throughout this work to analyze the damage, interfacial debonding, and stress transfer mechanisms in cementitious materials. In this study, experimental tests are crucial to calibrate and validate the further developed numerical models and give more insight into the studied problems. Therefore, the experimental results from this chapter will support the calibration and validation of the numerical models presented in Chapter 4.

Mechanical tests and microCT analyses were carried out considering two distinct types of cement matrix: (i) Matrix A with compressive strength of 40 MPa and (ii) Matrix B with compressive strength of 80 MPa. All the mechanical tests were carried out in Laboratório de Estruturas e Materiais (LEM/DEC) of PUC-Rio. At the same time, the microCT analyses were performed in Plataforma Multiusuário de Micro Tomografia Computadorizada at Universidade Federal Fluminense. Figure 3.1 summarizes a schematic workflow for the experimental tests and analyses carried out in this thesis.

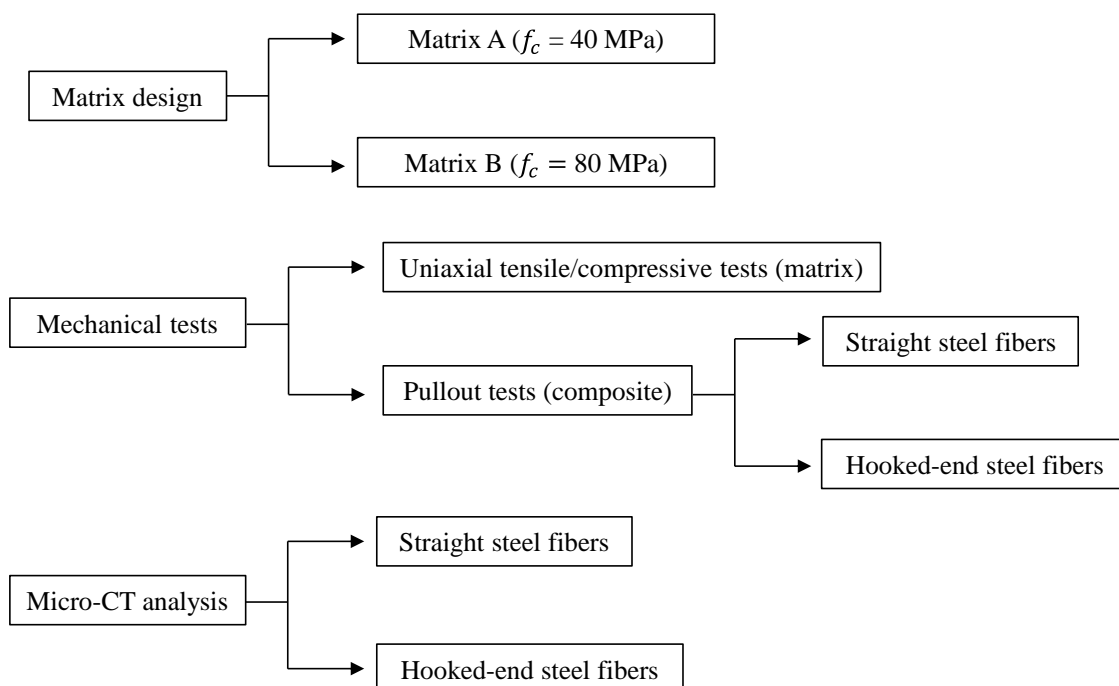


Figure 3.1 – Schematic workflow for the experimental tests carried out in this thesis.

3.1. Matrix A

3.1.1. Materials and methods

Matrix design

Matrix A was designed for the water/cement ratio of 0.5. The cementitious material was composed in mass by Portland cement CII-F32, as defined by the Brazilian standard ABNT NBR 16697 [115]. The coarse gneiss aggregate (coarse sand) has a maximum diameter of 9.5 mm and a fineness module of 5.41. The natural quartz sand (fine sand) was used in two distinct fractions: the first fraction was represented by the passing material in a 4.75 mm screen size and retained on a screen size of 0.85 mm; the retained material represented the second fraction on a 150 μm screen. The natural quartz sand originally had a maximum diameter of 2.36 mm and a fineness module of 2.68.

The additions included SILMIX [®] active silica type D (densified), POZOFLY [®] fly ash, and a quartz powder filler sourced from the ceramic industry and referred to in this study as #325 silica. The superplasticizer GLENIUM [®] 3500 was used to provide the necessary workability. Table 3.1 summarizes the concrete mix proportions for Matrix A.

Table 3.1 – Matrix A mix proportions.

Materials	kg/m³
Portland cement (CII-F32)	360.0
Fine sand	830.0
Coarse sand	100.0
#325 silica	70.0
Fly ash	170.0
Microsilica	45.0
Water	164.0
Superplasticizer	20.0
Viscosity modifier	3.0

A flow slump test was also carried out according to the Brazilian standard ABNT NBR 15823-2 [116], obtaining a diameter of 27 mm \pm 3 mm, as indicated in Figure 3.2. The entire molding process was carried out to minimize the incorporation of air voids into the cementitious matrix. Thus, in addition to

assessing the mortar's flowability, tapping and manual vibration of the specimens were applied.



Figure 3.2 – Flow test carried out with Matrix A.

3.1.1.1. Mechanical characterization

Uniaxial compressive test

Uniaxial compression tests and determination of the Young's modulus of Matrix A were carried out at 28 days, in accordance with the Brazilian standards ABNT NBR 5739 [117] and ABNT NBR 8522 [118], respectively. Three 200 mm high and 100 mm in diameter cylinders were cast.

Before molding, the recipient was coated with a layer of demolding oil. During molding, the concrete was compacted solely through external vibration, using external blows with a rubber hammer. After 24 hours, the test specimens were demolded, wrapped in plastic film, and placed in an environment with controlled temperature of 25° C and humidity of 95%. Approximately 24 hours before testing, the specimens underwent a facing process on the base and top to ensure surface regularity and parallelism between the faces. This procedure ensures uniform stress transfer during loading. The uniaxial compression tests were conducted on an MTS

311 servo-hydraulic universal testing machine with hydraulic grips and a maximum load capacity of 1000 kN. Two vertical displacement transducers (LVDTs) coupled to cylindrical rings were positioned around the test specimen for strain measurement to assess the Young's modulus (Figure 3.3). In this way, the strain value of the specimen was obtained by the ratio of the simple arithmetic mean measured relative displacement to the initial reference length given by the distance between the rings. The stress was calculated as the ratio between the applied load and the cross-sectional area of the test specimen. The elastic modulus corresponds to the slope of the initial region of the stress-strain curve, up to approximately 30% of the maximum stress. The tests were controlled by the axial displacement of the LVDT with a rate of 0.1 mm/min. Additionally, Figure 3.3 presents the experimental setup for the uniaxial compressive tests carried out in this thesis.



Figure 3.3 – Setup for the uniaxial compression tests in Matrix A.

Pullout tests

In order to assess damage evolution and stress transfer mechanisms at the fiber/matrix interface, validating numerical models to be subsequently developed in this study, pullout tests were conducted. DRAMIX® 3D 80/60 steel fibers with a length of 60 mm and a diameter of 0.75 mm were used. Additionally, two fiber geometries were selected for the pullout tests: (i) straight steel fibers and (ii) hooked-end steel fibers. All fibers had an embedment length of $L = 40$ mm. Recognizing that the primary objective of the pullout tests was to validate damage

evolution mechanisms at the fiber/matrix interface occurring at a smaller observation scale, and considering that the samples would be later taken to an X-ray microCT, six specimens were produced for conducting the pullout tests. The split cylindrical specimens had a total height of $H = 40$ mm. In order to position the steel fiber centrally in the specimen, facilitating subsequent observation of the damaged region in the microCT, there is a gradual reduction of the internal cross-sectional area of the cylinder ($d_{int} = 11$ mm) and a hole with a diameter of 0.75 mm at the base of the mold to allow passage of the fiber. The design of this specimen allows for the performance of mechanical tests and is also compatible with microCT scanning.

It is essential to highlight the novelty of the proposed specimen since past works in the literature consider samples with a distinct geometry for the pullout experiments. The schematic representation of the specimen is presented in Figure 3.4. Figure 3.5 shows some specimens after the molding process, where "R" refers to the straight steel fiber geometry, and "G" refers to the hooked-end steel fiber geometry.

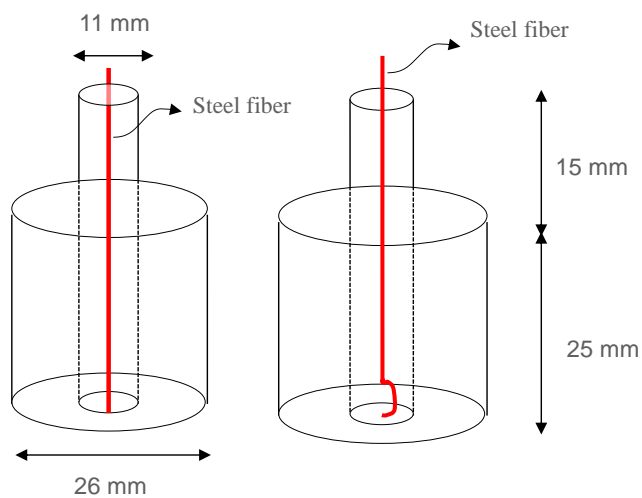


Figure 3.4 – Schematic representation and specimen dimensions for the pullout tests.



Figure 3.5 – Specimens for the pullout test ("R" for straight and "G" for hooked-end steel fiber).

The pullout tests were conducted on the EMIC® DL 3000 electromechanical universal testing machine with a maximum load capacity of 30 kN. A 2 kN load cell was attached to the experimental setup. The test control was achieved by displacing the actuator's internal LVDT at a rate of 0.5 mm/min. The samples were clamped in grips, representing a fixed boundary condition. Fiber slippage was obtained by the machine displacement. Direct measurement through machine displacement was validated in previous experimental studies by Trindade [119] and Castoldi [120], where it was observed that slippages obtained from LVDT measurement were similar to those obtained by the internal acquisition of the testing machine. The sample's base had its displacement restricted due to the presence of a metallic ring secured with screws. Figure 3.6 (a) and (b) present the experimental setup and the details regarding the fixed specimen.

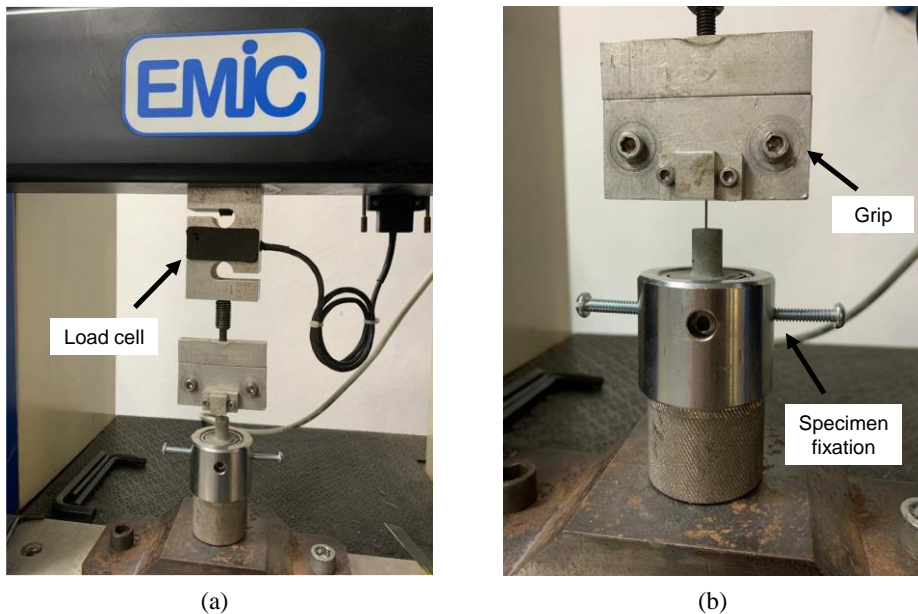


Figure 3.6 – (a) Pullout test configuration and (b) detail for the specimen fixation.

The maximum shear strength (τ_{max}) was obtained through the experimental pullout loads, following the relationship presented in Equation 3.1, where P_{max} refers to the maximum pullout load, r is the fiber radius and L_C is the embedded length.

$$\tau_{max} = \frac{P_{max}}{2 \pi r L_C} \quad (3.1)$$

3.1.1.2. MicroCT analysis

The microCT scanning was performed in a Zeiss-Xradia Versa 510 in the Plataforma Multiusuário de Micro Tomografia Computadorizada at Universidade Federal Fluminense (UFF). The samples were scanned at a voxel size of 5 μm for higher level of detail. All acquisition was taken using camera binning 1, with field of view of 2048 x 2048 pixels. The parameters used in the image acquisition protocol are shown in Table 3.2.

Table 3.2 – Image acquisition data for the microCT analyses.

Information	Value
Optical lens	0.4X – 1X
Source sample distance (mm)	40.0
Detector sample distance (mm)	120.0
Voxel size (μm)	5.0
Voltage (kV)	80.0
Power (W)	7.0
Exposition time (s)	6.4 – 8.0

All specimens were imaged prior to pullout testing. Twelve microCT scans were carried out considering the distinct types of matrix, steel fiber geometry, and the pullout stage (before, partial, or complete pullout). The information regarding the microCT analyses developed in this thesis is summarized in detail in Table 3.3.

Table 3.3 – MicroCT scans carried out in this research.

Matrix type	Steel fiber geometry	Scenario
Matrix A	Straight fiber (Sample <i>S01</i>)	(1) Before pullout (2) Partial pullout ($\delta = 7$ mm)
	Hooked-end fiber (Sample <i>H01</i>)	(3) Before pullout (4) Partial pullout ($\delta = 7$ mm)
Matrix B	Straight fiber (Sample <i>S02</i>)	(5) Before pullout (6) Partial pullout ($\delta = 7$ mm) (7) Complete pullout
	Hooked-end fiber (Sample <i>H02</i>)	(8) Before pullout (9) Partial pullout ($\delta = 7$ mm) (10) Complete pullout
	Hooked-end fiber shifted up (Sample <i>H03</i>)	(11) Before pullout (12) Partial pullout ($\delta = 7$ mm)

Considering the region of interest of the samples and the desired resolution in order to adequately capture the microcracks at the fiber/matrix interface, the

height of the scans was approximately 15 mm. Figure 3.7 presents the equipment used for the microCT analyses and a schematic representation of the specimens placed in the microCT test position, highlighting the approximate scanned region of interest (ROI). Additionally, Figure 3.8 presents an example of the scanned volume of one of the microCT analyses carried out in this work.

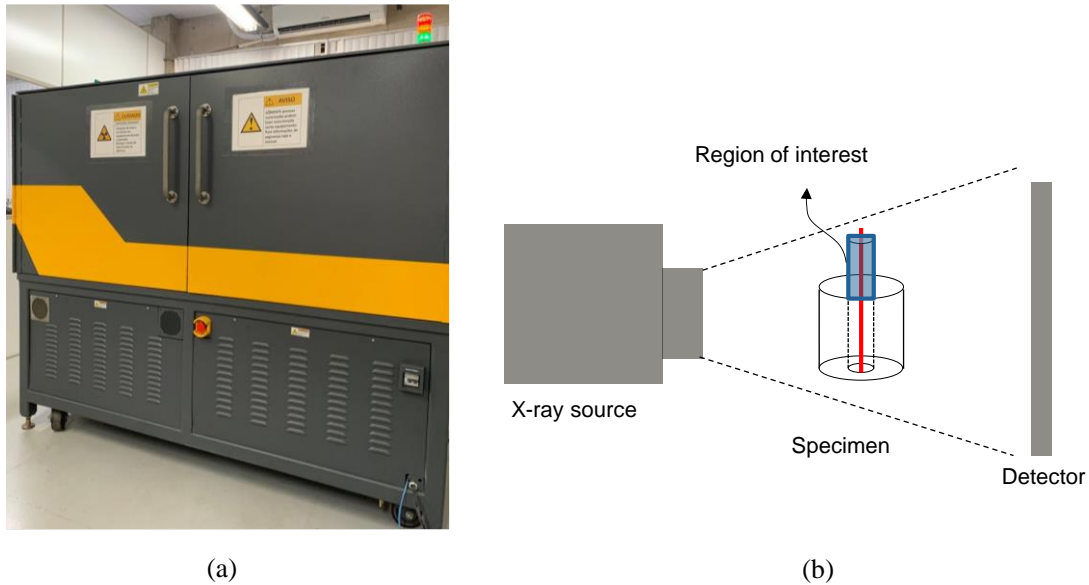


Figure 3.7 – (a) Zeiss-Xradia 510 Versa equipment for the microCT analyses; (b) schematic representation of the CT scanning and specimen region of interest.

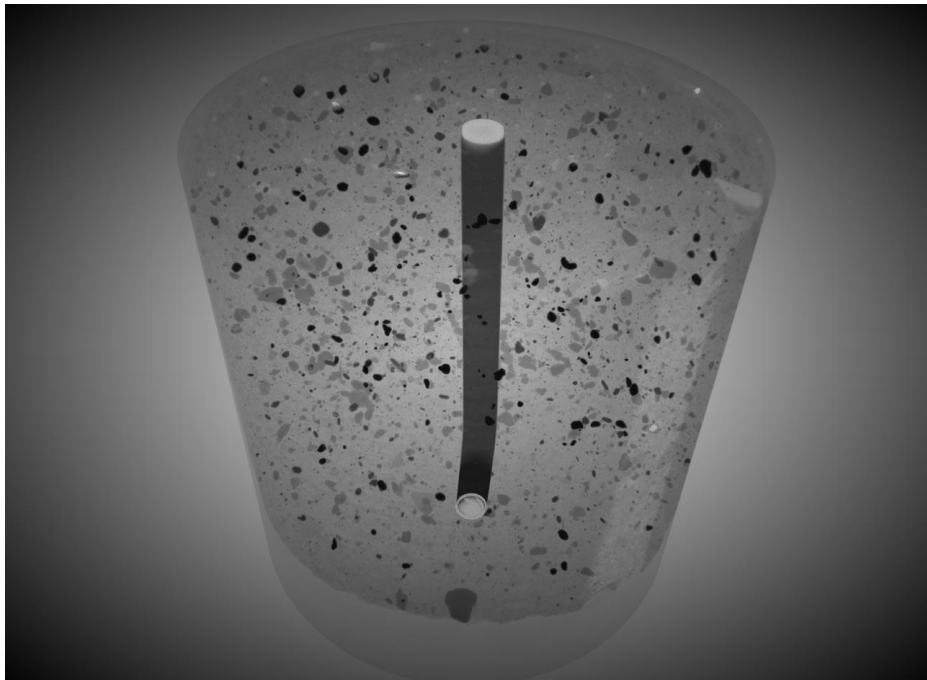


Figure 3.8 – X-ray scanned volume for the straight steel fiber in Matrix A.

3.1.2. Results

Uniaxial compression tests

The compressive strength result was 40.9 ± 2 MPa with a Young's modulus of 29.7 ± 1.33 GPa. The representative curve for the test is shown in Figure 3.9.

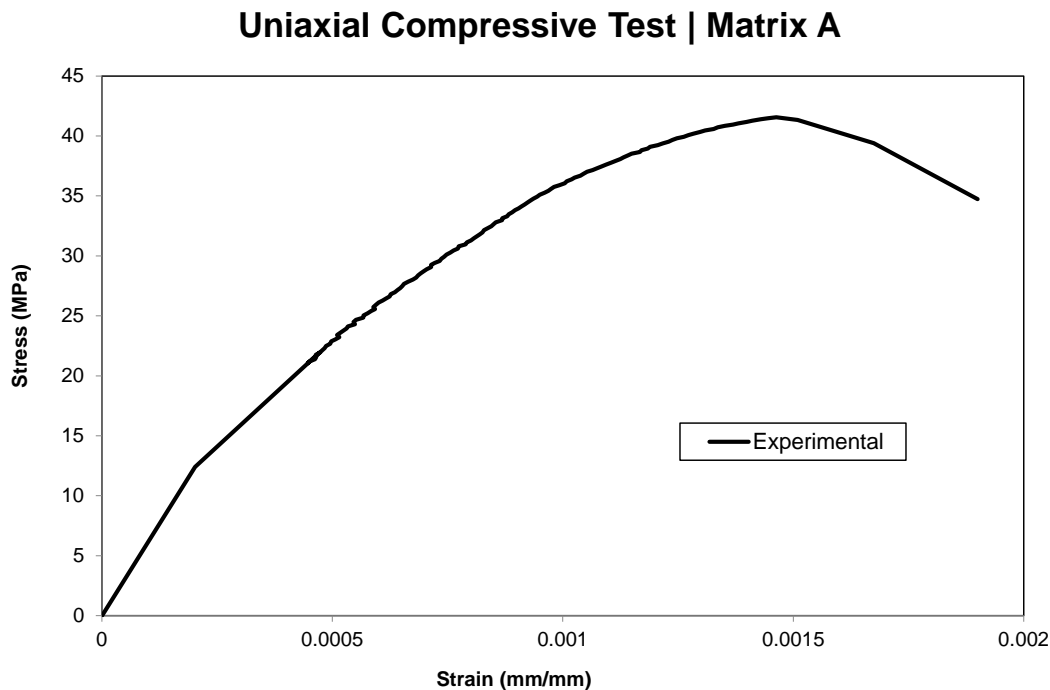


Figure 3.9 – Stress-strain representative curve for the uniaxial compressive test of Matrix A.

Direct tensile tests

The stress-strain curves for Matrix A were previously carried out by Pereira [13] through direct tensile tests. The tensile strength result was $6.04 \text{ MPa} \pm 0.9$ MPa. For more information regarding the uniaxial tensile tests, refer to the work of Pereira [13].

Pullout tests

Figure 3.10 and Figure 3.11 display the pullout force-displacement curves obtained for straight and hooked-end steel fiber, considering Matrix A with good consolidation, respectively. It is relevant to observe that these tests continued until the fiber sliding reached a value of 7 mm, indicating that the fiber was not completely pulled out from the cementitious matrix. This value represents an

intermediate stage regarding fiber pullout, where a sufficient concentration of damage was observed for the investigations carried out in this thesis.

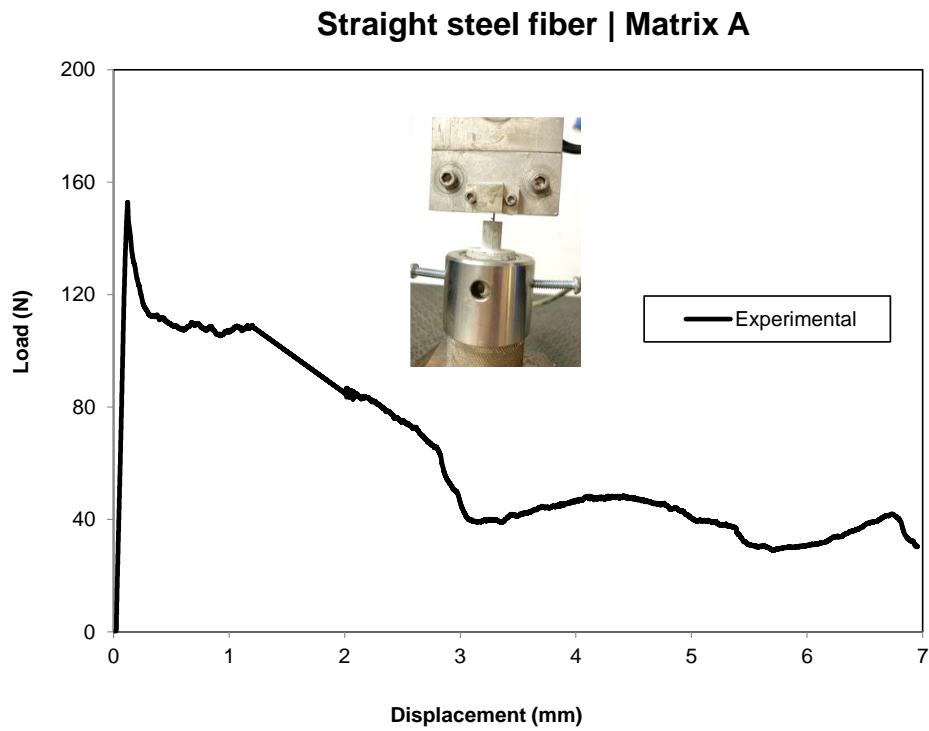


Figure 3.10 – Pullout load-displacement of the straight steel fiber in Matrix A.

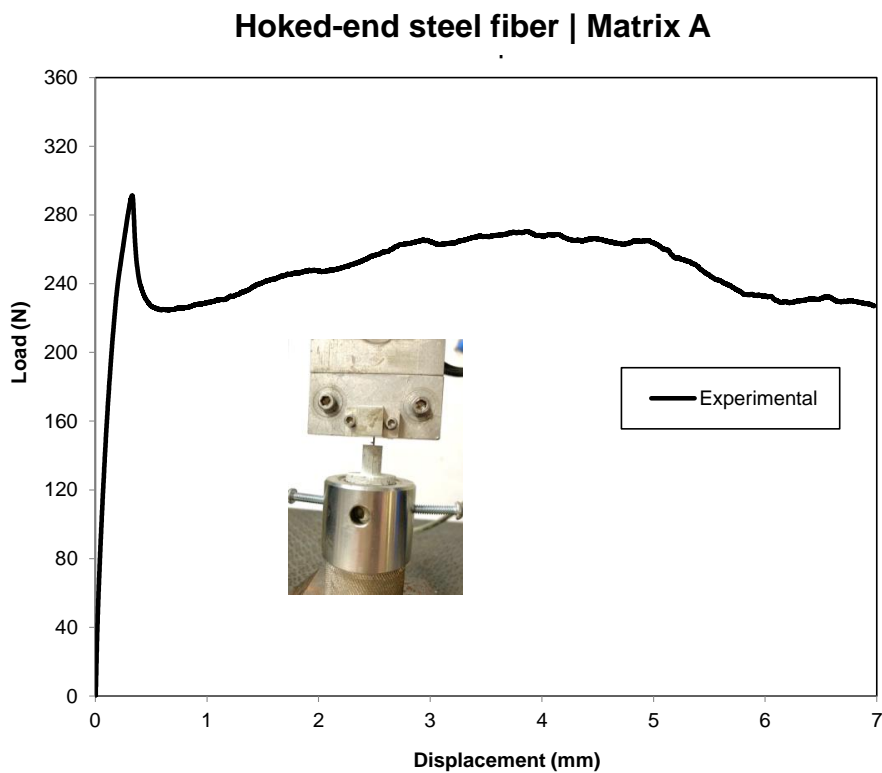


Figure 3.11 – Pullout load-displacement of the hooked-end steel fiber in Matrix A.

From the results obtained in the test with the straight fiber, it can be observed that the pullout force initially increases linearly until the onset of the fiber debonding process. This mechanism is indicated by the nonlinear shape of the pullout curve until reaching the maximum load value. Therefore, the fiber undergoes deformation before the debonding process is initiated. From this point on, the behavior is governed by frictional shear strength and continues until the fiber is completely debonded from the cementitious matrix. Finally, after complete debonding, the fiber is then pulled out.

In the case of the hooked-end steel fiber, a similar mechanism is observed until the peak load. However, this scenario's maximum pullout force value is approximately 80% higher than in the straight fiber case. This fact is justified by the fiber's greater adhesion and mechanical anchoring due to the fiber hook. Thus, the hook is deformed until the onset of the fiber debonding process. In this case, the area under the load-displacement curve is larger for the hooked-end fiber than for the straight fiber scenario.

In this scenario, due to the increased anchorage resulting from the presence of the hook, leading to a higher pullout force, a greater concentration of damage and microcracks is expected in the regions of the interface and near the hook. MicroCT analyses will verify these inferences and will be described in the subsequent section.

Additional pullout tests were also conducted for specimens that exhibited poor consolidation, leading to the incorporation of many voids in the cementitious matrix. This more significant incorporation of voids is attributed to the initial castings which do not consider the manual vibration and tamping process during the molding. The results of the pullout load-displacement curves for this specific group of samples are indicated in Figure 3.12 and Figure 3.13. These results demonstrate that, due to the incorporation of air voids, the fiber sliding reaches significantly lower values than Matrix A with good consolidation.

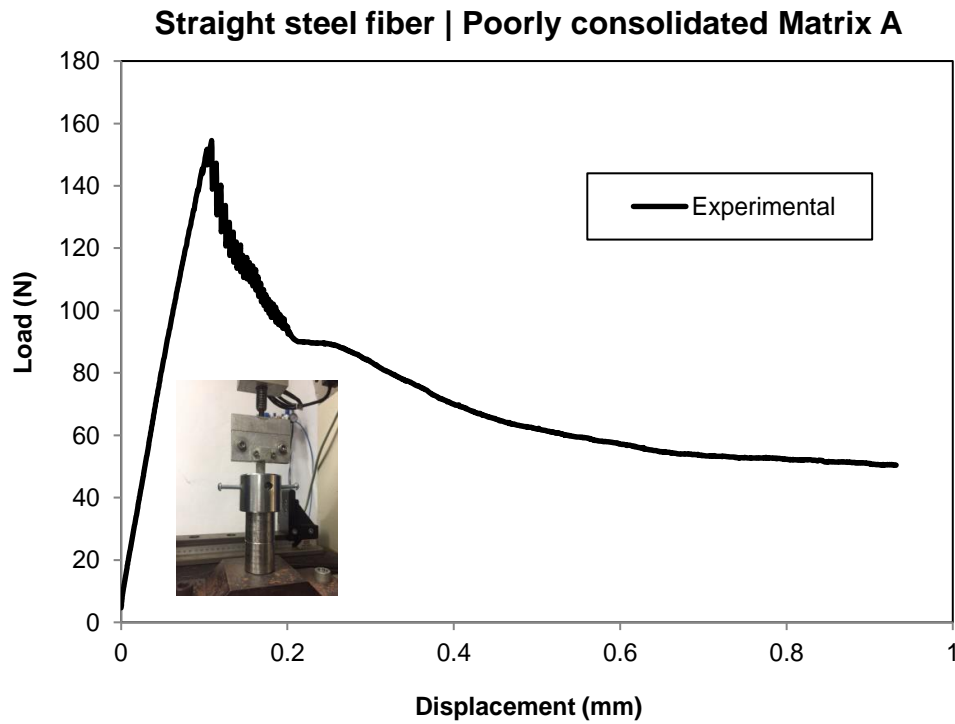


Figure 3.12 – Pullout load-displacement of the straight steel fiber in the poorly consolidated Matrix A.

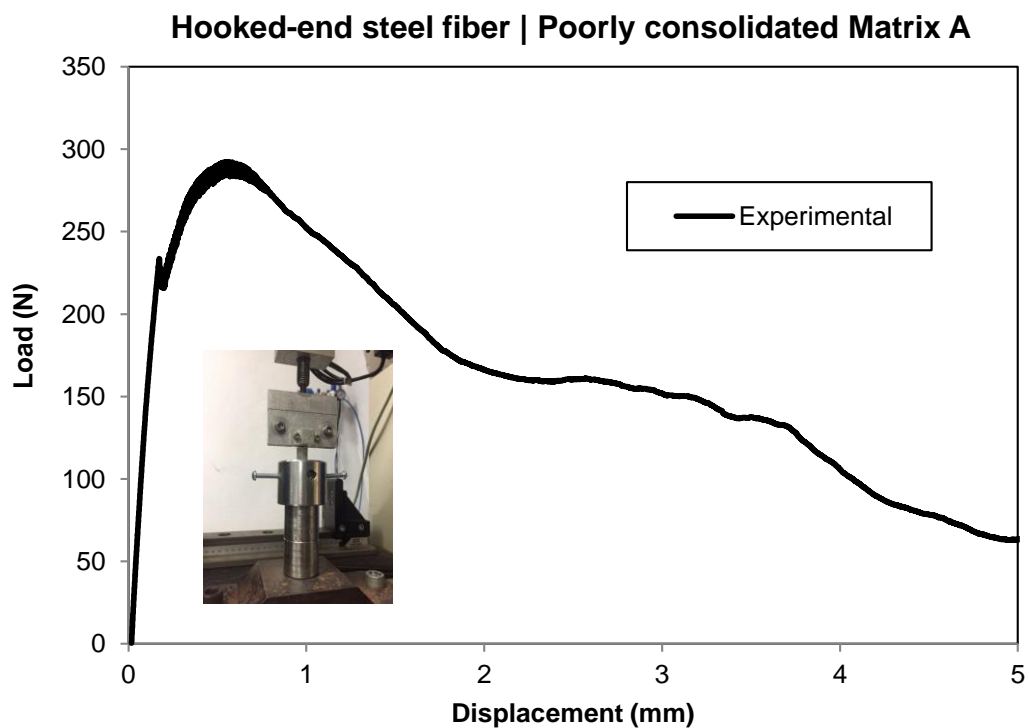


Figure 3.13 – Pullout load-displacement of the hooked-end steel fiber in the poorly consolidated Matrix A.

MicroCT analyses

The samples before and after the pullout test for the straight steel fiber are shown in Figure 3.14, while the sample regarding the hooked-end steel fiber is presented in Figure 3.15. All tomography analyses aimed to maintain the same position (x , y , z) for image capture. For qualitative comparison in the before/after pullout phases, images were selected so that the slice numbering corresponding to the analysis before pullout matched that of the analysis conducted after the test. Thus, it is possible to make an approximate qualitative comparison regarding the evolution of damage and microcracks in the region of interest.

Comparing the images from before and after the pullout test for the straight fiber (Figure 3.14), it is possible to observe that the concentration of microcracks and damage is near the top of the sample (in red color). Few microcracks are observed along the fiber length, and the perturbations due to the fiber debonding are more prominent in the upper part of the specimen. For the hooked-end steel fiber (Figure 3.15), more microcracks can be identified along the fiber length. It is important to highlight that, for Figure 3.15, the fiber hook is outside the region of interest. Matrix spalling is also observed in both cases near the fiber exit point.

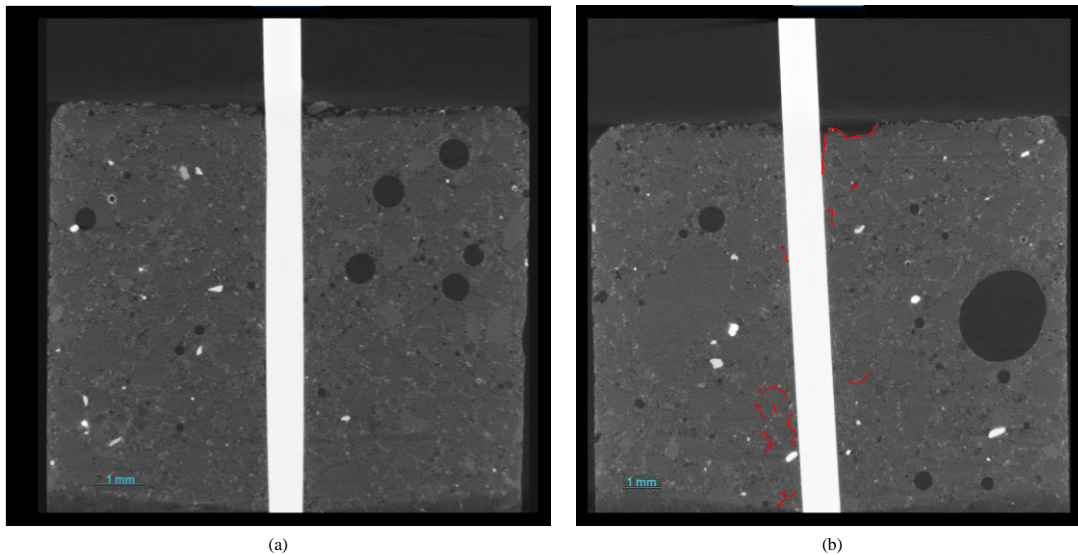


Figure 3.14 – Micrograph (0.4x) of straight steel fiber in Matrix A: (a) before pullout; (b) partial debonding (fiber pullout of 7 mm). Damaged areas are indicated in red color.

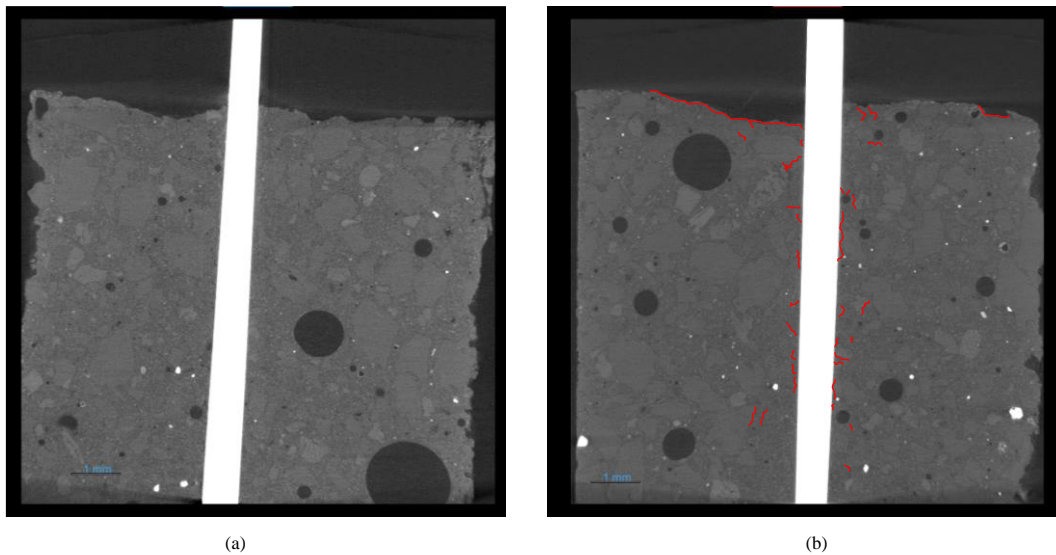


Figure 3.15 – Micrograph (0.4x) of hooked-end steel fiber in Matrix A: (a) before pullout; (b) partial debonding (fiber pullout of 7 mm). Damaged areas are indicated in red color.

Figure 3.16 displays the before/after pullout test images obtained by microCT for the straight fiber in the poorly consolidated Matrix A. In addition, Figure 3.17 shows images of the poorly consolidated Matrix A for the hooked fiber before/after the pullout process. Due to the higher number of defects observed in the matrix, the fiber/matrix adhesion is lower, leading to a greater concentration of cracks and damage compared to the previous cases.

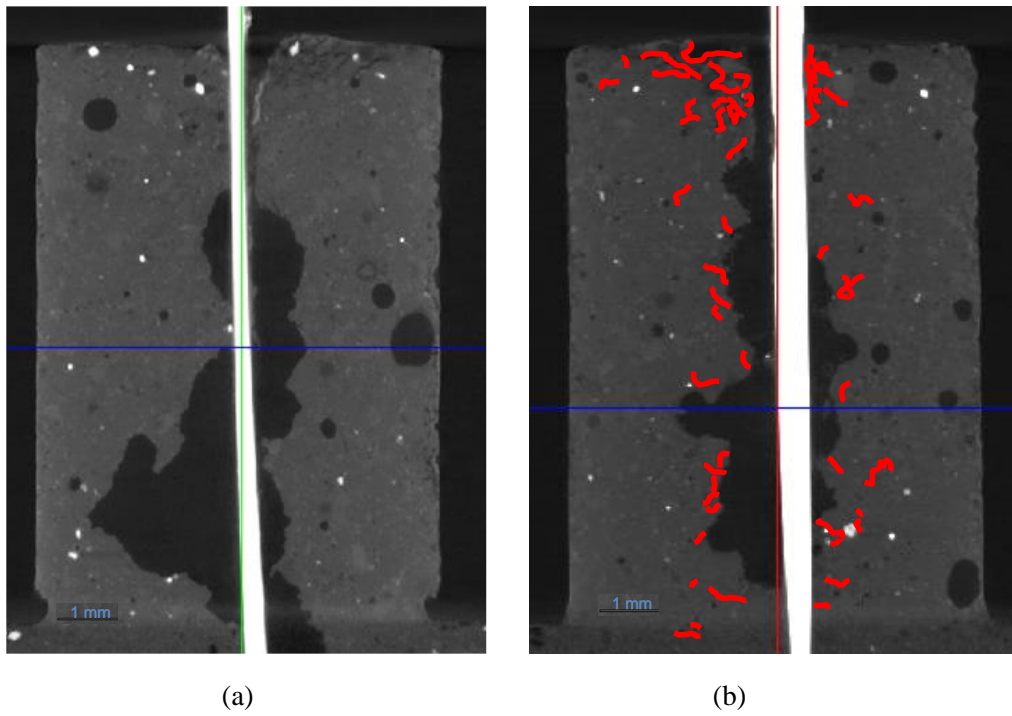


Figure 3.16 – Micrograph (1x) of straight steel fiber in poorly consolidated Matrix A: (a) before pullout; (b) after pullout. Damaged areas are indicated in red color.

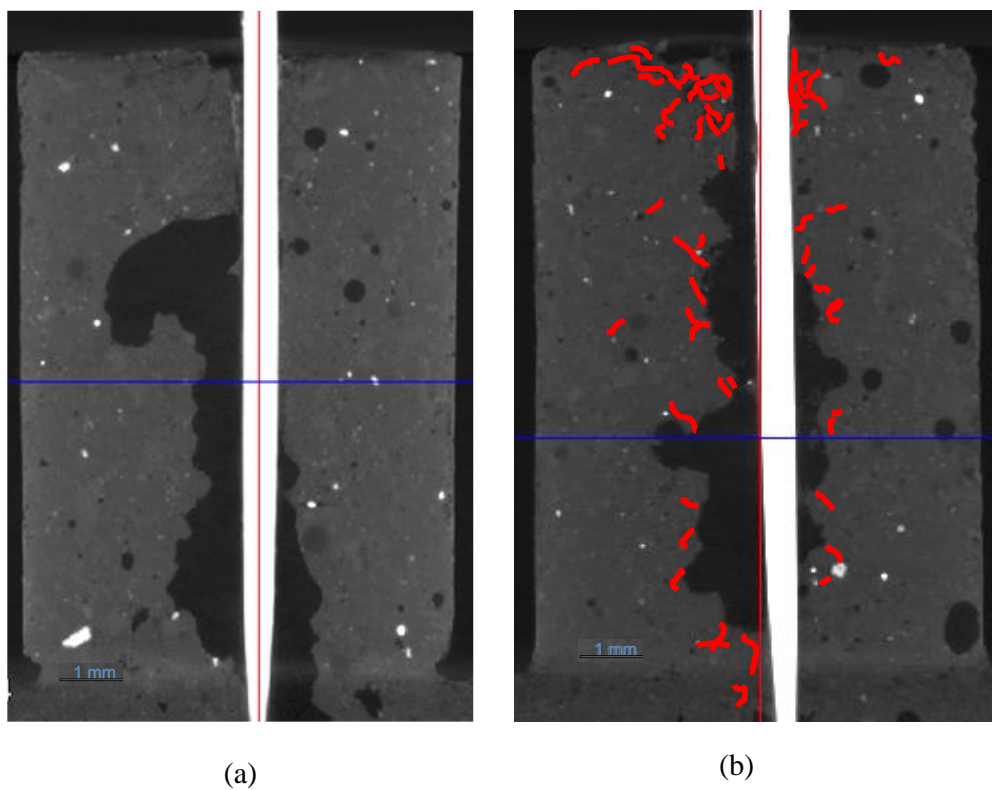


Figure 3.17 – Micrograph (1x) of hooked-end steel fiber in poorly consolidated Matrix A: (a) before pullout; (b) after pullout. Damaged areas are indicated in red color.

3.2. Matrix B

3.2.1. Materials and methods

Matrix design

Matrix B was designed for a water/cement ratio of 0.4. The cementitious material was composed in mass by Portland cement CPV, as defined by the Brazilian standard ABNT NBR 16697 [115]. The used quartz sand had a maximum diameter of 1.18 mm and a density of approximately 2.67 g/cm³.

The additions included metakaolin from Metacaulim do Brasil Indústria e Comércio Ltda. The superplasticizer GLENIUM ® 3500 was used to provide the necessary workability. Teixeira [18] previously carried out a flow test and obtained a spread of 375 mm. Table 3.4 summarizes the concrete mix proportions for Matrix B.

Table 3.4 – Matrix B mix proportions.

Materials	kg/m ³
Portland cement (CPV)	242.0
Quartz sand	484.0
Fly ash	48.0
Metakaolin	194.0
Water	186.0
Superplasticizer	7.0

3.2.1.1. Mechanical characterization

The mechanical tests carried out for Matrix B follow the same procedures described in Section 3.1.1.1 for Matrix A.

3.2.1.2. MicroCT analyses

The microCT analyses carried out for Matrix B follow the same procedures described in Section 3.1.1.2 for Matrix A.

3.2.2. Results

Uniaxial compressive tests

Uniaxial compression tests were also conducted for Matrix B. The compressive strength result was 81.3 ± 7 MPa with a Young's modulus of 25 ± 1.4 GPa. The representative curve for the three sample tests is shown in Figure 3.18.

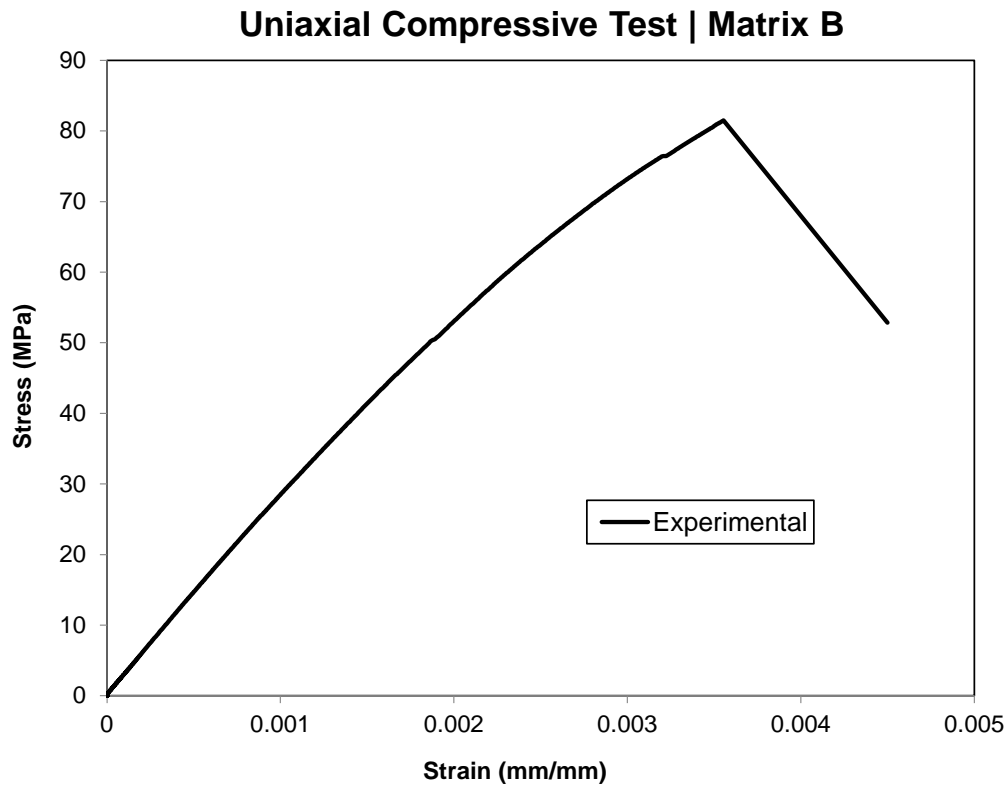


Figure 3.18 - Stress-strain curve for the uniaxial compressive test for Matrix B.

Indirect tensile tests

To characterize the tensile behavior of Matrix B, indirect tensile tests were conducted following the recommendations of ASTM D3967-16 standard [121]. The specimens were tested on the MTS 810 machine with a capacity of 500 kN. The tests were controlled by the clip gauge opening with a rate of 0.1 mm/min.

To attach the clip gauge to the test specimens, diametrically opposed metal plates were affixed to the geometric center of the specimen using glue. The spacing between the plates was 8.37 mm. The load application was conducted using cardboard strips with an average thickness of $t = 0.48$ mm, affixed along the geometric centerline of the disc. Seven specimens were tested during the tensile tests. The setup for the test is indicated in Figure 3.19.

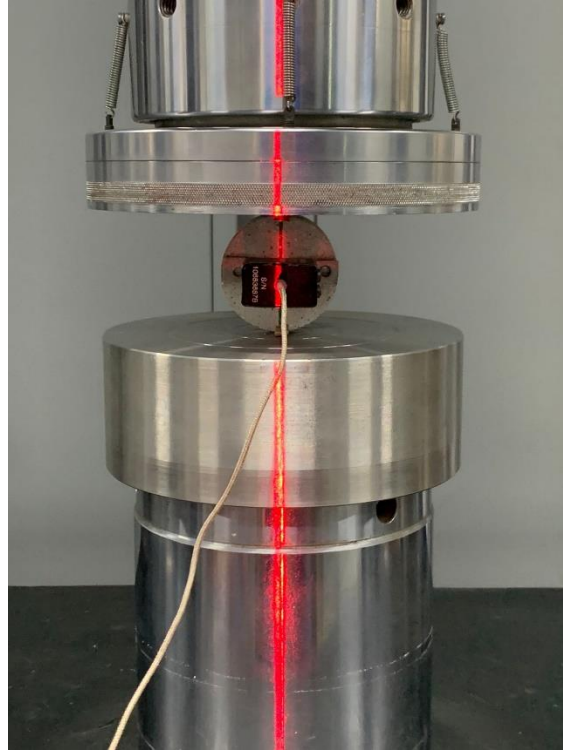


Figure 3.19 – Setup for the indirect tensile test.

The splitting tensile strength (σ_t) of the specimen with the flat patterns is calculated according to Equation 3.2, where P refers to the applied load, t is the thickness of the specimen, and D is the diameter of the specimen.

$$\sigma_t = \frac{2 * P}{\pi * t * D} \quad (3.2)$$

Moreover, Figure 3.20 displays the result of the representative stress-strain curve specific to the indirect tensile test. The tensile strength result was 4.39 MPa \pm 0.32 MPa.

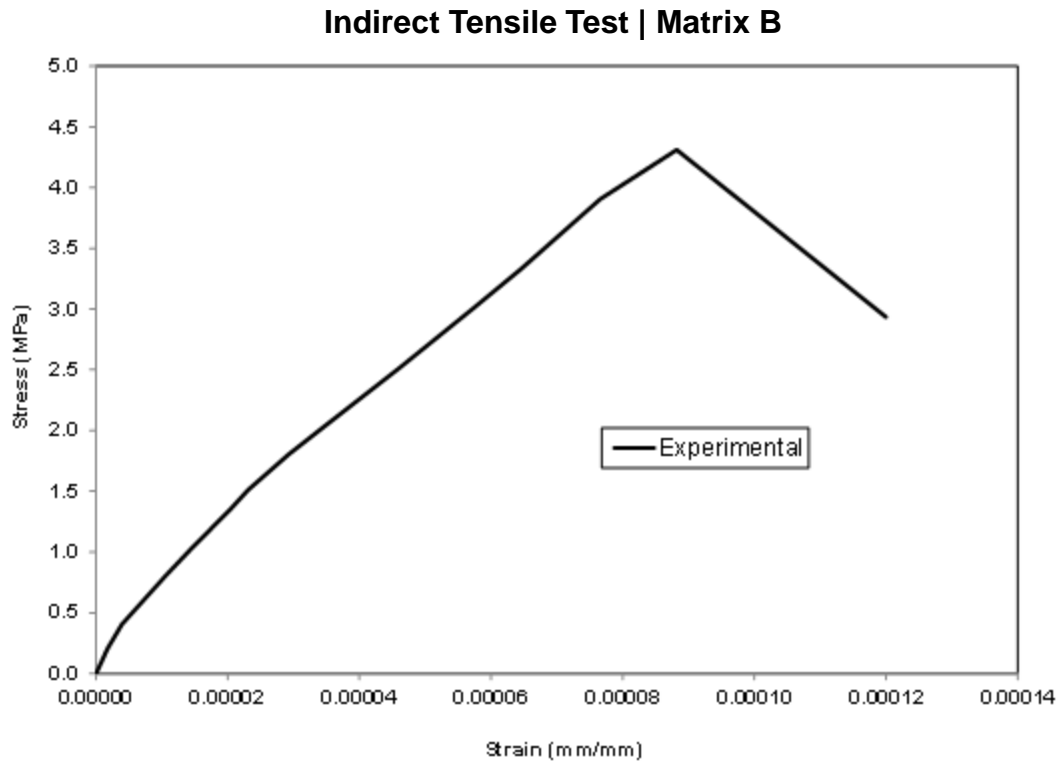


Figure 3.20 - Stress-strain curve for the indirect tensile test for Matrix B.

Pullout tests

The pullout tests for Matrix B were carried out considering the specimen geometry and test setup described in the previous section. Figure 3.21 and Figure 3.22 display the pullout force-displacement curves obtained for straight steel and hooked-end steel fibers considering Matrix B, respectively. It is relevant to observe that these tests continued until the fiber sliding reached a value of 7 mm, indicating that the fiber was not completely pulled out from the cementitious matrix.

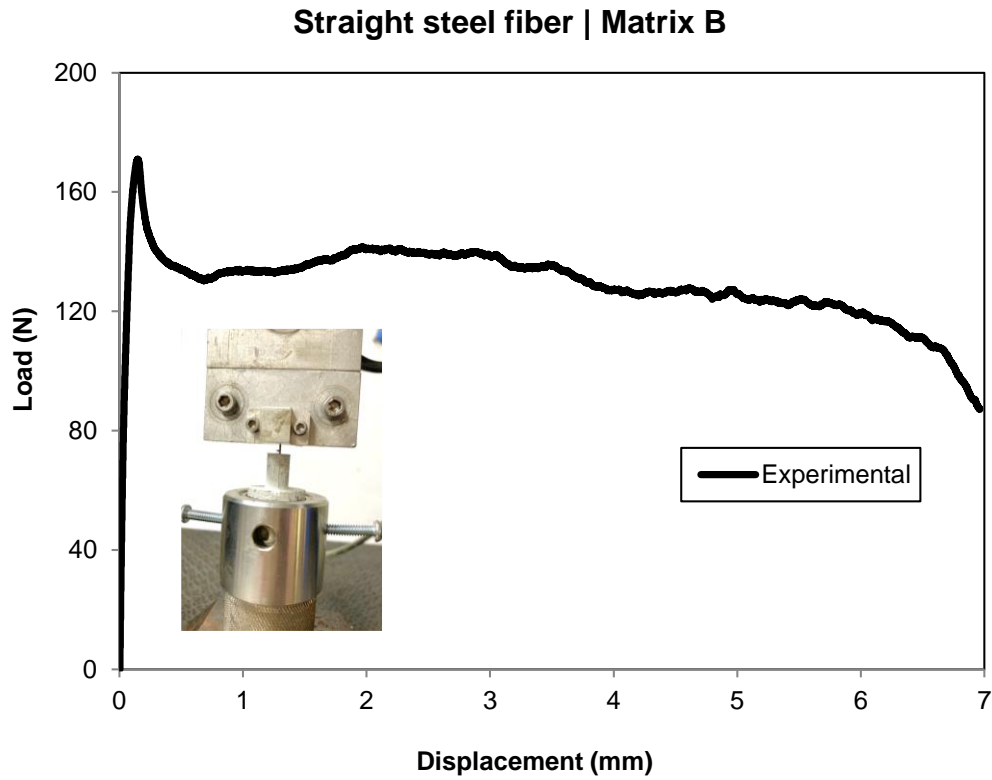


Figure 3.21 – Pullout load-displacement of the straight steel fiber for Matrix B.

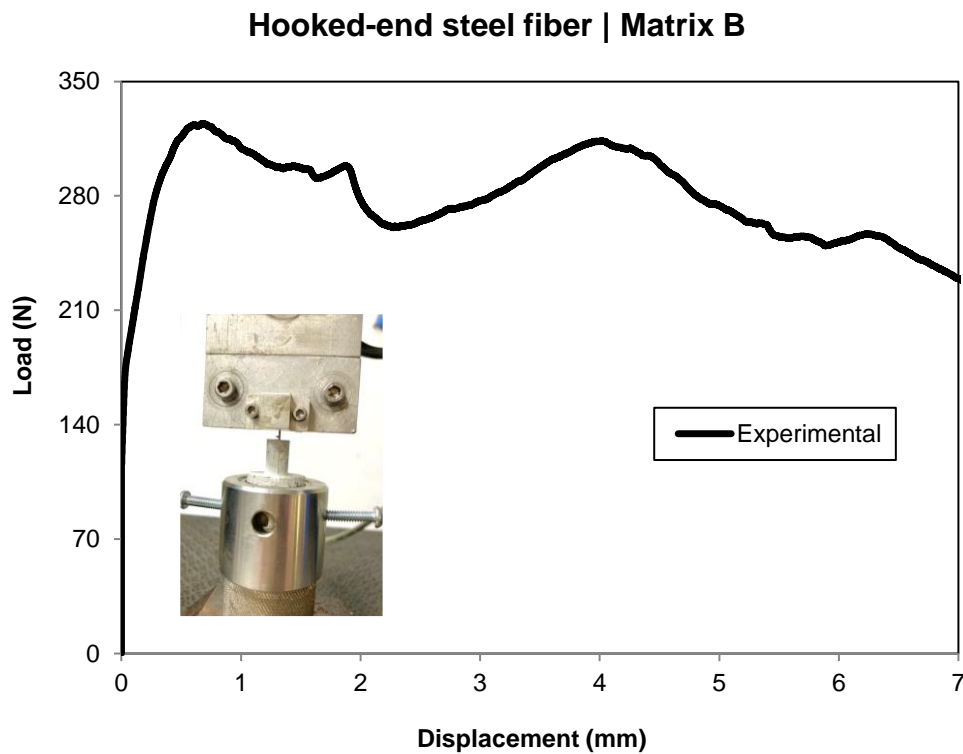


Figure 3.22 – Pullout load-displacement of the hooked-end steel fiber for Matrix B.

From the analysis of the results in Figure 3.21 and Figure 3.22, it is possible to observe that the maximum pullout load for straight steel fiber in Matrix B ($P \sim$

171 N) is slightly higher than the pullout load of the straight fiber in the Matrix A ($P \sim 153$ N). In the case of Matrix B, it is noted that the maximum pullout load for the hooked-end fiber is considerably higher when compared to the pullout of the same fiber geometry in Matrix A.

In summary, Figure 3.23 gathers the pullout load-displacement behavior for the pullout tests conducted in this study, considering the straight steel fiber geometry. From the analysis of this curve, a slightly higher maximum pullout load is observed for Matrix B compared to Matrix A's response. In this case, it can be inferred that the fiber geometry also influences the pullout behavior. The straight geometry facilitates the pullout process and induces a lower concentration of damage along its length, resulting in lower pullout loads.

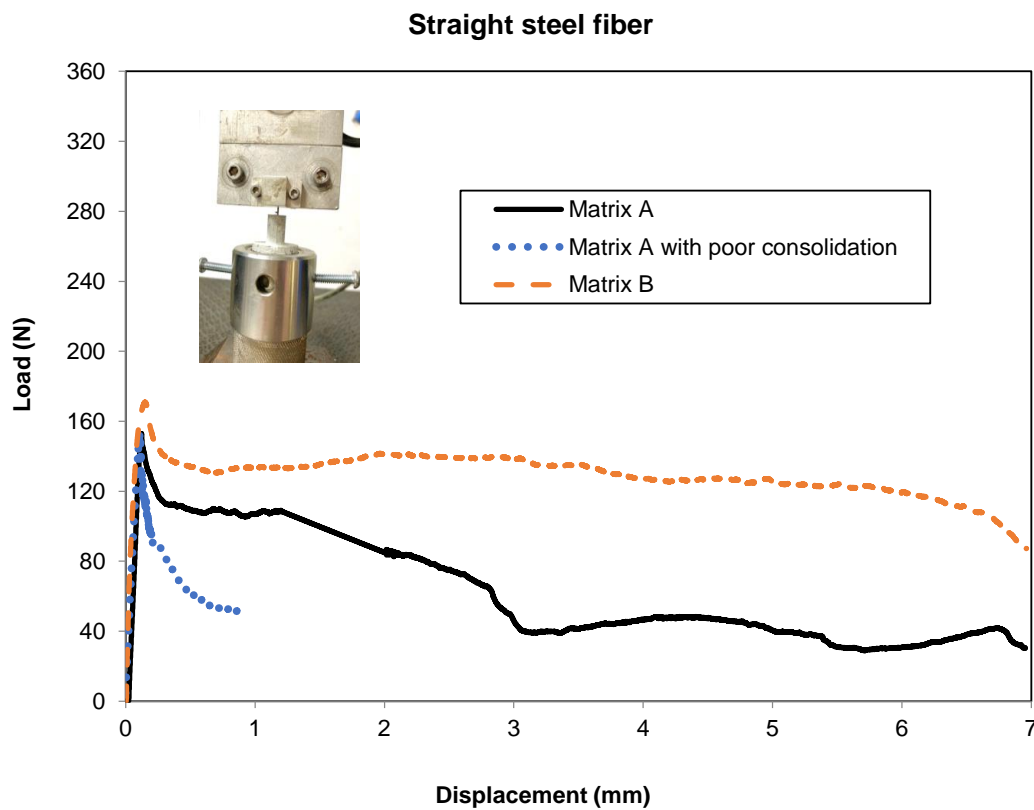


Figure 3.23 – Comparison of the pullout response for the straight steel fiber considering distinct types of cement matrix.

Figure 3.24 presents the pullout load-displacement behavior for the hooked-end steel fiber geometry. In this specific case, the maximum pullout loads are much higher than in the straight fiber scenario due to Matrix B behavior. In addition, the hook and its progressive deformation throughout the test create greater difficulty for the fiber to initiate its debonding/pullout process, justifying the higher load values

observed in Figure 3.24. Pullout energy (*i.e.*, the area under the pullout curve) is also higher for the hooked-end steel fiber in Matrix B.

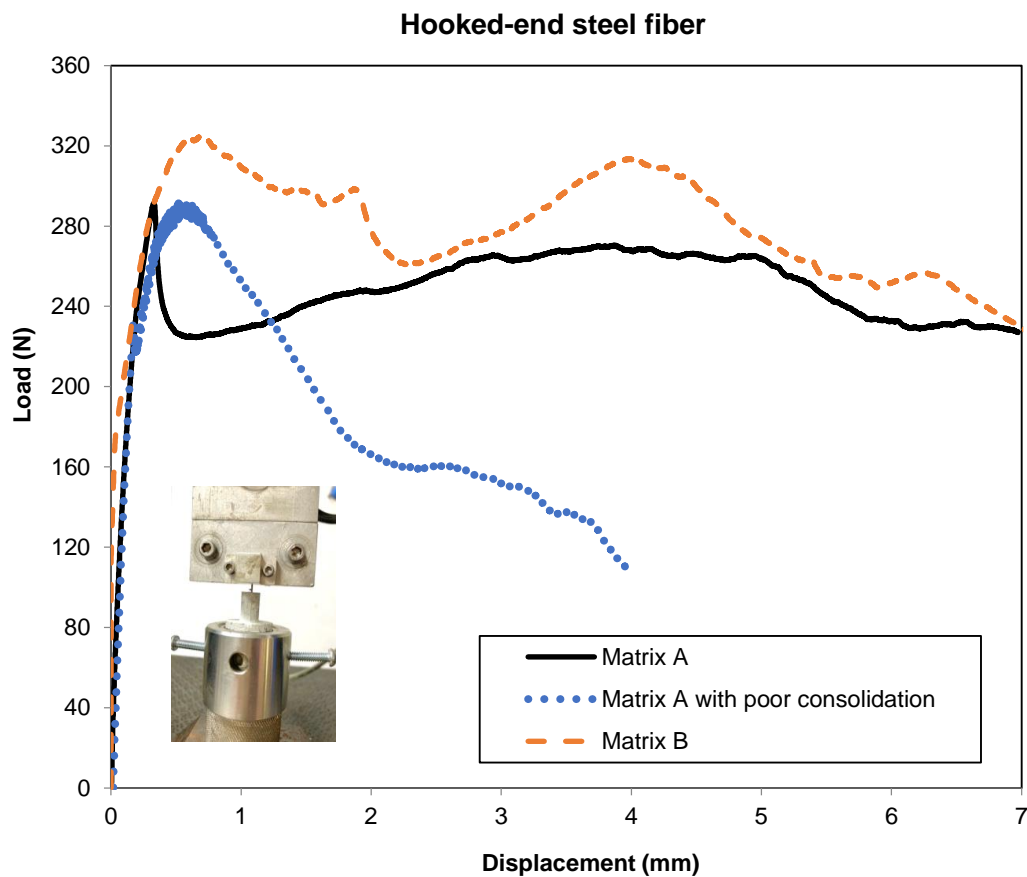


Figure 3.24 – Comparison of the pullout response for the hooked-end steel fiber considering distinct types of cement matrix.

MicroCT analyses

For the Matrix B samples *S02* and *H02*, microCT analyses were carried out considering the configurations and the region of interest specified in Section 3.1.1.2. The samples before and after the pullout test for the straight steel fiber are shown in Figure 3.25, while the sample with the hooked-end steel fiber is presented in Figure 3.26. To enable a consistent comparison, the same criterion based on the numbering of slices is applied in the analyses of Matrix B. Matrix spalling is once again observed in both cases near the fiber exit point.

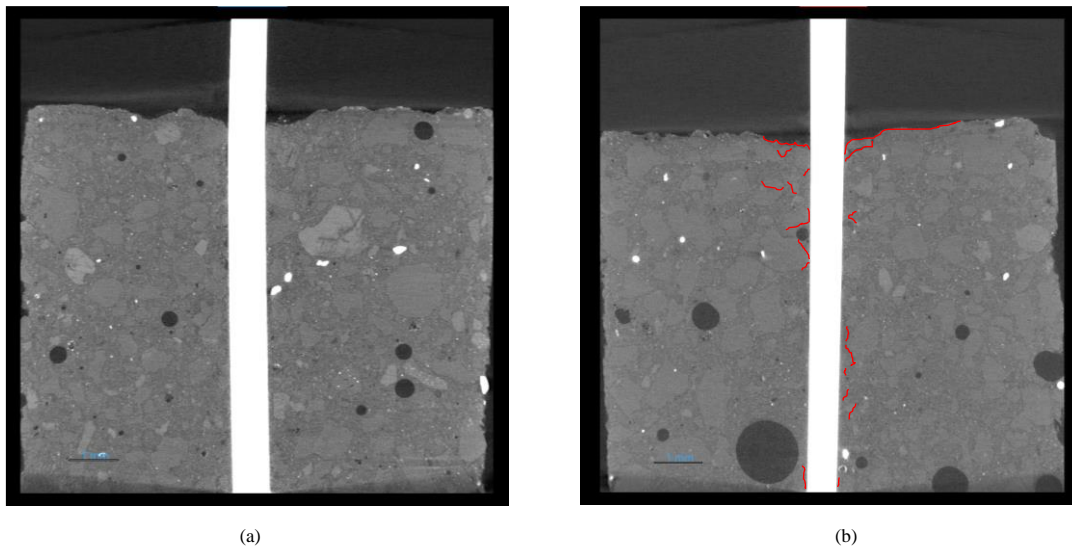


Figure 3.25 – Micrograph (0.4x) of straight steel fiber in Matrix B: (a) before pullout; (b) partial debonding (fiber pullout of 7 mm). Damaged areas are indicated in red color.

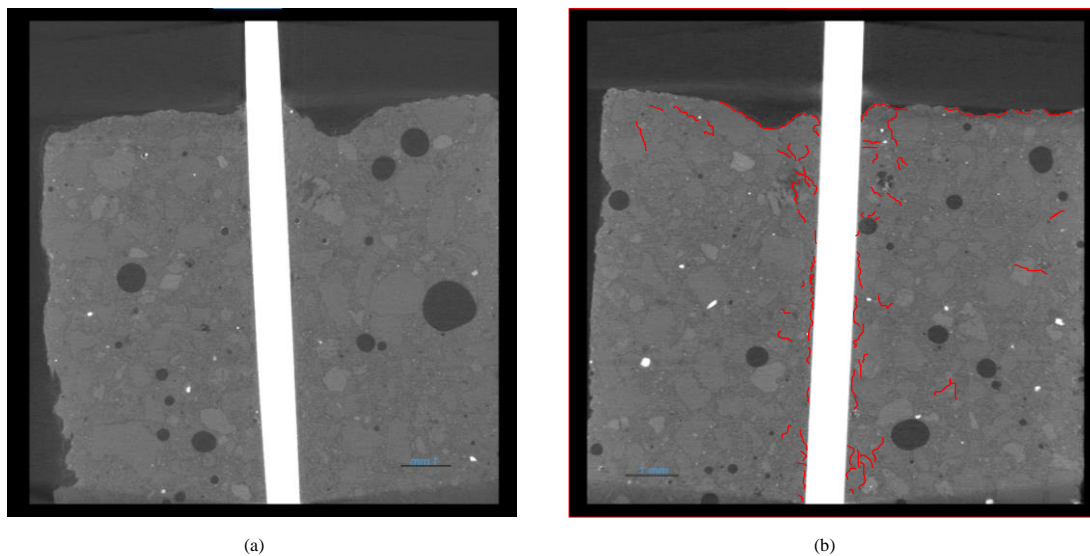


Figure 3.26 – Micrograph (0.4x) of hooked-end steel fiber Matrix B: (a) before pullout; (b) partial debonding (fiber pullout of 7 mm). Damaged areas are indicated in red color.

For the steel fiber with a hook, it is known that the initial mechanism associated with the pullout process is the deformation of the fiber hook. In order to analyze the damage concentration and microcracks in this region of the fiber/matrix interface based on microCT images, new specimens (samples *H03*) are molded by displacing the steel fiber to the top of the specimen. Figure 3.27 illustrates the new positioning of the fiber, ensuring that the hook is now located within the region of interest. Moreover, Figure 3.28 presents the images captured by the microCT.

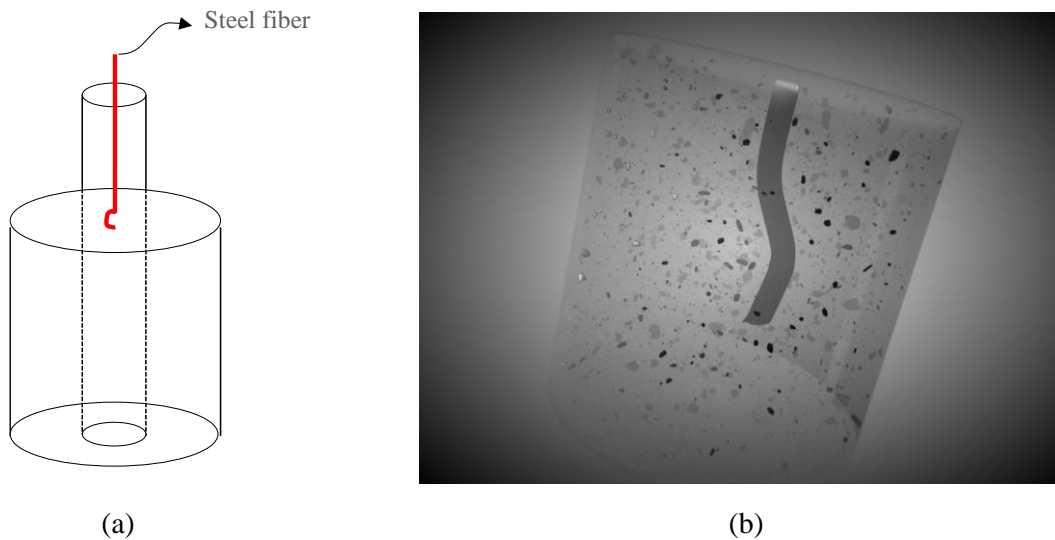


Figure 3.27 – New configuration for the microCT analyses for the *S03* samples: (a) schematic representation; (b) X-ray scanned volume.

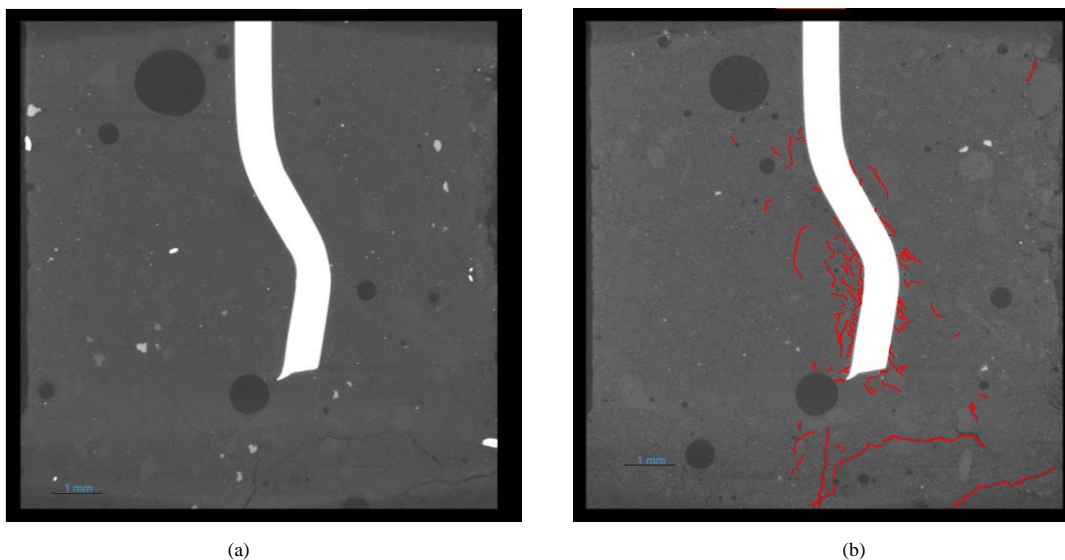


Figure 3.28 – Micrograph (0.4x) of the hook region in Matrix B: (a) before pullout; (b) partial debonding (fiber pullout of 7 mm). Damaged areas are indicated in red color.

From the analysis of Figure 3.28, it is possible to observe a higher concentration of microcracks in the hook-fiber/matrix interface regions. This region undergoes significant disturbances, especially at the beginning of the pullout test. It is important to highlight that the curved hook will be completely deformed until it becomes straight. From then on, the mechanism associated with the total pullout of the fiber follows the same mechanisms observed in the case of straight steel fiber geometry. From Figure 3.28, a greater crack opening is noticeable, especially in the

lower region immediately below the fiber hook zone. This fact suggests that pre-existing cracks in the cement matrix, such as those formed due to shrinkage, become larger after pullout.

Pullout tests were conducted to confirm that the hook deforms entirely before pullout until the fiber pullout from the cementitious matrix was completed. Figure 3.29 displays an image obtained through microCT after the complete pullout process, highlighting the concentration of cracks and damage in the fiber vicinity.

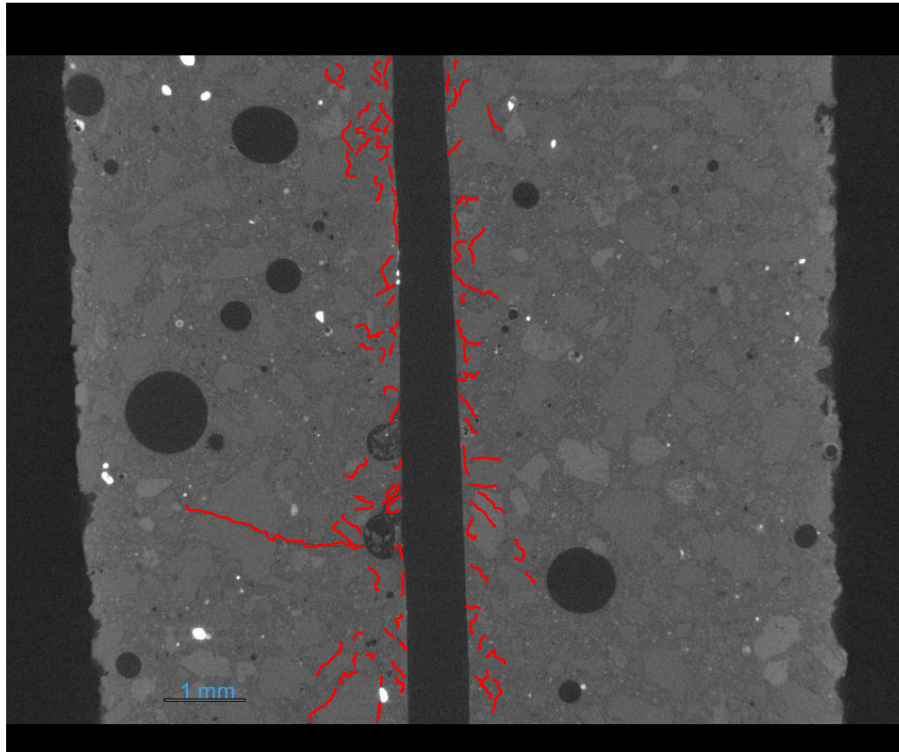


Figure 3.29 – Micrograph (0.4x) of the hook region in Matrix B after entire pullout. Damaged areas are indicated in red color.

The experimental curves for the mechanical characterization of Matrix A and Matrix B under tension and compression for all samples are detailed in Appendix A. Moreover, the microCT images before/after pullout without the microcrack/damage markings are presented in Appendix B.

4 Numerical modeling

This chapter focuses on a comprehensive exploration of numerical modeling methodologies aimed at simulating stress transfer mechanisms and damage evolution in cementitious composite materials. Initially, a review of analytical and finite element approaches employed for pullout simulation in cementitious composite materials is conducted. This review serves as the foundational basis regarding the state-of-the-art methodologies used by previous authors in the literature to investigate pullout behavior in fiber-reinforced concrete, particularly concerning the formulations applied to model the fiber/matrix interface.

Subsequently, the mathematical formulations implemented for the elastoplastic finite element models within this thesis are presented. The surface-based cohesive behavior, coupled with a damage constitutive law, is adopted to simulate the fiber/matrix interface, while the Concrete Damage Plasticity (CDP) constitutive model is employed for the cement behavior. The steel fiber behavior is simulated through an elastoplastic behavior derived from the stress/strain curve. Finally, this chapter showcases the results of numerical models and investigations on stress transfer and damage evolution in cementitious composites. Additionally, the chapter culminates in validating these numerical models through a comparative analysis of their outcomes with experimental results and microCT images obtained from pullout tests presented in Chapter 3.

4.1. Analytical and finite element models for pullout

As previously explored in Chapter 2, the pullout test has been studied by several authors in the literature, especially to predict and study the mechanical behavior of cement-based advanced materials. Several configurations can be used for experiments of this type. Depending on the fiber scale, these tests can occur inside microscopes with high-precision load cells. Another type of test is the two-sided pullout test, mainly used for durability investigations [36], [57].

Lawrence [122] pioneered one of the earliest pullout analytical models, specifically addressing the shear stress-slip behavior dependent on the elastic properties of the cement matrix and fibers. This model also introduced a criterion for bond stress to delineate fiber debonding, albeit limited to straight fibers under uniaxial loading. It considered the frictional slip in the debonded region and a linear elastic shear transfer in the remaining part of the fiber (Figure 4.1). Subsequently, Laws et al. [123] applied Lawrence's model [122] to investigate glass fiber-reinforced cement composites, considering a linear stress transfer at the fiber/matrix interface. The analysis suggested that augmenting the interfacial bond would have a modest impact on the strength of short fiber composites, but would significantly increase frictional stresses at the interface.

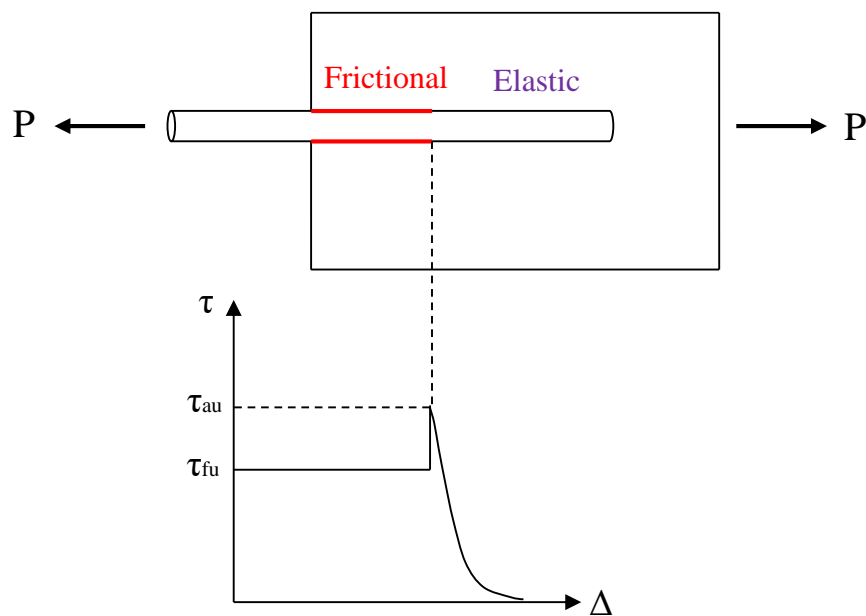


Figure 4.1 - Analytical stress-slip (τ - Δ) pullout model proposed by Lawrence [122].

Over the decades, multiple fiber pullout one-dimensional analytical models were developed for the fiber pullout problem [124]–[126]. These models consider a shear-lag model for the fiber embedded length considering full bond conditions, gradual debonding, and frictional fiber sliding [48]. The shear lag models assume that the load is transferred from the matrix to the fibers by the generation of shear stresses at the fiber/matrix interface, neglecting the transfer of normal stresses to the fiber ends. In this sense, the model tends to underestimate the stiffness of short fiber composites, for which the transfer of normal stresses is particularly important as shear. Additionally, Naaman et al. [43] investigated the force distributions in the

fiber and matrix, observing a decrease in frictional resistance as slip increased. This behavior is indicated in Figure 4.2, where the stress-slip (τ - Δ) diagram is displayed alongside the load-slip (P - Δ) curve. The general trend involves initially elastic shear stresses at the interface, followed by a gradual increase in load starting at P_{crit} , representing the critical slip. The gradual debonding continues until Δ_0 , where the entire fiber is debonded, and shear behavior becomes frictional. Between Δ_{crit} and Δ_0 , stress transfer comprises a mix of adhesional and frictional stresses.

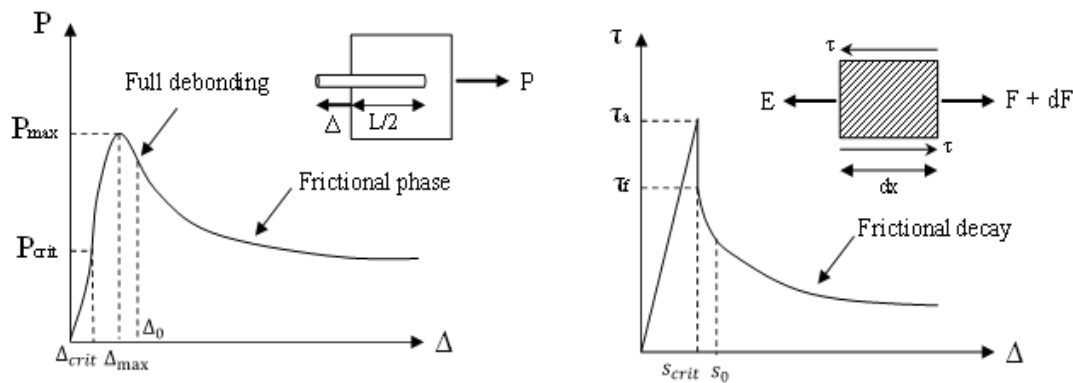


Figure 4.2 – Pullout analytical model proposed by Naaman [43].

Sometime later, Leung and Li [127] introduced a two-end debonding theory, where debonding can initiate from both ends of the fiber, marking an advancement over traditional shear-lag analytical models. Alternatively, Gopalaratnam and Shah [124] assumed that the interfacial shear bond stresses are initially elastic; however, debonding gradually occurs at the interface, and the stress transfer is shifted to a frictional mechanism.

Regarding the hooked-end pullout analytical models, Alwan et al. [128] developed a model to predict the contribution of anchorage forces in hooked-end steel fibers based on a frictional pulley along with two plastic hinges. In this research, the mechanical bond provided by the hook is adopted as a function of the work needed to straighten the fiber during pullout. More recently, Sujivorakul et al. [55] proposed another model combining the frictional bond and mechanical anchorage components, adopting a nonlinear spring component to simulate the mechanical anchorage mechanism (Figure 4.3).

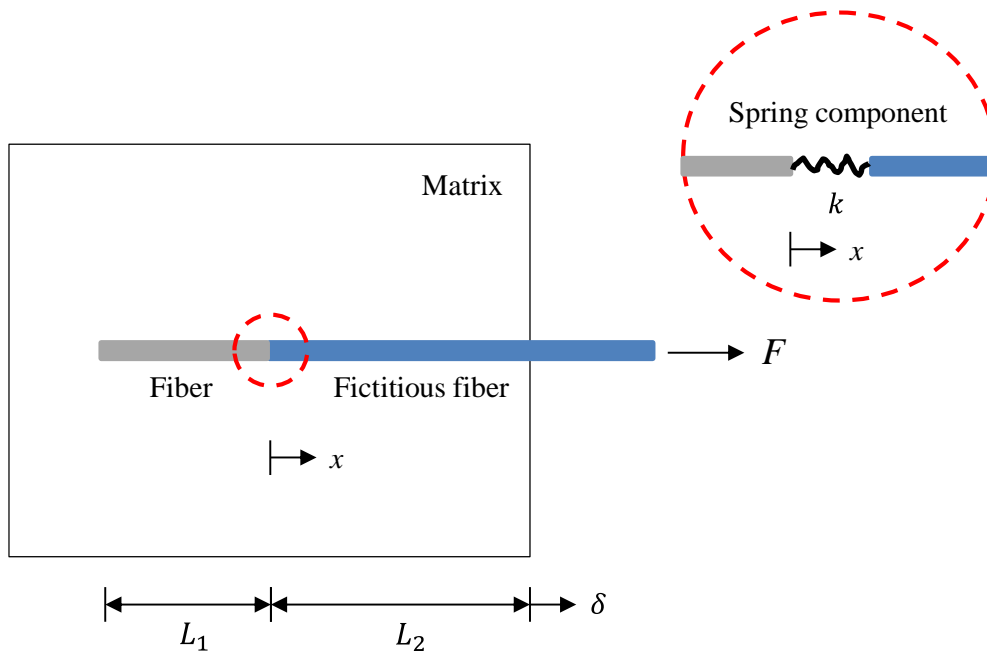


Figure 4.3 – Representative pullout model proposed by Sujivorakul et al. [55]

For the development of pullout finite element models, it is necessary to first define the behavior of the fiber/matrix interface considering the adhesive bonding, debonding, and friction mechanisms. Next, elastoplastic constitutive models for the cement matrix and the fiber are defined to run the numerical simulations [48], [57].

The bond-slip of the fiber/matrix interface can be compared with the bond-slip of a reinforcement bar in concrete. Several models are presented in the literature for modeling the bond-slip of reinforced concrete [56]. Spring elements were initially proposed by Ngo and Scordelis [129] using a linear constitutive law. More recently, nonlinear spring elements have been considered in the work of Davalos et al. [130]. Moreover, interface elements have been proposed with a nonlinear constitutive law to model the adhesive bond of the interface [131], as well as embedded elements that combine the material behavior and the bond effects within the same finite element [132], represented in Figure 4.4.

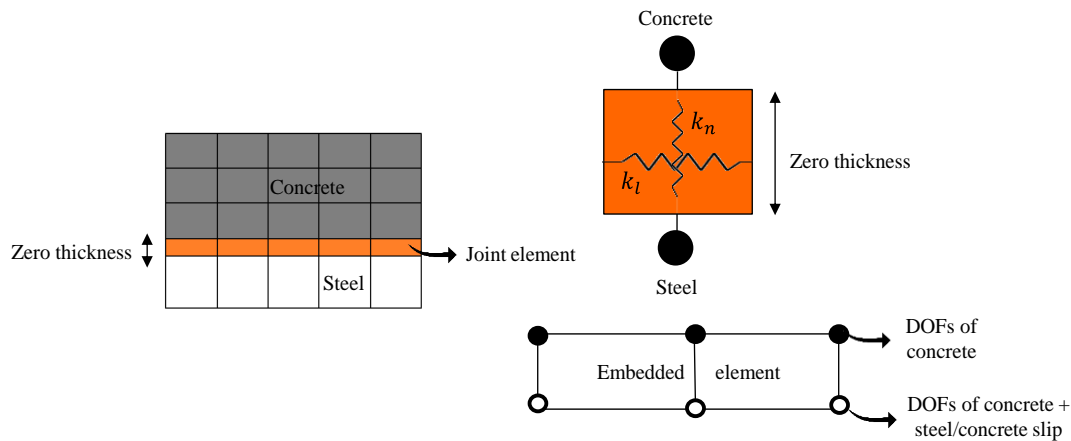


Figure 4.4 – Finite element formulations carried out for modeling adhesive bonding (Adapted from [56]).

Notably, the numerical model should represent adhesive bonding, debonding, and friction at the interface. Combining the mechanisms within a single element is not possible in most commercial FEM packages, which can be solved by either combining multiple elements (cohesive elements with contact or gap elements) or by user-defined implementations/subroutines inside in-house frameworks. When using spring components, it is possible to model delamination mechanisms, with the spring components situated behind the crack tip failing sequentially [133]. Alternatively, cohesive interface elements are also employed for modeling adhesive bond and debonding in cementitious materials, especially in the context of several fracture mechanics case studies [134].

Alternative ways to model bond-slip and fiber/matrix interaction for reinforced concrete and cement composite materials are also carried out through a surface-based contact simulation. This approach uses leader and follower surfaces to model the interface behavior of composites (Figure 4.5), as presented in previous works of Abbas et al. [135], Alfano and Sacco [136], and Rezazadeh et al. [137]. The mathematical background regarding this interaction for modeling the pullout behavior in cement materials will be detailed in Section 4.2.

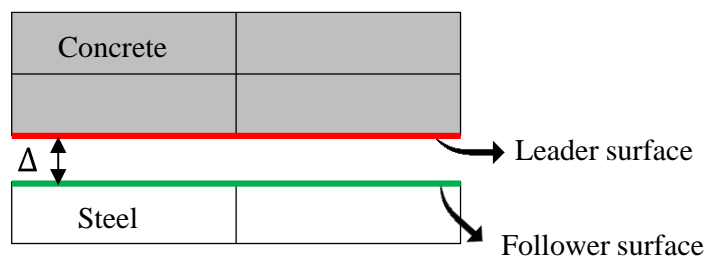


Figure 4.5 – Schematic representation of the surface-based contact formulation.

4.2. Numerical methodology

The main objective of this section is to present the numerical methodology carried out in this thesis for the computational modeling of the damage and stress transfer mechanisms in fiber-reinforced concrete applications.

According to the topics discussed in the previous chapters of this thesis, three components must be considered to simulate the pullout behavior in cement composite materials: the cement matrix, the fiber, and the fiber/matrix interface. The following subsections detail the mathematical formulation employed to simulate the elastoplastic behavior of each component for the pullout tests. All the numerical models from this thesis were developed using the commercial finite element software ABAQUS®.

4.2.1. Cement matrix

4.2.1.1. Concrete damage plasticity (CDP) model

The CDP constitutive model has been originally developed by Rabotnov [138], where the material constitutive equation with scalar isotropic damage can be expressed according to Equation 4.1.

$$\sigma = (1 - d) D_0^{el} : (\varepsilon - \varepsilon^{pl}) \quad (4.1)$$

where σ is the Cauchy stress tensor, d is the scalar stiffness degradation variable, ε is the strain tensor and D_0^{el} is the initial/undamaged elastic material stiffness. The effective stress tensor can be defined according to Equation 4.2.

$$\bar{\sigma} = D_0^{el} : (\varepsilon - \varepsilon^{pl}) \quad (4.2)$$

where ε^{pl} is the plastic strain. In the formulation, it is necessary to propose the evolution of the scalar degradation variable (Equation 4.3).

$$d = d(\bar{\sigma}, \tilde{\varepsilon}^{pl}) \quad (4.3)$$

The evolution of the damage scalar variable is governed by a set of the effective stress tensor $\bar{\sigma}$ and hardening (softening) variables $\tilde{\varepsilon}^{pl}$. The stiffness

degradation is initially isotropic and defined by degradation variable d_c in a compression zone and variable d_t in a tension zone. Finally, the Cauchy stress tensor is related to the effective stress tensor $\bar{\sigma}$ through the scalar degradation parameter $(1 - d)$, as expressed in Equation 4.4.

$$\sigma = (1 - d) \bar{\sigma} \quad (4.4)$$

The damage states in tension and compression are defined independently by two hardening variables $(\tilde{\varepsilon}_t^{pl}, \tilde{\varepsilon}_c^{pl})$, which are referred to equivalent plastic strains in tension and compression, respectively (Equation 4.5). The evolution of the hardening variables is given by Equation 4.6.

$$\tilde{\varepsilon}^{pl} = \begin{bmatrix} \tilde{\varepsilon}_c^{pl} \\ \tilde{\varepsilon}_t^{pl} \end{bmatrix} \quad (4.5)$$

$$\dot{\tilde{\varepsilon}}^{pl} = h(\bar{\sigma}, \tilde{\varepsilon}^{pl}) \cdot \dot{\varepsilon}^{pl} \quad (4.6)$$

Cracking (tension) and crushing (compression) in concrete are represented by increasing values of the hardening/softening variables. These variables control the yield surface evolution and the elastic stiffness degradation. In this sense, the yield function indicates a surface in effective stress space that determines the states of failure or damage. The yield function is expressed in Equation 4.7 for the inviscid plastic-damage model.

$$F(\bar{\sigma}, \tilde{\varepsilon}^{pl}) \leq 0 \quad (4.7)$$

The plastic flow is governed by a flow potential function $G(\bar{\sigma})$ defined in the effective stress space according to the non-associative flow rule (Equation 4.8):

$$\dot{\varepsilon}^{pl} = \dot{\lambda} \frac{\partial G(\bar{\sigma})}{\partial \bar{\sigma}} \quad (4.8)$$

For the CDP model, four constitutive parameters identify the shape of the flow potential surface and the yield surface. In this model, for the flow potential G , the Drucker-Prager hyperbolic function is considered for small elastic strains, as presented in Equation 4.9.

$$G = \sqrt{(f_c - m f_t \operatorname{tg} \beta)^2 + \bar{q}^2} - \bar{p} \operatorname{tg} \beta - \sigma \quad (4.9)$$

where f_t and f_c are the uniaxial tensile and compressive strengths of concrete, respectively. Moreover, β is the dilation angle measured in the p - q plane at high confining pressure, while m is an eccentricity of the plastic potential surface. The flow potential surface is defined in the p - q plane, where $\bar{p} = -\frac{1}{3}\bar{\sigma}I$ is the hydrostatic pressure stress and $\bar{q} = \sqrt{\frac{3}{2}\bar{S} \cdot \bar{S}}$ is the Mises equivalent stress. In addition, \bar{S} is the deviatoric part of the effective stress tensor $\bar{\sigma}$.

The non-associative flow rule requires the definition of a loading surface. The plastic damage concrete model uses a yield condition based on the loading function proposed by Lubliner et al. [139] and described in Equation 4.10.

$$F = \frac{1}{1 - \alpha} (\bar{q} - 3 \alpha \bar{p} + \theta(\tilde{\varepsilon}^{pl}) \langle \bar{\sigma}_{\max} \rangle - \gamma \langle -\bar{\sigma}_{\max} \rangle) - \bar{\sigma}_c(\tilde{\varepsilon}_c^{pl}) \quad (4.10)$$

The shape of the loading surface in the deviatoric plane is given by the parameter γ . The parameter α is calculated based on the Kupfer's curve. Additionally, $\bar{\sigma}_{\max}$ refers to the algebraically maximum eigenvalue of $\bar{\sigma}$. The function $\theta(\tilde{\varepsilon}^{pl})$ is detailed in Equation 4.11, where $\bar{\sigma}_t$ and $\bar{\sigma}_c$ are the effective tensile and compressive cohesion stresses, respectively. Subsequently, Equation 4.12 defines the parameter α , which depends on the ratio of the biaxial compressive strength and uniaxial compressive strength. Therefore, it is necessary to carry out biaxial laboratory tests to obtain parameter α .

$$\theta(\tilde{\varepsilon}^{pl}) = \frac{\bar{\sigma}_c(\tilde{\varepsilon}_c^{pl})}{\bar{\sigma}_t(\tilde{\varepsilon}_t^{pl})} (1 - \alpha) - (1 + \alpha) \quad (4.11)$$

$$\alpha = \frac{\left(\frac{f_{b0}}{f_c}\right) - 1}{2 \left(\frac{f_{b0}}{f_c}\right) - 1} \quad (4.12)$$

Other parameters, such as the tensile uniaxial strength and the concrete's uniaxial or biaxial compressive strength, should be taken from experimental curves.

Moreover, the parameter γ (Equation 4.13) is defined based on full triaxial concrete tests.

$$\gamma = \frac{3(1 - \rho)}{2\rho + 3} \quad (4.13)$$

where the coefficient ρ (Equation 4.14) is defined at a given hydrostatic pressure stress \bar{p} . J_2 is the second invariant of stress deviator calculated for the yield surface tensile meridian $\sigma_1 > \sigma_2 = \sigma_3$ (TM) and compressive meridian, $\sigma_1 = \sigma_2 > \sigma_3$ (CM). According to Lubliner et al. [139], typical values for ρ are between 0.64 to 0.80.

$$\rho = \frac{(\sqrt{J_2})_{TM}}{(\sqrt{J_2})_{CM}} \quad (4.14)$$

Based on the experimental stress-strain curves for both uniaxial tension and compression, it is possible to obtain the dependence between stress-cracking strain ($\tilde{\varepsilon}_t^{ck}$) in uniaxial tension and stress-crushing strain ($\tilde{\varepsilon}_c^{in}$) in uniaxial compression. In this sense, we need to transform the stress-strain values given in the experimental curves to obtain the plastic strain values. Firstly, we must define the scalar damage variable d , as indicated in Equation 4.15.

$$d_c = 1 - \frac{\sigma_c}{\sigma_{cu}} \quad (4.15)$$

where σ_c refers to the compression stresses from the uniaxial compression curve and σ_{cu} is the ultimate compressive stress. The elastic strains in compression ($\varepsilon_{el,c}$) can be calculated in terms of the compression stresses and the Young's modulus E , as indicated in Equation 4.16.

$$\varepsilon_{el,c} = \frac{\sigma_c}{E} \quad (4.16)$$

Additionally, the inelastic strains $\varepsilon_{in,c}$ in compression are assessed by subtracting the total strains from the elastic strain values (Equation 4.17):

$$\varepsilon_{in,c} = \varepsilon_c - \varepsilon_{el,c} \quad (4.17)$$

Finally, the plastic strain values can be calculated according to Equation 4.18.

$$\varepsilon_{pl,c} = \varepsilon_{in,c} - \frac{d_c}{1 - d_c} * \frac{\sigma_c}{E} \quad (4.18)$$

Equations 4.15-4.18 are analogous in the case of tension values. Figure 4.6 and Figure 4.7 present which values from the CDP model are interpreted in compression and tension, respectively.

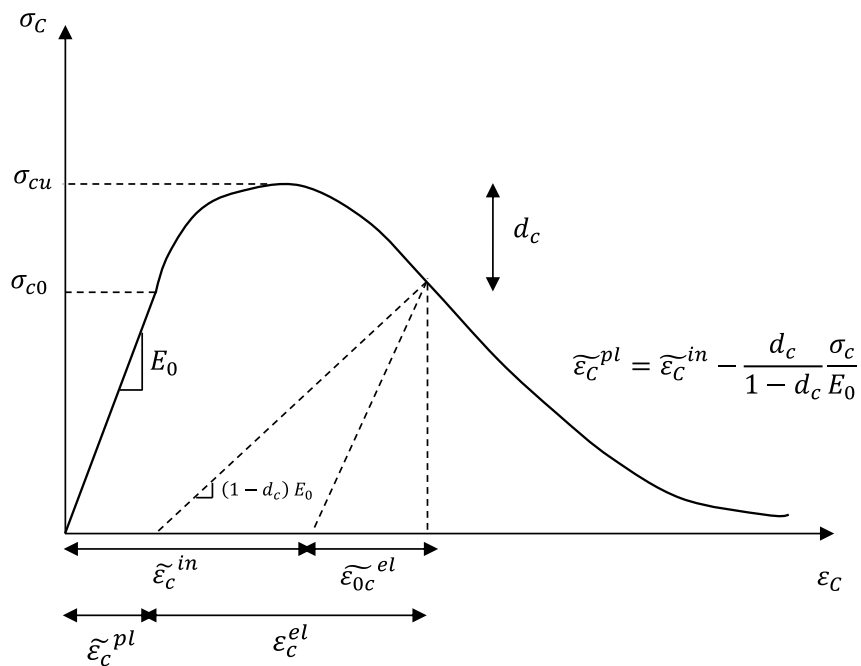


Figure 4.6 – Dependence of stress-strain curve in compression for CDP model (Adapted from [140]).

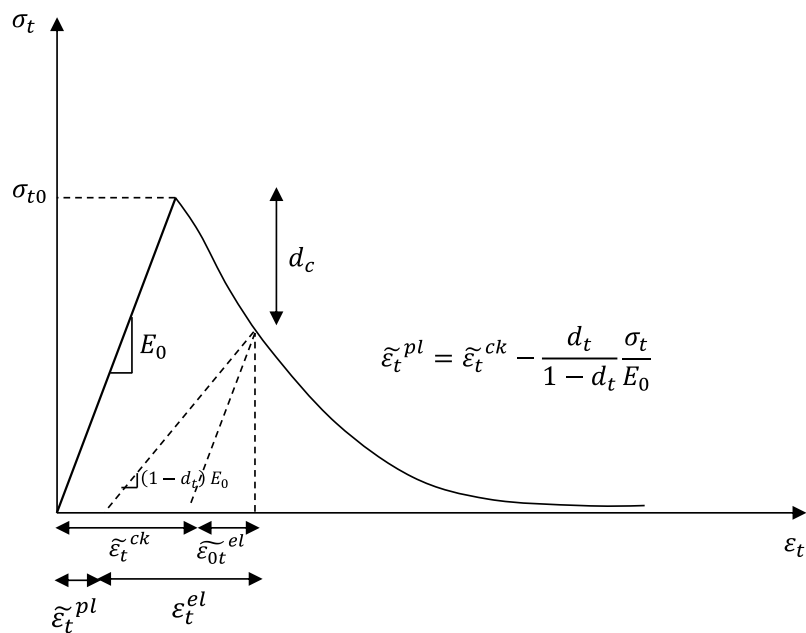


Figure 4.7 – Dependence of stress-strain curve in tension for CDP model (Adapted from [140]).

Figure 4.8 summarizes a schematic representation of the parameters required for the CDP model used for the pullout simulations developed in this thesis. The range determination for parameters α , β , ρ and m is obtained through a comprehensive literature review of previous studies.

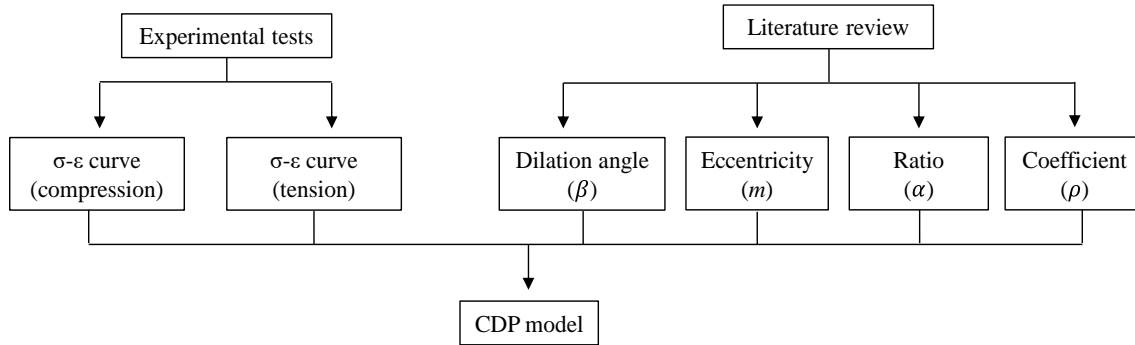


Figure 4.8 – Required input parameters for the CDP model.

4.2.2. Steel fiber

4.2.2.1. Plastic behavior

In ABAQUS® commercial software, the plastic behavior of a material is given in terms of the true stress-true strain curve. The relationship between true and nominal strain is established by expressing the nominal strain ε_{nom} according to Equation 4.19, where L_0 is the original length and L refers to the current length.

$$\varepsilon_{nom} = \frac{L - L_0}{L_0} = \frac{L}{L_0} - 1 \quad (4.19)$$

Adding unity to both sides and taking the natural log of both sides of Equation 4.19, we can obtain Equation 4.20, where ε is the true strain.

$$\varepsilon = \ln(1 + \varepsilon_{nom}) \quad (4.20)$$

The relationship between true stress and nominal stress considers the incompressible nature of the plastic deformation and assumes that the elastic volumetric deformation is negligible. Therefore, we can write Equation 4.21:

$$L_0 * A_0 = L * A \quad (4.21)$$

where A_0 is the original area and A refers to the current area. The expression relating the current area to the original area is detailed in Equation 4.22.

$$A = A_0 \frac{L_0}{L} \quad (4.22)$$

Replacing Equation 4.22 into the definition of true stress ($\sigma = F/A$), we obtain Equation 4.23 that finally provides the relationship between true stress and nominal stress and strain.

$$\sigma = \frac{F}{A_0} * \frac{L}{L_0} = \sigma_{nom} (1 + \varepsilon_{nom}) \quad (4.23)$$

In this context, we provide the data pairs to define the true stress as a function of the true plastic strain. The first data pair defines the initial yield stress and the corresponding initial plastic strain. The true plastic strain ε_{pl} is obtained by subtracting the true elastic strain, defined as the true stress σ divided by the Young's modulus E , from the total strain value ε_t (Equation 4.24):

$$\varepsilon_{pl} = \varepsilon_t - \varepsilon_{el} = \varepsilon_t - \frac{\sigma}{E} \quad (4.24)$$

For the cases where the fiber post-peak curve is not available, perfect plastic behavior is assumed for the steel fiber.

4.2.3. Fiber/matrix interface

4.2.3.1. Surface-based cohesive behavior and friction formulation

The surface-based cohesive behavior is an alternative approach to simulate the interaction for pullout or pushout tests [135]–[137], [141]–[143]. This formulation provides a simplified way to simulate the cohesive interactions with a negligibly small interface thickness. A traction-separation constitutive model is associated with the cohesive surface. The surface-based cohesive contact formulation presents a similar mathematical background to the cohesive element formulation presented originally by Camanho et al. [144]. In the FE analysis of the interface surface, a zero-thickness cohesive zone is added with assigned interfacial properties. The cohesive zone elements will perform the role of an interfacial

surface in the finite element simulation, analogous to the bonded interfacial surface observed in real applications [142], [143]. In order to prevent over-constraints, a leader-follower surface to surface formulation is defined for the entities with cohesive behavior.

For the fiber-reinforced concrete applications, the follower contact elements are defined as the edges of the fiber, and the leader contact elements are defined as the matrix surface. The follower nodes are released from the leader surface when the interface separation meets the contact failure criterion. The interpenetration between the follower nodes and the leader surface is prevented by contact. Moreover, friction is assigned to cohesive contact surfaces. The distances between nodes on the leader-follower surfaces along the normal and shear directions are called contact separations δ . When surface-based cohesive contact is considered, tractions σ are determined by dividing the nodal cohesive force by the contact surface area at each contact node. The linear elastic traction-separation cohesive surface behavior is given by Equation 4.25.

$$\begin{bmatrix} \sigma_n \\ \tau_s \\ \tau_t \end{bmatrix} = \begin{bmatrix} K_{nn} & K_{ns} & K_{nt} \\ K_{sn} & K_{ss} & K_{st} \\ K_{tn} & K_{ts} & K_{tt} \end{bmatrix} * \begin{bmatrix} \delta_n \\ \delta_s \\ \delta_t \end{bmatrix} \quad (4.25)$$

where K denotes the interfacial stiffness, and subscripts n , s and t refer to the normal direction, shear direction 1 (mode II), and shear direction 2 (mode III), respectively.

In this work, mixed-mode stiffness coefficients are assumed to be zero. We assume isotropic cohesive behavior, *i.e.*, stiffness and strength are equivalent in the three orthogonal directions. The failure of the interface adhesion can be simulated through the definition of a damage initiation criterion and a damage evolution law. A progressive damage traction-separation behavior with exponential damage evolution law is adopted and indicated schematically in Figure 4.9, where δ_i and δ_f refer to the onset (damage equal to zero) and total (damage equal to 1) separation values, respectively; T_{max} is the maximum traction value and α is the non-dimensional parameter that defines the rate of damage evolution.

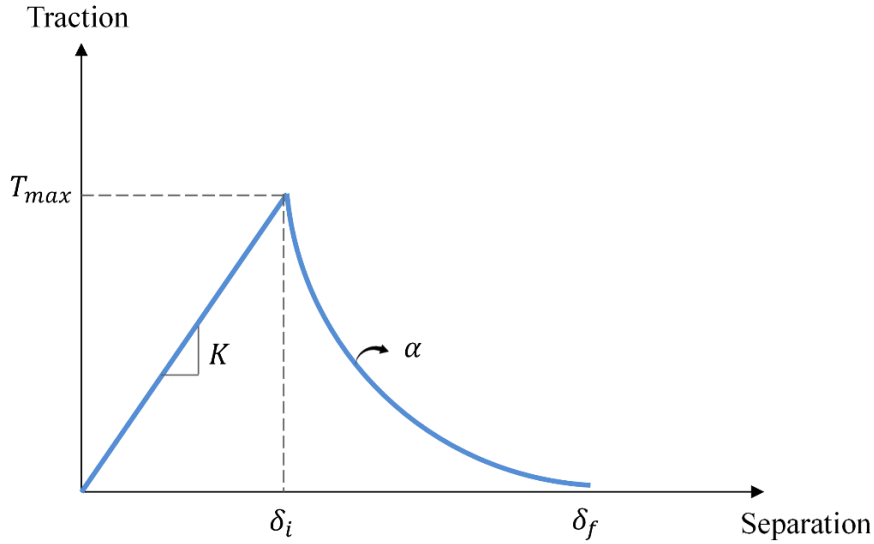


Figure 4.9 – Exponential traction-separation response for the cohesive zone interaction

The onset of cohesive damage is defined by a damage initiation criterion, written in terms of a quadratic separation presented in Equation 4.26:

$$\left\{ \frac{\langle \delta_n \rangle}{\delta_n^{max}} \right\}^2 + \left\{ \frac{\langle \delta_s \rangle}{\delta_s^{max}} \right\}^2 + \left\{ \frac{\langle \delta_t \rangle}{\delta_t^{max}} \right\}^2 = 1 \quad (4.26)$$

where δ_n is the separation in the pure normal mode, and δ_s and δ_t are the separations in the first and second shear directions, respectively.

When the damage initiation criterion is met, interfacial adhesion degradation starts, and the exponential damage law gives the interface stiffness degradation rate. The adhesion failure for any contacting pair between cement and steel can be obtained by a scalar damage variable D that represents the overall damage at the contact point, with an initial value equal to zero (Equations 4.27 to 4.29):

$$\sigma_n = \begin{cases} (1 - D) * \bar{\sigma}_n \\ \bar{\sigma}_n \end{cases} \quad (4.27)$$

$$\tau_s = (1 - D) * \bar{\tau}_s \quad (4.28)$$

$$\tau_t = (1 - D) * \bar{\tau}_t \quad (4.29)$$

where $\bar{\sigma}_n$, $\bar{\tau}_s$ and $\bar{\tau}_t$ are the contact stress components predicted by the elastic traction-separation behavior for the current separations.

When the damage initiation criterion is fulfilled, D increases from 0 to 1, according to the associated displacement δ , as indicated in Equation 4.30.

$$D = 1 - \left\{ \frac{\delta_i}{\delta} \right\} \left\{ 1 - \frac{1 - \exp\left(-\alpha \left(\frac{\delta - \delta_i}{\delta_f - \delta_i}\right)\right)}{1 - \exp(-\alpha)} \right\} \quad (4.30)$$

The Coulomb friction law was considered to model the tangential contact. Moreover, tangential slipping occurs when the shear stress on the contact surface exceeds the friction limit between the surfaces. The Coulomb friction model is widely employed to explain the interaction between contacting surfaces. The models developed in this thesis employ a friction coefficient μ to define the frictional response between the interacting surfaces. Several studies adopt the tangential behavior with friction coefficients for the interaction between cement and steel around 0.1 and 0.5 [145]–[152]. In the current study, μ parameter was determined by calibrating the numerical simulations to the experimental measurements. Figure 4.10 presents a shear stress-slip response regarding the friction behavior in the tangential direction for the pullout models developed in this thesis.

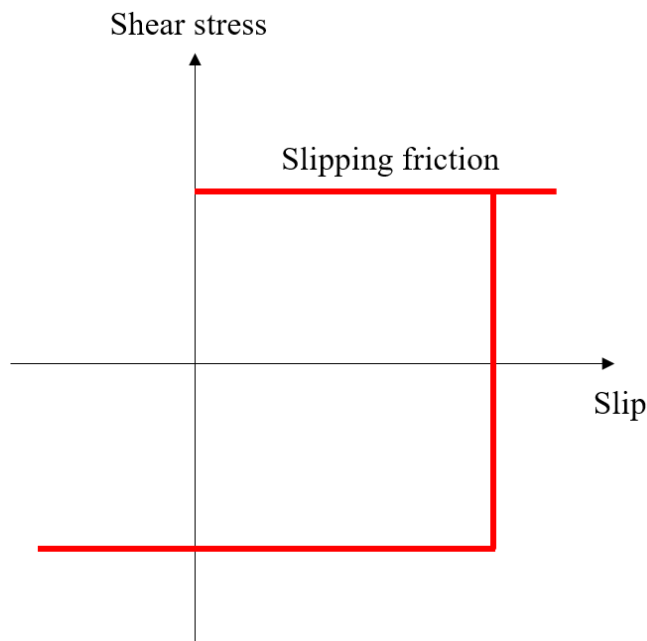


Figure 4.10 – Friction behavior in the tangential direction for the pullout FE models.

Finally, the normal behavior is described by a pressure-overclosure contact model. This model minimizes the penetration of the leader surface by the follower nodes. The constraint induces pressure when the surfaces are in contact and sets the pressure to zero when separated. Separated surfaces come into contact when the clearance between them reduces to zero [153]. Figure 4.11 illustrates a schematic representation of the pressure-overclosure model.

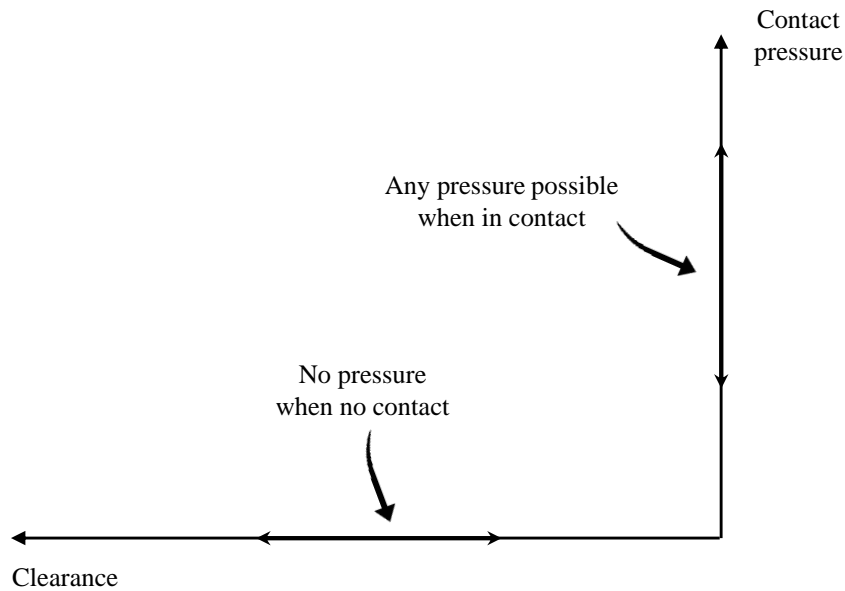


Figure 4.11 – Pressure-overclosure model (Adapted from [153]).

The contact pressure p is a function of the overclosure distance h , which is the penetration distance during the iterations before equilibrium in the increment is achieved. The basic model is described by the conditions listed in Equation 4.31.

$$\begin{aligned} p &= 0 \text{ for } h < 0 \text{ (open)} \\ h &= 0 \text{ for } p > 0 \text{ (closed)} \end{aligned} \quad (4.31)$$

Debonding at the interface leads to large displacements that need to be incorporated into the finite element models. During the simulation, the individual nodes on the follower surface try to contact the closest associated point on the leader surface. Next, a discretization of the contact area is carried out between both surfaces. Figure 4.12 presents a hypothetical solid with a leader surface (round nodes) and a follower surface (triangular nodes). Four nodes (green triangles) of the follower surface fall within the contact detection zone, finding the closest leader surface nodes. The first step in a contact simulation is to check whether the follower surface is close enough to the leader surface. For this verification, a maximum

detection distance (d_{max}) is calculated. If a follower node falls within the contact detection zone of the leader surface, the follower node is considered a possible contact node in the current load step, as indicated in Figure 4.12.

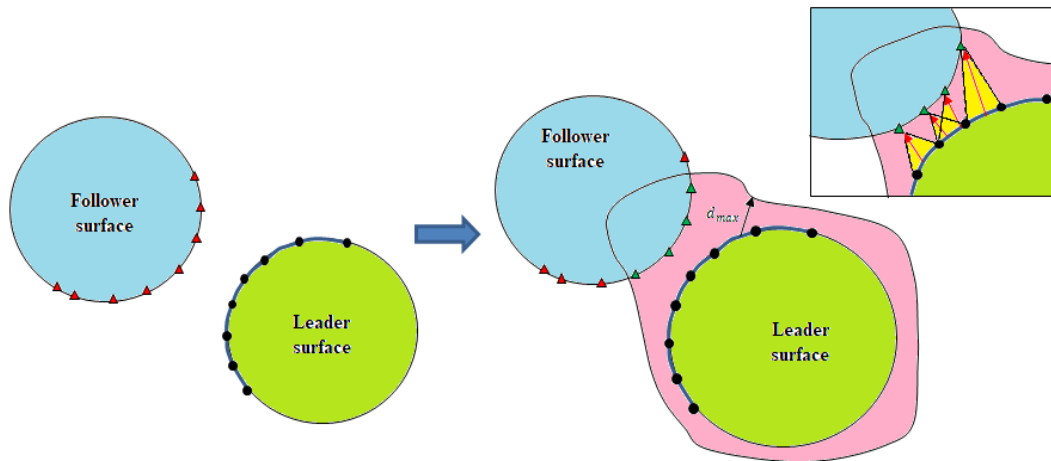


Figure 4.12 – Contact detection using the maximum detection distance (Adapted from [154]).

4.3. Results and discussions

In Section 4.2, we have elucidated the methodology and mathematical formulations governing the numerical models developed in this thesis. This section presents the results and discussions arising from these models, beginning with establishing a proof-of-concept pullout model for straight and hooked-end steel fibers (Section 4.3.1). The information regarding this model is taken from Cox [155]. The pullout load-displacement curves generated by the model are validated against the experimental curves provided by the author, thereby highlighting the efficacy of our numerical approach.

Subsequently, we extend our numerical modeling by incorporating the experimental setup developed and tested in Chapter 3 of the thesis (Section 4.3.2). The subsequent models are carried out in the commercial software ABAQUS®, and their results are compared against the corresponding experimental curves. Furthermore, we investigate the damage evolution by comparing the damage area results with the X-ray tomography images obtained in Chapter 3. This comparative analysis enhances our understanding of the model's predictive capabilities and fidelity in capturing cementitious composite materials' stress transfer and damage evolution mechanisms.

4.3.1. Proof of concept models

The conceptual models consider straight and hooked-end steel fiber pullout tests carried out by Cox [155]. All the pullout experiments were performed using a 250 kN hydraulic test bench with a 2000 N load cell in order to generate and accurately measure the pullout force. Subsequently, this force was transferred to the steel fiber by a manually tightened friction clamp. The pullout displacement was measured by means of two LVDTs with an accuracy of 0.0001 mm. Figure 4.13 presents the experimental setup used for the tests.

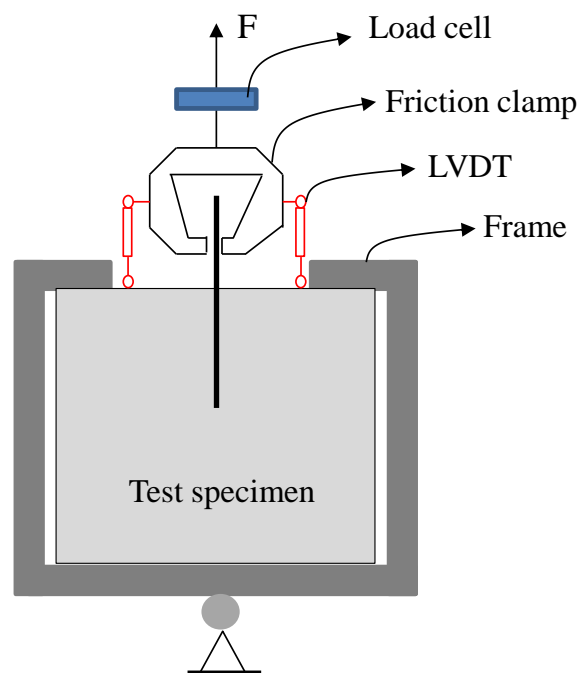


Figure 4.13 – Schematic setup representation of the pullout test performed by Cox (Adapted from [155]).

Figure 4.14 and Figure 4.15 show, respectively, the stress-strain behavior in tension and compression for the cementitious matrix. This curve is necessary to define the concrete damage plasticity constitutive model used to conduct the computational analyses. Additionally, Figure 4.16 presents the yield stress-plastic strain behavior of steel fiber.

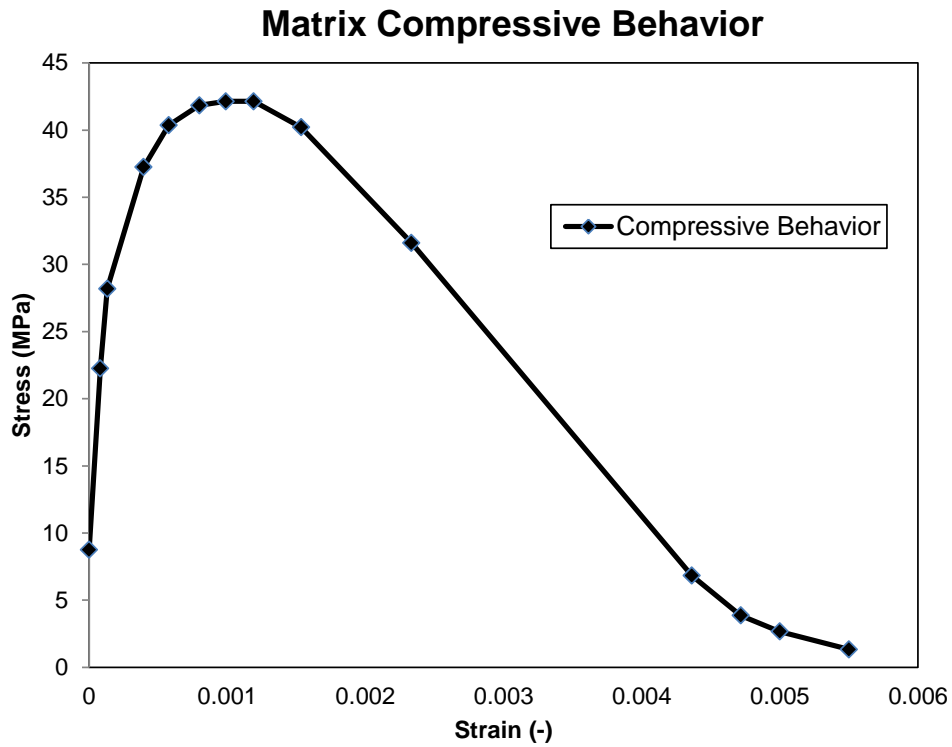


Figure 4.14 – Matrix compressive behavior for Cox's experimental test.

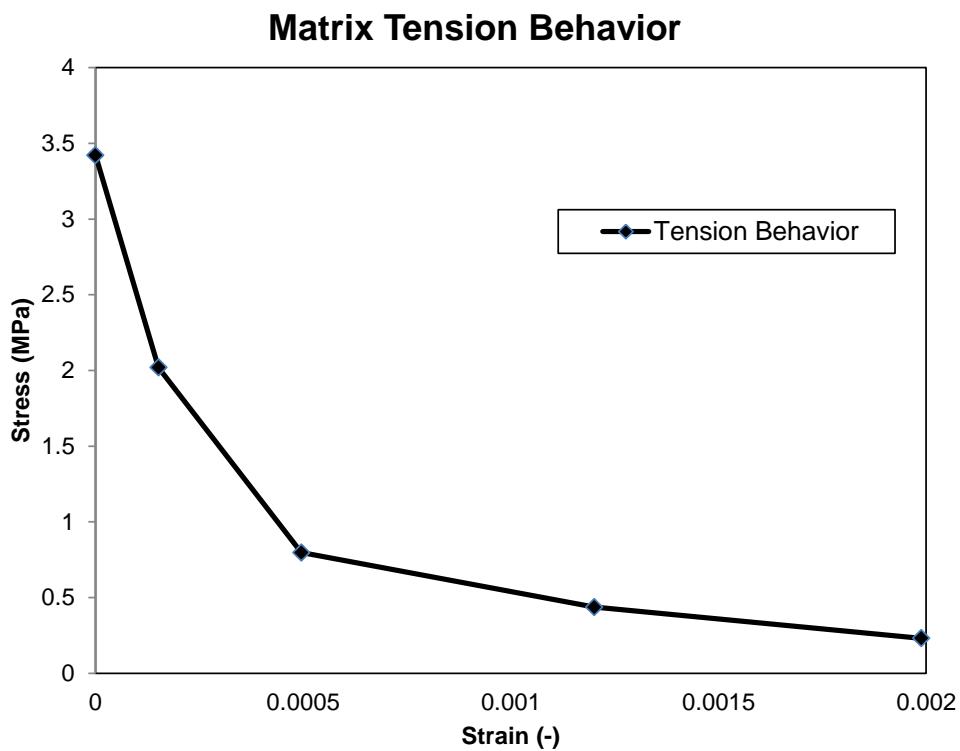


Figure 4.15 – Matrix tension behavior for Cox's experimental test.

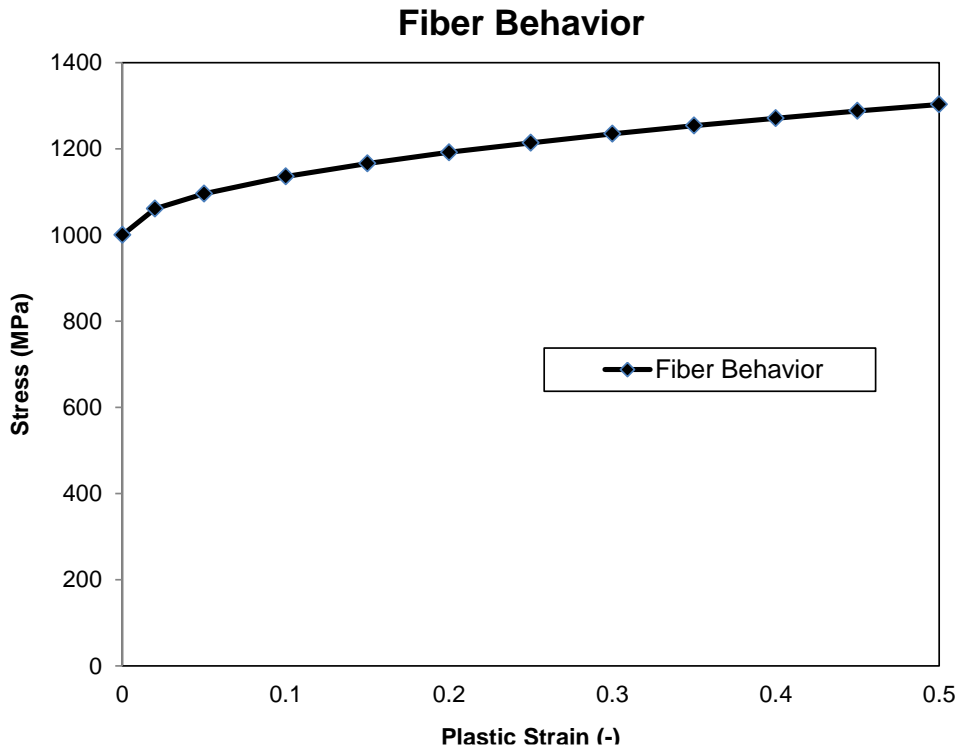


Figure 4.16 – Fiber post-peak behavior for Cox’s experimental test.

For a straight fiber pullout test, an axisymmetric finite element model is carried out for the analyses. The CDP model is adopted for the cement matrix, while elastoplastic behavior is considered for the steel fiber. Figure 4.17 presents the geometric representation and the boundary conditions for the straight fiber pullout numerical model, where a prescribed displacement is applied at the fiber top node. Moreover, the definition of interactions in the straight fiber/matrix interface region is also represented in Figure 4.17. It is important to emphasize that the parameters used to define the constitutive models of the cementitious matrix and the fiber in the numerical models depend on the stress-strain curve in tension and compression.

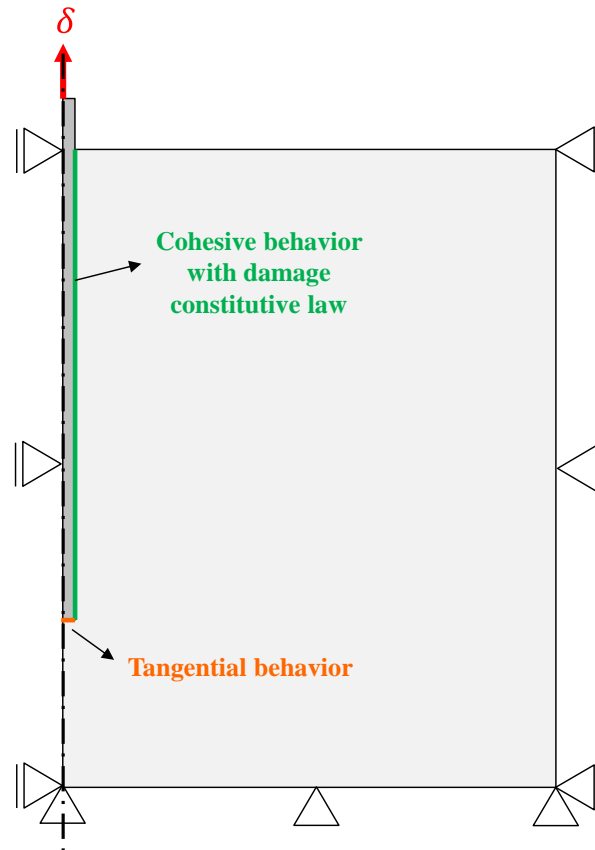


Figure 4.17 – Geometry and boundary conditions for the straight fiber proof of concept model.

The definition of the constitutive parameters for the fiber/matrix interface is also very relevant to the numerical model. Two contact surfaces are defined: the leader surface, the cementitious matrix, and a follower surface, which is associated with the fiber. A traction-separation zone with cohesive behavior and an exponential damage law is applied along the embedded lateral length of the fiber. Additionally, a tangential behavior is considered for the interface between the fiber's horizontal base and the matrix from the definition of a friction coefficient, whose numerical value is determined from the experimental data of the test.

The matrix shrinkage is not considered in the analyses for the numerical pullout model with straight fiber. A prescribed displacement δ is applied to the fiber top. From the model, it is possible to obtain the pullout load-displacement behavior, and the analysis of all stress transfer mechanisms that occur during the test, especially in the fiber/matrix interface region. Table 4.1 presents the parameters selected for the numerical model of straight fiber pullout considering the experimental data reported by Cox [155].

Table 4.1 – Interface parameters for the straight pullout proof of concept model.

Parameter	Value
Friction coefficient (-)	0.3
Elastic stiffness (N/mm ²)	8.5
Maximum traction (MPa)	0.4
Maximum separation (mm)	0.3
Exponential parameter (-)	4.2
Damage evolution type	Displacement
Softening type	Exponential

Contact modeling requires further study with respect to the finite element (FE) mesh, which leads to the need of mesh dependency tests. In the case of this first application, three different meshes were constructed to compare the results and verify the convergence of the analyses, as shown in Figure 4.18.

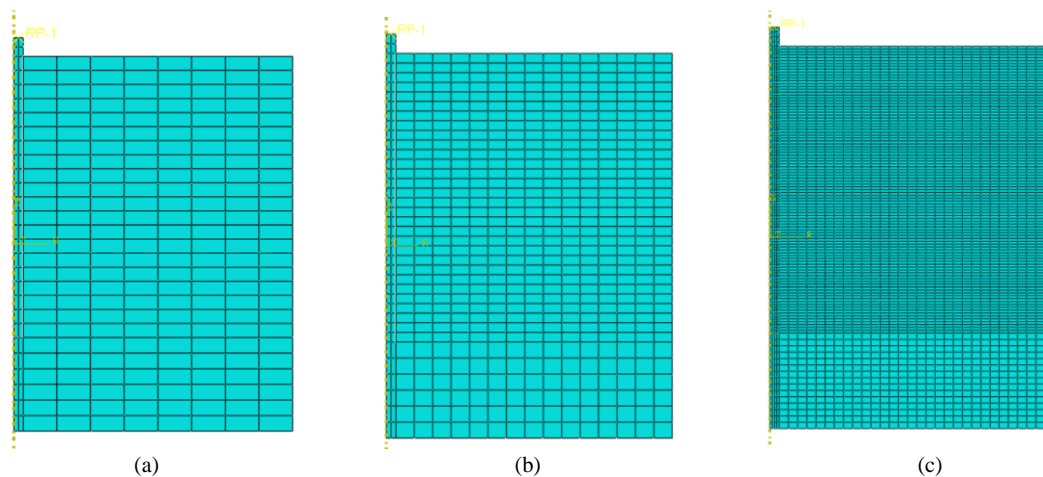


Figure 4.18 – Mesh dependence tests considering (a) coarse mesh with ~265 elements; (b) intermediate mesh with ~620 elements; (c) fine mesh with ~3930 elements.

Figure 4.19 presents the pullout load-displacement results for the three distinct finite element meshes presented in Figure 4.18. From a comparison between the values of the numerical curves and the experimental response, it is possible to infer that the proposed axisymmetric model can adequately predict the pullout load-displacement behavior, especially for the meshes with intermediate and high refinement.

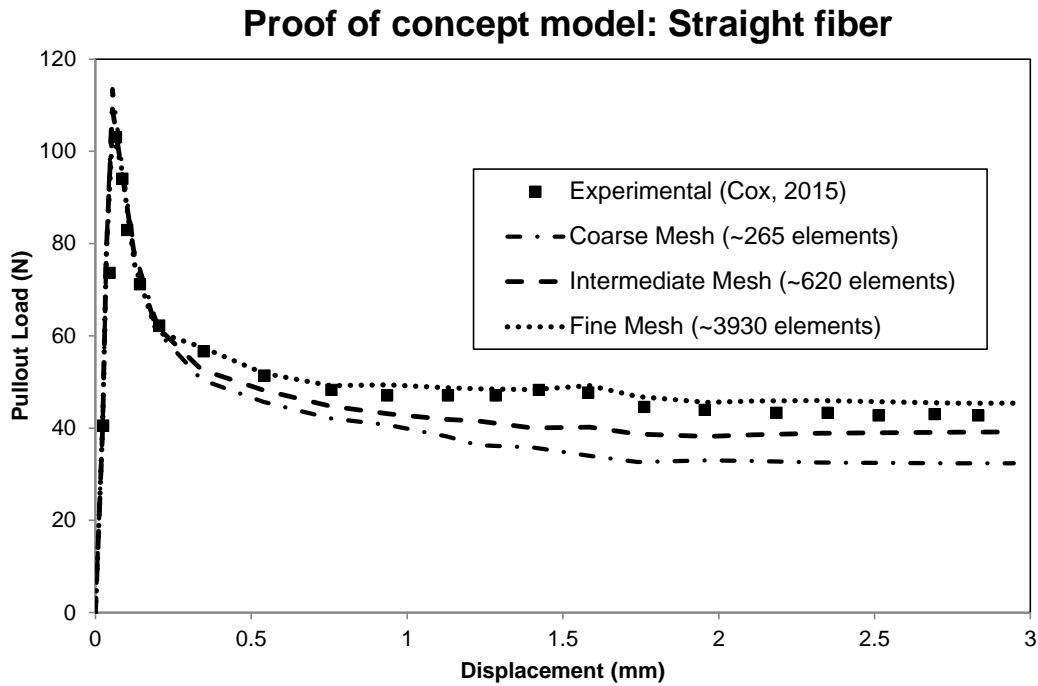


Figure 4.19 – Pullout load-displacement curves considering three distinct meshes and the experimental reference for the straight pullout proof of concept model.

In addition to the pullout load-displacement behavior, it is interesting to propose a computational model capable of identifying and predicting the mechanisms that act during the fiber pullout process: fiber deformation, debonding, and friction. Figure 4.20 shows the images of the numerical model that illustrate the mechanisms verified during the test considering the intermediate FE mesh (~620 elements).

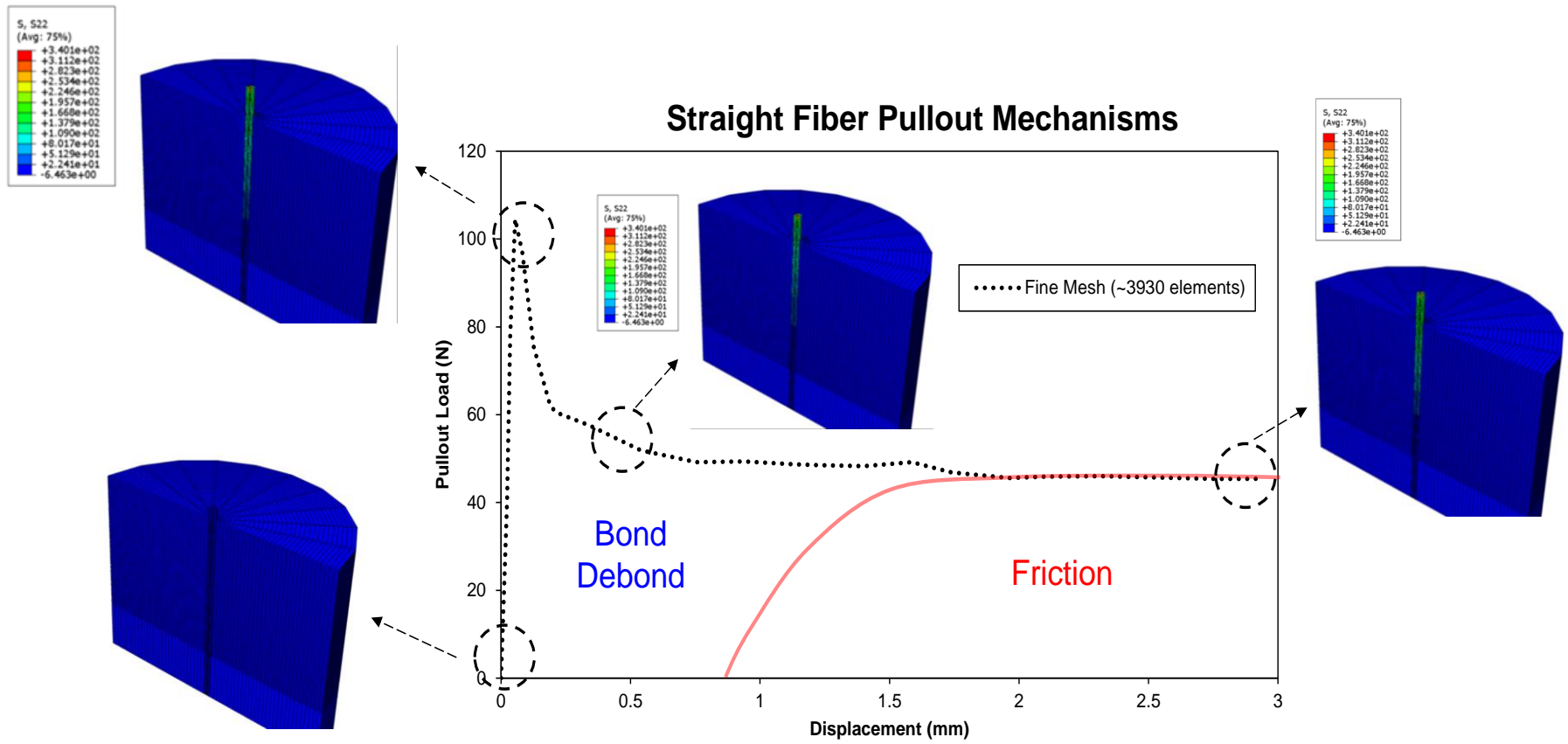


Figure 4.20 – Straight fiber pullout mechanisms detected in the numerical model (stress units in MPa).

A 2D plane stress finite element model is carried out for the hooked-end fiber pullout test analyses. The CDP (concrete damaged plasticity) constitutive model is adopted for the cement matrix, while elastoplastic behavior is considered for the steel fiber. Figure 4.21 presents the geometric representation and the boundary conditions for the hooked-end fiber pullout proof of concept model, where a prescribed displacement is applied at the fiber top node. Moreover, the definition of interactions in the hooked-end fiber/matrix interface region is also represented in Figure 4.21.

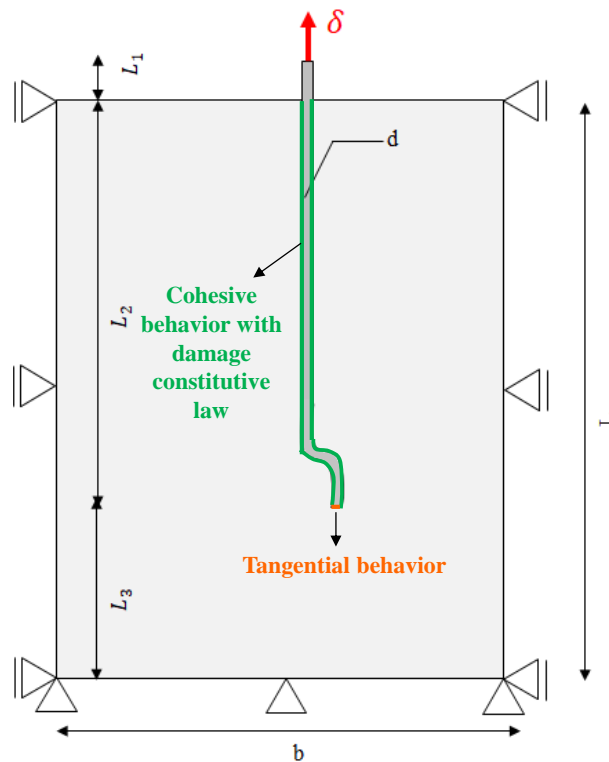


Figure 4.21 – Interface behavior for the hooked-end fiber pullout model.

The numerical model of pullout with straight fiber does not consider matrix shrinkage. In addition, the non-linear geometric effects due to large fiber deformations are considered in the numerical simulations. Moreover, a prescribed displacement δ is applied to the upper left node of the fiber. The interaction properties of the fiber/matrix interface for the hooked-end pullout test model need to be calibrated according to the experimental data. Table 4.2 presents the parameters selected for the numerical model of the hooked-end fiber pullout conceptual model.

Table 4.2 – Interface parameters for the hooked-end pullout proof of concept model.

Parameter	Value
Friction coefficient (-)	0.4
Elastic stiffness (N/mm ²)	11.0
Maximum traction (MPa)	0.7
Maximum separation (mm)	0.5
Exponential parameter (-)	6.0
Damage evolution type	Displacement
Softening type	Exponential

In the case of this second conceptual model, three different meshes were built to compare the results and verify the convergence of the analyses, as shown in Figure 4.22. Due to stress concentration, mesh refinement is preferred for contact problems involving hooked-end fiber geometry, especially around the fiber hook. Moreover, local refinement is done near the contact surface to minimize the follower surface (fiber) penetration by the leader surface (cement matrix).

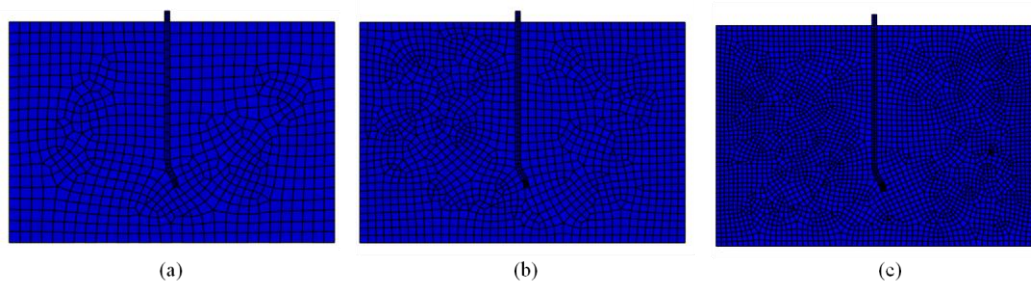


Figure 4.22 – Mesh dependence tests considering (a) coarse mesh with ~777 elements; (b) intermediate mesh with ~1450 elements; (c) fine mesh with ~3500 elements.

Figure 4.23 presents the pullout load-displacement results for the second conceptual model and the three different finite element meshes presented in Figure 4.22. From a comparison between the values of the numerical curves and the experimental response, it is possible to infer that the proposed model can properly predict the pullout load-displacement behavior, especially for the fine mesh (~3500 elements).

Proof of concept model: Hooked-end fiber

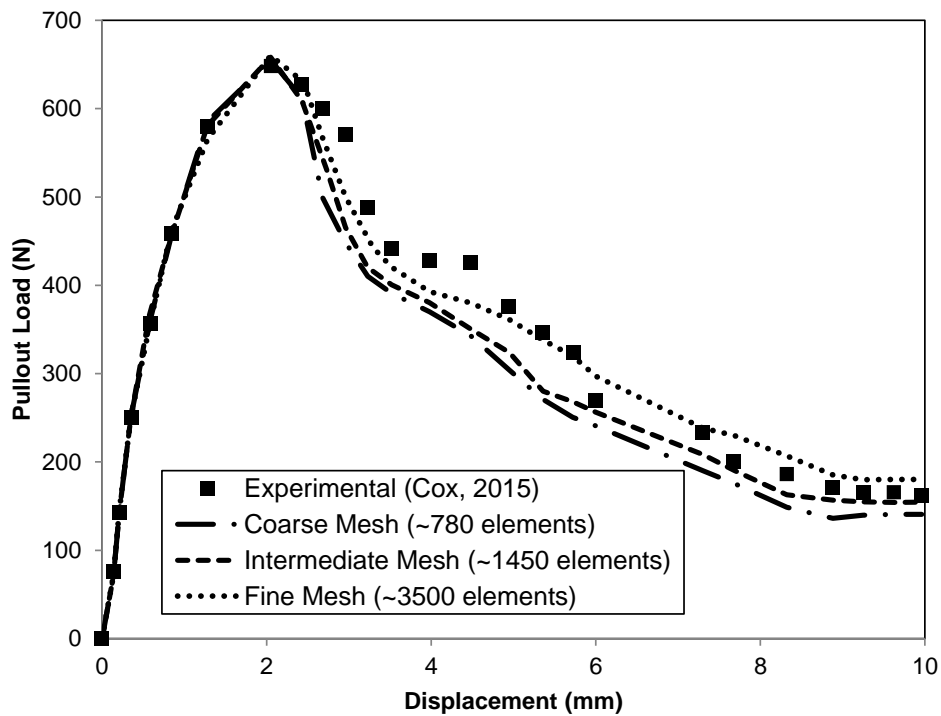


Figure 4.23 – Pullout load-displacement curves considering three distinct meshes and the experimental reference for the hooked-end pullout proof of concept model.

Finally, Figure 4.24 presents the images of the numerical model that illustrate the mechanisms verified during the numerical test for the mesh with the best convergence. The colormap represented in Figure 4.24 indicates the plastic strains (PE) at each load stage during the pullout test.

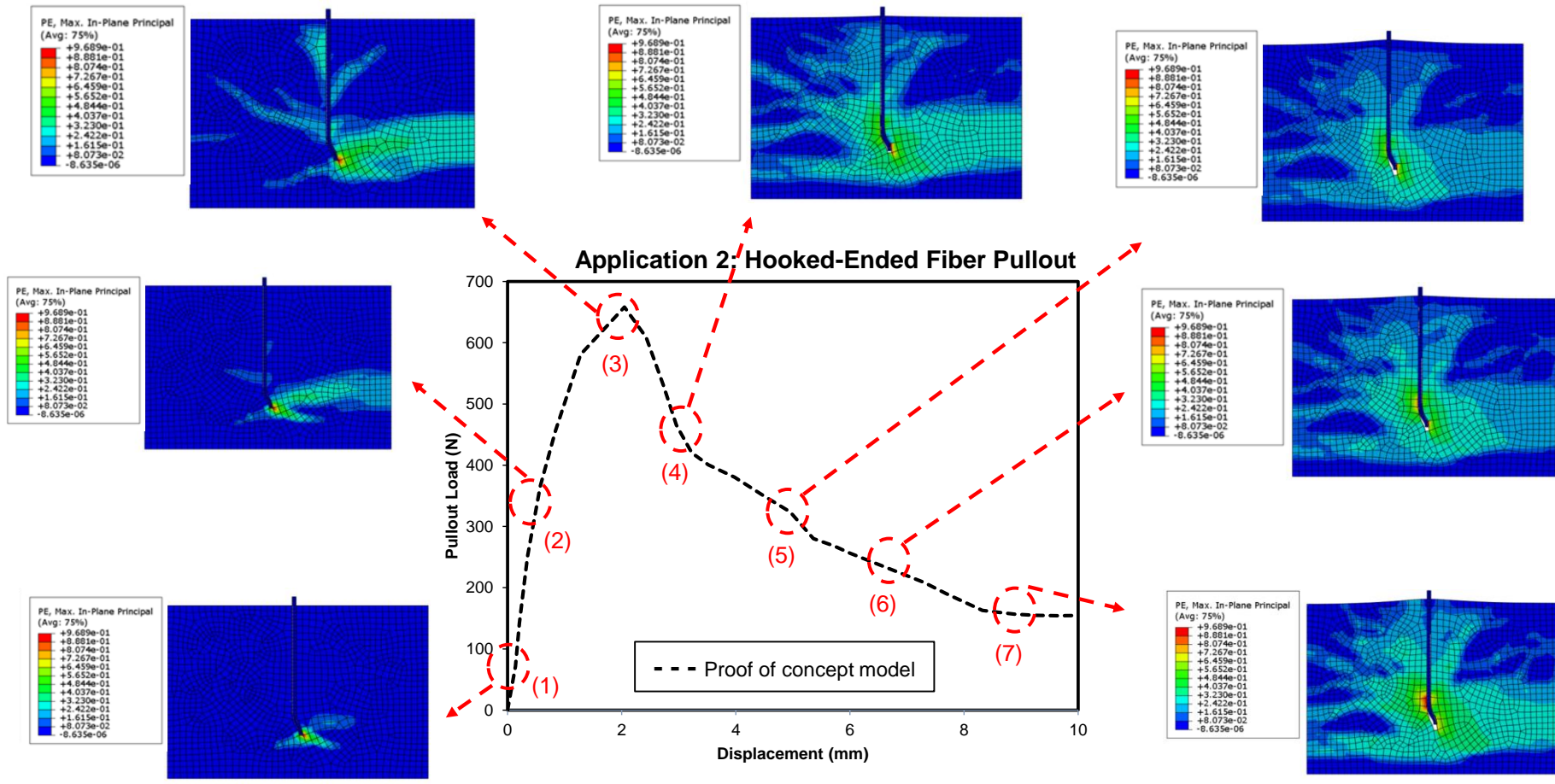
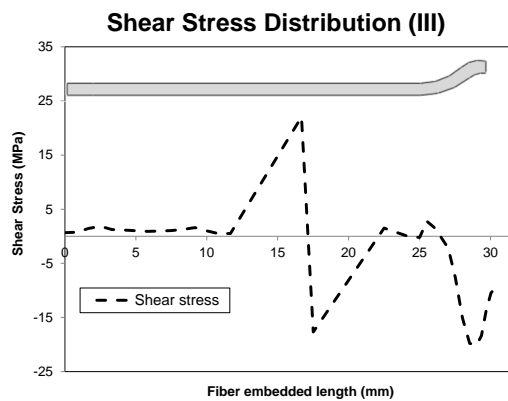
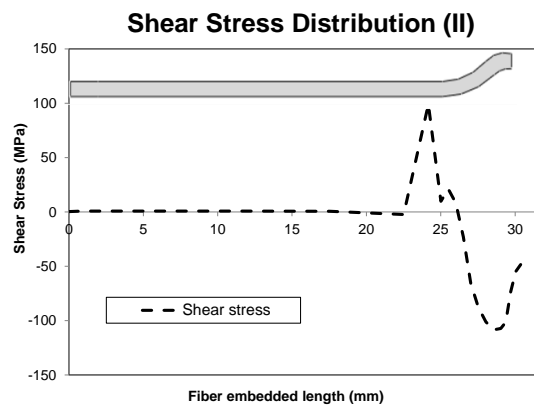
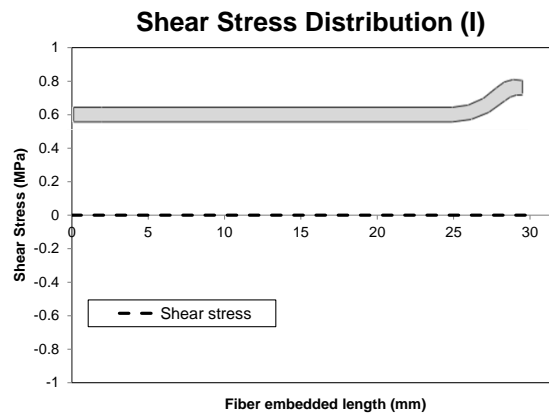
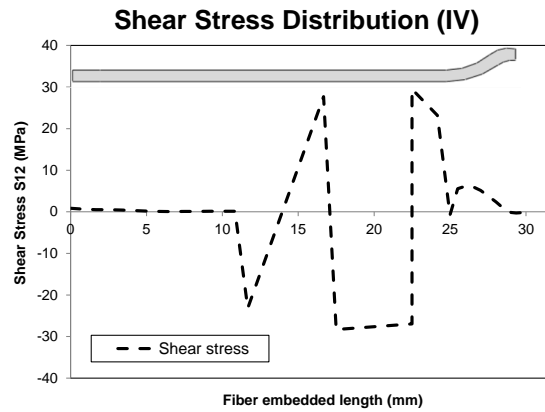


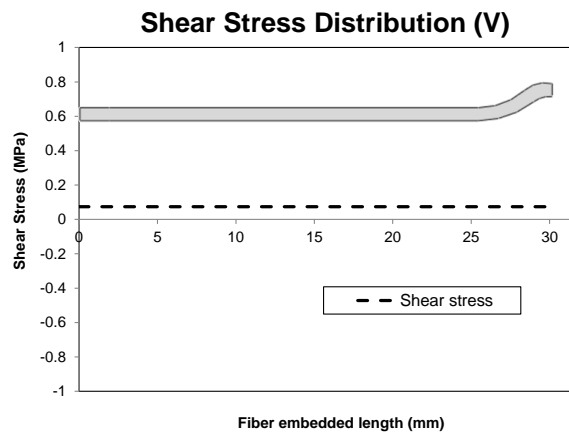
Figure 4.24 – Hooked-end fiber pullout mechanisms detected in the second conceptual model.

The stress transfer mechanisms along the fiber length and the fiber/matrix interface region are essential to define how cement composite materials behave mechanically. As detailed in Chapter 2, the fiber works as a bridge to transfer adhesive and shear stresses during the pullout process. Consequently, the numerical model must detect these mechanisms to better understand how this transfer occurs. Figure 4.25 (a) to (e) shows the evolution of shear stresses that act along the fiber length considering the second proof of concept model.





(d)



(e)

Figure 4.25 – Shear stress transfer mechanisms detected by second conceptual model: (a) first step of the analysis; (b) during the fiber hook deformation; (c) and (d) at fiber debonding; (e) final steps of the analysis.

According to Figure 4.25, there is a relatively large stress oscillation during the pullout process. This mechanism indicates the tension-relaxing cycle endured by the cement matrix. On the other hand, it can be attributed to the spalled matrix being assigned with zero stiffness at the moment of spalling, whereas the real failure process is gradual. According to Leung et al. [156] and Li et al. [157], due to the local curvature of the fiber and residual stress at the interface, the matrix tends to crack and spall. This effect directly impacts the effective embedment length and deformation within the fiber. Moreover, snubbing friction near the fiber exit point can increase the pullout resistance.

Additional verifications are carried out at one fiber interface node of the numerical model to verify the normal stress-normal opening curve and the shear stress-slip opening behavior. The results are presented in Figure 4.26 and Figure 4.27 and indicate the local expected behavior.

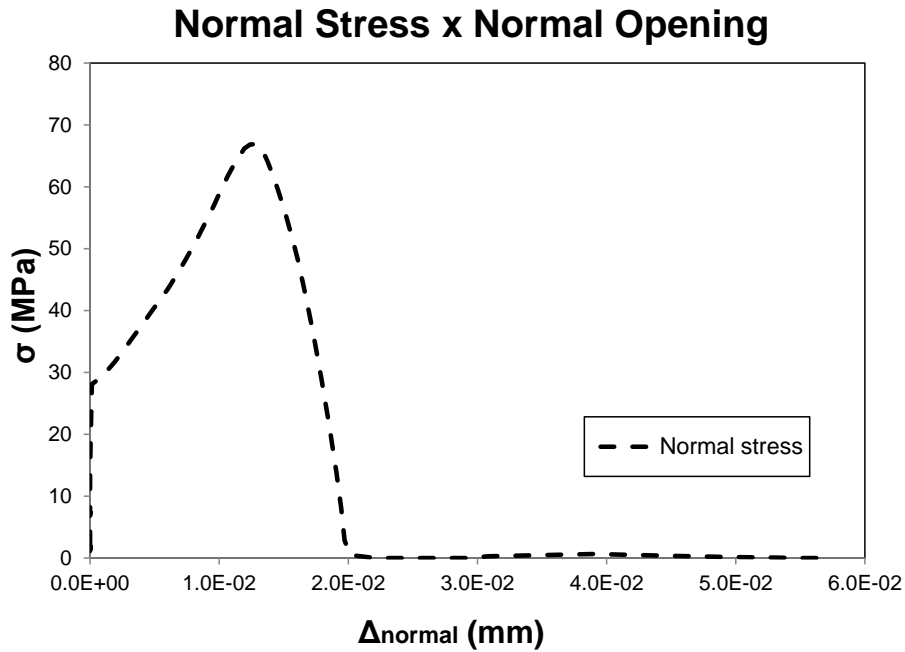


Figure 4.26 – Normal stress-normal opening behavior at one interface fiber node of the model.

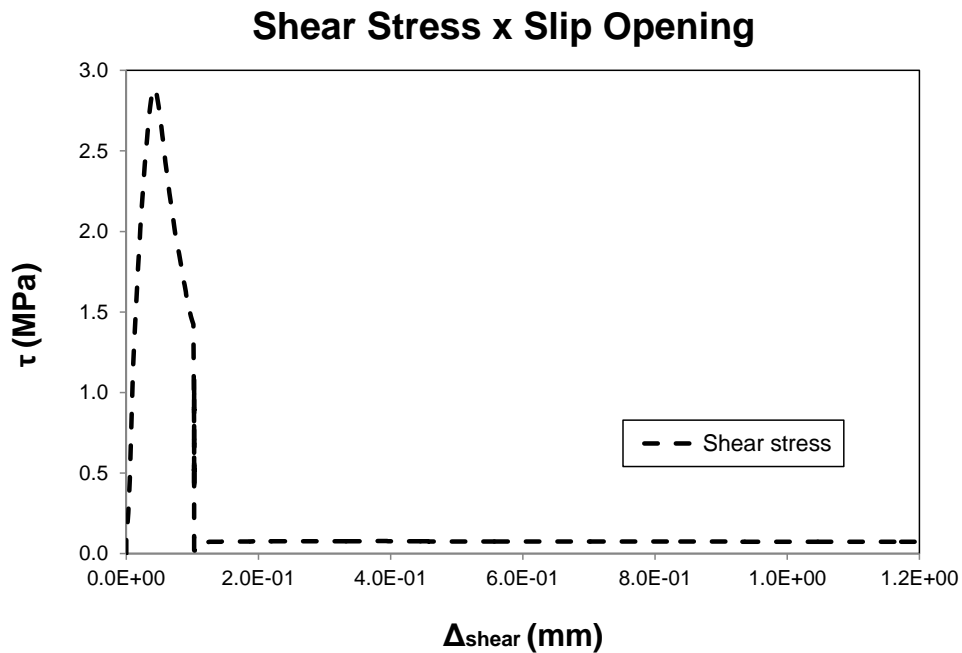


Figure 4.27 – Shear stress-slip opening behavior at one interface fiber node of the model.

In the initial steps of the computational pullout model (Figure 4.28(a)), it is possible to identify the concentration of plastic deformations, especially in the region of the fiber hook, which indicates the hook deformation process and the loss of its adhesion at the base with the matrix. In this loading stage, damage concentration occurs predominantly in the hook region, not evolving to other model areas. After a given increase in the pullout load, it is possible to observe the

evolution of damage to other regions of the model (Figure 4.28(b)), especially in the region along the embedded longitudinal length of the fiber and in some regions away from the interface, which demonstrates the evolution of damage also in the cement matrix. This step refers to the gradual debonding mechanism of the fiber to the cementitious matrix, inducing the evolution of damage in the previously mentioned areas. Finally, the model becomes governed purely by friction (Figure 4.28(c)). At this stage, the fiber debonding process had already finished, and several model regions (fiber, matrix, and interface) started presenting some level of plastic deformation and damage.

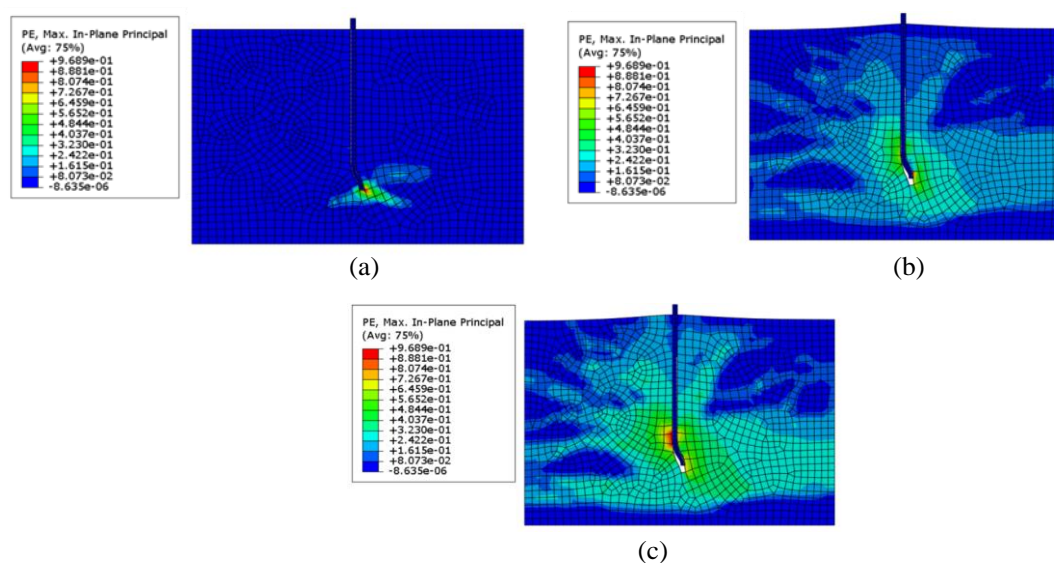


Figure 4.28 – Plastic strain evolution at the pullout model: (a) first steps; (b) during fiber debonding; (c) after fiber debonding.

Finally, a sensitivity analysis is carried out to investigate the influence of the interface parameters on the peak load for the proof of concept models. This procedure is conducted since none of the required interface numerical parameters have a physical interpretation.

The analyses were carried out using the Design of Experiments (DOE) methodology in Minitab 18 ® software, adopting a central circumscribed composite design (CCC) with a full quadratic polynomial model. The default configuration of statistical analyses considers a 95% confidence interval for the simulations and a 5% significance level. Pareto charts were generated to determine which contact parameters influence the pullout peak load. Twenty-five models were simulated for the straight and hooked-end fiber proof of concept models. Figure 4.29 and Figure

4.30 present the Pareto charts with absolute values of the standardized effects from the most significant to the least. A reference line (*p-value*) is also included to indicate the statistically significant effects for the maximum pullout load in straight and hooked-end fiber models.

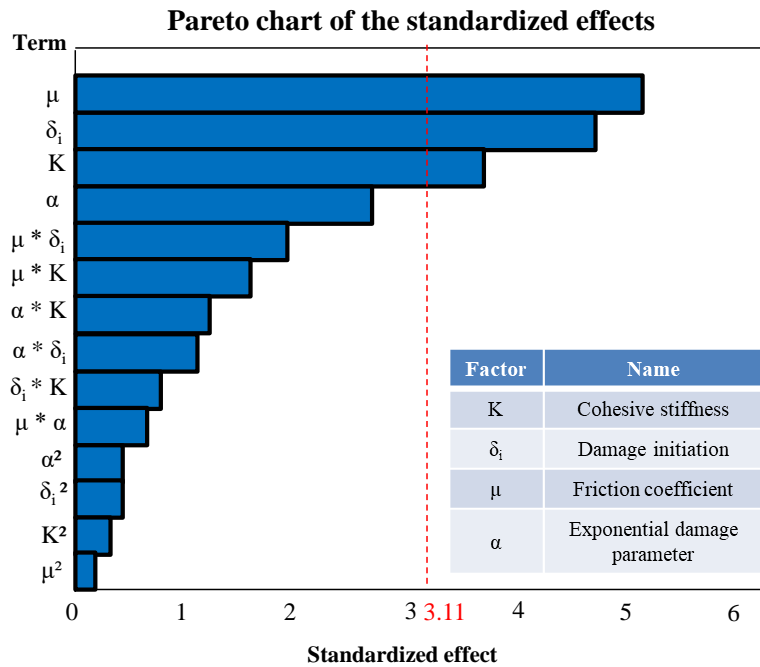


Figure 4.29 – Pareto chart of the standardized effects for the maximum pullout load in straight fiber proof of concept model.

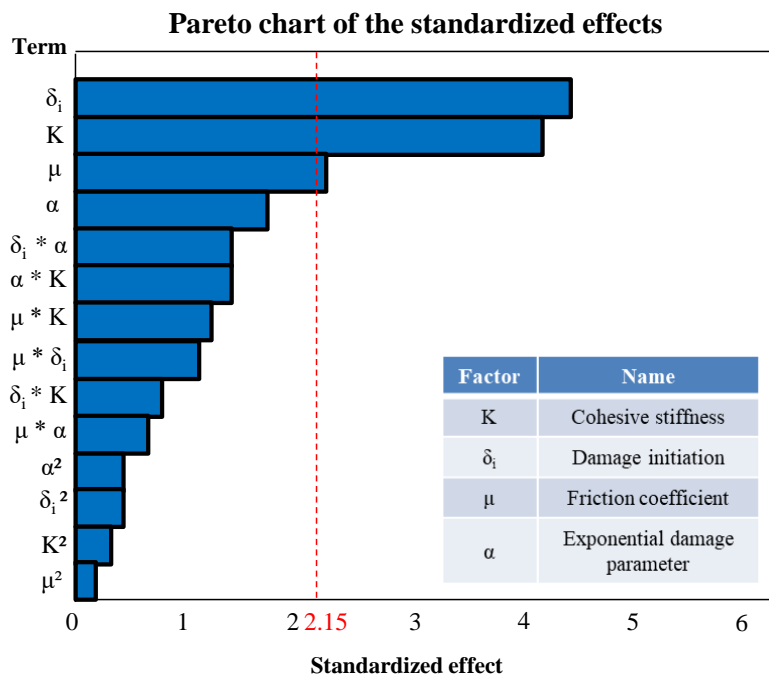


Figure 4.30 – Pareto chart of the standardized effects for the maximum pullout load in hooked-end fiber proof of concept model.

The Pareto chart presented in Figure 4.29 for the straight fiber model indicates that the friction coefficient, the damage separation, and the cohesive stiffness parameter are the most relevant parameters for the maximum pullout load. In terms of the pullout load-displacement curve, it can be observed that an increase in the friction coefficient and the damage initiation parameter directly impacts the vertical translation of the peak load. The higher their values, the greater the peak. The cohesive stiffness parameter also induces modifications in the peak load value, and its horizontal translation. The friction coefficient refers to the resistance to relative motion between the matrix and fiber contacting surfaces. On the other hand, the damage initiation parameter determines the threshold at which damage starts to develop in the interface region. Finally, the cohesive stiffness parameter defines the stiffness and resistance to separating the matrix and the fiber.

For the hooked fiber model (Figure 4.30), the three contact parameters are also relevant for the maximum pullout load, emphasizing the damage initiation variable as the most significant. The same translational behavior observed in the straight fiber model is noted in this case. Despite not demonstrating sensitivity from the DOE analyses, the exponential damage softening parameter has a significant impact on the pullout load-displacement curve behavior, as it is associated with the shape of the exponential softening curve.

The sensitivity analysis of parameters for the proof-of-concept models allows a better understanding of the influence of each interface parameter on the pullout load-displacement curve. With an understanding of the impact of each parameter on the global pullout curve and using the same numerical methodology, models are developed considering the exact geometry of the specimens tested in the laboratory for this thesis, as detailed in the next section.

4.3.2. Developed pullout models

This section presents the finite element models considering the novel experimental setup and the pullout curves presented in Section 3.1 of Chapter 3. The pullout models encompass the two types of cement matrix considered in this thesis: Matrix A (compressive strength of 40 MPa) and Matrix B (compressive strength of 80 MPa), and two distinct types of geometry: straight and hooked-end steel fibers.

4.3.2.1. Straight steel fiber in Matrix A

An axisymmetric model was carried out using ABAQUS ® commercial software for the straight fiber in both cement matrices. The mechanical behavior of the cement matrix was considered elastoplastic using the CDP (concrete damage plasticity) constitutive model. Therefore, the cement matrix's uniaxial compression and tension curves were used to define the matrix behavior. Moreover, the elastic parameters from the cement matrix were taken from the compressive uniaxial tests carried out in Section 3.1 and are shown in Table 4.3. Table 4.3 also presents the required mechanical parameters for the CDP model considering typical values for cement and used by previous works in the literature [139], [158], [159].

The steel fiber was modeled considering perfect plastic behavior with a Young's modulus of 200 GPa, Poisson ratio equal to 0.3, and tensile strength of 1225 MPa. All the fiber properties were taken from DRAMIX ® specifications (Table 4.4).

Table 4.3 – Elastic and mechanical parameters for the matrix A.

Parameter	Value
Young's modulus (GPa)	29.60
Poisson ratio (-)	0.25
Tensile strength (MPa)	4.79
Compressive strength (MPa)	42.65
Dilation angle (°)	38.00
Eccentricity (-)	0.10
f_{b0}/f_{c0} (-)	1.16
K (-)	0.67
Viscosity parameter	0.00

Table 4.4 – Elastic and mechanical parameters for the steel fiber.

Parameter	Value
Young's modulus (GPa)	200.0
Poisson ratio (-)	0.30
Tensile strength (MPa)	1225.0

Figure 4.31 presents the boundary conditions for the axisymmetric pullout finite element model with particular emphasis on the contact area between the cement matrix and the steel fiber. Displacement control was adopted for the model, applying a prescribed displacement δ at the top edge of the steel fiber. The

additional displacement boundary conditions consider symmetry effects and prevent lateral displacements of the specimen. The four-node axisymmetric element with full integration scheme was used for the numerical simulations.

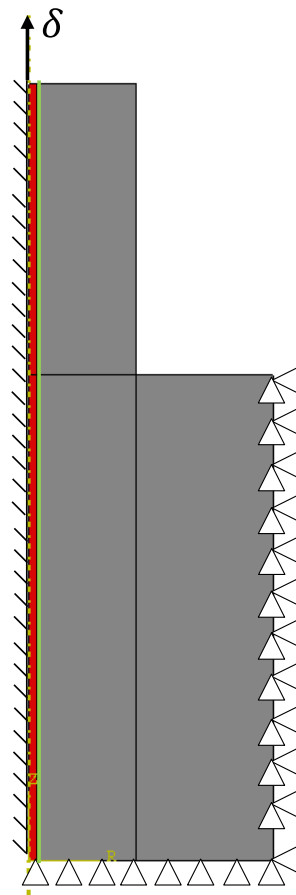


Figure 4.31 – Boundary conditions adopted for the model and contact region between the surfaces (in green color).

Accurate calibration of contact parameters is crucial in developing a reliable finite element model for simulating pullout tests. In this sense, it is necessary to calibrate key contact parameters, such as the friction coefficient, the damage initiation parameter, the cohesive stiffness parameters, and the exponential damage variable associated with the damage constitutive model at the fiber/matrix interface.

In this work, the interface parameters were calibrated to the experimental results presented in Chapter 3. This calibration was adjusted through a trial and error method. The final parameters obtained after this procedure are indicated in Table 4.5.

Table 4.5 – Interface parameters for Matrix A and straight steel fiber after the calibration with the experimental results.

Parameter	Value
Friction coefficient μ (-)	0.3
Damage initiation δ_i (mm)	1.5
Cohesive stiffness K (MPa/mm)	12.0
Exponential damage parameter α (-)	1.2

Mesh convergence tests were conducted to ensure the accuracy and reliability of the finite element model for simulating pullout experiments. Six element meshes were selected. All meshes used four-node axisymmetric elements to capture the system behavior. The mesh sizes and corresponding number of elements are as follows: Mesh A (90 elements), Mesh B (120 elements), Mesh C (350 elements), Mesh D (600 elements), Mesh E (1000 elements), Mesh F (2500 elements) and Mesh G (5000 elements). The vertical displacement of two selected interface nodes was evaluated to assess the convergence of the FE model. Following the analyses with distinct mesh sizes, it was observed that the models exhibited convergence with the 1000-element mesh.

Considering the cement matrix, steel fiber, and interface parameters presented in Table 4.3, Table 4.4 and Table 4.5, Figure 4.32 presents the pullout load-displacement response for the straight steel fiber in Matrix A.

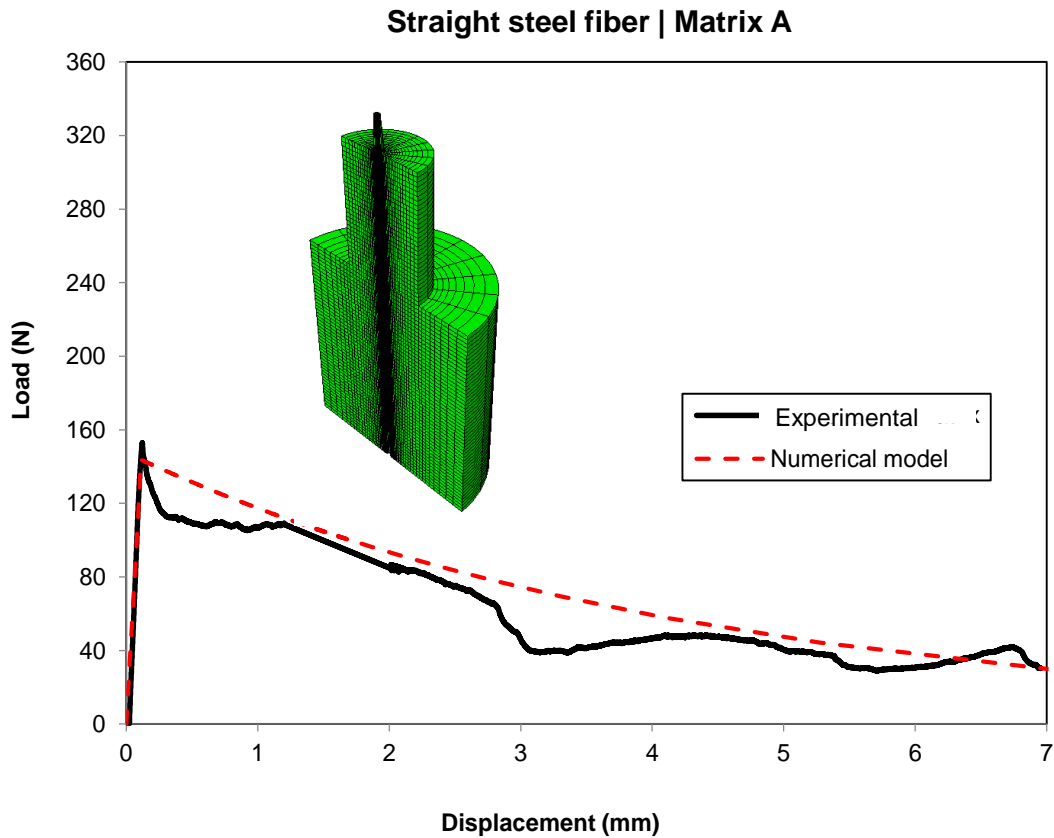


Figure 4.32 – Pullout load-displacement experimental and numerical results for the straight fiber in Matrix A.

As presented in the proof of concept models, Figure 4.33 shows the evolution of shear stresses that act along the fiber length considering the straight fiber model in Matrix A. At the beginning of the analysis ($\delta = 0$ mm), the shear stresses are zero. In the stage corresponding to the peak load on the graph (onset of fiber debonding), a significant level of oscillation in shear stresses is observed, especially at fiber ends. This pattern continues until the fiber response is totally governed by friction (Figure 4.33 (d)).

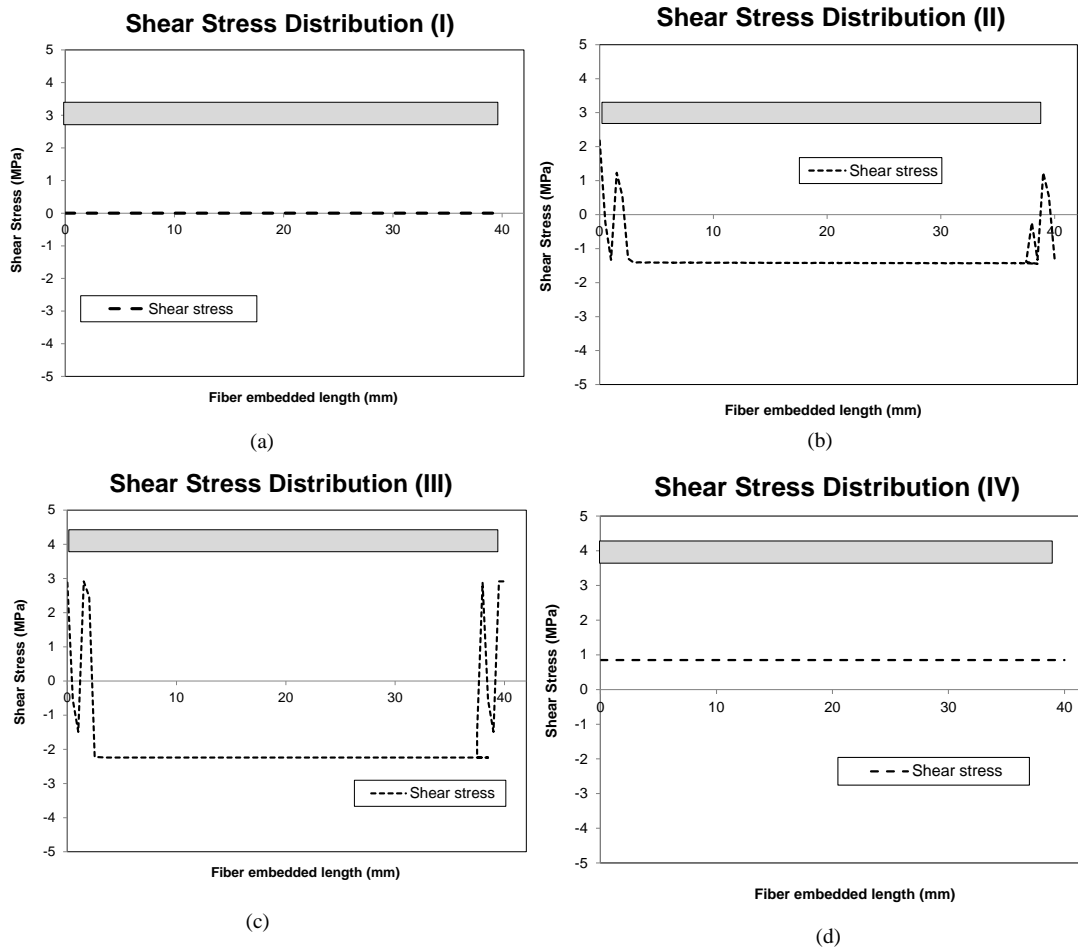


Figure 4.33 – Shear stress transfer mechanisms detected for the straight fiber in Matrix A model: (a) at the first step; (b) at peak load; (c) during debonding; (d) during friction.

Figure 4.34 displays the concentration of plastic deformations captured by the numerical model during the analyses, indicating a higher concentration of these deformations in the upper region of the specimen. Additionally, Figure 4.35 illustrates the damaged regions (in red color) captured by the finite element model and the comparison with images obtained via microCT. The qualitative comparison of the microCT images and the numerical model shows a larger concentration of damage at the top of the fiber, where matrix spalling is observed.

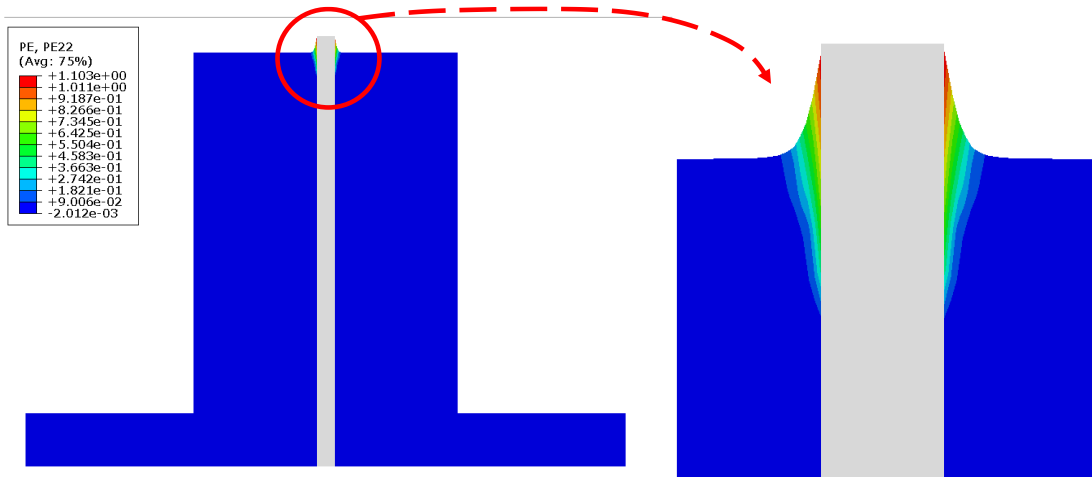


Figure 4.34 – Plastic strain concentration in the upper part of the specimen captured by the numerical model at $\delta = 1$ mm.

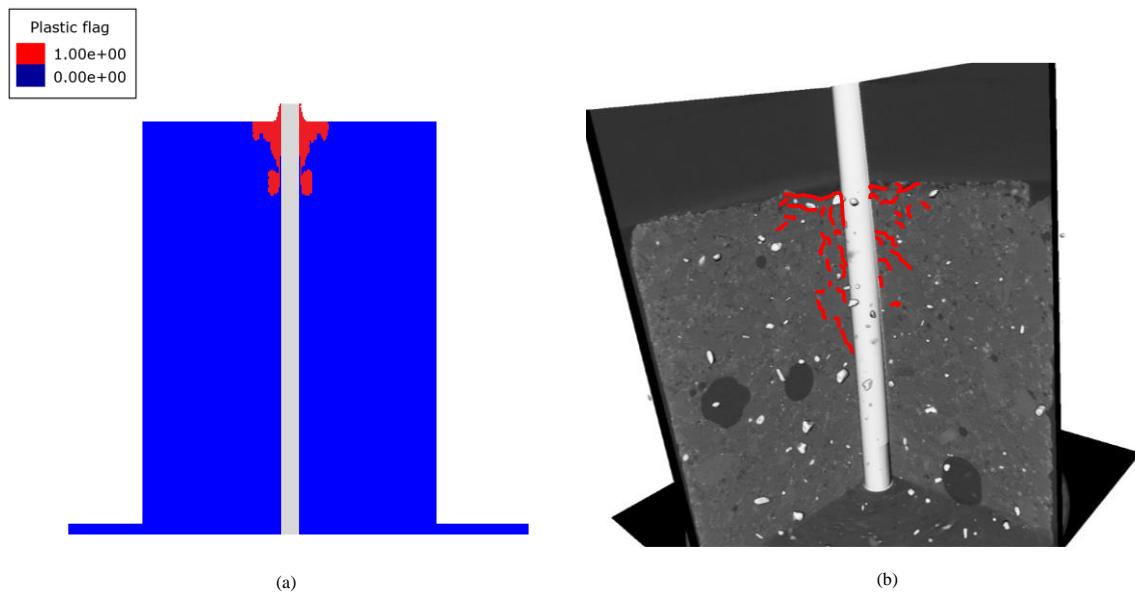


Figure 4.35 – Concentration of damage for the straight steel fiber in Matrix A (region of interest) at $\delta = 7$ mm: (a) numerical model; (b) microCT analysis.

4.3.2.2. Straight steel fiber in Matrix B

The same axisymmetric model is considered to simulate the straight steel fiber in Matrix B. Table 4.6 presents the elastic and mechanical properties of the cement matrix, while Table 4.7 gathers the interface parameters obtained after calibration with the experimental curve. The four-node axisymmetric element with a full integration scheme was used for the numerical simulation.

Table 4.6 – Elastic and mechanical parameters for Matrix B.

Parameter	Value
Young's modulus (GPa)	25.00
Poisson ratio (-)	0.25
Tensile strength (MPa)	4.39
Compressive strength (MPa)	81.3
Dilation angle (°)	40.00
Eccentricity (-)	0.10
f_{b0}/f_{c0} (-)	1.16
K (-)	0.67
Viscosity parameter	0.00

Table 4.7 – Interface parameters for Matrix B and straight steel fiber after the calibration with the experimental results.

Parameter	Value
Friction coefficient μ (-)	0.4
Damage initiation δ_i (mm)	2.4
Cohesive stiffness K (MPa/mm)	10.0
Exponential damage parameter α (-)	0.8

Figure 4.36 presents the pullout load-displacement response for the straight steel fiber in Matrix B.

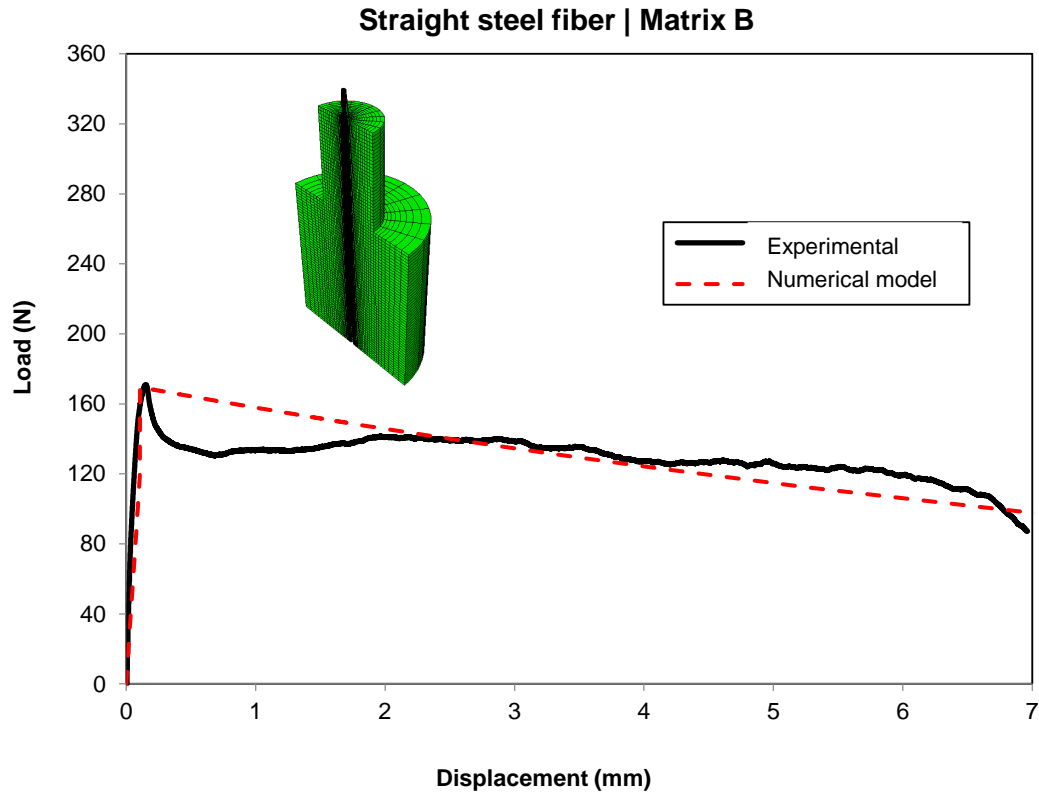


Figure 4.36 – Pullout load-displacement experimental and numerical results for the straight fiber in Matrix B.

Figure 4.37 shows the evolution of shear stresses along the fiber length in Matrix B. It is possible to observe a similar stress transfer mechanism since the fiber geometry is the same as in the previous section. The most significant oscillations in shear stress values are particularly observed at the fiber ends. Due to its straight geometry, this occurs primarily when the fiber loses contact with the matrix (at the base) and begins to debond, as well as at its upper end, where it is being pulled out.

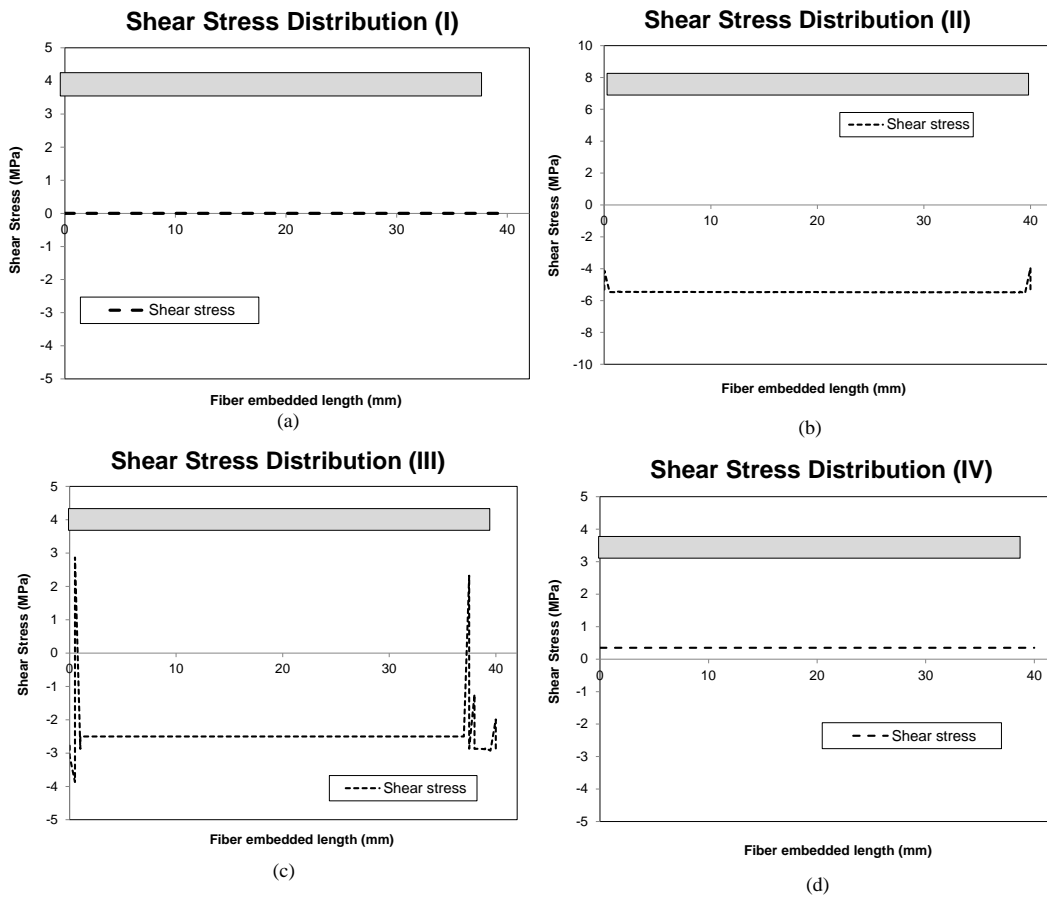


Figure 4.37 – Shear stress transfer mechanisms detected for the straight fiber in Matrix B model: (a) at the first step; (b) at the peak load; (c) during debonding; (d) during friction.

Figure 4.38 displays the concentration of plastic deformations captured by the numerical model during the analyses, indicating a higher level of damage in the upper regions of the model. Additionally, Figure 4.39 presents the damaged regions (in red color) captured by the finite element model and the comparison with images obtained via microCT. The damaged areas are narrower in the case of Matrix B than in Matrix A scenario.

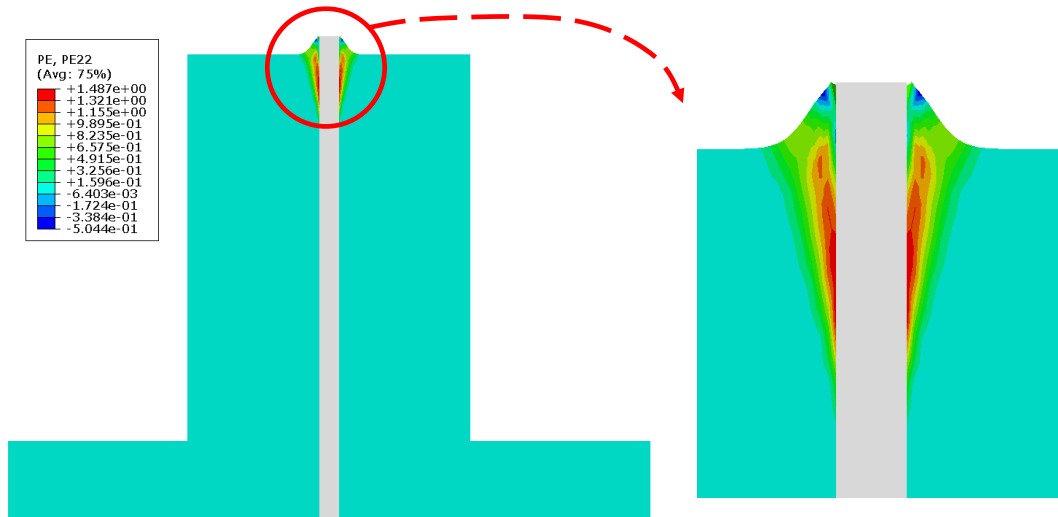


Figure 4.38 – Plastic strain concentration in the upper part of the specimen in Matrix B captured by the numerical model at $\delta = 1$ mm.

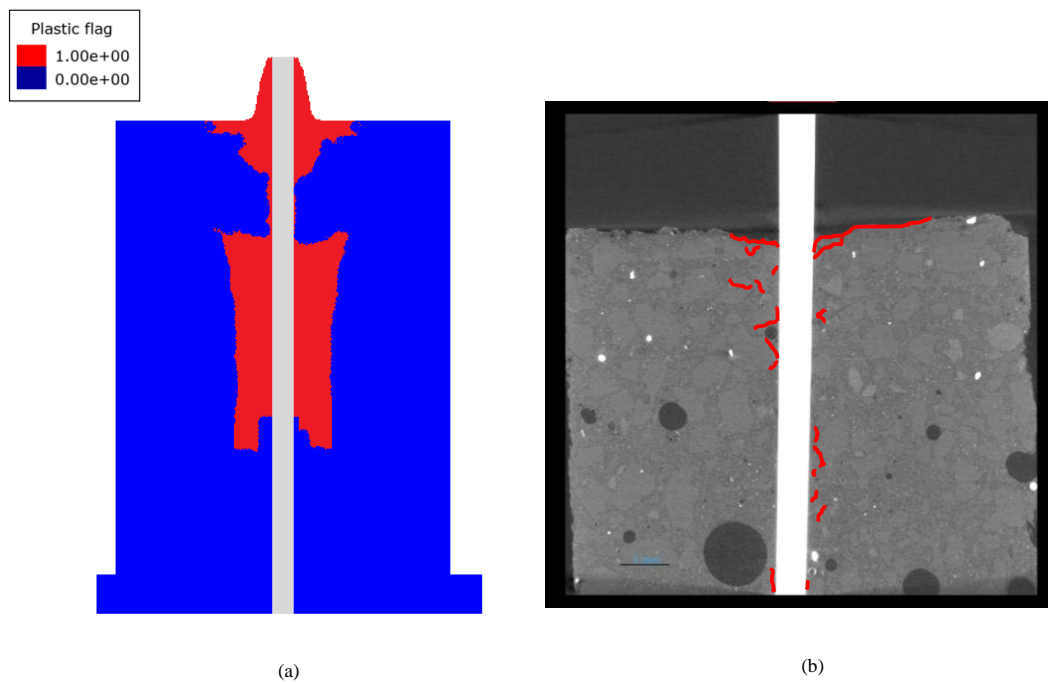


Figure 4.39 – Concentration of damage for the straight steel fiber in Matrix B at $\delta = 7$ mm: (a) numerical model; (b) microCT analysis.

4.3.2.3. Hooked-end steel fiber in Matrix A

For the hooked-end steel fiber model, a three-dimensional model was carried out using ABAQUS ® commercial software in both types of cement matrix. The choice of the 3D model for the hooked fiber was made to provide a more appropriate visualization of the pullout mechanisms observed in the laboratory tests carried out in this study. The mechanical behavior of the cement matrix and the steel fiber was the same as in the straight fiber models (Figure 3.9, Table 4.3 and Table 4.4). Displacement control was adopted for the model, applying a prescribed displacement δ at the top edge of the steel fiber. The additional displacement boundary conditions consider symmetry effects and prevent lateral displacements of the specimen. The ten-node quadratic tetrahedron element with full integration scheme was used for the numerical simulations. One-half of the test specimen is considered in the numerical modeling for symmetry effects. Figure 4.40 presents the boundary conditions for the 3D model.

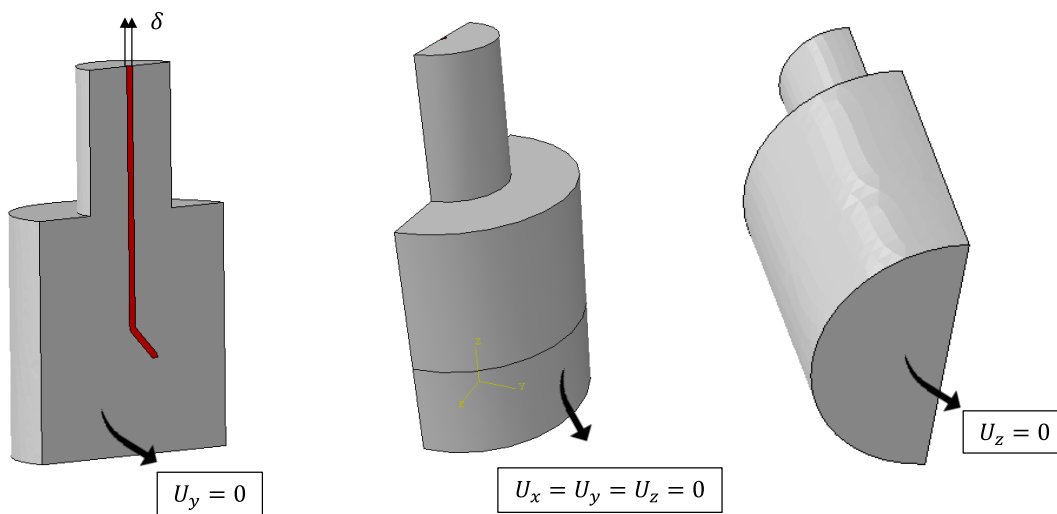


Figure 4.40 – Boundary conditions adopted for the 3D model for the hooked-end steel fiber.

Additionally, Figure 4.41 presents the X-Z view with the details regarding the surface-to-surface cohesive behavior applied at the fiber/matrix interaction for the 3D model. Additional partitions in the fiber part are carried out to aid in finite element mesh generation.

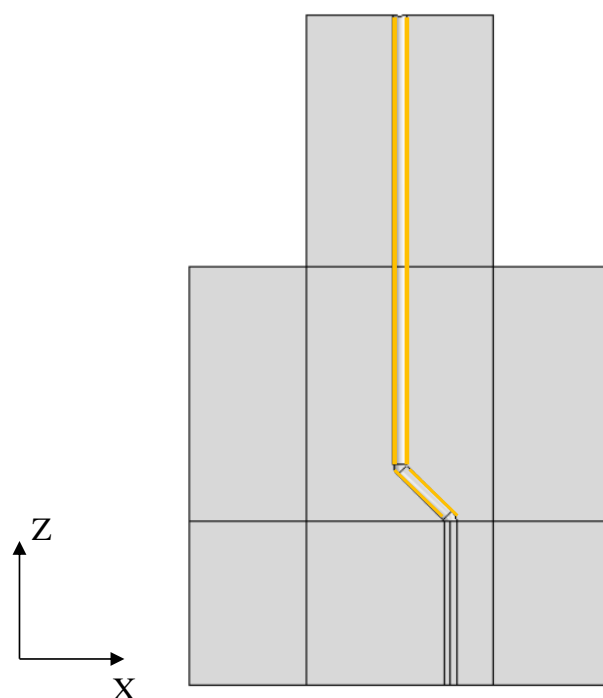


Figure 4.41 – Contact region between the fiber/matrix surface (in yellow color).

The interface parameters were calibrated to the experimental results presented in Chapter 3. This calibration was adjusted against the experimental results through a trial and error method. The final parameters obtained after this procedure are indicated in Table 4.8.

Table 4.8 – Interface parameters for Matrix A and hooked-end steel fiber after the calibration with the experimental results.

Parameter	Value
Friction coefficient μ (-)	0.3
Damage initiation δ_i (mm)	1.9
Cohesive stiffness K (MPa/mm)	18.5
Exponential damage parameter α (-)	0.8

In the same way as in the previous models, a mesh convergence study for the hooked-end fiber model was carried out. A 1000-node mesh presented good convergence regarding the displacement of two selected model nodes. Figure 4.42 presents the pullout load-displacement response for the hooked-end steel fiber in Matrix A and the comparison with the experimental results presented in Chapter 3.

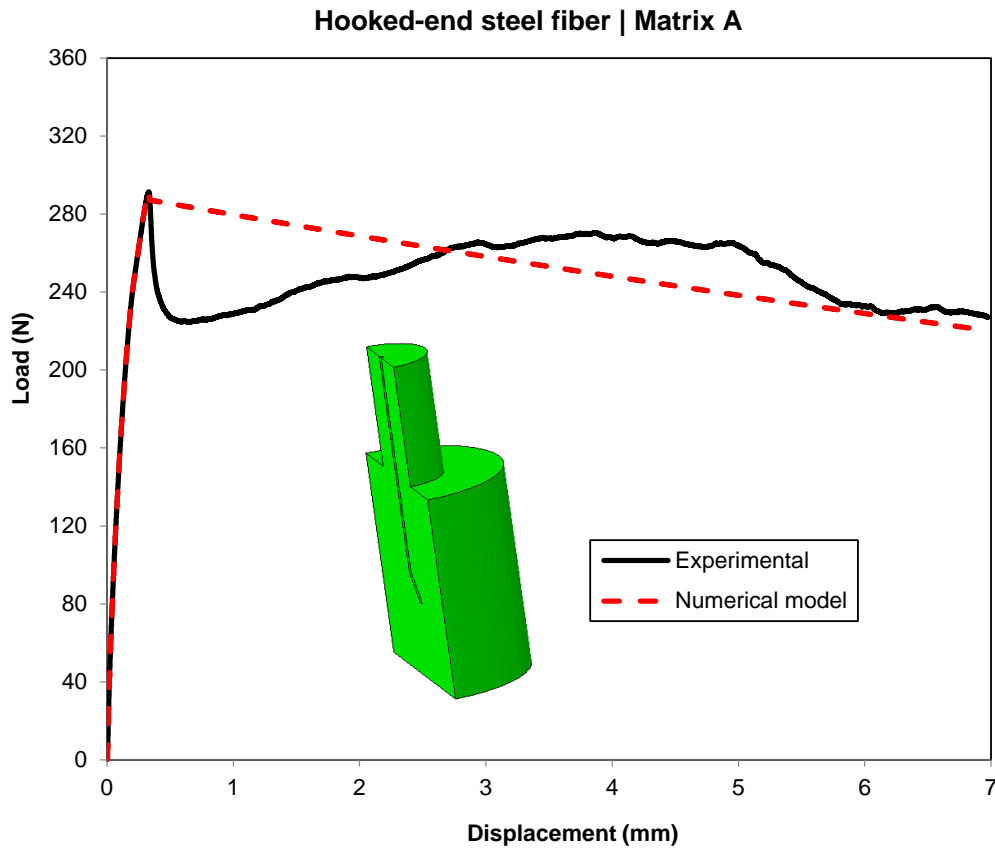


Figure 4.42 – Pullout load-displacement experimental and numerical results for the straight fiber in Matrix A.

Figure 4.43 shows the evolution of shear stresses that act along the fiber length considering the hooked-end fiber model in Matrix A. In the first step of the analysis, the shear stresses are zero. In the stage corresponding to the peak load on the graph (onset of fiber debonding), a significant level of oscillation in shear stresses is observed due to the deformation near the fiber hook.

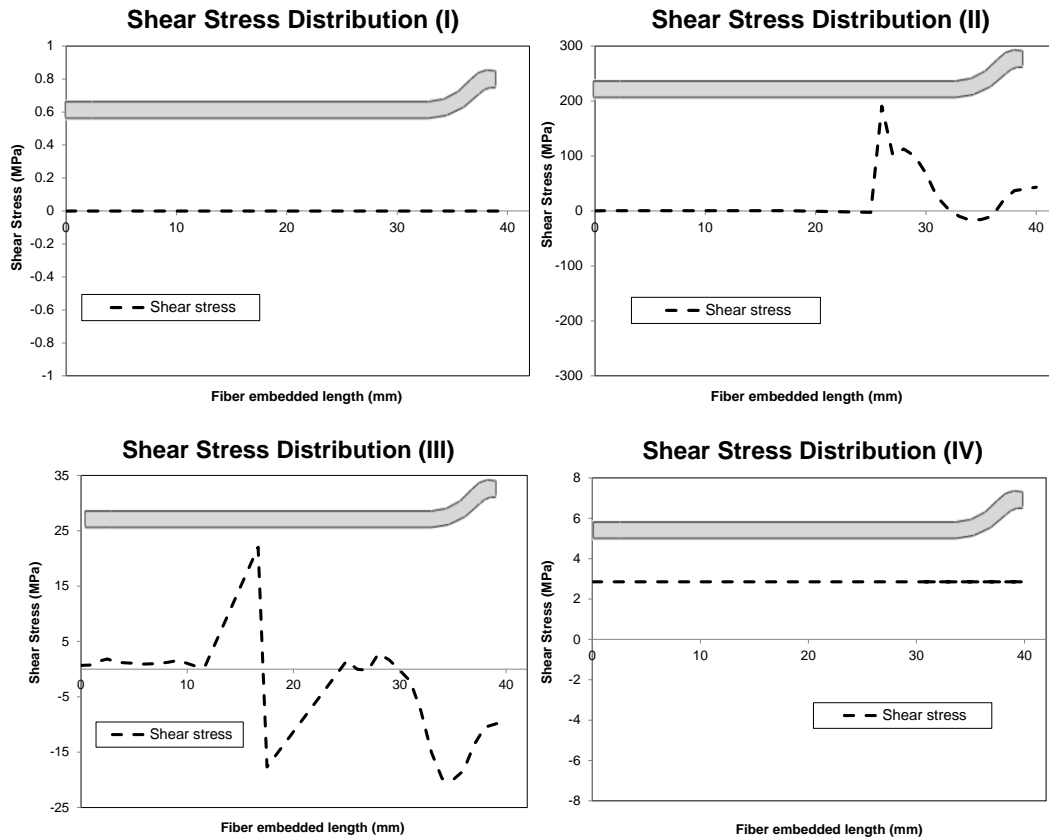


Figure 4.43 – Shear stress transfer mechanisms detected for the hooked-end fiber in Matrix A model: (a) at the first step; (b) at the peak load; (c) during debonding; (d) during friction.

Figure 4.44 displays the concentration of plastic deformations captured by the numerical model during the analyses, indicating a higher level of damage near the fiber hook, as expected. Additionally, Figure 4.45 presents the damaged regions (in red color) captured by the finite element model and the comparison with images obtained via microCT. The qualitative comparison of the damaged regions predicted by the numerical model and the results from the microCT images are in good agreement.

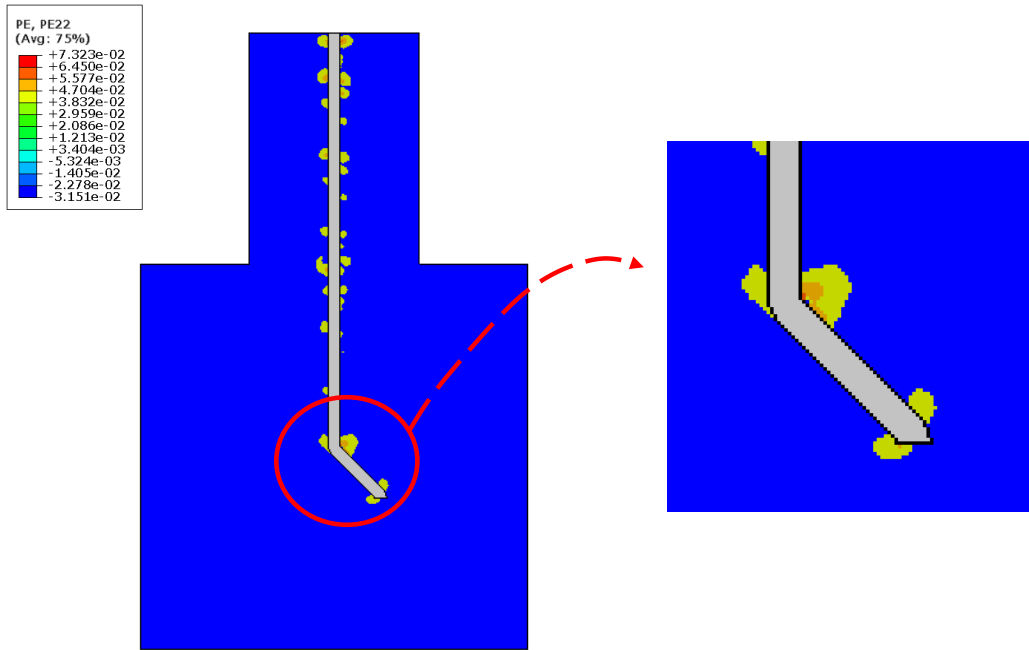


Figure 4.44 – Plastic strain concentration on the specimen captured by the numerical model at $\delta = 1$ mm.

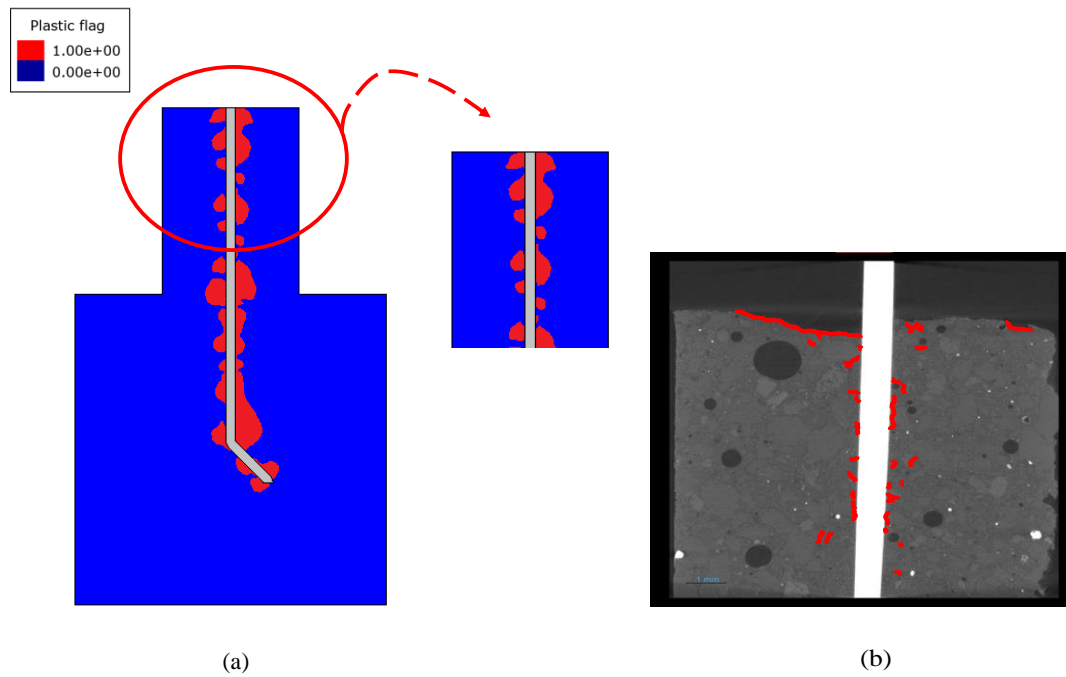


Figure 4.45 – Concentration of damage for the hooked-end steel fiber in Matrix A at $\delta = 7$ mm: (a) numerical model; (b) microCT analysis.

4.3.2.4. Hooked-end steel fiber in Matrix B

Finally, considering the same 3D model from the previous section, the last model is developed for the hooked-end steel fiber in Matrix B. The elastic and mechanical properties of Matrix B are indicated in Table 4.6, while Table 4.9 gathers the interface parameters obtained after the calibration step with the experimental data.

Table 4.9 – Interface parameters for Matrix B and straight steel fiber after the calibration with the experimental results.

Parameter	Value
Friction coefficient μ (-)	0.5
Damage initiation δ_i (mm)	2.8
Cohesive stiffness K (MPa/mm)	19.0
Exponential damage parameter α (-)	1.2

Figure 4.46 presents the pullout load-displacement response for the hooked-end steel fiber in Matrix B.

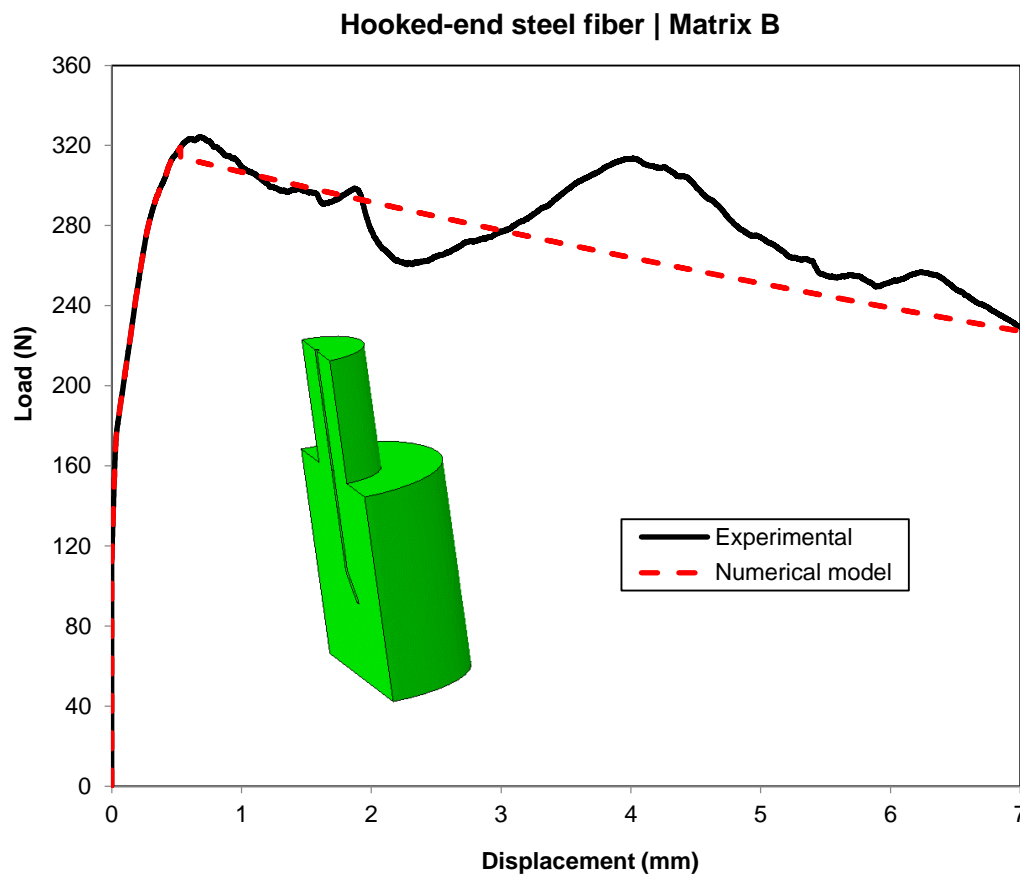


Figure 4.46 – Pullout load-displacement experimental and numerical results for the straight fiber in Matrix B.

Figure 4.47 shows the evolution of shear stresses along the fiber length in Matrix B. The numerical model captures the stress levels for this configuration, which are higher than in the case of the straight fiber, given that the hook provides greater anchoring to the fiber. Additionally, due to the high strength of the matrix, there is increased difficulty in pulling the fiber away from the cementitious matrix. Moreover, the models related to Matrix B also exhibit higher deformation values, especially for the fiber and in the fiber/matrix interface. This inference also agrees with the observations made in the experimental studies by Isla et al. [62].

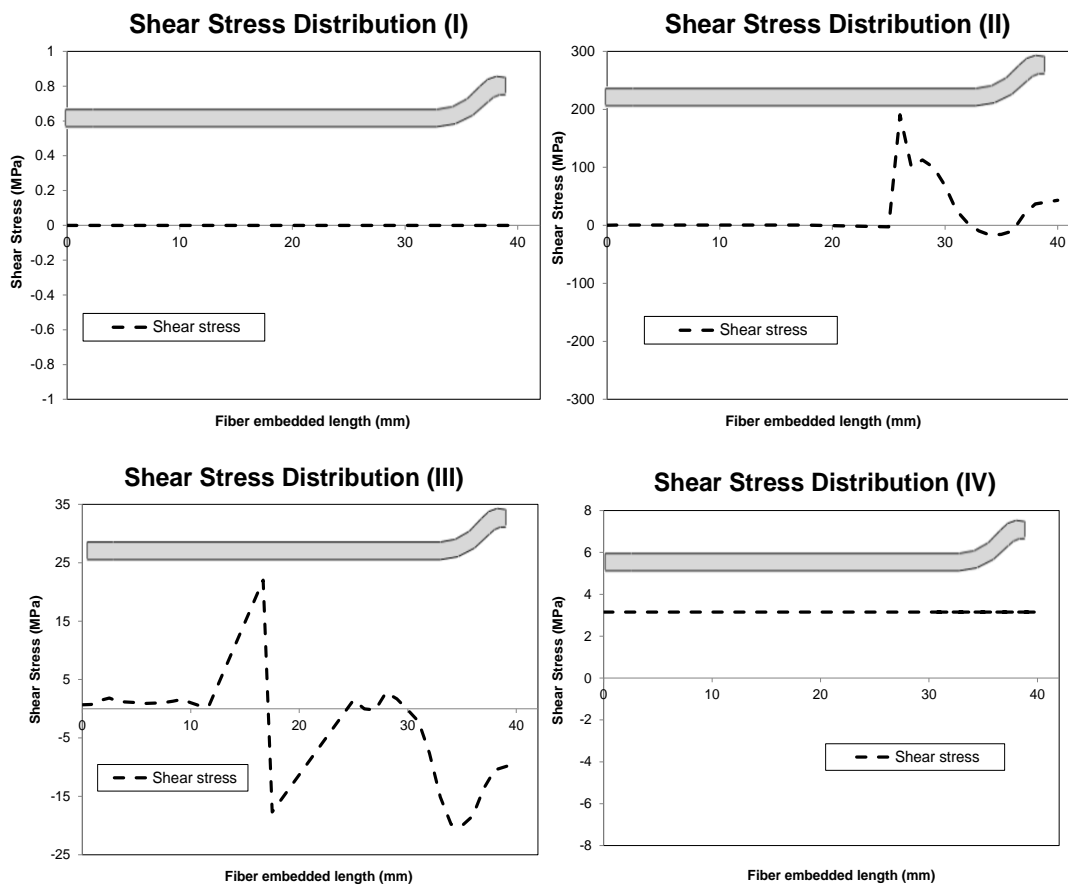


Figure 4.47 – Shear stress transfer mechanisms detected for the hooked-end fiber Matrix B model: (a) at the first step; (b) at the peak load; (c) during debonding; (d) during friction.

Figure 4.48 displays the concentration of plastic deformations captured by the numerical model during the analyses. Additionally, Figure 4.49 presents the damaged regions (in red color) captured by the finite element model and the comparison with images obtained via microCT. As expected, the numerical model exhibits a higher level of damage for this configuration, attributed to the higher strength of the matrix and increased fiber anchorage due to the presence of the hook.

Thus, the qualitative comparison of the damaged regions predicted by the numerical model and the results from the microCT images are in good agreement.

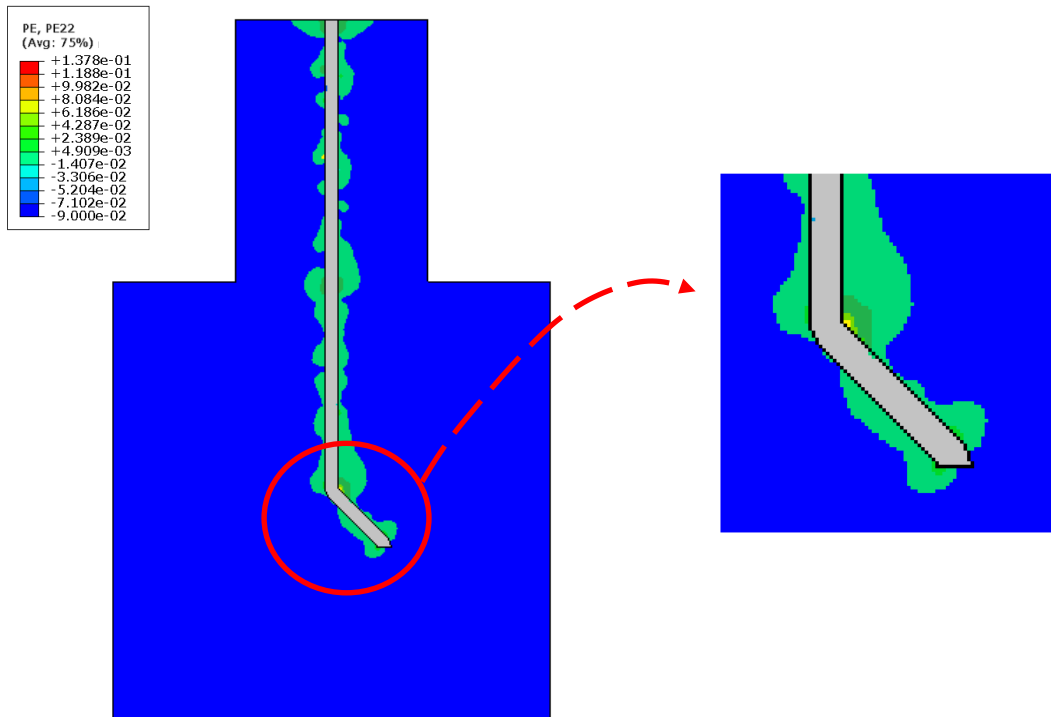


Figure 4.48 – Plastic strain concentration captured by the numerical model at $\delta = 5$ mm.

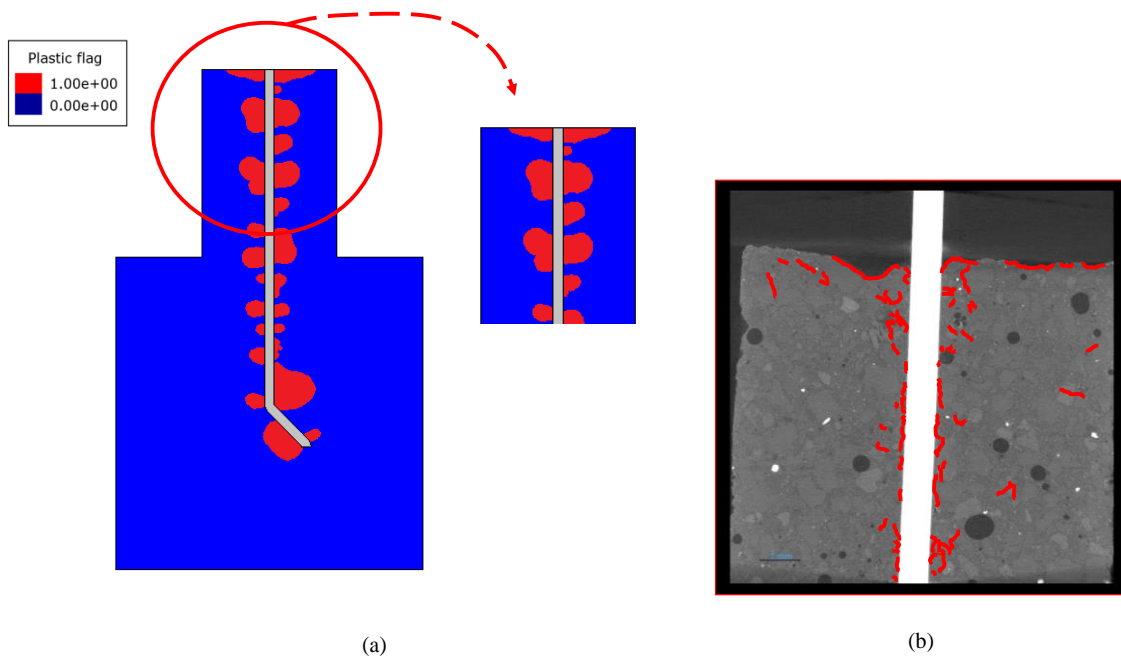


Figure 4.49 – Concentration of damage for the hooked-end steel fiber in Matrix B at $\delta = 7$ mm:
(a) numerical model; (b) microCT analysis.

In calibrating parameters of the pullout numerical models using the trial and error method based on experimental curves, it is crucial to acknowledge the inherent complexity of the problem, often leading to multiple solutions. This challenge means that various combinations of interface parameters may generate results closely resembling the experimental curve. Typical values from the literature are employed for the numerical parameters with physical interpretations, such as friction coefficients. However, as discussed in previous sections, many contact parameters lack direct physical interpretation. Hence, a combination of calibration against experimental data and values derived from analogous literature works is employed.

This iterative calibration process minimizes the difference between model predictions and experimental observations. In this case, the inherent uncertainties and challenges regarding contact problems are worth emphasizing. Additionally, there is a lack of specific experimental tests to calibrate the contact parameters. Therefore, a pragmatic approach is adopted, prioritizing parameter sets that fit well with the experimental curve and demonstrate consistency with physical principles and trends observed in related studies. This calibration strategy ensures that the numerical model captures the essential system behavior while maintaining a balance between the accuracy and interpretability of the parameters. Moreover, the qualitative validation of damage propagation through comparison between the numerical model and microCT images confirms that the employed calibration leads to satisfactory results in terms of Engineering.

5

Numerical case study on the pushout shear strength of conventional and expanding cement-casing sections for well integrity

The study of the interfacial debonding of cement and damage mechanisms is not limited solely to applications involving cement composite materials and the fiber/matrix interface. In the oil and gas industry, a good bond between the well casing and cement is often considered essential for avoiding generating microannulus leakage paths along the interface between the two materials. A common method for characterizing the casing-to-cement bond is to perform laboratory pushout tests, analogous to the pullout tests carried out with fibers.

This chapter investigates pushout tests conducted on conventional class G and well cement samples containing expanding additive. A finite element model incorporating the same methodology presented in Chapter 4 is proposed to simulate the behavior of cement sections under pushout loading conditions. The results from the FE model were compared with the experimental responses, demonstrating good agreement in simulating the pushout behavior of conventional class G cement and expanding cement samples. Notably, the significant findings of this work fill a critical gap in the literature. Few experimental tests and elastoplastic numerical models have been carried out in the literature to comprehensively capture the damage evolution and predict the pushout shear strength in cement-casing interactions in P&A scenarios.

Article published – *Geoenergy Science and Engineering*

DOI: 10.106/j.geoen.2024.212638

5.1.

The cement/casing interface problem in O&G applications

The interaction between cement and steel plays an important role in several engineering applications, such as in the construction and the O&G industries. In structural engineering, the combination of cement and steel reinforcement is

commonly used to create reinforced concrete structures, which are known for their strength and durability given by the interface between both constituents [160], [161]. On the other hand, in the O&G industry, cement and steel are essential structural elements in wells that should ensure well integrity and provide zonal isolation [162], [163]. The interaction between cement and steel is considered critical for zonal isolation, as a strong bond may prevent the generation of microannulus leakage paths along the cement and steel interface. Several factors, including the type of cement, steel surface condition, and curing conditions, can influence the bond strength between cement and steel [162]–[164]. Another critical concern is when there is an excessive displacement of the steel casing due to high pressure or thermal expansion in real-scale well applications [160], [165].

The annular cement sheath can suffer damage due to thermal and mechanical loads, changes in in-situ stresses, and deformation of the surrounding rocks. This damage can cause a separation between the casing and the cement, creating a hydraulic pathway called microannulus [164]–[166]. To prevent the formation of microannulus, a strong bond between the cement and the casing is necessary. In production well sections, more complex arrangements can be found. These include casing–cement–casing–cement–formation, providing two annular spaces filled with cement. Typical cases involve 7" casing and 9 5/8" or 9 5/8" x 13 3/8". For well abandonment, it is necessary to install plugs inside the casing to prevent fluid migration from the well to the surface [167].

The pushout test is an experimental method to evaluate the shear strength between cement and steel [168]. In pushout experiments involving cement and steel casings, a compressive load is applied to the cement plug bonded to a steel casing, simulating the forces experienced during wellbore operations [166], [169]. Studies regarding the interaction between well casing and cement interface strength originally started with the predecessor works [170], [171]. De Andrade et al. [172] developed a novel laboratory setup to study cement-sheath-failure mechanisms during thermal cyclings, such as debonding and crack formation. Moreover, Corina et al. [145] studied the cement-plug sealing of neat- and silica-cement systems placed in pipes with three different levels of surface roughness using a test cell filled with a cement plug. The authors verified a gas leak in all samples at low differential pressure through leak sources at the cement/steel interface in this work. Similarly, Tabatabaei et al. [146] studied the mixed-mode interfacial strength of cementitious

materials at the casing-cement or rock-cement interfaces and compared their experimental results with analytical elasticity solutions available in the literature. Kamali et al. [147] investigated the shear bond strength of distinct cementitious barrier materials, such as expansive cement and a geopolymer, and pointed out that the slurry additives used in the preparation impact the hydraulic sealability of the material. Similarly, Murcia et al. [148] carried out pushout tests to examine the interfacial bond strength between the cement and rock formation with and without applying a novel polymer-based sealant for plugging and abandonment (P&A) application, where the sealant can be used for stronger bond between the steel and the rock. Tabatabaei et al. [173] performed a series of pushout tests to evaluate how the addition of surface-modified cement additive using graphite nanoplatelets (GNPs) influences the bond strength in different scenarios of oil-based mud residues. More recently, Cheng et al. [174] studied the bond behavior between sandwich pipe layers also through the execution of pushout tests. The pipes comprised a strain-hardening cementitious composite filling core for oil and gas transportation in deep waters. Alternatively, Lavrov et al. [175] recently conducted pushout tests cemented within Portland cement slurry under constant electrical potential difference. The authors concluded that, at a high potential difference voltage, the duration of the potential application presents an impact on the interfacial bonding between cement and casing.

Numerical modeling is a powerful technique to understand the contact forces and deformations between two bodies and material interfaces. However, few works in the literature directly deal with modeling the casing-cement pushout test, especially considering the cement's and interface's nonlinear constitutive behavior. Coquard and Cerasi [149] developed a preliminary elastoplastic finite element model to simulate the ensuing deformation of the cement/casing system under a constant force. Cement behavior was modeled using the Mohr-Coulomb failure criterion. For the steel casing, the Von-Mises criterion was adopted. The interface between both materials was modeled using Coulomb's law of friction. However, the authors pointed out that specific mechanisms should be incorporated into the formulation to get more accurate results, especially regarding the normal behavior of the interface. Lavrov et al. [165] have also worked on a linear elastic finite element model to simulate the pushout behavior between cement sections and steel casing. This study estimated the normal stress expected at the cement-steel interface

as cement shrinks towards the pipe in the pushout test. Jin et al. [150] proposed a 3D mesoscale elastoplastic model for reinforced concrete. The contact between steel bars and surrounding concrete was modeled using a surface-to-surface approach. The tangential behavior was simulated by a penalty formulation and Coulomb's law of friction. Moreover, a hard-contact relationship was considered to simulate the normal behavior between the surfaces. A similar approach has been adopted in the works of Jin et al. [151] and Chriatti et al. [152].

However, one alternative finite element formulation for simulating the normal contact behavior between surfaces is the cohesive zone model (CZM). This formulation was first introduced by Barenblatt [176] and Dugdale [177], who studied brittle fractures and cracks, and yielding of steel sheets with slits, respectively. The CZM approach places cohesive interface elements associated with a traction-separation constitutive model at the interface between cement and steel. Abbas et al. [135] proposed a three-dimensional mesoscopic frictional cohesive zone model to simulate the concrete-steel interface in reinforced concrete applications. In this model, a cohesive zone model is associated with Coulomb's law of friction to model the steel-concrete interface pull-out test simulations. Similarly, Lin et al. [141] updated the bilinear cohesive zone model to include the frictional contact effect between the surfaces. Once again, the Coulomb model was adopted to simulate the tangential behavior between concrete and steel bars. Alfano and Sacco previously developed a similar approach [136], proposing a combination between interface damage and friction in a cohesive-zone model. Rezazadeh et al. [137] proposed damage-based approaches for assessing the bond damage evolution in a glass-fiber-reinforced polymer (GFRP). The FE model considers the nonlinear behavior of the concrete and the GFRP bar-concrete interface using cohesive elements and a hard-based contact in the normal direction. A similar approach was also carried out by Ali et al. [142] in the numerical simulation of a hybrid composite with shape memory alloys and GFRP interface.

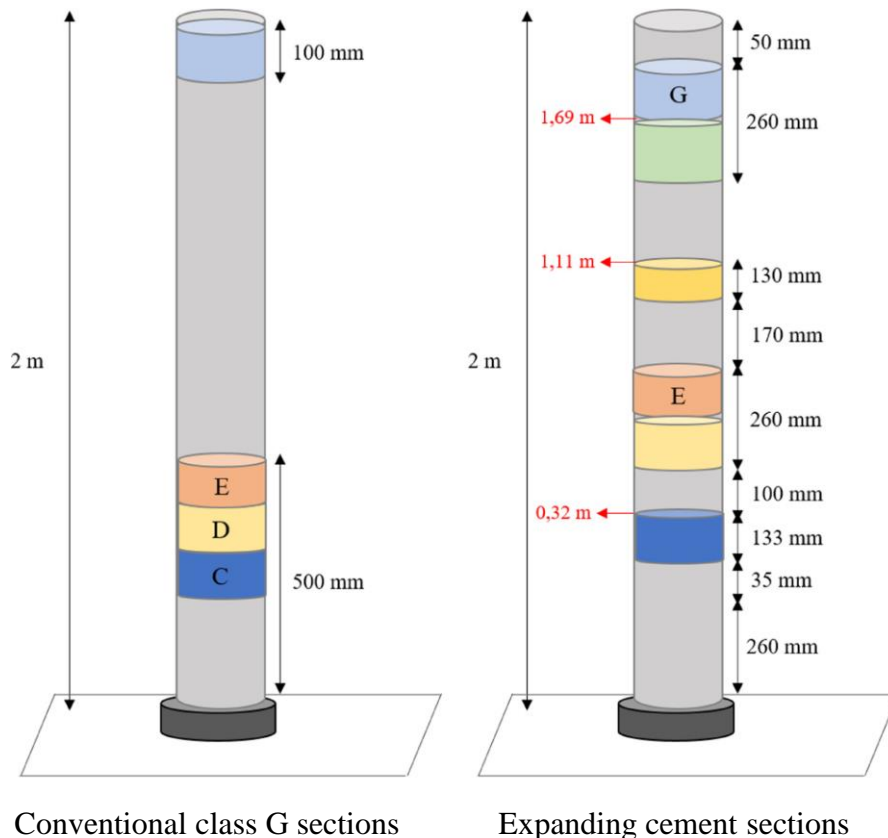
This chapter proposes a numerical study of the pushout shear strength of conventional and expanding cement-casing sections. The experimental program involves the preparation of well cement samples, uniaxial compressive strength, and pushout tests and was detailed in Congro et al. [34]. The experimental pushout tests were conducted by researchers from NORCE and the University of Stavanger in collaboration with industry partners within the BRANOR project. These

experimental tests serve as pivotal references for the finite element modeling discussed in the current chapter of the thesis. These tests provided crucial data for developing and validating the proposed models.

In this context, the slurries were injected into the bottom of two vertical 9 5/8-in an outer diameter casing of 2 meters length (Figure 5.1 (a)). Next, the assemblies were cut into shorter sections approximately 10-13cm long, as indicated in Figure 5.1 (b).



(a)



(b)

Figure 5.1 – (a) Sections cut for pushout testing; (b) Cement sections inside the 2-meter casing before the cut for pushout experiments (Adapted from [34]).

The pushout tests were performed using an Enerpac VLP series hydraulic press. The cement plug was placed on top of a 110 mm long empty 9 5/8-in casing section and had a piston element placed on top of the cement plug [34]. The diameter of the piston element was about 5 mm less than the diameter of the cement plug to prevent mechanical contact between the piston and the inner casing wall. The empty 9 5/8-in casing section was identical to the 9 5/8-in casing that housed the cement plug but with an inner diameter enlarged by approximately 5 mm, allowing the cement plug to eject freely from its original 9 5/8-in casing housing [34]. Additional details regarding the cement slurries recipes, curing conditions and pushout tests are explicitly outlined in [34].

Next, elastoplastic finite element models are developed to predict the pushout behavior of the tested cement sections for P&A applications. Cement is simulated as an elastoplastic material using the Mohr-Coulomb constitutive model; steel is considered a linear elastic material. The surface-based cohesive approach presented and carried out in Chapter 4 for the fiber pullout experiments was used to simulate the interaction between cement and steel. Similarly to the works of [135], [141], [149]–[152], the friction behavior of the interface follows Coulomb's law. We calibrate the computational model using recent full-scale diameter pushout measurements. Sensitivity analyses are also carried out to verify which model parameters influence the pushout response since some parameters calibrated for the numerical analyses do not have a physical interpretation. This comprehensive study explores the pushout shear strength. It brings a methodological advancement by integrating experimental and numerical approaches for a better understanding of cement-casing interactions in P&A scenarios.

5.2. Finite element models for pushout tests

To simulate the pushout tests for conventional and expanding cement, an axisymmetric model was carried out in the commercial software ABAQUS ®. This choice assumed that the behavior of the cement would be symmetric around the axis of the well casing. In real-scale applications, the casing will not be perfectly smooth or circular. Surface roughness and irregularities may affect the frictional response and partly explain sample-to-sample variations observed experimentally

[34]. However, for the proposed numerical model, simplifying assumptions are adopted that do not consider the effects of casing imperfections.

The mechanical behavior of the conventional class G cement was considered elastoplastic using the Mohr-Coulomb plasticity constitutive model. The two steel casings were modeled with linear elastic behavior, assuming isotropy and homogeneity. This simplification was made based on the assumption that the deformation of the casing would remain within the elastic range during the pushout tests.

Table 5.1 gathers the numerical parameters considered for the conventional class G cement, and Table 5.2 presents the elastic parameters for the steel casing. Finally, Table 5.3 presents the constitutive parameters for the expansive cement sections.

Table 5.1 – Constitutive parameters for the conventional class G cement.

Parameter	Value
Young's modulus (GPa)	9.10
Poisson ratio (-)	0.07
Friction angle (°)	5.00
Dilation angle (°)	5.00
Cohesion (MPa)	1.00

Table 5.2 – Elastic parameters for the steel casing.

Parameter	Value
Young's modulus (GPa)	210.0
Poisson ratio (-)	0.30

Table 5.3 – Constitutive parameters for the expanding cement.

Parameter	Value
Young's modulus (GPa)	12.5
Poisson ratio (-)	0.15
Friction angle (°)	5.00
Dilation angle (°)	5.00
Cohesion (MPa)	1.00

Figure 5.2 presents the boundary conditions for the axisymmetric pushout finite element models with particular emphasis on the contact area between the cement section and the casing. According to the experimental observations [34], displacement control was adopted for the models, applying a prescribed displacement δ at the top edge of the cement plug part. The additional displacement

boundary conditions consider the symmetry effects and prevent lateral displacements of the casing.

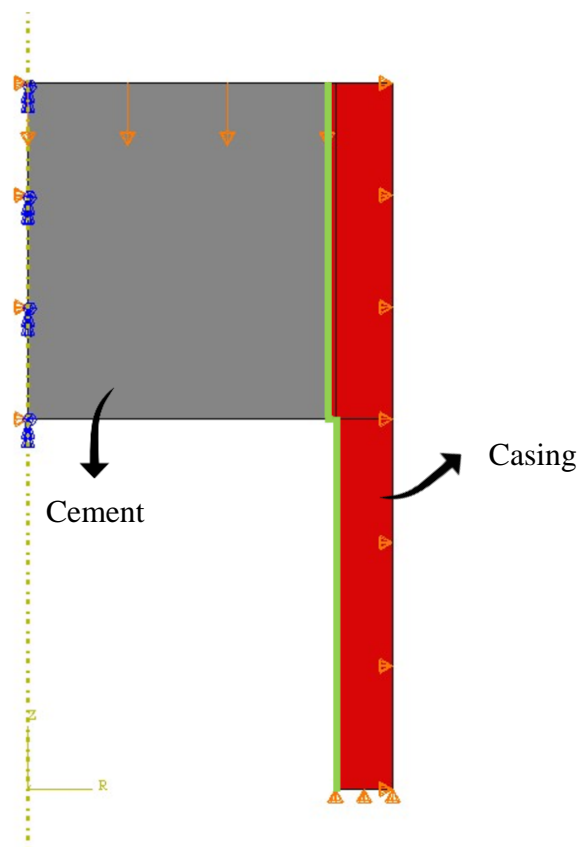


Figure 5.2 – Boundary conditions for the model and contact region between the surfaces (in green color).

5.3. Sensitivity analyses

Accurate calibration of contact parameters is crucial in developing a reliable finite element model for simulating pushout tests. In this section, we focus on calibrating several key contact parameters, including the friction coefficient, the damage initiation parameter, the cohesive stiffness parameters, and the exponential damage variable associated with the damage constitutive model. These parameters capture the interfacial behavior and bond strength between the cement and casing during pushout loading. In this work, the interface parameters were calibrated to the experimental results available in Congro et al. [34]. This calibration procedure was carried out through a trial and error method. The final parameters obtained after this process are indicated in Table 5.4 and Table 5.5. The sensitivity analyses consider an example of a conventional class G cement plug.

Table 5.4 – Interface parameters for the conventional class G cement and the steel casing after the calibration with the experimental results.

Specimen/ Parameter	Friction coefficient (-)	Damage initiation (mm)	Cohesive stiffness (MPa/mm)	Exponential damage parameter (-)
Plug C	0.50	0.35	2.80	1.50
Plug D	0.30	0.12	2.10	0.80
Plug E	0.40	0.45	3.12	3.50

Table 5.5 – Interface parameters for the expanding cement and the steel casing after the calibration with the experimental results.

Specimen/ Parameter	Friction coefficient (-)	Damage initiation (mm)	Cohesive stiffness (MPa/mm)	Exponential damage parameter (-)
Plug E	0.40	0.45	10.00	1.00
Plug G	0.35	0.81	6.00	2.00

The friction coefficient represents the resistance to the relative motion between the contact surfaces. In pushout tests, it is essential to calibrate this parameter to simulate the frictional behavior between the cement and casing accurately. The damage initiation parameter determines the threshold at which damage starts to develop in the material. In pushout tests, it captures the initiation and propagation of the damage at the cement-casing interface. The cohesive stiffness parameters define the stiffness and resistance to separating cement and casing. These parameters significantly influence the bond strength and interfacial behavior during pushout loading. The normal and tangential stiffness parameters are considered equal for simplification purposes. This assumption has been adopted in the literature in several cement/steel interface problems, such as the works of Feng et al.; Jiang et al.; Jiang et al.; Giasuddin et al. [178]–[181]. Finally, the exponential damage variable is associated with the damage constitutive model and determines the damage growth rate in the cement/casing interface. Calibration of this variable is essential to capture damage evolution during pushout loading.

The sensitivity analyses were carried out using Design of Experiments (DOE), particularly the Response Surface Methodology (RSM). The sensitivity analyses were carried out in Minitab 18 ® software and adopted a central circumscribed composite design (CCC) and a full quadratic polynomial model. The default configurations of statistical analyses consider a 95% confidence interval for the simulations and 5% significance level. Pareto charts are generated to check if

the contact numerical parameters influence the pushout peak load. Figure 5.3 presents the Pareto charts with the absolute values of the standardized effects from the most significant to the least. A reference line (*p-value*) is also included to indicate which effects are statistically significant for the maximum pushout load in conventional class G cement sections.

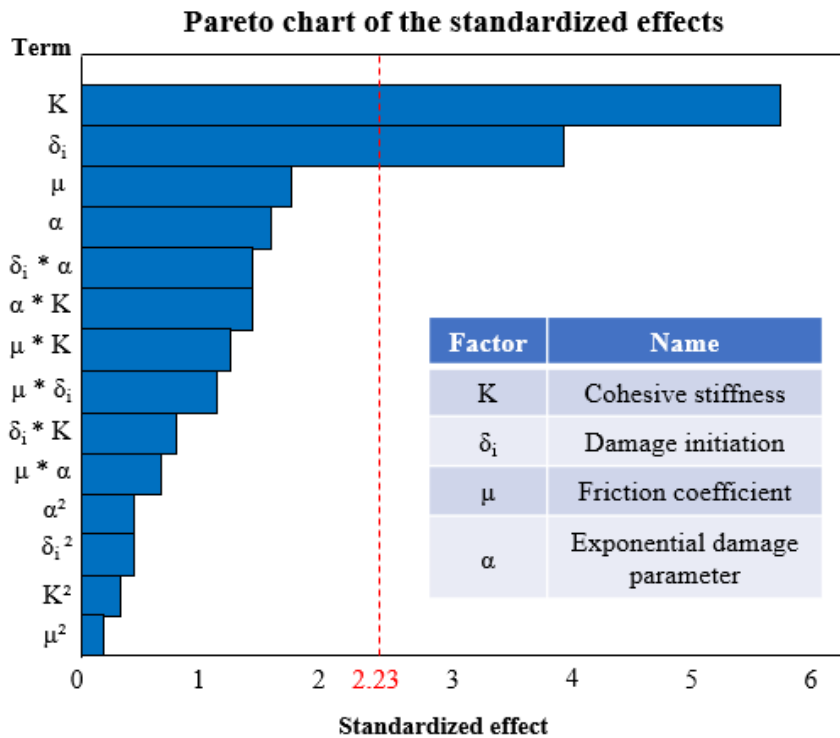


Figure 5.3 – Pareto chart of the standardized effects for the pushout maximum load in conventional class G samples.

The Pareto chart indicates that the tangential cohesive stiffness parameter plays an important role for conventional class G cement, the primary input parameter influencing the pushout maximum load. The second significant input parameter is the damage initiation displacement, which refers to the relative displacements between the follower nodes (cement) on the follower surface and the corresponding point on the leader surface (steel).

The statistical analysis using DOE allows the generation of response surface plots that confirm the influence of each input parameter in the system response, as indicated in Figure 5.4 (a) and (b).

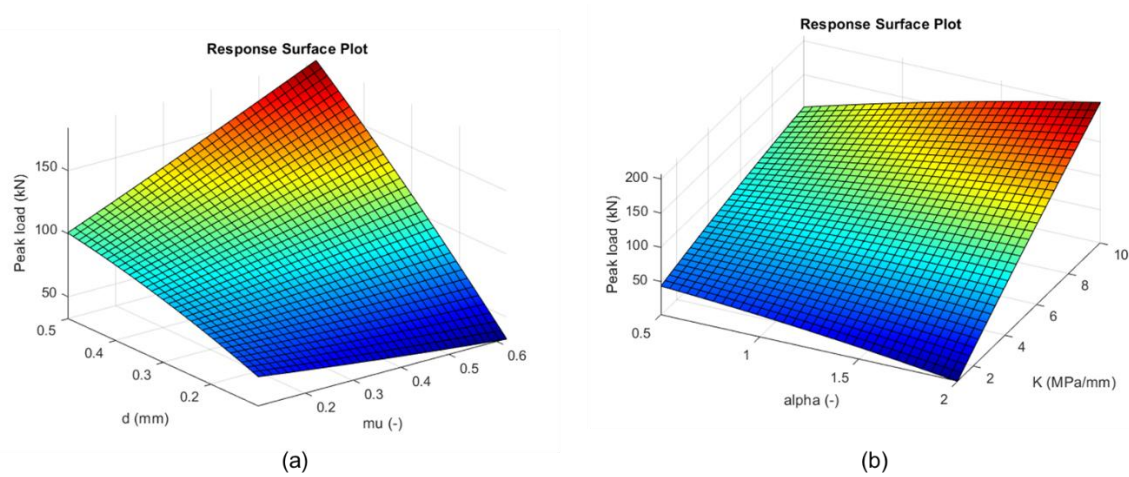


Figure 5.4 – Response surface plots: (a) Peak load variation in terms of friction coefficient and damage initiation parameter; (b) Peak load variation in terms of exponential damage parameter and cohesive interface stiffness.

5.4. Mesh convergence tests

To ensure the accuracy and reliability of the FE model for simulating pushout experiments, mesh convergence tests were conducted. Seven different FE meshes were selected. All meshes used four-node axisymmetric elements to capture the system behavior. The mesh sizes and corresponding number of elements are as follows: Mesh A (98 elements), Mesh B (153 elements), Mesh C (300 elements), Mesh D (500 elements), Mesh E (924 elements), Mesh F (2500 elements) and Mesh G (5000 elements).

The vertical displacements of two selected model nodes were evaluated to assess the convergence of the FE model. These nodes were strategically chosen to represent critical points where the displacement behavior is expected to provide insight into the pushout behavior of the cement and casing interface.

Following the analyses of the pushout using different mesh sizes, it was observed that the models exhibited convergence with the 500-element mesh. Convergence in this context means that further refining the mesh did not significantly change the results, and the displacement values reached a stable and consistent behavior. Thus, Mesh D, with 500 elements, was deemed appropriate for accurately capturing the behavior of the cement and casing interface during pushout loading.

5.5. Results

5.5.1. Conventional class G sections

In order to evaluate the behavior of conventional class G cement short sections, three FE models were developed for three tested sections (named as sections ‘C’, ‘D’, and ‘E’). The pushout load-displacement curves for each section were analyzed and compared to the experimental pushout tests conducted in the laboratory and reported with more details in Congro et al. [34]. Figure 5.5 illustrates the pushout load-displacement curve for section ‘C’, Figure 5.6 for section ‘D’, and Figure 5.7 for section ‘E’. The input parameters used in these simulations were derived from Table 5.1, Table 5.2 and Table 5.4.

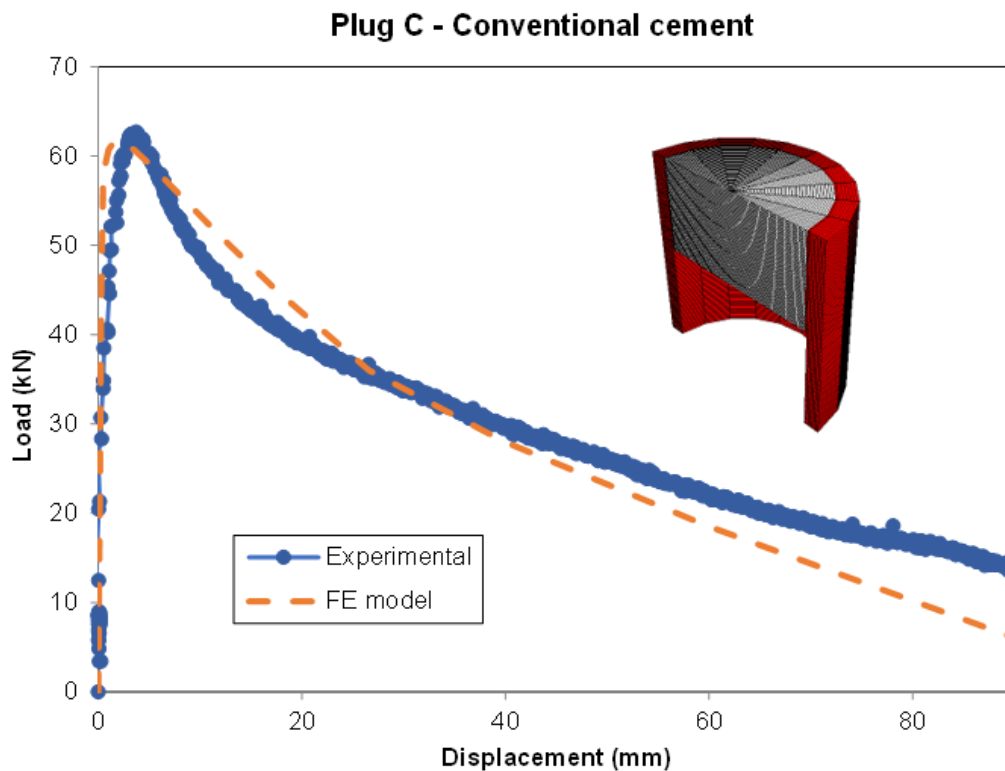


Figure 5.5 – Pushout load-displacement experimental and numerical results for section ‘C’ conventional cement.

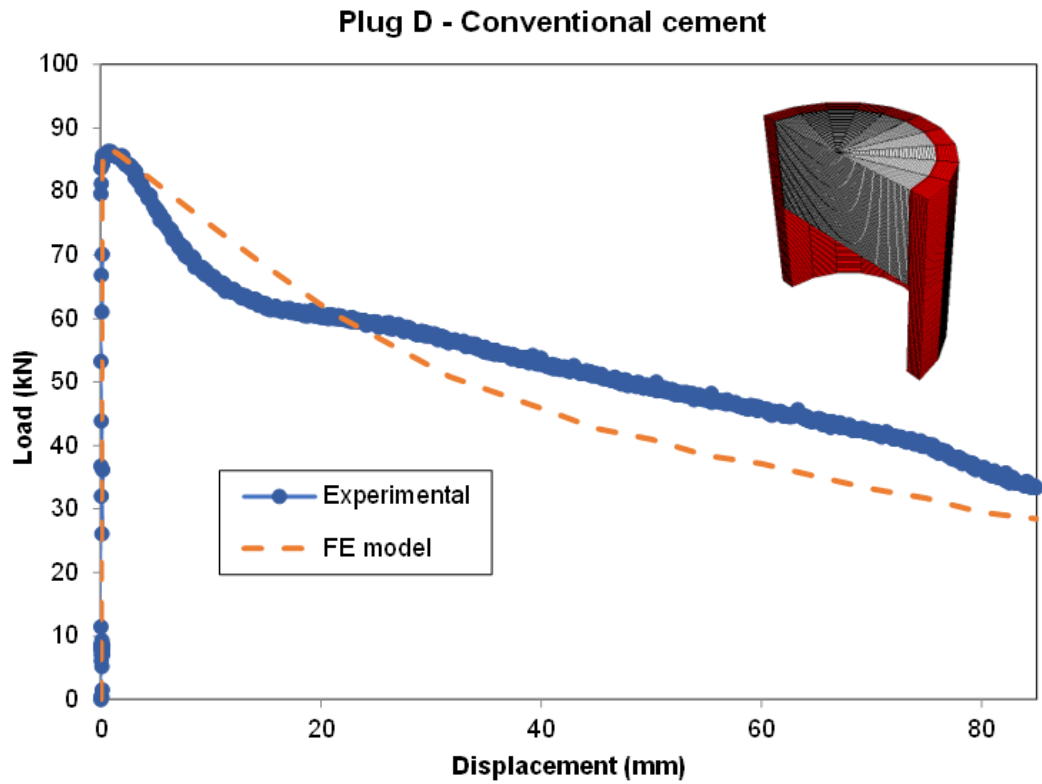


Figure 5.6 – Pushout load-displacement experimental and numerical results for section ‘D’ conventional cement.

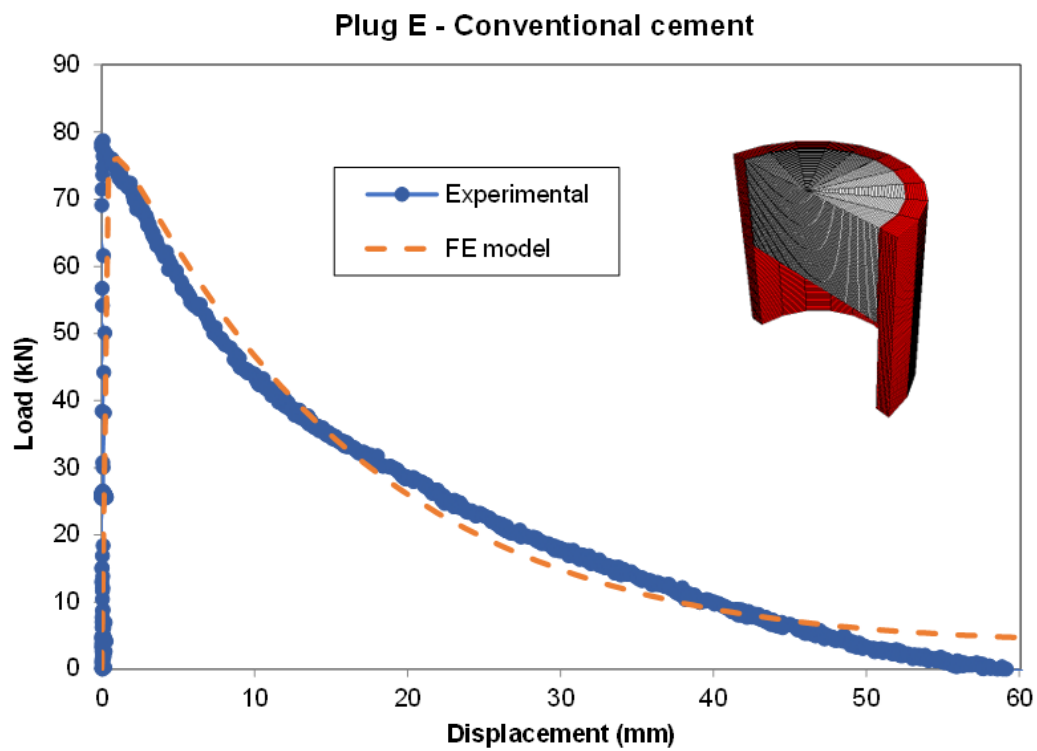


Figure 5.7 – Pushout load-displacement experimental and numerical results for section ‘E’ conventional cement.

The results obtained from the FE models exhibit good agreement with the experimental pushout tests. Notably, the peak loads of the FE models closely match the peak loads obtained in the laboratory experiments. This alignment between the experimental and numerical results indicates the effectiveness and accuracy of the FE model in capturing the behavior of the conventional class G cement sections. Figure 5.5 shows an initial linear increase in load with displacement, followed by a more gradual increase until reaching the peak load.

Similarly, Figure 5.6 depicts the pushout load-displacement curve for section 'D'. The FE model effectively replicates the experimental trend, displaying a comparable linear increase in load until reaching the peak load. Finally, Figure 5.7 illustrates the pushout load-displacement curve for section 'E'.

Figure 5.8 confirms the evolution of section damage based on a plastic flag (0 for intact material and 1 for plasticized material). Figure 5.9 presents the plastic strain evolution for section 'C' before adhesion loss at the interface for distinct levels of displacement. Plastic strains are concentrated in the vicinity of the casing and evolve from top to bottom of the section.

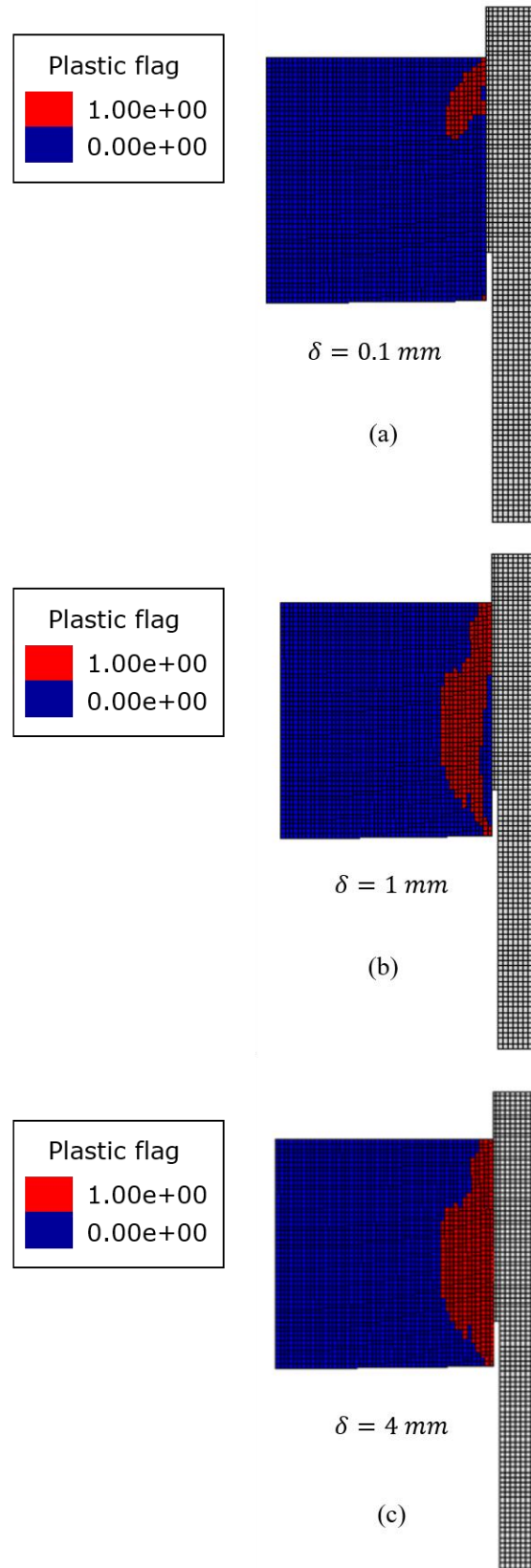


Figure 5.8 – Plastic flag for section ‘C’: (a) $\delta = 0.1 \text{ mm}$; (b) $\delta = 1 \text{ mm}$; (c) $\delta = 4 \text{ mm}$.

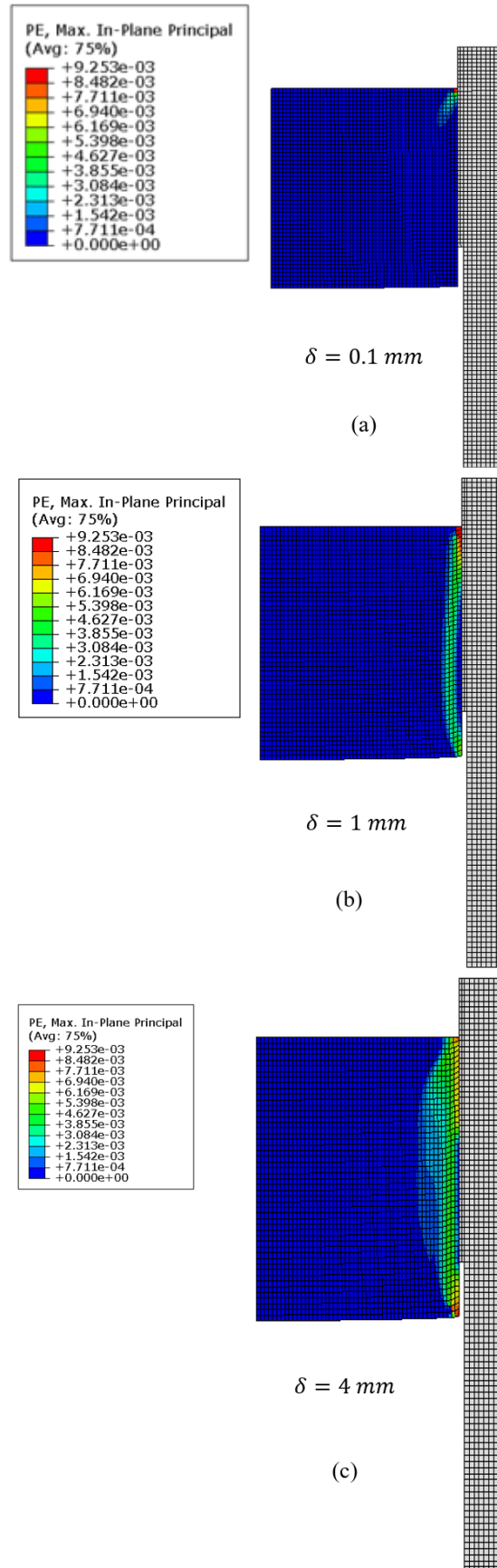


Figure 5.9 – Plastic strain evolution for section 'C': (a) $\delta = 0.1 \text{ mm}$; (b) $\delta = 1 \text{ mm}$; (c) $\delta = 4 \text{ mm}$.

5.5.2. Expanding cement sections

The same approach is carried out for the expanding cement sections. The input parameters used in these simulations were derived from Table 5.1, Table 5.2 and Table 5.5. The expansion effect physically observed in the experimental tests is captured by the model through calibration of the expansive cement and interface parameters. In a similar way, the pushout load-displacement curves given by the model are also in close agreement with the experimental response carried out at the laboratory, including the maximum pushout load (Figure 5.10 and Figure 5.11).

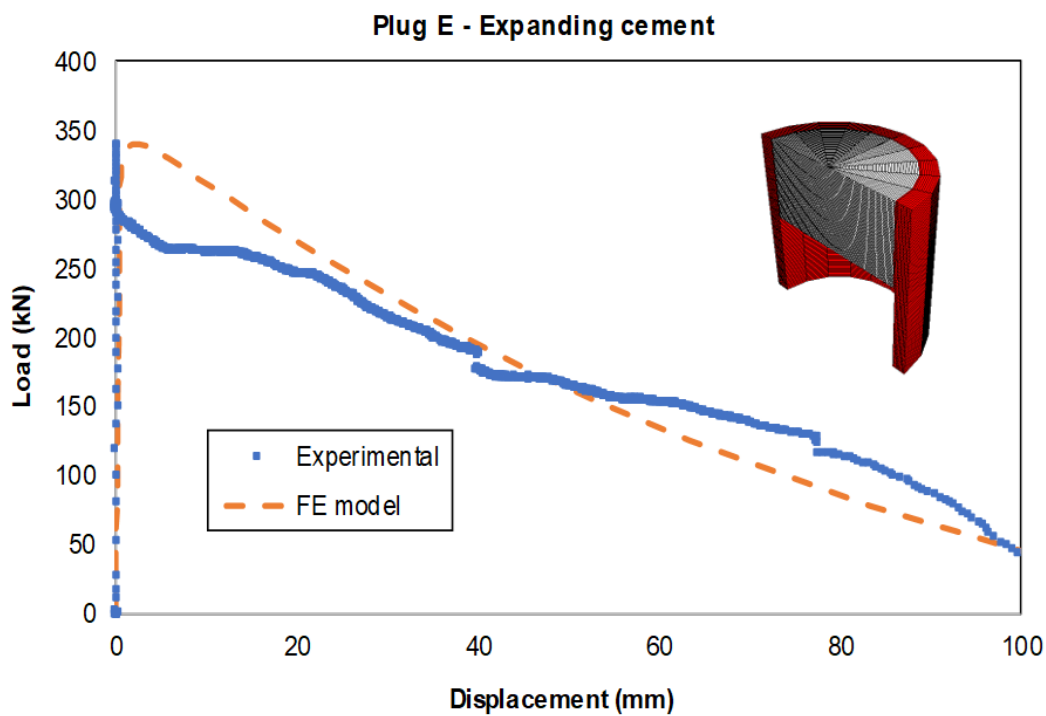


Figure 5.10 – Pushout load-displacement experimental and numerical results for section ‘E’ expanding cement.

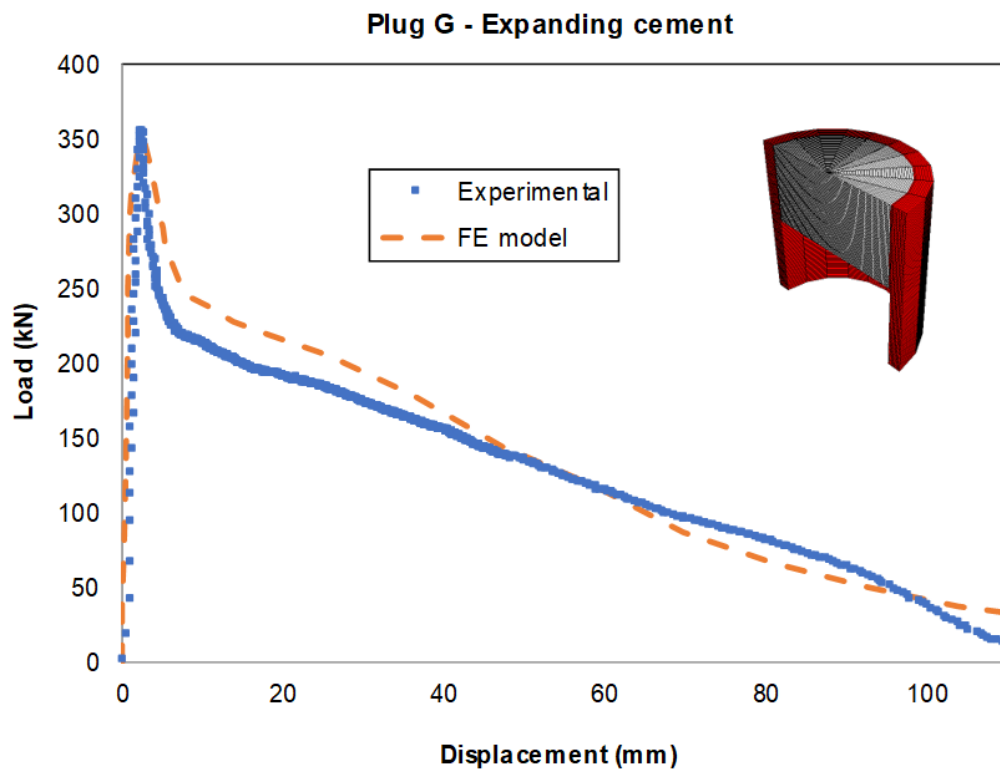


Figure 5.11 – Pushout load-displacement experimental and numerical results for section ‘G’ expanding cement.

Figure 5.12 and Figure 5.13 present the plastic strain for section ‘E’ at the interface for distinct levels of displacement before loss of adhesion and the damage evolution, respectively. The equivalent plastic deformation shows smaller values than those of conventional cement. In terms of the level of damage, it is possible to observe that the damaged region (in red color) is narrower for the expansive cement section, affecting only the casing-cement interface surroundings. These significant results demonstrate the novelty of the analyses developed in this chapter since these applications and models have not yet been widely explored by other authors in the literature.

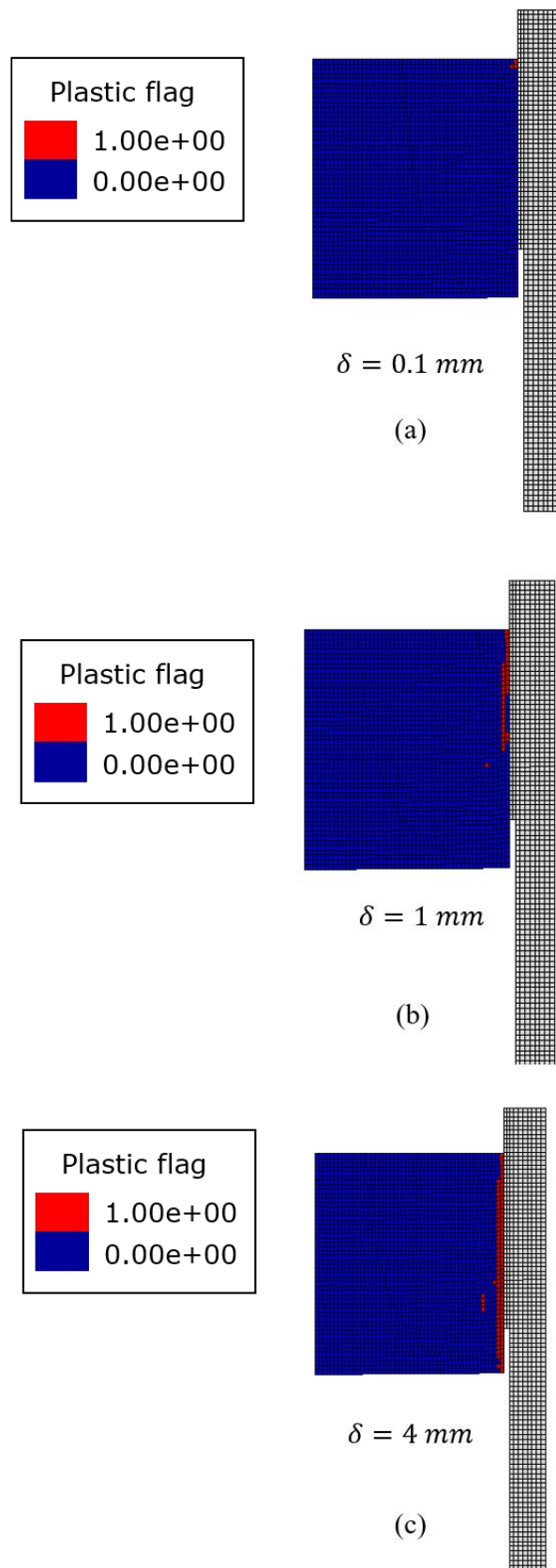


Figure 5.12 – Plastic flag for section ‘E’: (a) $\delta = 0.1 \text{ mm}$; (b) $\delta = 1 \text{ mm}$; (c) $\delta = 4 \text{ mm}$.

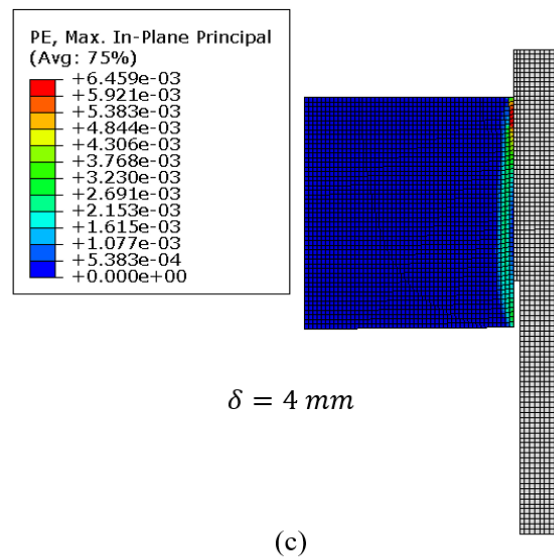
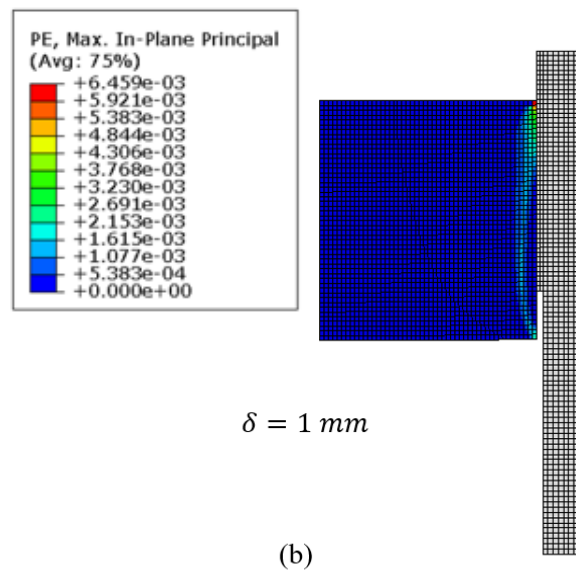
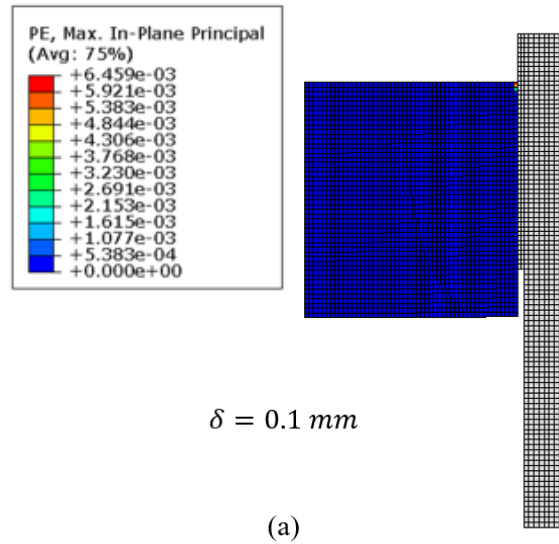


Figure 5.13 – Plastic strain evolution for section ‘E’: (a) $\delta = 0.1 \text{ mm}$; (b) $\delta = 1 \text{ mm}$; (c) $\delta = 4 \text{ mm}$

Furthermore, the results demonstrated that expanding cement samples exhibited higher pushout loads than conventional sections, indicating potential for improved performance in well casing applications. The calibration of contact parameters in the FE models highlighted the significance of the friction coefficient, with values ranging from 0.3 to 0.5 for conventional class G cement sections. The damage initiation separation and the cohesive stiffness parameter emerged as the most relevant parameters impacting the maximum pushout load in the FE models.

Finally, Figure 5.14 presents the load-displacement curve for section 'C' of conventional class G cement and the evolution of plastic deformations associated with each stage of the pushout test. In addition, Figure 5.15 presents the same comparison for the expansive cement section 'E'.

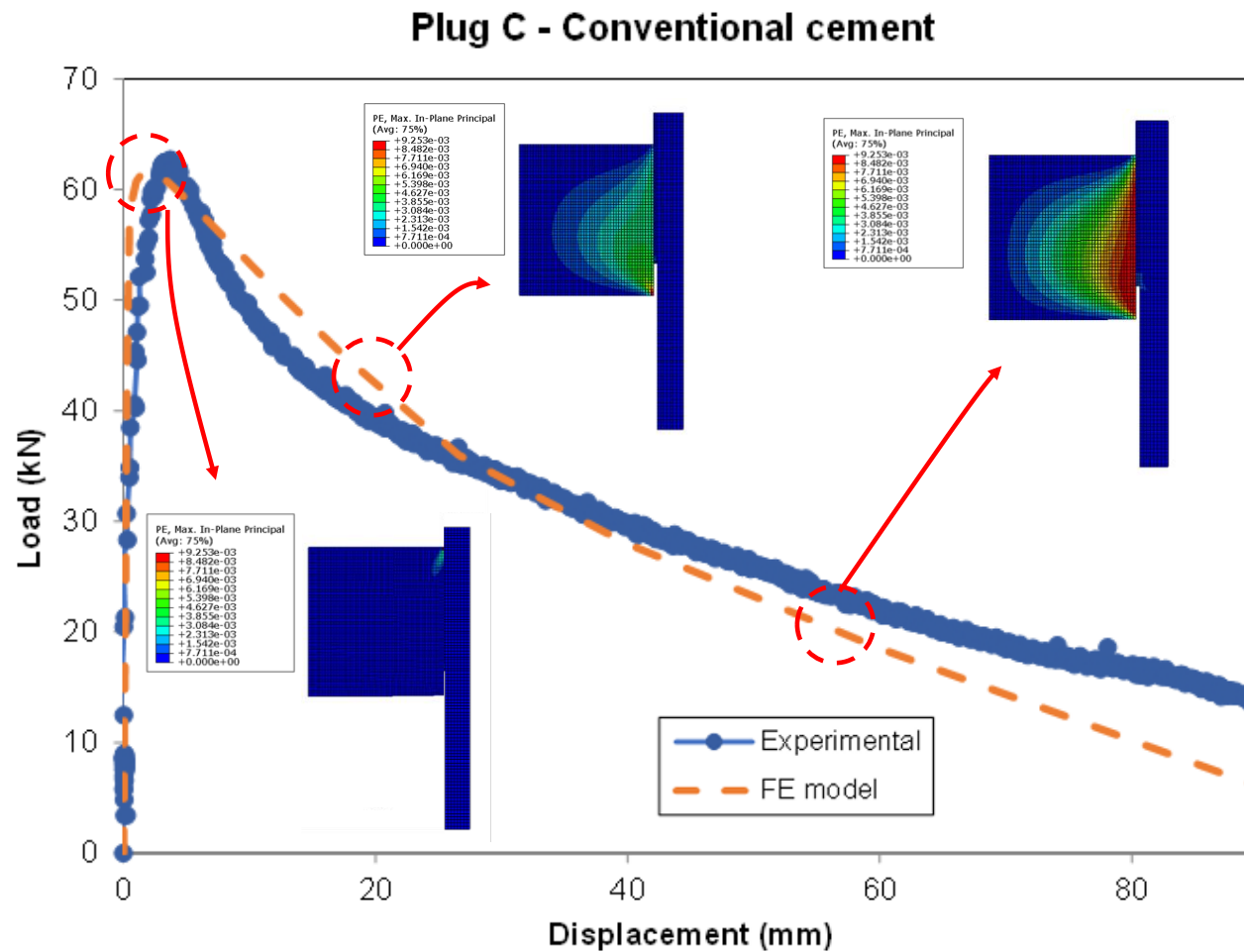


Figure 5.14 – Plastic strains associated with the pushout load-displacement curve for conventional cement section ‘C’.

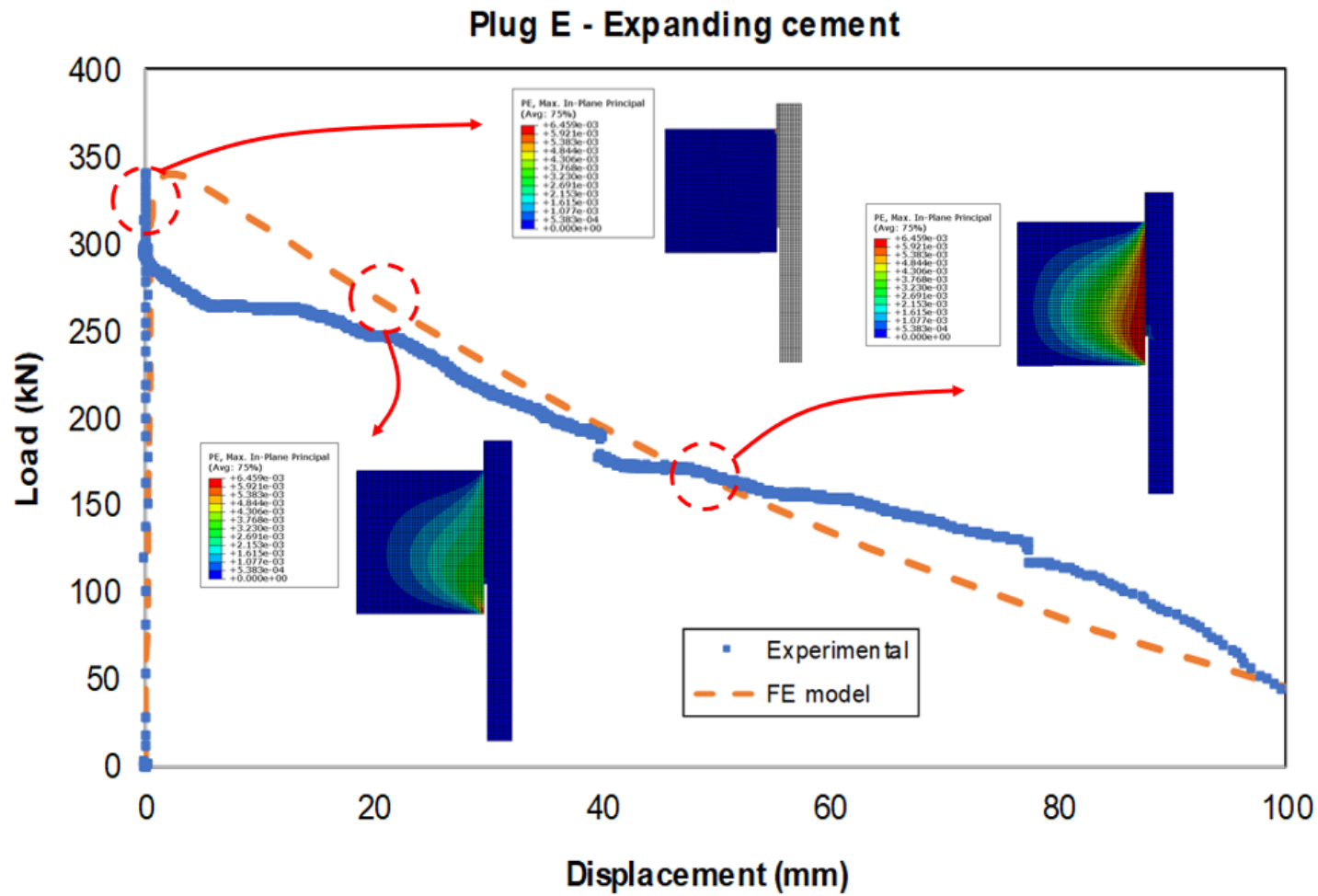


Figure 5.15 – Plastic strains associated with the pushout load-displacement curve for expansive cement section ‘E’.

6

Conclusions and suggestions for future works

6.1.

Conclusions

This doctoral thesis contributes significantly to understanding the mechanical behavior and damage mechanisms at the interface of cementitious materials, particularly in the context of fiber-reinforced composites used in the construction and O&G industries. The research addresses a critical gap in the literature, proposing numerical models for interfacial debonding and damage evolution, considering distinct cement matrix types and steel fiber geometries.

The experimental program developed a novel pullout test setup to investigate straight and hooked-end steel fibers embedded in two distinct types of cement matrix. The tests provided crucial insights into the influence of fiber geometry, matrix strength, and air voids on the pullout behavior. MicroCT analyses offered a detailed view of the damage mechanisms, revealing microcracks at the fiber/matrix interface and showcasing the impact of matrix consolidation on pullout performance.

Regarding the experimental tests, a slightly higher maximum pullout load is observed for Matrix B than for Matrix A's response, showing that the fiber geometry also influences the pullout behavior. The straight geometry facilitates the pullout process and induces a lower concentration of damage along its length, resulting in lower pullout loads. For the hooked-end fiber, the maximum pullout loads are much higher than in the straight fiber scenario due to the higher strength of Matrix B. In addition, the hook and its progressive deformation throughout the test create greater difficulty for the fiber to initiate its debonding/pullout process, justifying the higher load values. Pullout energy (*i.e.*, the area under the pullout curve) is also higher for the hooked-end steel fiber in Matrix B. A wider concentration of damage and cracks is observed, especially near the fiber hook, which is subject to significant levels of deformation. In this sense, in all observed configurations of the pullout test, the fiber undergoes deformation before initiating the debonding process and subsequent pullout from the cement matrix.

The numerical models, employing concrete damage plasticity and a surface-based cohesive approach, demonstrated good agreement with experimental pullout load-displacement curves. The models successfully captured the concentration of damage in specific regions, such as the upper region in straight fiber scenarios and along the fiber length, particularly near the hook, in hooked-end fiber configurations. In the straight fiber models, the damage regions are concentrated in the upper region of the specimen, where matrix spalling is frequently observed. In the hooked-end fiber models, damage is wider along the fiber length, concentrating high levels of damage and deformations in the fiber hook. The numerical model exhibits a higher level of damage for this configuration, attributed to the higher strength of Matrix B and increased fiber anchorage due to the presence of the hook. Sensitivity analyses underscored the importance of calibrating interface parameters for accurate predictions, with the friction coefficient, damage initiation parameter, and tangential cohesive stiffness proving to be most influential. The methodology proved to be robust, offering valuable insights into the pullout behavior of cement composite materials.

For the interfacial debonding considering the well integrity application in P&A scenarios, finite element models using the same methodology from the pullout tests were considered to investigate the bond strength and the behavior of conventional and expanding cement sections in pushout tests. The calibration of contact parameters in the FE models highlighted the importance of the friction coefficient parameter, with values ranging from 0.3 to 0.5 for conventional class G cement sections. The damage initiation separation and the cohesive stiffness parameter emerged as the most relevant interface variables impacting the maximum pushout load in the FE models. The computational results demonstrated excellent agreement with the experimental response for conventional and expanding cement sections, validating their reliability and accuracy. Regarding damage evolution patterns, the damaged region in standard cement sections is more extensive and shows higher strains than the expansive cement.

Some limitations regarding the methodology for both applications include calibrating the interface numerical parameters with the experimental pullout/pushout response, for which the solution is not unique. This fact poses a challenge, as various combinations of interface parameters may generate results closely resembling the experimental curve. While typical values from literature are

used for numerical parameters, such as friction coefficients, many contact parameters lack direct physical interpretation. Therefore, the calibration against experimental data prioritizes parameter sets that fit the experimental curve and demonstrate consistency with physical principles and trends observed in related studies. Calibrations considering more experimental results can be conducted to corroborate the ranges of contact parameters obtained from the experiments and models developed in this thesis.

6.2. Suggestions for future works

This thesis aimed to gain more insight into the cement interface's damage and stress transfer mechanisms, considering distinct applications. This goal was achieved by developing a workflow using numerical models and laboratory experiments. There are several possibilities for future works when working with experimental and numerical investigations regarding cement composite materials. These suggestions are listed considering three major groups/areas: improvements in the experimental workflow, improvements in the mathematical model, and applications to other material types.

6.2.1. Improvements in the experimental workflow

(i) Perform in-situ microCT pullout tests: This suggestion aims to enhance the experimental workflow by reducing execution time. By conducting pullout experiments inside the microCT, researchers can observe real-time fiber behavior without the need for separate imaging processes, thus streamlining data acquisition and analysis;

(ii) Automate microcrack detection using AI algorithms: Automating the process of microcrack detection in microCT images with AI algorithms enables efficient and accurate identification of microcracks. This procedure saves significant time in data analysis, allowing researchers to focus on interpreting results rather than manual image processing;

(iii) Analyze and compare the propagation process of microcracks using alternative experimental techniques, such as optical microscopy or acoustic

emission: The comparison between these techniques and the images obtained through the microCT can provide complementary insights into the interface mechanisms studied in this thesis;

(iv) Perform microCT tests with conventional and expansive class G cement samples: The main goal is to detect damage in the samples and qualitatively validate this information with the numerical model results obtained in this thesis.

(v) Investigate the pullout mechanisms considering distinct steel fiber inclinations.

6.2.2. Improvements in the mathematical model

(i) Incorporate matrix shrinkage hypothesis into the numerical pullout models: by integrating the hypothesis of matrix shrinkage, researchers can more accurately simulate the cement matrix behavior. This enhancement provides insights into how matrix properties affect fiber/matrix interactions, contributing to a more comprehensive understanding of pullout mechanisms;

(ii) Incorporate the chemical effects of fiber treatment in the numerical models: this suggestion focuses on exploring the impact of fiber treatment on pullout behavior. By integrating this information into finite element models, researchers can assess the efficiency of fiber treatments and optimize them for improved performance in cement composite materials.

(iii) Incorporate the effects of defects introduced by poor consolidation into the numerical models: This suggestion aims to deepen the investigations into the effect of poorly consolidated cementitious matrices on pullout behavior and damage mapping.

6.2.3. Applications to other material types

(i) Apply the developed workflow to other types of cement matrixes or fiber types and geometries: The application of the developed workflow expands the scope of the research, investigating stress transfer mechanisms in various matrix compositions, fiber types (e.g., polypropylene, natural fibers) and geometries (e.g., twisted, corrugated, undulated). Therefore, it provides insights into material behavior beyond the matrix compositions and fiber geometries studied in this thesis.

References

- [1] A. A. Abdul-Razzak and A. A. Mohammed Ali, "Influence of cracked concrete models on the nonlinear analysis of High Strength Steel Fibre Reinforced Concrete corbels," *Compos. Struct.*, vol. 93, no. 9, pp. 2277–2287, Aug. 2011, doi: 10.1016/j.compstruct.2011.03.016.
- [2] S.-J. Lee and J.-P. Won, "Flexural behavior of precast reinforced concrete composite members reinforced with structural nano-synthetic and steel fibers," *Compos. Struct.*, vol. 118, pp. 571–579, Dec. 2014, doi: 10.1016/j.compstruct.2014.07.042.
- [3] B. Bendtsen and J. G. Sanjayan, "Assessment of shear capacity methods of steel fiber reinforced concrete beams using full scale prestressed bridge beams," *Mater. Struct.*, vol. 48, no. 11, pp. 3473–3483, Nov. 2015, doi: 10.1617/s11527-014-0415-3.
- [4] Z. Dai, F. Shi, B. Zhang, M. Li, and Z. Zhang, "Effect of sizing on carbon fiber surface properties and fibers/epoxy interfacial adhesion," *Appl. Surf. Sci.*, vol. 257, no. 15, pp. 6980–6985, May 2011, doi: 10.1016/j.apsusc.2011.03.047.
- [5] J. Feng, W. W. Sun, X. M. Wang, and X. Y. Shi, "Mechanical analyses of hooked fiber pullout performance in ultra-high-performance concrete," *Constr. Build. Mater.*, vol. 69, pp. 403–410, Oct. 2014, doi: 10.1016/j.conbuildmat.2014.07.049.
- [6] S. Abdallah, M. Fan, X. Zhou, and S. Le Geyt, "Anchorage Effects of Various Steel Fibre Architectures for Concrete Reinforcement," *Int. J. Concr. Struct. Mater.*, vol. 10, no. 3, pp. 325–335, Sep. 2016, doi: 10.1007/s40069-016-0148-5.
- [7] S. Abdallah and M. Fan, "Anchorage mechanisms of novel geometrical hooked-end steel fibres," *Mater. Struct.*, vol. 50, no. 2, p. 139, Apr. 2017, doi: 10.1617/s11527-016-0991-5.
- [8] Q. Wu, M. Li, Y. Gu, S. Wang, L. Yao, and Z. Zhang, "Effect of sizing on interfacial adhesion of commercial high strength carbon fiber-reinforced resin composites," *Polym. Compos.*, vol. 37, no. 1, pp. 254–261, Jan. 2016,

- doi: 10.1002/pc.23176.
- [9] B. A. Budiman, F. Triawan, F. Adziman, and I. P. Nurprasetio, “Modeling of stress transfer behavior in fiber-matrix composite under axial and transverse loadings,” *Compos. Interfaces*, vol. 24, no. 7, pp. 677–690, Sep. 2017, doi: 10.1080/09276440.2017.1262666.
- [10] Y. Yu, B. Zhang, Z. Tang, and G. Qi, “Stress transfer analysis of unidirectional composites with randomly distributed fibers using finite element method,” *Compos. Part B Eng.*, vol. 69, pp. 278–285, Feb. 2015, doi: 10.1016/j.compositesb.2014.09.035.
- [11] Z. Yang, B. Zhang, L. Zhao, and X. Sun, “Stress transfer around a broken fiber in unidirectional fiber-reinforced composites considering matrix damage evolution and interface slipping,” *Sci. China Physics, Mech. Astron.*, vol. 54, no. 2, pp. 296–302, Feb. 2011, doi: 10.1007/s11433-010-4148-1.
- [12] M. Congro, “Modelagem Numérica do Comportamento Mecânico de Materiais Compósitos Cimentícios em uma Abordagem Multiescala,” Pontifícia Universidade Católica do Rio de Janeiro, Rio de Janeiro, 2020.
- [13] E. V. Pereira, “Influência de Fibras de Aço no Comportamento Mecânico e nos Mecanismos de Fissuração de Concretos Autoadensáveis,” Pontifical Catholic University of Rio de Janeiro, 2017.
- [14] P. H. T. T. Silveira, “Estudo do concreto reforçado com fibras de aço e sua aplicação em dormentes ferroviários.,” Pontifical Catholic University of Rio de Janeiro, 2018.
- [15] R. de S. Castoldi, “Influence of surface modifications on sisal fiber durability and interface bond towards cement-based matrices,” Pontifícia Universidade Católica do Rio de Janeiro, Rio de Janeiro, Brazil, 2023.
- [16] I. Barbosa da Silva Junior, “Propriedades mecânicas e fluência de compósitos cimentícios têxteis reforçados com fibras de sisal,” Pontifícia Universidade Católica do Rio de Janeiro, Rio de Janeiro, Brazil, 2020.
- [17] L. O. de Souza, “Mecanismos de fissuração e autocicatrização de compósitos cimentícios reforçados com tecido de curauá,” Pontifícia Universidade Católica do Rio de Janeiro, Rio de Janeiro, Brazil, 2017.
- [18] F. P. Teixeira, “Mechanical Behavior of Natural Fiber Cement Based Composites for Structural Applications,” Pontifical Catholic University of Rio de Janeiro, 2020.

- [19] C. Mejia, D. Roehl, J. Rueda, and R. Quevedo, "A new approach for modeling three-dimensional fractured reservoirs with embedded complex fracture networks," *Comput. Geotech.*, vol. 130, no. December 2020, p. 103928, 2021, doi: 10.1016/j.compgeo.2020.103928.
- [20] E. C. Mejia Sanchez, J. A. Rueda Cordero, and D. Roehl, "Numerical simulation of three-dimensional fracture interaction," *Comput. Geotech.*, vol. 122, no. March, p. 103528, 2020, doi: 10.1016/j.compgeo.2020.103528.
- [21] M. Congro, C. M. Sanchez, and D. Roehl, "XFEM and Interface Element Models Applied to Fracture of Fiber Reinforced Concrete Beams," in *XXXVIII CILAMCE - Ibero-Latin American Congress on Computational Methods in Engineering*, 2017, no. November, doi: 10.20906/CPS/CILAMCE2017-0195.
- [22] M. Congro, F. L. G. Pereira, L. M. S. Souza, and D. Roehl, "A Hybrid Parameter Homogenization Workflow for Assessing the Mechanical Behavior of a Steel Fiber-Reinforced Concrete," *Mech. Compos. Mater.*, Jan. 2024, doi: 10.1007/s11029-023-10163-1.
- [23] M. Congro, E. C. M. Sanchez, D. Roehl, and E. Marangon, "Fracture modeling of fiber reinforced concrete in a multiscale approach," *Compos. Part B Eng.*, vol. 174, p. 106958, Oct. 2019, doi: 10.1016/j.compositesb.2019.106958.
- [24] G. T. Caravello, M. Congro, and D. Roehl, "Numerical modeling of the flexural response of ultrahigh performance fiber-reinforced concrete (UHPFRC) using the XFEM fracture model Numerical Modeling of the Elastoplastic Flexural Response of Ultrahigh Performance of Fiber Reinforced Concrete (UHPF," in *Proceedings of XLIII CILAMCE*, 2022, no. November.
- [25] M. Congro, C. Mejía, and D. Roehl, "Probabilistic Assessment of the Load Capacity of Fiber Reinforced Concrete," no. October, pp. 81–88, 2018, doi: 10.21452/bccm4.2018.02.05.
- [26] L. Zanotto, M. Congro, and D. Roehl, "Damage Evolution Investigation in Steel and Polypropylene Fiber Reinforced Con," in *XLI CILAMCE – Ibero-Latin American Congress on Computational Methods in Engineering*, 2020, no. November.
- [27] M. Congro, D. Roehl, and C. Mejia, "Mesoscale computational modeling of

- the mechanical behavior of cement composite materials,” *Compos. Struct.*, vol. 257, p. 113137, Feb. 2021, doi: 10.1016/j.compstruct.2020.113137.
- [28] M. Congro, D. Roehl, and E. C. M. Sanchez, “Computational Mesoscale Modeling for the Mechanical Behavior of Fiber Reinforced Concrete,” 2022, pp. 357–364.
- [29] L. F. Santos, M. Congro, C. Mejía, and D. Roehl, “Flexural response of polypropylene fiber reinforced concrete using the fiber composite mode,” in *Proceedings of 42nd Ibero-Latin-American Congress on Computational Methods in Engineering (XLII CILAMCE)*, 2021, no. November, pp. 1–7.
- [30] M. Congro, V. M. de A. Monteiro, A. L. T. Brandão, B. F. dos Santos, D. Roehl, and F. de A. Silva, “Prediction of the residual flexural strength of fiber reinforced concrete using artificial neural networks,” *Constr. Build. Mater.*, vol. 303, p. 124502, Oct. 2021, doi: 10.1016/j.conbuildmat.2021.124502.
- [31] M. Congro, V. Moreira de Alencar Monteiro, F. de Andrade Silva, D. Roehl, and A. L. T. Brandão, “A novel hybrid model to design fiber-reinforced shotcrete for tunnel linings,” *Tunn. Undergr. Sp. Technol.*, vol. 132, p. 104881, Feb. 2023, doi: 10.1016/j.tust.2022.104881.
- [32] M. Congro, F. Lins, G. Pereira, L. M. S. Souza, D. Roehl, and F. L. G. Pereira, “Parameter Sensitivity Analysis in Steel Fiber Reinforced Concrete,” in *Proceedings of XL CILAMCE*, 2019, pp. 1–14, [Online]. Available: <https://www.researchgate.net/publication/337291060>.
- [33] M. Congro and D. Roehl, “Numerical investigation of the pullout behavior of steel fiber-reinforced concrete,” in *Proceedings of the XLIV Ibero Latin-American Congress on Computational Methods in Engineering*, 2023, p. 8.
- [34] M. Congro, H. J. Skadsem, K. Béltran-Jiménez, and D. Roehl, “Experimental and numerical study on the pushout shear strength for conventional and expanding cement-casing sections for well integrity,” *Geoenergy Sci. Eng.*, 2024.
- [35] A. E. Naaman, “Fiber reinforced concrete: five decades of progress,” 2018, pp. 35–56, doi: 10.21452/bccm4.2018.02.01.
- [36] A. Bentur and S. Mindess, *Fibre Reinforced Cementitious Composites*, 2nd ed. New York: Taylor & Francis, 2007.
- [37] A. M. Neville, *Properties of concrete*, vol. 1, no. 5. 2011.

- [38] S. C. Lee, J. H. Oh, and J. Y. Cho, “Compressive behavior of fiber-reinforced concrete with end-hooked steel fibers,” *Materials (Basel)*, vol. 8, no. 4, pp. 1442–1458, 2015, doi: 10.3390/ma8041442.
- [39] P. K. Mehta and P. J. M. Monteiro, *Concrete: Microstructure, Properties and Materials*, 1st ed., vol. 1. McGraw Hill, 2001.
- [40] L. M. S. Souza, “Estudo de hidratação e nanoindentação de pastas de cinza da casca de arroz e cinza do bagaço de cana-de-açúcar com hidróxido de cálcio,” Universidade Federal do Rio de Janeiro, 2011.
- [41] F. de A. Silva, N. Chawla, and R. D. de T. Filho, “Tensile behavior of high performance natural (sisal) fibers,” *Compos. Sci. Technol.*, vol. 68, no. 15–16, pp. 3438–3443, 2008, doi: 10.1016/j.compscitech.2008.10.001.
- [42] C. Sujivorakul, “Modeling bond components of deformed steel fibers in FRC composites,” in *International Workshop High Performance Fiber Reinforced Cement Composites*, 2003, pp. 35–48.
- [43] A. E. Naaman and H. Najm, “Bond-slip mechanisms of steel fibers in concrete,” *ACI Mater. J.*, vol. 88, no. 2, pp. 135–145, 1991.
- [44] A. D. Figueiredo, “Concreto com Fibras de Aço,” São Paulo, 2000.
- [45] P. Rossi, P. Acker, and Y. Malier, “Effect of steel fibres at two different stages: The material and the structure,” *Mater. Struct.*, vol. 20, no. 6, pp. 436–439, Nov. 1987, doi: 10.1007/BF02472494.
- [46] A. E. Naaman and S. P. Shah, “Pull-Out Mechanism in Steel Fiber-Reinforced Concrete,” *J. Struct. Div.*, vol. 102, no. 8, pp. 1537–1548, Aug. 1976, doi: 10.1061/JSDEAG.0004409.
- [47] C. DiFrancia, T. C. Ward, and R. O. Claus, “The single-fibre pull-out test. 1: Review and interpretation,” *Compos. Part A Appl. Sci. Manuf.*, vol. 27, no. 8, pp. 597–612, Jan. 1996, doi: 10.1016/1359-835X(95)00069-E.
- [48] V. M. do C. F. Cunha, “Steel fibre reinforced self-compacting concrete (from micro-mechanics to composite behaviour),” University of Minho, 2010.
- [49] V. C. Li and H. Stang, “Interface property characterization and strengthening mechanisms in fiber reinforced cement based composites,” *Adv. Cem. Based Mater.*, vol. 6, no. 1, pp. 1–20, Jun. 1997, doi: 10.1016/S1065-7355(97)90001-8.
- [50] J. R. Homrich and A. E. Naaman, “Stress-Strain Properties of SIFCON in Compression,” in *International Concrete Abstracts Portal*, 1987, pp. 283–

304.

- [51] M. Maage, “Interaction between steel fibers and cement based matrixes,” *Matériaux Constr.*, vol. 10, no. 5, pp. 297–301, Sep. 1977, doi: 10.1007/BF02478831.
- [52] P. Bartos, “Review paper: Bond in fibre reinforced cements and concretes,” *Int. J. Cem. Compos. Light. Concr.*, vol. 3, no. 3, pp. 159–177, Aug. 1981, doi: 10.1016/0262-5075(81)90049-X.
- [53] R. J. Gray, “Analysis of the effect of embedded fibre length on fibre debonding and pull-out from an elastic matrix,” *J. Mater. Sci.*, vol. 19, no. 3, pp. 861–870, Mar. 1984, doi: 10.1007/BF00540456.
- [54] C. S. Chin and R. Y. Xiao, “Experimental and Nonlinear Finite Element Analysis of Fiber-Cementitious Matrix Bond-Slip Mechanism,” 2012, pp. 145–152.
- [55] C. Sujivorakul, A. M. Waas, and A. E. Naaman, “Pullout Response of a Smooth Fiber with an End Anchorage,” *J. Eng. Mech.*, vol. 126, no. 9, pp. 986–993, Sep. 2000, doi: 10.1061/(ASCE)0733-9399(2000)126:9(986).
- [56] A. Casanova, L. Jason, and L. Davenne, “Bond slip model for the simulation of reinforced concrete structures,” *Eng. Struct.*, vol. 39, pp. 66–78, Jun. 2012, doi: 10.1016/j.engstruct.2012.02.007.
- [57] A. E. Naaman, G. Namur, H. Najm, and J. Alwan, “Bond mechanisms in fiber-reinforced cement-based composites,” Ann Arbor, MI, 1989.
- [58] S. Abdallah, M. Fan, and D. W. A. Rees, “Bonding Mechanisms and Strength of Steel Fiber–Reinforced Cementitious Composites: Overview,” *J. Mater. Civ. Eng.*, vol. 30, no. 3, p. 04018001, Mar. 2018, doi: 10.1061/(ASCE)MT.1943-5533.0002154.
- [59] G. Chanvillard, “Analyse expérimentale et modélisation micromécanique du comportement des fibres d’acier tréfilées ancrées dans une matrice cimentaire,” Université de Sherbrooke, 1992.
- [60] N. Banthia and J.-F. Trottier, “Concrete Reinforced with Deformed Steel Fibers, Part I: Bond-Slip Mechanisms,” *ACI Mater. J.*, vol. 91, no. 5, pp. 435–446, 1994.
- [61] M. Jamee, F. J. Alaei, and E. Zeighami, “Effect of matrix strength on pull-out behaviour of hooked steel fibre-reinforced cementitious composites,” *Can. J. Civ. Eng.*, vol. 49, no. 11, pp. 1703–1713, Nov. 2022, doi:

- 10.1139/cjce-2021-0421.
- [62] F. Isla, G. Ruano, and B. Luccioni, “Analysis of steel fibers pull-out. Experimental study,” *Constr. Build. Mater.*, vol. 100, pp. 183–193, Dec. 2015, doi: 10.1016/j.conbuildmat.2015.09.034.
- [63] T. Abu-Lebdeh, S. Hamoush, W. Heard, and B. Zornig, “Effect of matrix strength on pullout behavior of steel fiber reinforced very-high strength concrete composites,” *Constr. Build. Mater.*, vol. 25, no. 1, pp. 39–46, Jan. 2011, doi: 10.1016/j.conbuildmat.2010.06.059.
- [64] D.-Y. Yoo and S. Kim, “Comparative pullout behavior of half-hooked and commercial steel fibers embedded in UHPC under static and impact loads,” *Cem. Concr. Compos.*, vol. 97, pp. 89–106, Mar. 2019, doi: 10.1016/j.cemconcomp.2018.12.023.
- [65] Z. Wu, K. H. Khayat, and C. Shi, “How do fiber shape and matrix composition affect fiber pullout behavior and flexural properties of UHPC?,” *Cem. Concr. Compos.*, vol. 90, pp. 193–201, Jul. 2018, doi: 10.1016/j.cemconcomp.2018.03.021.
- [66] M. Ju, Y. Park, and C. Park, “Cracking control comparison in the specifications of serviceability in cracking for FRP reinforced concrete beams,” *Compos. Struct.*, vol. 182, pp. 674–684, Dec. 2017, doi: 10.1016/j.compstruct.2017.09.016.
- [67] Y. S. Jenq and S. P. Shah, “Crack Propagation in Fiber-Reinforced Concrete,” *J. Struct. Eng.*, vol. 112, no. 1, pp. 19–34, Jan. 1986, doi: 10.1061/(ASCE)0733-9445(1986)112:1(19).
- [68] M. F. Arif, N. Saintier, F. Meraghni, J. Fitoussi, Y. Chemisky, and G. Robert, “Multiscale fatigue damage characterization in short glass fiber reinforced polyamide-66,” *Compos. Part B Eng.*, vol. 61, pp. 55–65, May 2014, doi: 10.1016/j.compositesb.2014.01.019.
- [69] M. F. Arif, F. Meraghni, Y. Chemisky, N. Despringre, and G. Robert, “In situ damage mechanisms investigation of PA66/GF30 composite: Effect of relative humidity,” *Compos. Part B Eng.*, vol. 58, pp. 487–495, Mar. 2014, doi: 10.1016/j.compositesb.2013.11.001.
- [70] A. BERNASCONI, P. DAVOLI, A. BASILE, and A. FILIPPI, “Effect of fibre orientation on the fatigue behaviour of a short glass fibre reinforced polyamide-6,” *Int. J. Fatigue*, vol. 29, no. 2, pp. 199–208, Feb. 2007, doi:

- 10.1016/j.ijfatigue.2006.04.001.
- [71] N. Sato, T. Kurauchi, S. Sato, and O. Kamigaito, “Microfailure behaviour of randomly dispersed short fibre reinforced thermoplastic composites obtained by direct SEM observation,” *J. Mater. Sci.*, vol. 26, no. 14, pp. 3891–3898, Jul. 1991, doi: 10.1007/BF01184987.
- [72] J. J Horst and J. L. Spoormaker, “Fatigue fracture mechanisms and fractography of short-glassfibre-reinforced polyamide 6,” *J. Mater. Sci.*, vol. 32, no. 14, pp. 3641–3651, 1997.
- [73] N. Despringre, Y. Chemisky, K. Bonnay, and F. Meraghni, “Micromechanical modeling of damage and load transfer in particulate composites with partially debonded interface,” *Compos. Struct.*, vol. 155, pp. 77–88, Nov. 2016, doi: 10.1016/j.compstruct.2016.06.075.
- [74] Z. Xia, T. Okabe, and W. A. Curtin, “Shear-lag versus finite element models for stress transfer in fiber-reinforced composites,” *Compos. Sci. Technol.*, vol. 62, no. 9, pp. 1141–1149, Jul. 2002, doi: 10.1016/S0266-3538(02)00072-6.
- [75] A. Pupurs, “Fiber failure and debonding in composite materials,” in *Modeling Damage, Fatigue and Failure of Composite Materials*, Elsevier, 2016, pp. 173–196.
- [76] C. M. Landis, M. A. McGlockton, and R. M. McMeeking, “An Improved Shear Lag Model for Broken Fibers in Composite Materials,” *J. Compos. Mater.*, vol. 33, no. 7, pp. 667–680, Apr. 1999, doi: 10.1177/002199839903300704.
- [77] T. Okabe, N. Takeda, Y. Kamoshida, M. Shimizu, and W. A. Curtin, “A 3D shear-lag model considering micro-damage and statistical strength prediction of unidirectional fiber-reinforced composites,” *Compos. Sci. Technol.*, vol. 61, no. 12, pp. 1773–1787, Sep. 2001, doi: 10.1016/S0266-3538(01)00079-3.
- [78] H. Zhang, Y. J. Huang, Z. J. Yang, S. L. Xu, and X. W. Chen, “A discrete-continuum coupled finite element modelling approach for fibre reinforced concrete,” *Cem. Concr. Res.*, vol. 106, pp. 130–143, Apr. 2018, doi: 10.1016/j.cemconres.2018.01.010.
- [79] A. Zhou, H. Wei, T. Liu, D. Zou, Y. Li, and R. Qin, “Interfacial technology for enhancement in steel fiber reinforced cementitious composite from nano

- to macroscale,” *Nanotechnol. Rev.*, vol. 10, no. 1, pp. 636–652, Jul. 2021, doi: 10.1515/ntrev-2021-0037.
- [80] Z. Zhao *et al.*, “A review on the properties, reinforcing effects, and commercialization of nanomaterials for cement-based materials,” *Nanotechnol. Rev.*, vol. 9, no. 1, pp. 303–322, Apr. 2020, doi: 10.1515/ntrev-2020-0023.
- [81] W. Zheng, H. Li, and Y. Wang, “Compressive behaviour of hybrid fiber-reinforced reactive powder concrete after high temperature,” *Mater. Des.*, vol. 41, pp. 403–409, Oct. 2012, doi: 10.1016/j.matdes.2012.05.026.
- [82] D. A. S. Rambo, F. de A. Silva, and R. D. Toledo Filho, “Mechanical behavior of hybrid steel-fiber self-consolidating concrete: Materials and structural aspects,” *Mater. Des.*, vol. 54, pp. 32–42, Feb. 2014, doi: 10.1016/j.matdes.2013.08.014.
- [83] T. Sugama, N. Carciello, L. E. Kukacka, and G. Gray, “Interface between zinc phosphate-deposited steel fibres and cement paste,” *J. Mater. Sci.*, vol. 27, no. 11, pp. 2863–2872, 1992, doi: 10.1007/BF01154093.
- [84] C. A. Casagrande, S. H. P. Cavalaro, and W. L. Repette, “Ultra-high performance fibre-reinforced cementitious composite with steel microfibres functionalized with silane,” *Constr. Build. Mater.*, vol. 178, pp. 495–506, Jul. 2018, doi: 10.1016/j.conbuildmat.2018.05.167.
- [85] Y.-W. Chan and S.-H. Chu, “Effect of silica fume on steel fiber bond characteristics in reactive powder concrete,” *Cem. Concr. Res.*, vol. 34, no. 7, pp. 1167–1172, Jul. 2004, doi: 10.1016/j.cemconres.2003.12.023.
- [86] Z. Wu, C. Shi, and K. H. Khayat, “Influence of silica fume content on microstructure development and bond to steel fiber in ultra-high strength cement-based materials (UHSC),” *Cem. Concr. Compos.*, vol. 71, pp. 97–109, Aug. 2016, doi: 10.1016/j.cemconcomp.2016.05.005.
- [87] Y. Lee, S.-T. Kang, and J.-K. Kim, “Pullout behavior of inclined steel fiber in an ultra-high strength cementitious matrix,” *Constr. Build. Mater.*, vol. 24, no. 10, pp. 2030–2041, Oct. 2010, doi: 10.1016/j.conbuildmat.2010.03.009.
- [88] J. Qi, Z. Wu, Z. J. Ma, and J. Wang, “Pullout behavior of straight and hooked-end steel fibers in UHPC matrix with various embedded angles,” *Constr. Build. Mater.*, vol. 191, pp. 764–774, Dec. 2018, doi: 10.1016/j.conbuildmat.2018.10.067.

- [89] H. Elaqla, N. Godin, G. Peix, M. R'Mili, and G. Fantozzi, "Damage evolution analysis in mortar, during compressive loading using acoustic emission and X-ray tomography: Effects of the sand/cement ratio," *Cem. Concr. Res.*, vol. 37, no. 5, pp. 703–713, May 2007, doi: 10.1016/j.cemconres.2007.02.008.
- [90] T. Sugiyama, M. A. B. Pomentilla, T. Hitomi, and N. Takeda, "Application of synchrotron microtomography for pore structure characterization of deteriorated cementitious materials due to leaching," *Cem. Concr. Res.*, vol. 40, no. 8, pp. 1265–1270, Aug. 2010, doi: 10.1016/j.cemconres.2009.10.009.
- [91] M. A. B. Pomentilla and T. Sugiyama, "Application of Microfocus X-Ray CT to Investigate the Frost-Induced Damage Process in Cement-Based Materials," in *Advances in Computed Tomography for Geomaterials*, Wiley, 2010, pp. 124–131.
- [92] P. D. Nieuwoudt, "Time-dependent Behaviour of Cracked Steel Fibre Reinforced Concrete," Stellenbosch University, 2016.
- [93] C. Y. Li and B. Mobasher, "Finite Element Simulations of Fiber Pullout Toughening in Fiber Reinforced Cement Based Composites," *Adv. Cem. Based Mater.*, vol. 7, no. 3–4, pp. 123–132, Apr. 1998, doi: 10.1016/S1065-7355(97)00087-4.
- [94] R. Gettu, R. Zerbino, and S. Jose, "Factors Influencing Creep of Cracked Fibre Reinforced Concrete: What We Think We Know & What We Do Not Know," 2017, pp. 3–12.
- [95] M. Ohtsu, T. Okamoto, and S. Yuyama, "Moment Tensor Analysis of Acoustic Emission for Cracking Mechanisms in Concrete," *Struct. J.*, vol. 95, no. 2, pp. 87–95, 1998.
- [96] M. Abdelrahman, M. K. ElBatanouny, and P. H. Ziehl, "Acoustic emission based damage assessment method for prestressed concrete structures: Modified index of damage," *Eng. Struct.*, vol. 60, pp. 258–264, Feb. 2014, doi: 10.1016/j.engstruct.2013.12.037.
- [97] H. Xargay, M. Ripani, P. Folino, N. Núñez, and A. Caggiano, "Acoustic emission and damage evolution in steel fiber-reinforced concrete beams under cyclic loading," *Constr. Build. Mater.*, vol. 274, p. 121831, Mar. 2021, doi: 10.1016/j.conbuildmat.2020.121831.
- [98] Y. Obara, I. Tanikura, J. Jung, R. Shintani, and S. Watanabe, "Evaluation of

- Micro-damage of Concrete Specimens under Cyclic Uniaxial Loading by X-ray CT Method,” *J. Adv. Concr. Technol.*, vol. 14, no. 8, pp. 433–443, Aug. 2016, doi: 10.3151/jact.14.433.
- [99] D. L. Carnì, C. Scuro, F. Lamonaca, R. S. Olivito, and D. Grimaldi, “Damage analysis of concrete structures by means of acoustic emissions technique,” *Compos. Part B Eng.*, vol. 115, pp. 79–86, Apr. 2017, doi: 10.1016/j.compositesb.2016.10.031.
- [100] A. Carpinteri, G. Lacidogna, F. Accornero, A. . Mpalaskas, T. E. Matikas, and D. G. Aggelis, “Influence of damage in the acoustic emission parameters,” *Cem. Concr. Compos.*, vol. 44, pp. 9–16, Nov. 2013, doi: 10.1016/j.cemconcomp.2013.08.001.
- [101] P. R. Prem and A. R. Murthy, “Acoustic emission monitoring of reinforced concrete beams subjected to four-point-bending,” *Appl. Acoust.*, vol. 117, pp. 28–38, Feb. 2017, doi: 10.1016/j.apacoust.2016.08.006.
- [102] D. G. Aggelis, D. Soulioti, M. N. Barkoula, A. S. Paipetis, T. E. Matikas, and T. Shiotani, “Acoustic Emission Monitoring Of Steel-Fiber Reinforced Concrete Beams Under Bending,” *J. Acoust. Emiss.*, vol. 28, 2010, doi: <https://www.ndt.net/?id=10822>.
- [103] T. WAJIMA, S. OKUDA, Y. CHEN, M. BESSHO, and T. NISHIYAMA, “Observation of Pore Spaces and Microcracks Using a Fluorescent Technique in Some Reservoir Rocks of Oil, Gas and Geothermal Fields in the Green Tuff Region, Japan,” *Resour. Geol.*, vol. 50, no. 3, pp. 191–200, Sep. 2000, doi: 10.1111/j.1751-3928.2000.tb00069.x.
- [104] Y. Chen, Y. Nagaya, and T. Ishida, “Observations of Fractures Induced by Hydraulic Fracturing in Anisotropic Granite,” *Rock Mech. Rock Eng.*, vol. 48, no. 4, pp. 1455–1461, Jul. 2015, doi: 10.1007/s00603-015-0727-9.
- [105] R. Lorenzoni, “Uso da microtomografia computadorizada para avaliação de danos na microestrutura de pasta de cimento submetida a carregamento cíclico e a temperaturas elevadas,” Pontifical Catholic University of Rio de Janeiro, Rio de Janeiro, Brazil, 2017.
- [106] R. Lorenzoni, “Characterization of strain-hardening cement-based composites: Deep Learning, in-situ X-ray microCT and Digital Volume Correlation,” Pontifical Catholic University of Rio de Janeiro, Rio de Janeiro, Brazil, 2021.

- [107] E. N. Landis, “Micro–macro fracture relationships and acoustic emissions in concrete,” *Constr. Build. Mater.*, vol. 13, no. 1–2, pp. 65–72, Mar. 1999, doi: 10.1016/S0950-0618(99)00009-4.
- [108] J.-Y. Wang and J.-Y. Guo, “Damage investigation of ultra high performance concrete under direct tensile test using acoustic emission techniques,” *Cem. Concr. Compos.*, vol. 88, pp. 17–28, Apr. 2018, doi: 10.1016/j.cemconcomp.2018.01.007.
- [109] W. Ren, Z. Yang, R. Sharma, C. Zhang, and P. J. Withers, “Two-dimensional X-ray CT image based meso-scale fracture modelling of concrete,” *Eng. Fract. Mech.*, vol. 133, pp. 24–39, Jan. 2015, doi: 10.1016/j.engfracmech.2014.10.016.
- [110] Y. Huang, Z. Yang, W. Ren, G. Liu, and C. Zhang, “3D meso-scale fracture modelling and validation of concrete based on in-situ X-ray Computed Tomography images using damage plasticity model,” *Int. J. Solids Struct.*, vol. 67–68, pp. 340–352, Aug. 2015, doi: 10.1016/j.ijsolstr.2015.05.002.
- [111] W. TIAN, F. DANG, and Y. XIE, “Quantitative study on crack of meso-damage and fracture concrete based on CT technique,” *Sadhana*, vol. 40, no. 1, pp. 263–276, Feb. 2015, doi: 10.1007/s12046-014-0305-y.
- [112] J. Jung, M. Hamachi, Y. Obara, I. Tanikura, and S. Watanabe, “Analysis of Damage in Specimen Under Cyclic Uniaxial Loading Test by X-Ray CT Method,” 2014.
- [113] D. Lei, L. Yang, W. Xu, P. Zhang, and Z. Huang, “Experimental study on alarming of concrete micro-crack initiation based on wavelet packet analysis,” *Constr. Build. Mater.*, vol. 149, pp. 716–723, Sep. 2017, doi: 10.1016/j.conbuildmat.2017.05.159.
- [114] M. Lukovic, E. Schlangen, B. Savija, G. Ye, and O. Çopuroglu, “Using nano-indentation and microscopy to obtain mechanical properties,” in *15th Euroseminar on Microscopy Applied to Building Materials*, 2015, pp. 121–127.
- [115] A. B. D. N. T. ABNT, “ABNT NBR 16697: Cimento Portland – Requisitos,” 2018.
- [116] A. B. D. N. T. ABNT, “ABNT NBR 15823-2: Concreto auto-adensável Parte 2: Determinação do espalhamento e do tempo de escoamento - Método do cone de Abrams,” 2010.

- [117] A. B. D. N. T. ABNT, “ABNT NBR 5739 - Concreto - Ensaio de compressão de corpos de prova cilíndricos.” pp. 1–13, 2018.
- [118] A. B. D. N. T. ABNT, “ABNT NBR 8522 - Concreto - Determinação dos módulos estáticos de elasticidade e de deformação à compressão,” 2017.
- [119] A. C. C. Trindade, “Desenvolvimento e comportamento mecânico de compósitos geopoliméricos têxteis reforçados com fibra de juta,” Pontifical Catholic University of Rio de Janeiro, 2017.
- [120] R. de S. Castoldi, “Propriedades mecânicas e durabilidade de concretos reforçados com fibras de polipropileno e sisal.,” Pontifical Catholic University of Rio de Janeiro, 2018.
- [121] ASTM - American Society for Testing and Materials, “D3967 – 16 Standard Test Method for Splitting Tensile Strength of Intact Rock Core Specimens,” 2016. doi: 10.1520/D3967-16.
- [122] P. Lawrence, “Some theoretical considerations of fibre pull-out from an elastic matrix,” *J. Mater. Sci.*, vol. 7, no. 1, pp. 1–6, Jan. 1972, doi: 10.1007/BF00549541.
- [123] V. Laws, P. Lawrence, and R. W. Nurse, “Reinforcement of brittle matrices by glass fibres,” *J. Phys. D. Appl. Phys.*, vol. 6, no. 5, p. 309, Mar. 1973, doi: 10.1088/0022-3727/6/5/309.
- [124] Gopalaralnam V and Shah S, “Failure mechanisms and fracture of fiber reinforced concrete,” in *American Concrete Institute, ACI Special Publication*, 1987, pp. 1–25.
- [125] T. Y. Lim, P. Paramasivam, and S. L. Lee, “Analytical Model for Tensile Behavior of Steel-Fiber Concrete,” *ACI Mater. J.*, vol. 84, no. 4, 1987, doi: 10.14359/1454.
- [126] H. Stang, Z. Li, and S. P. Shah, “Pullout Problem: Stress versus Fracture Mechanical Approach,” *J. Eng. Mech.*, vol. 116, no. 10, pp. 2136–2150, Oct. 1990, doi: 10.1061/(ASCE)0733-9399(1990)116:10(2136).
- [127] C. K. Y. Leung and V. C. Li, “Effect of fiber inclination on crack bridging stress in brittle fiber reinforced brittle matrix composites,” *J. Mech. Phys. Solids*, vol. 40, no. 6, pp. 1333–1362, Aug. 1992, doi: 10.1016/0022-5096(92)90018-W.
- [128] J. M. Alwan, A. E. Naaman, and P. Guerrero, “Effect of mechanical clamping on the pull-out response of hooked steel fibers embedded in

- cementitious matrices,” *Concr. Sci. Eng.*, vol. 1, no. 1, pp. 15–25, 1999.
- [129] D. Ngo and A. C. Scordelis, “Finite Element Analysis of Reinforced Concrete Beams,” *ACI J. Proc.*, vol. 64, no. 3, 1967, doi: 10.14359/7551.
- [130] J. F. Davalos, Y. Chen, and I. Ray, “Numerical Modeling for the Interface Bond of Concrete and FRP Bar,” in *Earth & Space 2008*, Sep. 2008, pp. 1–11, doi: 10.1061/40988(323)27.
- [131] Laura N. Lowes, Jack P. Moehle, and Sanjay Govindjee, “Concrete-Steel Bond Model for Use in Finite Element Modeling of Reinforced Concrete Structures,” *ACI Struct. J.*, vol. 101, no. 4, 2004, doi: 10.14359/13336.
- [132] Giorgio Monti, Filip C. Filippou, and Enrico Spacone, “Analysis of Hysteretic Behavior of Anchored Reinforcing Bars,” *ACI Struct. J.*, vol. 94, no. 3, 1997, doi: 10.14359/477.
- [133] X. Liu, R. Duddu, and H. Waisman, “Discrete damage zone model for fracture initiation and propagation,” *Eng. Fract. Mech.*, vol. 92, pp. 1–18, Sep. 2012, doi: 10.1016/j.engfracmech.2012.04.019.
- [134] M. V. Cid Alfaro, A. S. J. Suiker, and R. De Borst, “Transverse Failure Behavior of Fiber-epoxy Systems,” *J. Compos. Mater.*, vol. 44, no. 12, pp. 1493–1516, Jun. 2010, doi: 10.1177/0021998309360941.
- [135] M. Abbas, B. Bary, and L. Jason, “A 3D mesoscopic frictional cohesive zone model for the steel-concrete interface,” *Int. J. Mech. Sci.*, vol. 237, p. 107819, Jan. 2023, doi: 10.1016/j.ijmecsci.2022.107819.
- [136] G. Alfano and E. Sacco, “Combining interface damage and friction in a cohesive-zone model,” *Int. J. Numer. Methods Eng.*, vol. 68, no. 5, pp. 542–582, Oct. 2006, doi: 10.1002/nme.1728.
- [137] M. Rezaadeh, V. Carvelli, and A. Veljkovic, “Modelling bond of GFRP rebar and concrete,” *Constr. Build. Mater.*, vol. 153, pp. 102–116, Oct. 2017, doi: 10.1016/j.conbuildmat.2017.07.092.
- [138] Y. N. Rabotov, *Creep problems in structural members*. North Holland, Amsterdam, 1969.
- [139] J. Lubliner, J. Oliver, S. Oller, and E. Oñate, “A plastic-damage model for concrete,” *Int. J. Solids Struct.*, vol. 25, no. 3, pp. 299–326, 1989, doi: 10.1016/0020-7683(89)90050-4.
- [140] T. Jankowiak and T. Lodygowski, “Identification of parameters of concrete damage plasticity constitutive model,” *Found. Civ. Environ. Eng.*, no. 6, pp.

- 53–69, 2005.
- [141] G. Lin, P. H. Geubelle, and N. R. Sottos, “Simulation of fiber debonding with friction in a model composite pushout test,” *Int. J. Solids Struct.*, vol. 38, no. 46–47, pp. 8547–8562, Nov. 2001, doi: 10.1016/S0020-7683(01)00085-3.
- [142] A. Ali, A. Lo Conte, C. A. Biffi, and A. Tuissi, “Cohesive surface model for delamination and dynamic behavior of hybrid composite with SMA-GFRP interface,” *Int. J. Light. Mater. Manuf.*, vol. 2, no. 2, pp. 146–155, Jun. 2019, doi: 10.1016/j.ijlmm.2019.01.006.
- [143] M. A. Minnicino and M. H. Santare, “Modeling the progressive damage of the microdroplet test using contact surfaces with cohesive behavior,” *Compos. Sci. Technol.*, vol. 72, no. 16, pp. 2024–2031, Nov. 2012, doi: 10.1016/j.compscitech.2012.09.009.
- [144] P. P. Camanho, C. G. Davila, and M. F. de Moura, “Numerical Simulation of Mixed-Mode Progressive Delamination in Composite Materials,” *J. Compos. Mater.*, vol. 37, no. 16, pp. 1415–1438, Aug. 2003, doi: 10.1177/0021998303034505.
- [145] A. N. Corina, N. Opedal, T. Vrålstad, R. Skorpa, and S. Sangesland, “The Effect of Casing-Pipe Roughness on Cement-Plug Integrity,” *SPE Drill. Complet.*, vol. 35, no. 02, pp. 237–251, Jun. 2020, doi: 10.2118/194158-PA.
- [146] M. Tabatabaei, A. Dahi Taleghani, and N. Alem, “Measurement of mixed mode interfacial strengths with cementitious materials,” *Eng. Fract. Mech.*, vol. 223, p. 106739, Jan. 2020, doi: 10.1016/j.engfracmech.2019.106739.
- [147] M. Kamali, M. Khalifeh, E. Eid, and A. Saasen, “Experimental Study of Hydraulic Sealability and Shear Bond Strength of Cementitious Barrier Materials,” *J. Energy Resour. Technol.*, vol. 144, no. 2, Feb. 2022, doi: 10.1115/1.4051269.
- [148] D. Heras Murcia, M. Reda Taha, and J. Stormont, “Innovative Sealant for Mitigating Methane Gas Emission in Abandoned Oil and Gas Wells,” Oct. 2022, doi: 10.2118/211726-MS.
- [149] R. Coquard and P. Cerasi, “Finite element modeling of a dual-cement well plug,” in *Proceedings of 15th International Conference on Greenhouse Gas Control Technologies, GHGT-15*, Mar. 2021, pp. 1–8.
- [150] L. Jin, M. Liu, R. Zhang, and X. Du, “3D meso-scale modelling of the

- interface behavior between ribbed steel bar and concrete,” *Eng. Fract. Mech.*, vol. 239, p. 107291, Nov. 2020, doi: 10.1016/j.engfracmech.2020.107291.
- [151] L. Jin, X. Li, R. Zhang, and X. Du, “Bond-slip behavior between concrete and deformed rebar at elevated temperature: Mesoscale simulation and formulation,” *Int. J. Mech. Sci.*, vol. 205, p. 106622, Sep. 2021, doi: 10.1016/j.ijmecsci.2021.106622.
- [152] L. Chiriatti, H. Mercado-Mendoza, K. L. Apedo, C. Fond, and F. Feugeas, “A study of bond between steel rebar and concrete under a friction-based approach,” *Cem. Concr. Res.*, vol. 120, pp. 132–141, Jun. 2019, doi: 10.1016/j.cemconres.2019.03.019.
- [153] Dassault Systèmes SIMULIA Corporation, “ABAQUS Analysis User’s Manual 6.11,” Providence, RI, USA, 2011.
- [154] V. A. Yastrebov, “Introduction to Computational Contact Mechanics, Part I. Basics (Lecture notes).” Paris, France, 2010.
- [155] S. B. Cox, “The Influence of Concrete Heterogeneity on the Pull-out Behaviour of Steel Fibres,” Eindhoven University of Technology, Eindhoven, Netherlands, 2015.
- [156] C. K. Y. Leung and N. Shapiro, “Optimal Steel Fiber Strength for Reinforcement of Cementitious Materials,” *J. Mater. Civ. Eng.*, vol. 11, no. 2, pp. 116–123, May 1999, doi: 10.1061/(ASCE)0899-1561(1999)11:2(116).
- [157] V. C. Li, Y. Wang, and S. Backer, “Effect of inclining angle, bundling and surface treatment on synthetic fibre pull-out from a cement matrix,” *Composites*, vol. 21, no. 2, pp. 132–140, Mar. 1990, doi: 10.1016/0010-4361(90)90005-H.
- [158] H. A. Rifaie, “Comparative Assessment of Commonly Used Concrete Damage Plasticity Material Parameters,” *Eng. Trans.*, vol. 70, no. 2, pp. 157–181, 2022.
- [159] L. M. e Silva, A. L. Christoforo, and R. C. Carvalho, “Calibration of Concrete Damaged Plasticity Model parameters for shear walls,” *Matéria (Rio Janeiro)*, vol. 26, no. 1, 2021, doi: 10.1590/s1517-707620210001.1244.
- [160] U. M. Angst *et al.*, “The steel–concrete interface,” *Mater. Struct.*, vol. 50, no. 2, p. 143, Apr. 2017, doi: 10.1617/s11527-017-1010-1.

- [161] T. . Soylev and R. François, “Quality of steel–concrete interface and corrosion of reinforcing steel,” *Cem. Concr. Res.*, vol. 33, no. 9, pp. 1407–1415, Sep. 2003, doi: 10.1016/S0008-8846(03)00087-5.
- [162] M. Al Ramadan, S. Salehi, G. Kwatia, C. Ezeakacha, and C. Teodoriu, “Experimental investigation of well integrity: Annular gas migration in cement column,” *J. Pet. Sci. Eng.*, vol. 179, pp. 126–135, Aug. 2019, doi: 10.1016/j.petrol.2019.04.023.
- [163] K. Beltrán-Jiménez *et al.*, “Restoration of annular zonal isolation using localized casing expansion (LCE) technology: Treatment of near-horizontal test sections containing a free-water channel,” *J. Pet. Sci. Eng.*, vol. 208, p. 109792, Jan. 2022, doi: 10.1016/j.petrol.2021.109792.
- [164] K. Beltrán-Jiménez *et al.*, “Assessment of Corrosion in the Interface Casing - Cement and its Effect on the Leakage Potential,” Mar. 2021, doi: 10.2118/204080-MS.
- [165] A. Lavrov, M. Bhuiyan, and A. Stroisz, “Push-out test: Why bother?,” *J. Pet. Sci. Eng.*, vol. 172, pp. 297–302, Jan. 2019, doi: 10.1016/j.petrol.2018.09.067.
- [166] A. Lavrov and M. Torsæter, *Physics and Mechanics of Primary Well Cementing*. Cham: Springer International Publishing, 2016.
- [167] T. Vrålstad, A. Saasen, E. Fjær, T. Øia, J. D. Ytrehus, and M. Khalifeh, “Plug and abandonment of offshore wells: Ensuring long-term well integrity and cost-efficiency,” *J. Pet. Sci. Eng.*, vol. 173, pp. 478–491, Feb. 2019, doi: 10.1016/j.petrol.2018.10.049.
- [168] N. J. Welch, L. P. Frash, D. H. Harp, and J. W. Carey, “Shear strength and permeability of the cement-casing interface,” *Int. J. Greenh. Gas Control*, vol. 95, p. 102977, Apr. 2020, doi: 10.1016/j.ijggc.2020.102977.
- [169] S. Sindhuja and P. Bhuvaneshwari, “Push-Out Test on Low-Density Concrete Filled Stiffened Steel Tubular Columns,” *Int. J. Civ. Eng.*, vol. 19, no. 12, pp. 1399–1413, Dec. 2021, doi: 10.1007/s40999-021-00638-4.
- [170] G. Evans and L. G. Carter, “Bounding studies of cementing compositions to pipe and formations,” in *Drilling and Production Practice*, OnePetro, 1962, pp. 1–5.
- [171] L. G. Carter and G. W. Evans, “A Study of Cement-Pipe Bonding,” *J. Pet. Technol.*, vol. 16, no. 02, pp. 157–160, Feb. 1964, doi: 10.2118/764-PA.

- [172] J. . De Andrade, S. . Sangesland, R. . Skorpa, J. . Todorovic, and T. . Vrålstad, “Experimental Laboratory Setup for Visualization and Quantification of Cement-Sheath Integrity,” *SPE Drill. Complet.*, vol. 31, no. 04, pp. 317–326, Dec. 2016, doi: 10.2118/173871-PA.
- [173] M. Tabatabaei, L. Santos, A. A. Al Hassan, and A. Dahi Taleghani, “Surface-Modified Graphite Nanoplatelets to Limit Deteriorative Impacts of Oil-Based Mud Residuals on Cement Bonding,” *SPE Drill. Complet.*, vol. 38, no. 02, pp. 235–242, Jun. 2023, doi: 10.2118/210155-PA.
- [174] H. Cheng, B. C. Pinheiro, S. F. Estefen, L. Xu, C. M. Paz, and M. Duan, “Ultimate bending strength of sandwich pipes with actual interlayer behavior,” *Thin-Walled Struct.*, vol. 161, p. 107476, Apr. 2021, doi: 10.1016/j.tws.2021.107476.
- [175] A. Lavrov *et al.*, “Effect of electric field on push-out strength of cemented steel pipes,” *AIMS Mater. Sci.*, vol. 8, no. 3, pp. 373–389, 2021, doi: 10.3934/matersci.2021024.
- [176] G. I. Barenblatt, “The Mathematical Theory of Equilibrium Cracks in Brittle Fracture,” 1962, pp. 55–129.
- [177] D. S. Dugdale, “Yielding of steel sheets containing slits,” *J. Mech. Phys. Solids*, vol. 8, no. 2, pp. 100–104, May 1960, doi: 10.1016/0022-5096(60)90013-2.
- [178] Y. Feng, X. Li, and K. E. Gray, “Development of a 3D numerical model for quantifying fluid-driven interface debonding of an injector well,” *Int. J. Greenh. Gas Control*, vol. 62, pp. 76–90, Jul. 2017, doi: 10.1016/j.ijggc.2017.04.008.
- [179] J. Jiang, J. Li, G. Liu, H. Yang, W. Li, and M. He, “Numerical study on debonding failure of cement plug/formation interface in open-hole temporary abandoned wells,” *J. Adhes. Sci. Technol.*, vol. 34, no. 22, pp. 2405–2423, Nov. 2020, doi: 10.1080/01694243.2020.1764699.
- [180] J. Jiang *et al.*, “Numerical simulation investigation on fracture debonding failure of cement plug/casing interface in abandoned wells,” *J. Pet. Sci. Eng.*, vol. 192, p. 107226, Sep. 2020, doi: 10.1016/j.petrol.2020.107226.
- [181] H. M. Giasuddin, J. G. Sanjayan, and P. G. Ranjith, “Analysis of Interfacial Debonding of Geopolymer Annular Sealing in CO₂ Geo-sequestration Wellbore,” *Energy Procedia*, vol. 37, pp. 5681–5691, 2013, doi:

10.1016/j.egypro.2013.06.490.

A. Appendix A

In Chapter 3, the results of the experimental tests refer to representative curves of the experimental tests carried out at the Laboratório de Estruturas e Materiais (LEM/DEC) at PUC-Rio. In this section, the uniaxial tensile and compressive tests for all specimens tested are shown in Figures A.1 to A.4.

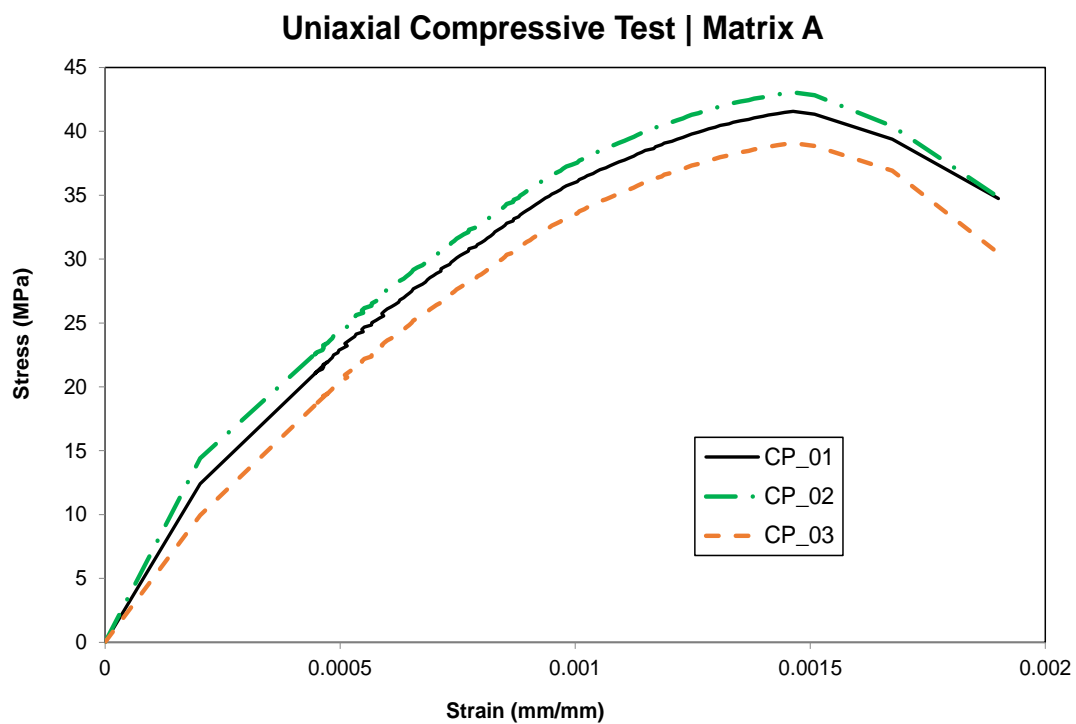


Figure A.1 – Uniaxial compressive tests for Matrix A.

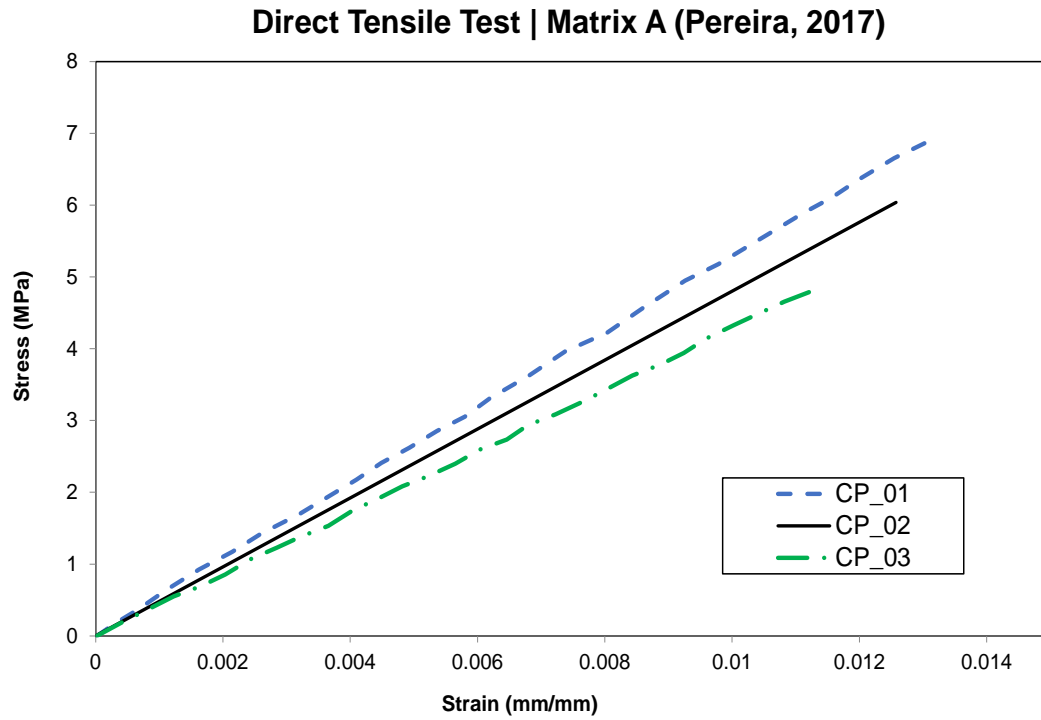


Figure A.2 – Uniaxial tensile tests for Matrix A [13].

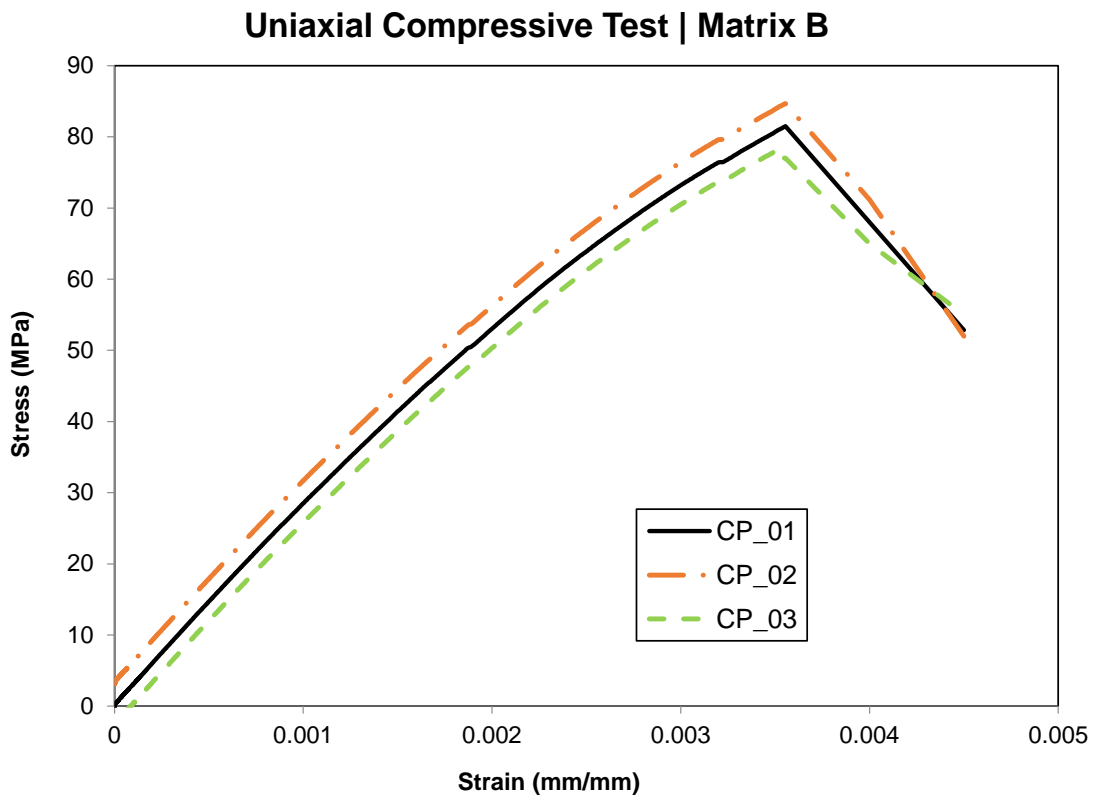


Figure A.3 – Uniaxial compressive tests for Matrix B.

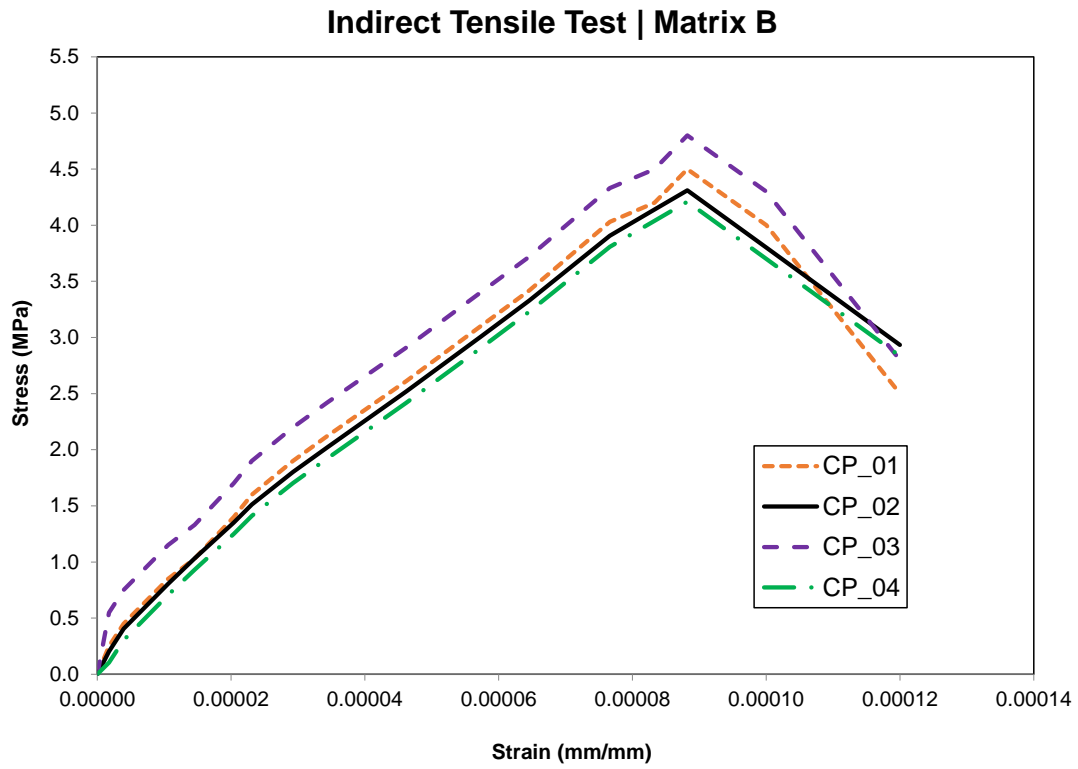


Figure A.4 – Indirect tensile tests for Matrix B.

B. Appendix B

In Chapter 3, images from the microCT before and after the pullout tests are presented. Since the microcracks in the images are very small and thin, visualizing them with the naked eye is challenging, which led to the marking of the images available in Chapter 3. For complementary purposes, Figures B.1 to B.8 show the same microCT images after the pullout test without the markings for each of the analyzed scenarios.

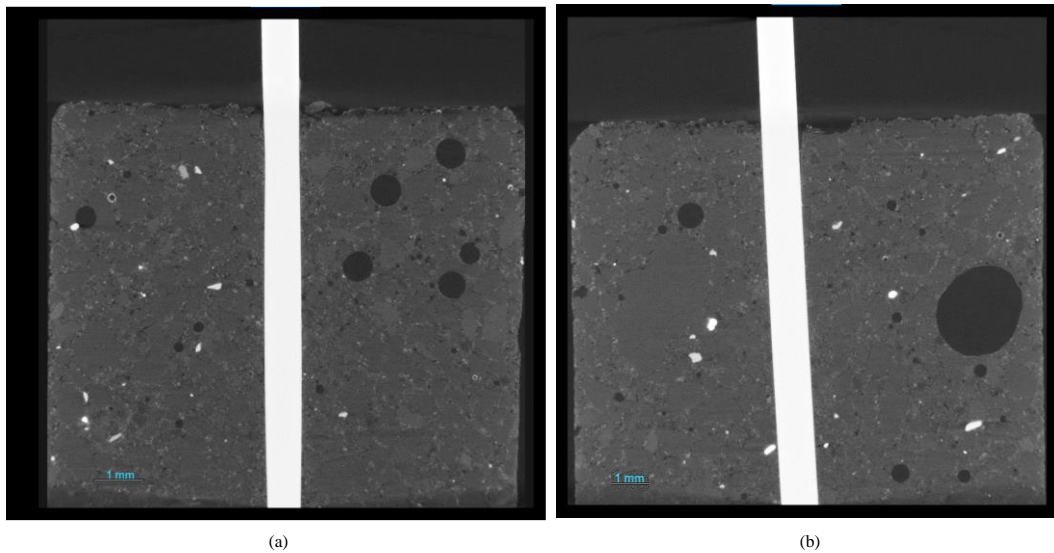


Figure B.1 – Micrograph (0.4x) of straight steel fiber in Matrix A: (a) before pullout; (b) partial debonding (fiber pullout of 7 mm). Microcracks/damage in (b) are not marked in red.

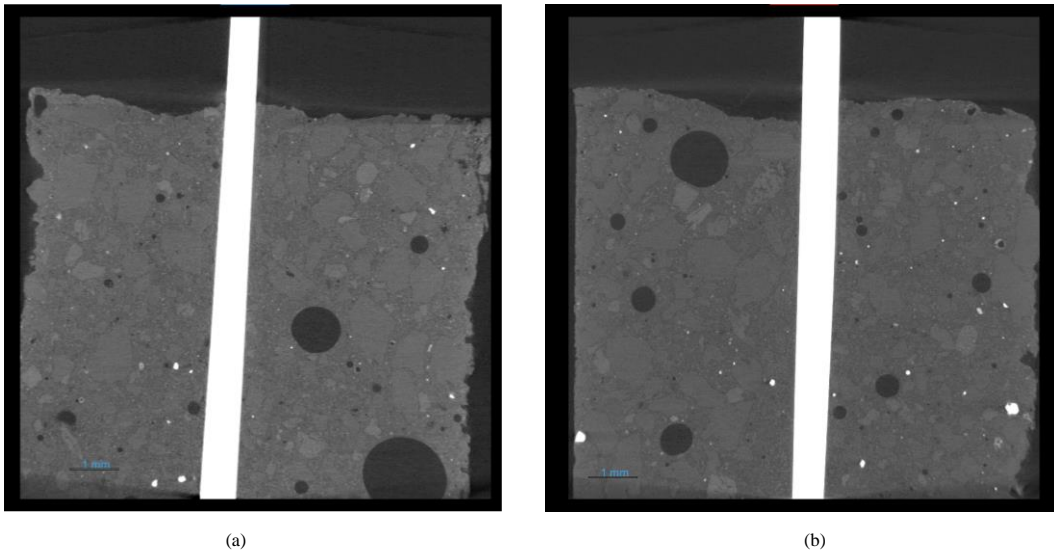


Figure B.2 – Micrograph (0.4x) of hooked-end steel fiber in Matrix A: (a) before pullout; (b) partial debonding (fiber pullout of 7 mm). Microcracks/damage in (b) are not marked in red.

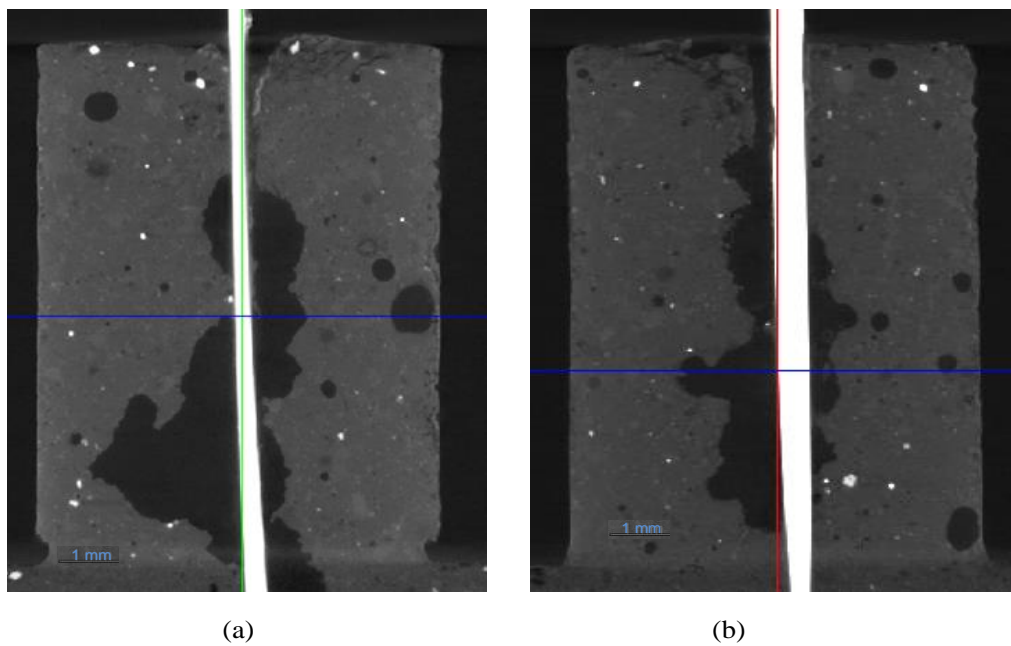


Figure B.3 – Micrograph (0.4x) of straight steel fiber in poorly consolidated Matrix A: (a) before pullout; (b) partial debonding (fiber pullout of 7 mm). Microcracks/damage in (b) are not marked in red.

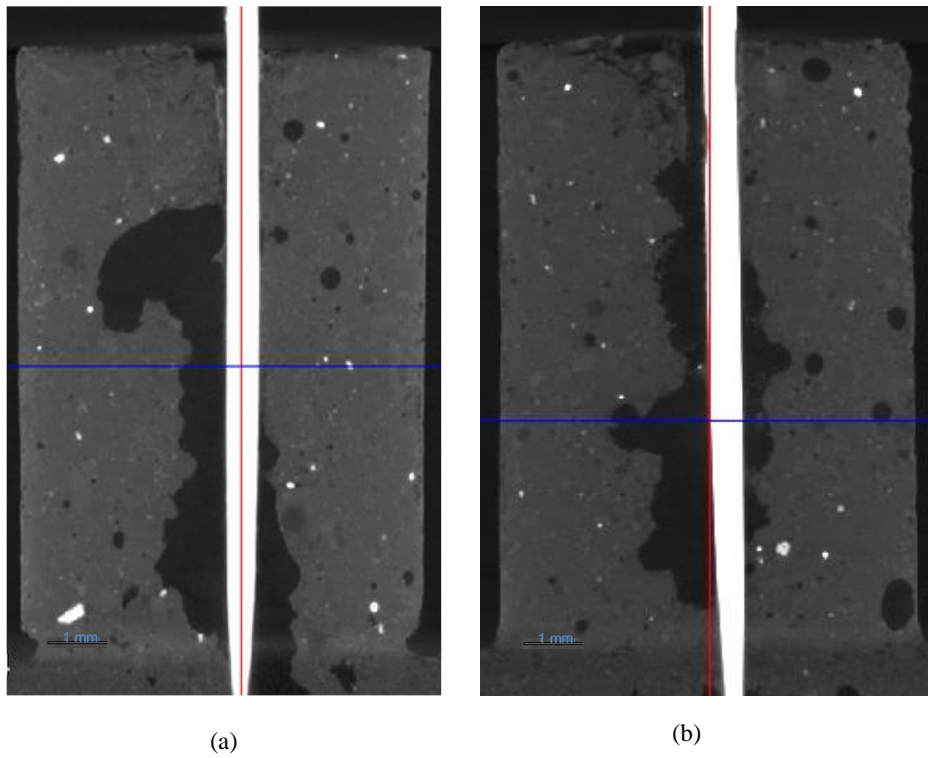


Figure B.4 – Micrograph (0.4x) of hooked-end steel fiber in poorly consolidated Matrix A: (a) before pullout; (b) partial debonding (fiber pullout of 7 mm). Microcracks/damage in (b) are not marked in red.

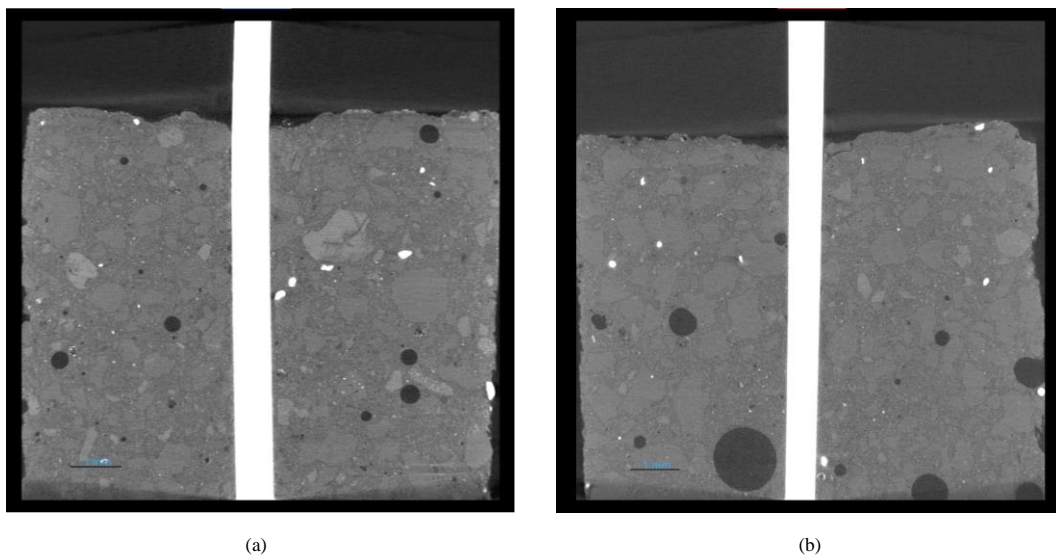


Figure B.5 – Micrograph (0.4x) of straight steel fiber in Matrix B: (a) before pullout; (b) partial debonding (fiber pullout of 7 mm). Microcracks/damage in (b) are not marked in red.

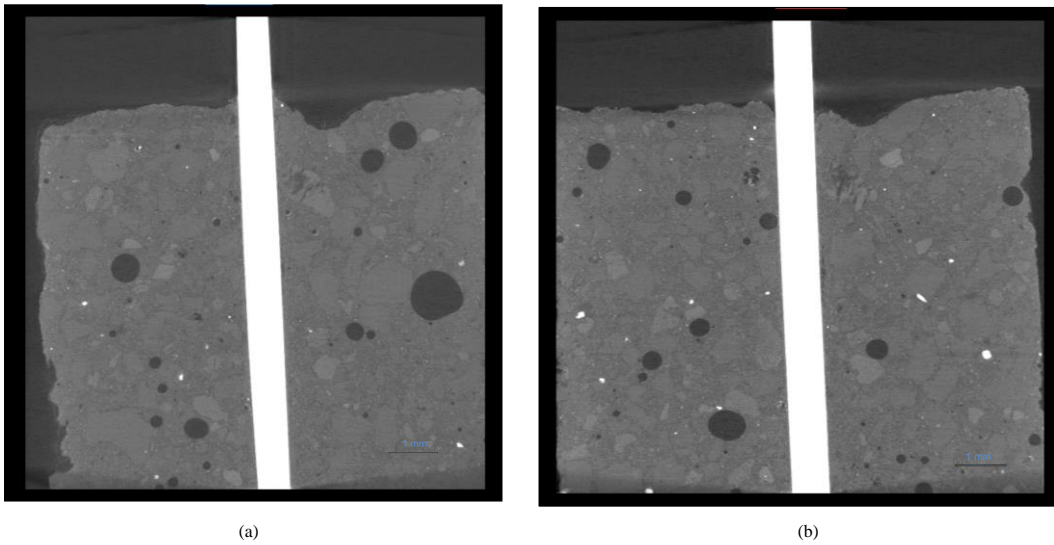


Figure B.6 – Micrograph (0.4x) of hooked-end steel fiber in Matrix B: (a) before pullout; (b) partial debonding (fiber pullout of 7 mm). Microcracks/damage in (b) are not marked in red.

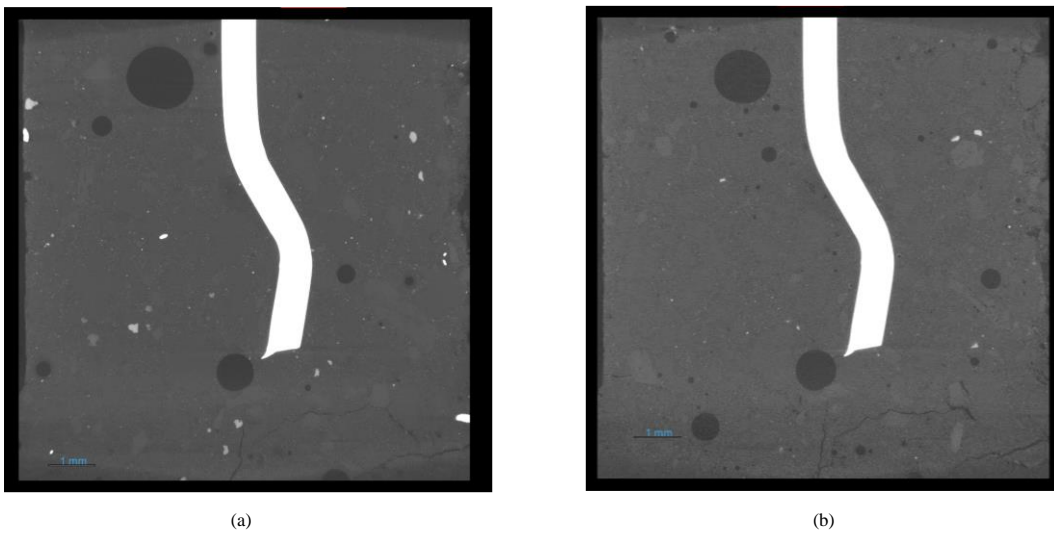


Figure B.7 – Micrograph (0.4x) of the hook region in Matrix B: (a) before pullout; (b) partial debonding (fiber pullout of 7 mm). Microcracks/damage in (b) are not marked in red.

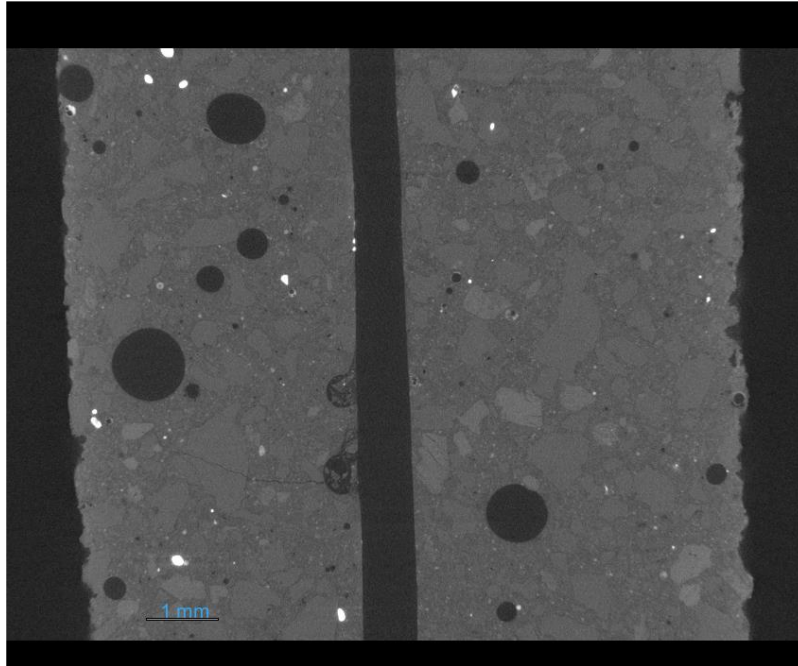


Figure B.8 – Micrograph (0.4x) of the hook region in Matrix B after entire pullout.
Microcracks/damage are not marked in red.